Conversion of Methane Using Two- and Three-Dimensional Metal Carbide Catalysts

by

Raj Kantikumar Thakur

A dissertation submitted to the Graduate Faculty of
Auburn University
in partial fulfillment of the
requirements for the Degree of
Doctor of Philosophy

Auburn, Alabama
May 2, 2020

natural gas, MXenes, carbides, zeolites, *syngas*, methane, aromatics, heterogenous catalysis

Approved by

Carlos A. Carrero, Assistant Professor of Chemical Engineering
Sushil Adhikari, Alumni Associate Professor of Biosystem Engineering
Zhihua Jiang, APPF Assistant Professor of Chemical Engineering
Andrew Adamczyk, Assistant Professor of Chemical Engineering

Abstract

After various decades of research aiming to discover desirable catalysts for the direct conversion of methane into valuable products, the modern chemical industry is calling forth finding alternative materials to on-purpose produce commodity chemicals. The emergence of new materials with attractive bulk, surface, and thermal properties, no matter its initial intended application, is becomes appealing to explore their catalytic activity in upgrading of natural gas. The discovery of two-dimensional metal carbides, so-called MXenes, has represented a breakthrough in various fields, especially in the energy conversion-storage sectors, and we aim to motivate the heterogeneous catalysts community by showing the attractiveness of MXenes towards upgrading natural gas. Multilayered vanadium carbide (*m*-V_2CT_x MXene) exhibits a unique morphology as compared to its three-dimensional counterpart, thus giving rise to novel and unique properties that interestingly were not yet explored in heterogeneous catalysis until our studies were reported. We found that at high temperatures (> 600 ^{0}C), the multilayered structure persists up-to a certain extent when reacting with nitrogen and hydrogen, while partial (V_2CT_x decorated with V_2O_3) and total (V_2CT_x transform into V_2O_5) oxidation occurs in the presence of CO_2 and air, respectively.

The unprecedented thermal and chemical stability of *m*-V_2CT_x triggered our interest in investigating the catalytic reactivity for methane conversion. We focused primarily on two of the most relevant reactions that the modern chemical industry is still waiting for the "*eureka*" moment for large scale implementation, the *Dry Reforming of Methane* (DRM), and *Methane Dehydroaromatization* (MDA).

We discovered that under DRM, the pristine *m*-V_2CT_x serves as a precursor to generating V_2O_3-V_8C_7/*m*-V_2CT_x, which shows attractive activity, unprecedented selectivity (H_2/CO~1), and

stability, which are amongst the major challenges faced when using the state-of-the-art nickel-based catalysts. Combining kinetic and spectroscopy studies, complemented with fundamentally designed isotopic labeled experiments, we provide mechanistic insights into the genesis of *m*-V_2CT_x as a selective and coke-resistant catalyst for DRM. While performing the studies mentioned above, we also discovered that under certain conditions, the intrinsic confined space within the *m*-V_2CT_x leads to the conversion of methane into aromatics. Herein, we show that the *m*-V_2CT_x can efficiently convert CH_4 into C_6H_6 with comparable activity to the-state-of-the-art Mo/ZSM-5. Finally, our unique results and the knowledge accumulated using *m*-V_2CT_x will be further expanded to develop supported metal oxide-based catalysts for industrially attractive reactions at elevated temperatures (>500°C).

Acknowledgments

When I began thinking about writing this part of my dissertation, I was amazed by the number of people who assisted me and deserves my sincere thankfulness. I tried my best to include all of them. However, I may have missed unintentionally some of them, and I would like to ask them for their forgiveness.

First, the words cannot express how grateful I feel towards my Ph.D. advisor Dr. Carlos A. Carrero, for his kindness and the unlimited support during my doctoral study at Auburn University. His enthusiasm and confidence in me were encouraging to develop and implement ideas and enabling thinking out of the box methodology. The success and position which I achieved could not have been possible without his motivation, encouragement and constructive feedback. He is a great researcher, an expert in the field of heterogeneous catalysis. Thus, it was a very rich, extremely helpful and fruitful experience during my doctoral study.

I want to thank the passionate and dedicated undergraduate students: Justin Smith, Megan Hoffman, Reid Adams, Whitney Stidham, Kaitlyn Lawrence, Natalie Stephens, and Nico Rivero, who helped me in the laboratory during last years and were also an important part of my successful outcome.

My biggest thanks to Jorge Moncada and Michael Julin. It was a very good coincidence to start up Ph.D. together. We started building up the laboratory together and got to learn a lot from each other's experiences. Rafael Sanchez, with his vast industrial experience, was very helpful, encouraging, and an inspiring figure.

I also would like to thank our collaborators Dr. Majid Beidaghi from the Materials Engineering Department at Auburn University, Dr Bruce Tatarchuk from the Chemical Engineering Department, Auburn University, Dr Sushil Adhikari from the Biosystem Engineering Department,

Auburn University, Dr Ive Hermans from the University of Wisconsin, Madison, Dr. Abhaya Datye from the University of New Mexico and Dr. Tej Choksi from the National University of Singapore for their support during my Ph.D.

I am grateful for the support from Dr Armin VahidMohammadi and Dr Majid Beidaghi for providing the V_2AlC MAX and V_2CT_x MXene phases and for the fruitful discussions on these material characterizations during the publication stage. I would like to thank Dr Bruce Tatarchuk and his student Mingyang Chi regarding the XPS measurements for the V_2CT_x MXenes and Mo/ZSM-5 samples. I also appreciate the support from Dr. Sushil Adhikari and his research team for providing access to the research facilities (N_2 physisorption, TGA, pyroprobe setup).

The kind help of Dr. Ive Hermans and his team at the University of Wisconsin-Madison is highly appreciated. I also appreciate their hospitality when I visited them to ran XPS, ICP and TPD experiments. They unconditionally shared their characterization techniques, and this definitely accelerated my progress.

I am grateful to the Department of Chemical Engineering at Auburn University and to my committee members: Dr. Sushil Adhikari, Dr. Zhihua Jiang, Dr. Andrew Adamczyk, and Dr. Martin Medina for their support and insights, that undoubtedly enhanced the quality of the research I pursued in my Ph.D. Special thanks to Dr Mario Eden, Dr Allan David, Elaine Manning, Karen Cochran, and Naomi Gehling for the administrative support I also would like to thank the entire Department of Chemical Engineering and the South Eastern Center for CO_2 Capture Utilization and Sequestration (SECCUS) for providing the funding to work in various projects, I was involved in during my time at Dr. Carrero's lab.

Our group thank Brian Schwieker for support with the construction of the reaction set up, Matt Montgomery for constructing the required stainless steel/glass/quartz-made parts, and Jeffrey

Hollis and his team for ensuring the optimal operation of the network interface between all the equipment connected to the reaction set up for the successful completion of this work.

A mixture of sincere apology with a lot of thanks to my lovely fiancée Prachi. All the extra time that I dedicated to the work was discounted from the precious time of being together with her. Thus, I owe her every single success I achieved in my career.

Last but not the least, I would like to thank my parents, my brother and my best friend Kerul Suthar for their unlimited support, encouragement and the efforts they extended.

Table of Contents

List of Tables

List of Figures

List of Abbreviations

NG	Natural Gas
LPG	Liquified Petroleum Gas
NGL	Natural Gas Liquid
FT	Fischer Tropsch
SMR	Steam Methane Reforming
DRM	Dry Reforming of Methane
GHSV	Gas Hourly Space Velocity
GC	Gas Chromatography
UHP	Ultra High Pure
MFC	Mass Flow Controller
TCD	Thermal Conductivity Detector
FID	Flame Ionization Detector
BET	Brunauer Emmett Teller
XRD	X-ray Diffraction
SEM	Scanning Electron Microscopy
XPS	X-ray Photoelectron Spectroscopy
BE	Binding Energy
EDS	Energy Dispersive Spectroscopy
IWI	Incipient Wetness Impregnation
AMV	Ammonium Meta Vanadate
MDA	Methane De-hydro Aromatization
ZSM-5	Zeolite Socony Mobil-5

CCGT	Combined Cycle Gas Turbine
OPEX	Operating Expenses
CHP	Combined Heat and Power
CNG	Compressed Natural Gas
2D	Two Dimensional
3D	Three Dimensional
OCM	Oxidative Coupling of Methane
BAS	Brønsted Acid Sites
LAS	Lewis Acid Sites
GHG	Green House Gas
ODH	Oxidative Dehydrogenation
RWGS	Reverse Water Gas Shift
WGS	Water Gas Shift
BTX	Benzene Toluene and Xylene

Chapter 1: Natural gas market and its conversion pathways

1.1.Introduction

The depletion of crude oil reserves and climate concerns are the strong driving forces to switch towards more sustainable processes.[1-3] Extensive research is being done to replace the decreasing non-renewable energy resources with renewable ones, and heterogeneous catalysis plays a pivotal role in achieving this goal. Natural gas, primarily composed of methane (CH_4), is considered as the cleanest of all the fossil fuels.[4] These qualities enterprise the operation of natural gas in homes/businesses, centralized power generation, and transport sector, etc. Additionally, the natural gas combustion generates 25 - 30% less CO_2 than oil and 40 - 50% less than coal.[5, 6] The copiousness of methane as the main constituent in natural gas, shale gas, and methane hydrates, etc. has prompted efforts towards its utilization and conversion into valuable/desirable chemicals and fuels. Consequently, natural gas is considered as an attractive alternative feedstock to fill the gap between conventional and non-conventional energy resources.[4] In the modern era of diminishing natural resources, methane conversion into desirable petroleum product/intermediate is not only an efficient way to convert natural gas but also results in the reduction of greenhouse gases (GHG), which will ultimately result in improved life quality.[7]

The place of origin determines the natural gas composition, although usually, the methane content is greater than 80%.

1.1.1 Applications of Natural gas

a. Electric power generation, often for the co-generation of electricity and heat (CHP; combined heat and power). The power generation sector remains the major consumer of natural gas in most of the regions; however, the price of the natural gas fuel will ultimately determine the range of its usage. With the introduction of new policies

scenario, the combined-cycle gas turbines (CCGT's) will remain as a preferred choice for the new power stations depending upon the plant specifications.[5] Combining plant operation economic with environmental aspects, the CCGTs have higher thermal efficiencies, relatively lower operation costs (OPEX) and fast construction time. Apart from the mentioned benefits, they have lower CO_2 emissions as compared to other fossil fuels-based technologies.[8]

b. Industrial applications such as drying, heating and mechanical drives (turbines, gas motors) as well as industrially integrated CHP
c. Residential and commercial (heating, cooking, cooling).
d. As fuel for the transportation sector (buses, trucks, cars, trains or ships) in the form of compressed natural gas (CNG), LPG or LNG.
e. Production of H_2 for energy purposes (e.g. refineries).
f. Production of chemicals.

The detailed consumption of natural gas by sectors can be seen in Figure 1.

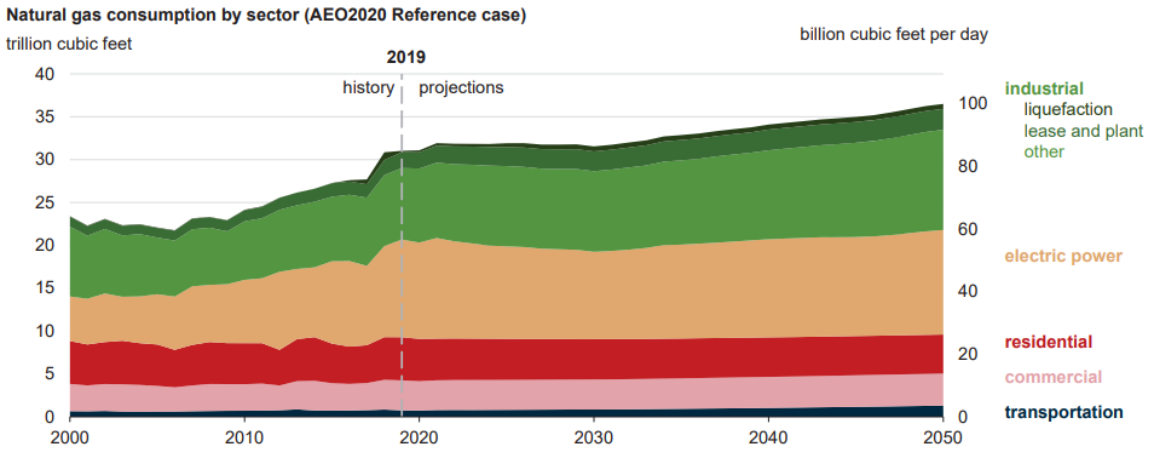

Figure 1. Natural gas consumption based on sector.[3] Source: Annual energy outlook 2020.

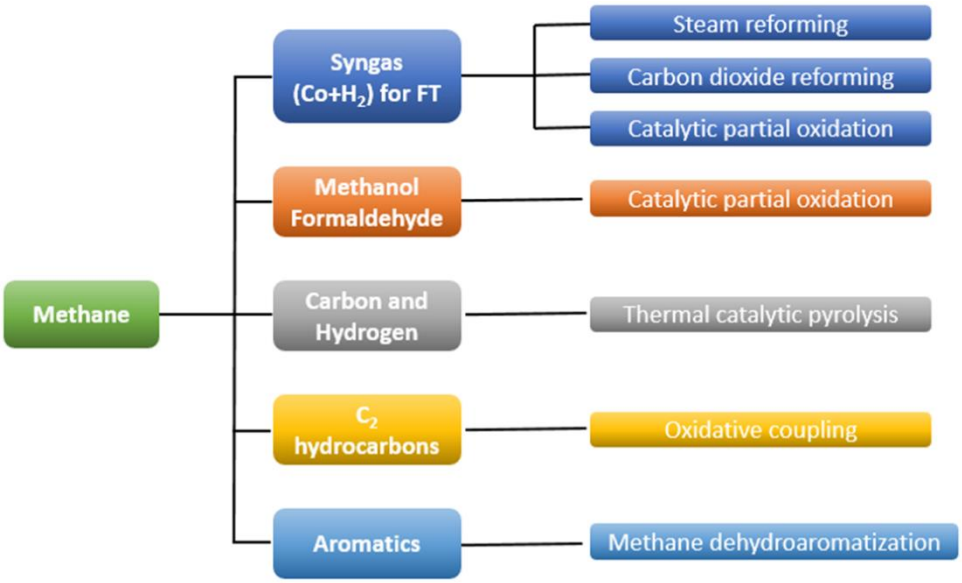

Figure 2. Natural gas (methane) major conversion pathways to fuels and chemicals.[9, 10]

During the past decades, extensive progress/research has been conducted to transform methane into higher-value hydrocarbons. Presently, the two catalytic routes to convert methane are the direct route and the indirect route. The conversion pathways can be found in Figure 2**.** The indirect route primarily involves two steps.

Step 1. Methane conversion into *syngas* (a mixture of CO and H_2) by reforming or by partial oxidation

Step 2. Conversion of *syngas* to valuable fuels and chemicals such as gasoline, dimethyl ether (DME), methanol, paraffin, either via Fischer Tropsch or via methanol to hydrocarbons (MTH) catalysis.

However, the direct route converts methane directly into the value-added products.

The indirect route is operated industrially, while the direct route is at the research scale. Examples of direct conversion routes are the oxidative coupling of methane (OCM) to ethylene and dehydroaromatization (MDA) to aromatics (benzene, toluene, and p-xylene).

However, the conversion can also be characterized according to the oxidative route or via non-oxidative route Figure 3.

Amongst the processes of direct conversion of methane to products via:

- Partial oxidation of methane to form methanol and formaldehyde,
- Oxidative coupling of methane to yield olefins (ethylene) are being studied intensively Figure 3

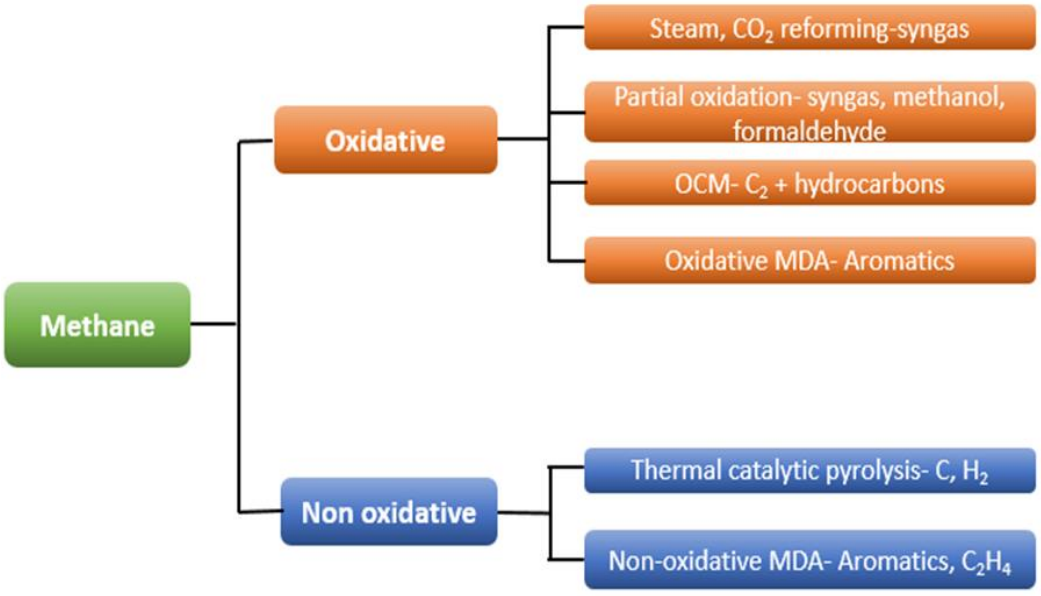

Figure 3. Natural gas (methane) major conversion pathways to fuels and chemicals via oxidative and non-oxidative pathways.[10]

However, so far these processes have not been demonstrated as economic. The methane de-hydroaromatization can be performed either via oxidative or via non-oxidative route, due to oxidative conditions the selectivity towards benzene is very low (~ 3% at 600 ºC) due to the formation of the copious amount of CO_x species. An additional example of catalytic methane conversion is the single-stage decomposition under oxygen-free conditions to yield hydrogen (H_2) and carbon (C) filaments without any CO_x impurities. The generated carbon can be used as a

support for catalysts, while the H_2 can be used in fuel cells. The reaction is generally carried out in a temperature range between 600 to 900 ºC using iron as a catalyst.[9]

1.2.Global energy context

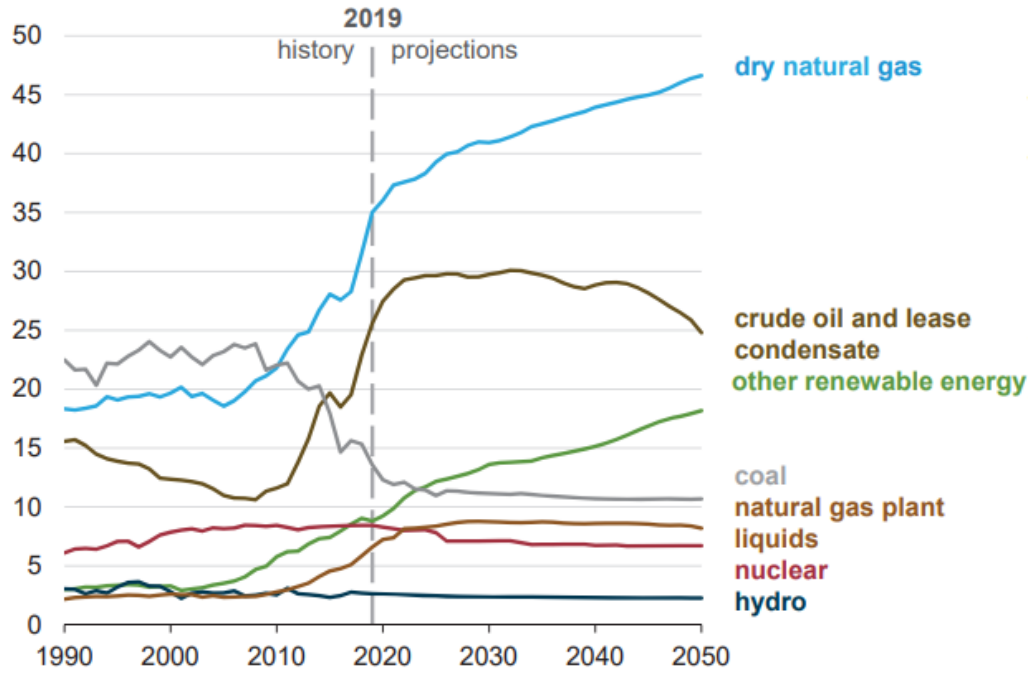

Figure 4. Energy production share. Source Annual Energy Outlook 2020.

In the modern era of industrialization and modernization, the cheap, abundant and uninterrupted energy supply forms the backbone for industrial and domestic purposes.[5] The overall human population is about 8 billion and the growth rate is rapid. It has been anticipated that the population will reach about 10 billion by the end of 2050. The trends in population and consumption rates will inevitably increase the pressure on the limited available natural resources. Figure 4 depicts the major source of energy. Natural gas production accounts for nearly 43% of U.S. energy production by 2050 in the Reference case.[1, 2] Production from shale gas and tight oil plays as a share of total U.S. Natural gas production is projected to continue to grow because of the large size of the associated resources.

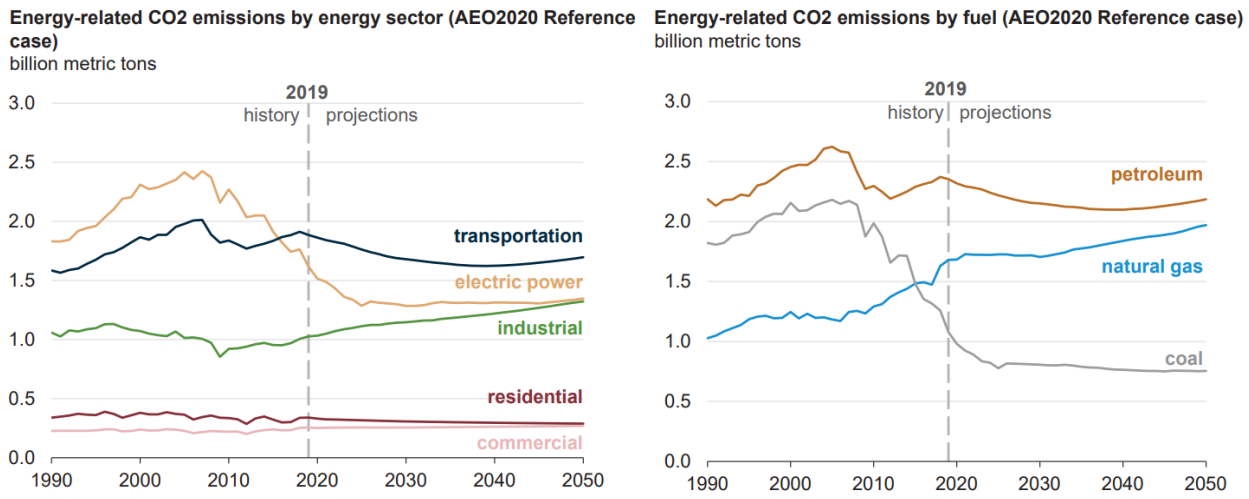

Figure 5. CO_2 emissions based on fuels and sectors. Source: Annual Energy Outlook 2020.

With the current fuel scenario Figure 4 and Figure 5, the carbon dioxide emissions will double by the year 2100 to 800 ppm and the rise in global fossil energy demand will further increase the anxieties about the energy crisis. Therefore it is necessary to develop/adopt energy efficiency technologies, renewable energy resources, carbon capture and storage (CCS), nuclear power.[11]

The unpredictability in oil prices has promoted an improvement in energy efficiency, and effort towards the decrease in oil dependence. Considering the natural gas, despite its unstoppable worldwide expansion, there is no global reference price, unlike oil. Primarily there are three major regional markets:

a. North America,
b. Asia-Pacific
c. Europe

Each region sets the natural gas prices in different mechanisms. Consequently, there always have been variances in price amongst these three major markets, owing to the dissimilar supply/demand balances and pricing systems. Likewise, the global coal market is distributed in numerous regional markets which are distinguished by their geography, the quality of coal or the infrastructure

limitations. The prices for coal directly depend on the severity of environmental policy and considering its competition with natural gas as a source for the generation of power.

The carbon capture storage (CCS) is one of the promising technologies to attain the internationally agreed target to limit the average global temperature increase (2 ºC). The use of CCS technologies and the retrofit of old fossil fuel plants has helped to improve the economic feasibility to reach the environmental goal set forth by the individual nations, especially in regions where the CO_2 capture/storage is easier due to its geological formations. However, some progress has been done to develop regulatory frameworks. A progressive carbon reduction necessitates a shift towards lower-carbon emission fuels in the transportation sector, although only this improvement will not be sufficient.[12]

Chemical product technologies also contribute in some way towards energy saving. The chemical industry plays an important role in the planning, generation, usage and storage of energy. However, the advancement in the catalytic process can be used to reduce both energy consumption and greenhouse gases (GHG) emissions in the industrial sector. About 90% of all chemical processes employ catalysts, as almost all petroleum refining processes. Likewise, catalysts are used every day in numerous applications such as catalytic converters in cars, indoor air control, etc. However, some catalysis applications still affect directly or indirectly energy-saving or the reduction of GHG emissions.[11]

1.3. The literature on methane (CH_4) and carbon dioxide (CO_2) conversion to valuable products (*syngas*, aromatics)

As the current atmospheric concentration of CO_2 is continuously rising, efforts must be put forth to avoid any negative effects. Stabilization of CO_2 levels in atmosphere required both significant and its active removal from the atmosphere. [13, 14] The increasing availability of cheap natural gas

(methane) and the global rise in carbon dioxide (CO_2) levels have attracted the interest of researchers worldwide towards their efficient conversion to value-added intermediates/chemicals/fuels, etc. Methane is one of the most abundant and relatively easy to extract hydrocarbons in the planet as proved after the recent discovery and extraction of shale gas in North America.[4] Methane is primarily produced in offshore areas and thus; its storage and transportation in gas form remain a challenge. Currently, liquefaction is the method of choice for methane transportation, although it demands a large amount of energy. Therefore, numerous technologies are developing to convert methane directly to desired products or via co-feeding with other reactants. This dissertation primarily focuses on the two non-matured technologies for the methane conversion, which are not yet at the industrial scale.

a. Dry reforming of methane (DRM) to produce *syngas* (CO and H_2)
b. Methane de-hydroaromatization (MDA) to produce aromatics (especially C_6H_6)

Dry reforming of methane (DRM) to produce *syngas*

The dry reforming of methane (CH_4) with carbon dioxide (CO_2) provides an effective solution to mitigate the two major greenhouse gases. DRM utilizes the abundant natural gas (CH_4) resources that are increasingly being extracted as we continue into the age of the shale gas revolution,[15] and also the major by-product (CO_2) resulting from power plants, petrochemical processes, etc, to generate *syngas* (CO and H_2).[6, 16] *Syngas* is a valuable feedstock for numerous energy-intensive industrial processes Figure 6.[17] Currently, methane is industrially converted into *syngas* via steam reforming (SMR), while dry reforming (DRM), bi-reforming (BIM), autothermal reforming (ATR) and partial oxidation (PO_x) are still at research scale.[18] Amongst the above-mentioned processes, dry reforming provides a 1:1 ratio of H_2 and CO, which is a preferred mixture to

produce chemicals and long-range hydrocarbons through the Fischer-Tropsch process.[19, 20] The catalytic routes to convert CO_2 can be found in Figure 7.

$$CH_4 + CO_2 \leftrightarrow 2CO + 2H_2 \qquad \Delta H^0_{298K} = 247 \text{ kJ mol}^{-1} \qquad (1)$$

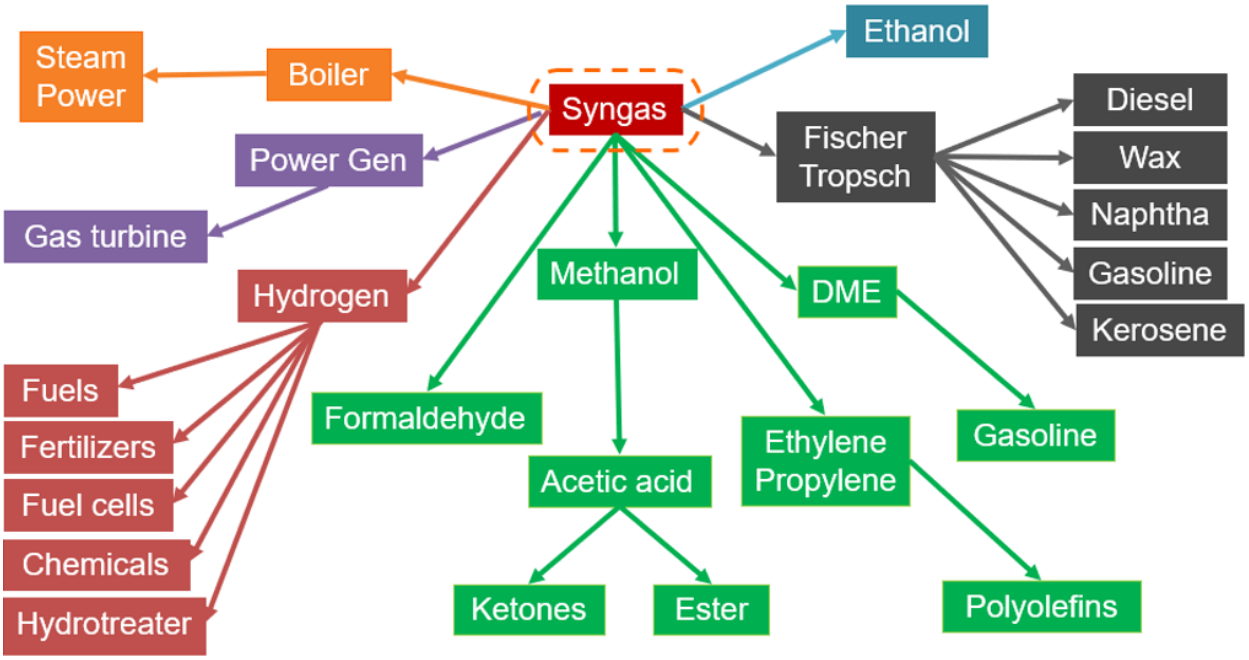

Figure 6. Product distribution from *syngas* as a starting material.
Source:fotosearch.com/CSP532/k50554598/

Dry reforming was proposed by Fischer and Tropsch in 1928 as an alternative to steam reforming and it has been extensively studied since then.[21-25] Typically, supported metal catalysts based on noble metals (Rh, Ru, Pd, Pt, and Ir) and non-noble (Ni, Co) metals are employed.[21-35] Noble metals catalysts have higher activity compared to Ni-based catalysts but due to limited availability and expensiveness of noble metals, they generally are not economical.[27-31, 36] Nickel's high levels of activity combined with its potential cost-effectiveness for commercial processes renders them a potential industrial catalyst for DRM. Bimetallic catalysts, like that of the promising Ni-Co systems, have proven to be the leading design for maximizing DRM catalytic performance and increasing the lifetime of the catalyst.[27, 35, 37, 38]

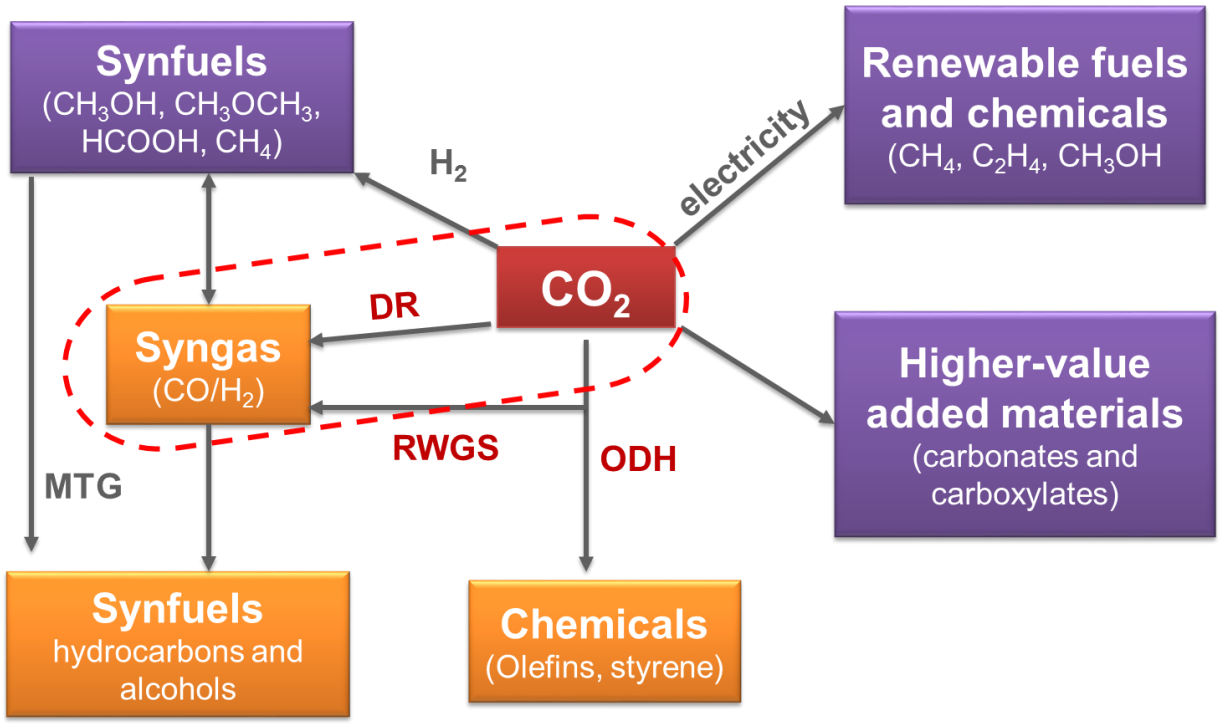

Figure 7. Catalytic CO_2 conversion routes via dry reforming, oxidative dehydrogenation, and reverse water gas shift. Source: New and future developments in catalysis, Activation of CO_2.

Researchers have also tried carbide-based materials, but a stable and active catalytic performance could not be observed.[19, 39-53] However, due to multiple thermodynamic equilibrium processes, undesired secondary gas-phase reactions such as methane thermal degradation (reaction 2), carbon monoxide disproportionation (reaction 3), carbon monoxide hydrogenation (reaction 4) and carbon dioxide hydrogenation (reaction 5) also take place thus compromising the stability of the catalyst. [27-31, 36]

$$CH_4 \rightarrow C_s + 2H_2 \qquad \Delta H^0_{298K} = 75 \text{ kJ mol}^{-1} \qquad (2)$$

$$2CO \leftrightarrow CO_2 + C_s \qquad \Delta H^0_{298K} = -172 \text{ kJ mol}^{-1} \qquad (3)$$

$$CO + H_2 \leftrightarrow H_2O + C_s \qquad \Delta H^0_{298K} = -132 \text{ kJ mol}^{-1} \qquad (4)$$

$$CO_2 + 2H_2 \leftrightarrow C_s + 2H_2O \qquad \Delta H^0_{298K} = -90 \text{ kJ mol}^{-1} \qquad (5)$$

Furthermore, the reverse water gas shift reaction RWGS (reaction 6) that leads to a lower H_2/CO ratio less than unity is usually present during the DRM reaction. The RWGS depends upon the equilibrium conditions at certain temperature range.[54]

$$CO_2 + H_2 \leftrightarrow CO + H_2O \quad \Delta H^0_{298K} = 41 \text{ kJ mol}^{-1} \qquad (6)$$

Numerous studies have concentrated on the development of high-performance catalytic materials; however, the industrialization of the dry reforming process has been delayed due to the lack of effective and economically viable catalysts/process. [21-35, 37, 38]

In our viewpoint, the main challenges in the DRM are

1. To design catalyst capable of decreasing the reaction temperature required to effectively convert CH_4 and CO_2. Lower temperature, besides resulting in lower OPEX will avoid both undesired side reactions and changes in catalyst structure (e.g. sintering)
2. To design a catalyst that avoids reverse water gas shift (RWGS) to better control the H_2/CO ratio
3. To diminish the reactions 2-4 (leading to coke formation) when supported metal catalyst like Ni, Pt, Pd are used, and
4. To suppress the deep oxidation of the metal carbide catalysts, leading to the metal oxide phase. Therefore, it is necessary to explore/identify new catalytic materials with good catalytic activity-stability-selectivity and easy handling capability to meet the requirements for large-scale operation.

Methane de-hydroaromatization (MDA) to produce aromatics

The abundant reserves of natural gas, primarily containing methane, along with the latest technological developments for its production motivate both the technological and scientific sectors to develop more efficient ways to convert methane to chemicals and fuels. The new

feedstock entering the cracker units, ethane separated from natural gas, replacing the naphtha obtained from crude oil has led to a deficit in aromatics, heavier olefins (propylene and butylenes) and chemicals production (LPG and aromatics) as shown in Figure 8. Therefore, it is essential to convert methane into aromatic products to bridge the gap between the production and consumption of this important family of chemicals, primarily BTXs.

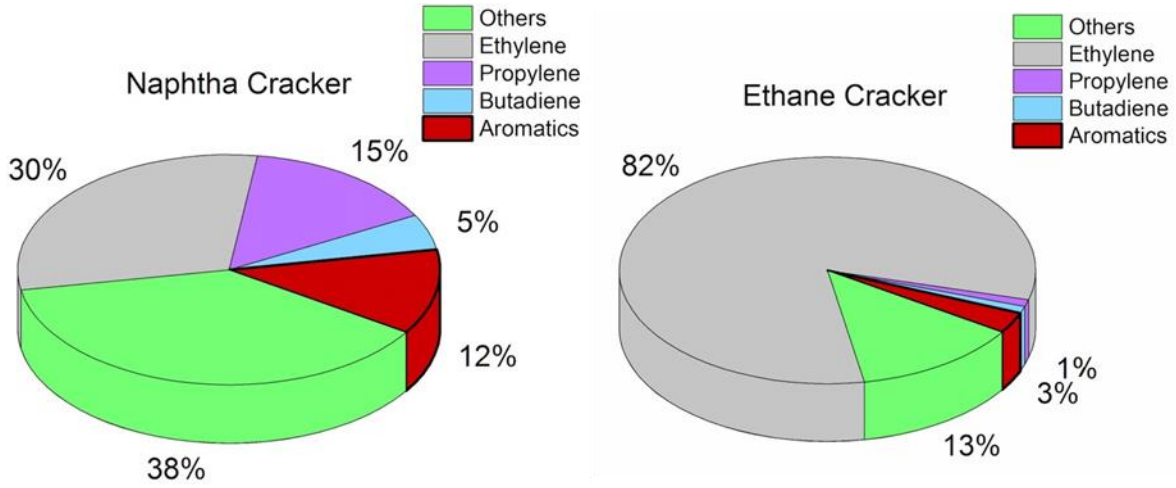

Figure 8. Products distribution from (left) naphtha and (right) ethane crackers. Source: A.T. Kearney analysis. Shale Gas: Threat or Opportunity for the GCC?

The absence of an appropriate catalytic process for direct conversion of methane to liquid hydrocarbons requires the development of catalyst to stand against the competitive *syngas* route. An example of current industrial technology to convert methane into liquid fuels involves the use of cobalt and iron-based catalysts at an elevated temperature (~600 °C) and high pressures (7-40 bar), thus consuming tremendous amounts of energy to produce desired liquids (formaldehyde, methanol, ethers, BTXs).[23]

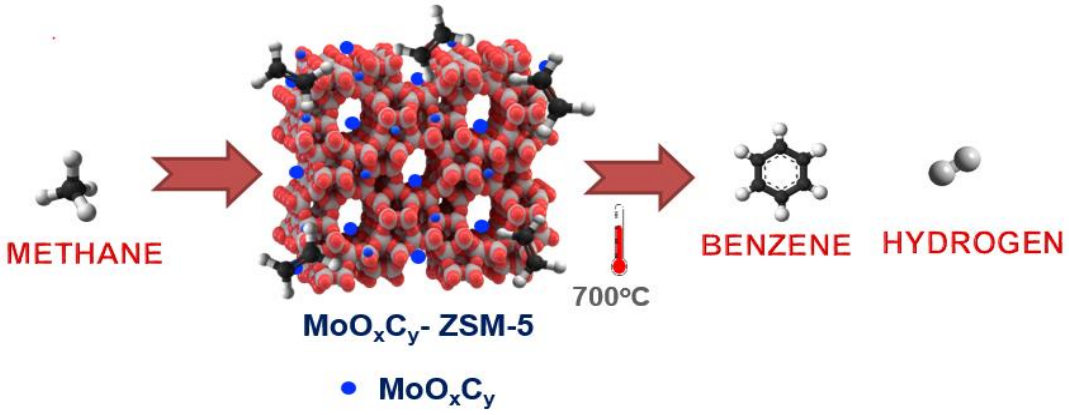

Figure 9. Schematic representation of methane dehydroaromatization (MDA) over Mo/ZSM-5 catalysts. Source of ZSM-5 image: https://commons.wikimedia.org/wiki/File:Zeolite-ZSM-5-vdW.png

Currently, non-oxidative and oxidative routes are used for the direct conversion of methane to aromatics at the laboratory scale. The non-oxidative path suffers from various drawbacks such as thermodynamic limitation in the maximum conversion of methane, strong endothermic conditions requiring high energy inputs, and rapid catalyst deactivation due to coke deposition.[4] These limitations may be mitigated by performing the oxidative path, but the low conversion of methane still remains an issue.[4, 55-57] The most widely used material for MDA is Mo supported on ZSM-5. Although molybdenum oxide supported on ZSM-5 is not active for MDA, its carbide form is active, which is formed after carburizing the oxide species(s) with a hydrocarbon [58-61] When the carburization process ends, the carbide specie(s) activate methane forming methyl radicals ($\dot{C}H_3$), which combine to form ethylene Figure 9 and Figure 10. The structure of ZSM-5 with a pore size of 5.4 $\dot{A}$, which is similar to the kinetic diameter of benzene, provides the confinement effect needed to promote the oligomerization of ethylene resulting in the formation of aromatics compounds.[60] Moreover, the Bronsted acid sites within ZSM-5 play an important role in the oligomerization of ethylene to form aromatics (reaction 7).[62]

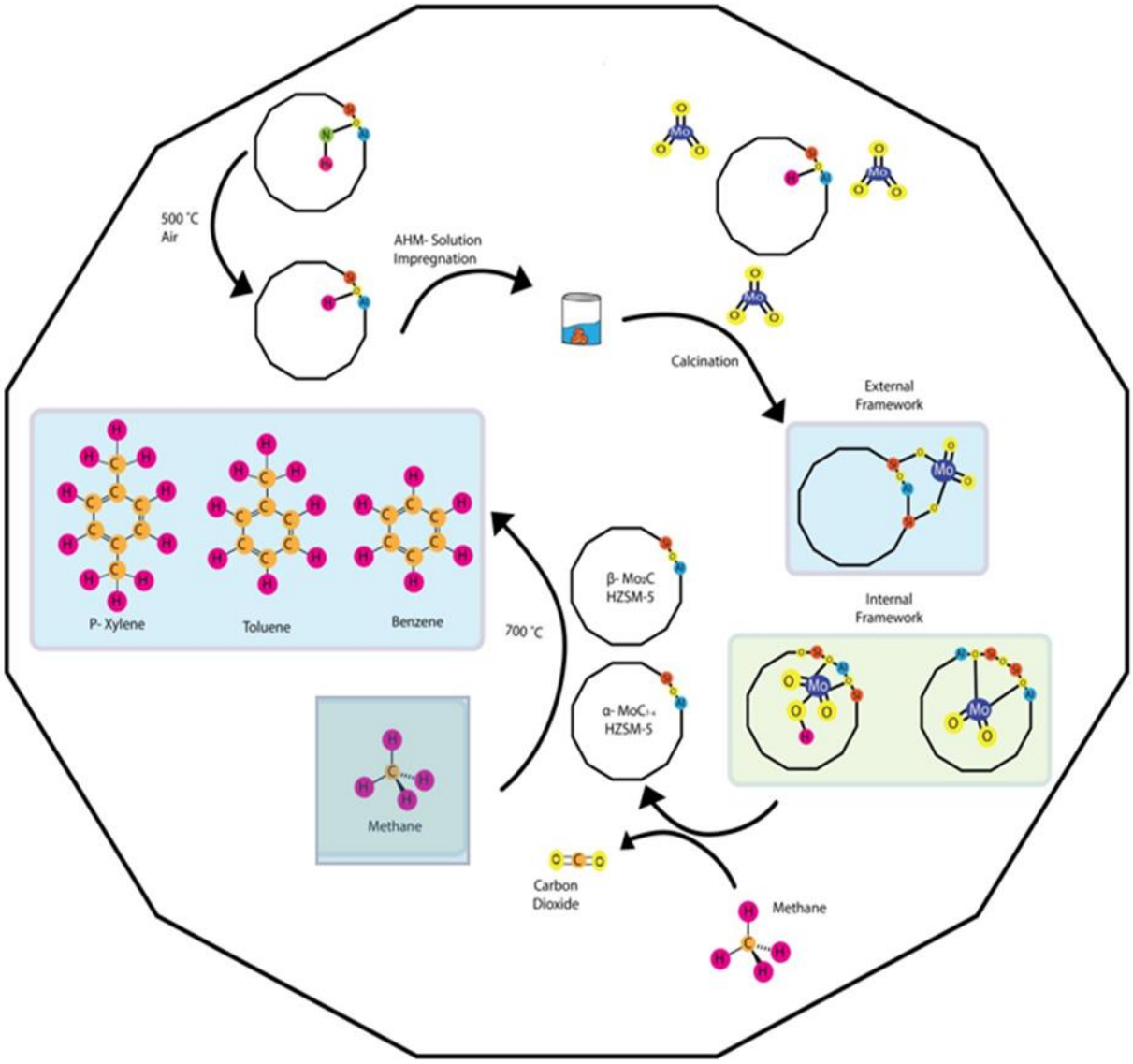

Figure 10. Schematic of the overall MDA process for the conversion of methane using molybdenum supported on ZSM-5 catalyst.

$$6CH_4 \rightarrow C_6H_6 + 9H_2 + \text{Coke} \qquad (7)$$

During the past two decades, numerous Mo-zeolite catalysts system have been tried for MDA reaction, Zhang et al. .[63] explored different catalysts prepared using HZSM-5, HZSM-8, HZSM-11, HBETA, HMCM-41, HSAPO-34, HMOR, HX, HY, HSAPO-5, HSAPO-11 etc.[4] Catalysts prepared using HMCM-41 and HSAPO-34 shown lower activity, while those prepared using

HMOR, HX and HY exhibit lower CH_4 conversion and produced CO and C2 hydrocarbons. Mo/HSAPO-5 and Mo/HSAPO-11 catalysts showed no selectivity towards aromatics. The best results were achieved using HZSM-5, HZSM-8 and HZSM-11 zeolites. Furthermore, Mo supported on, for instance, FSM-16,[64] $SiO_{2,}$[64] $Al_2O_{3,}$[64] HMCM-22,[65] HMCM-36,[66] HMCM-49,[67] HMCM-56,[68] ITQ-2,[69] ITQ-13,[70] IM-5,[71] and TNU-9[72] have also been explored. Different transition metal ions (TMI) with 2-4wt% metal ion content using Mo, W, Fe, V, and Cr, confined inside the HZSM-5 were evaluated by Lunsfored et al. [73] and found that Mo exhibits superior catalytic performance as compared to other transition metal ions.

Ichikawa et al. [74] reported 5% (wt.) Re/HZSM-5 as a promising catalyst for MDA. Bao and co-workers varied Mo contents varying between 2, 4, 6, 8, and 10 % wt. confined inside HMCM-22 zeolite. Various researchers have tried to improve the Mo_2C/ZSM-5 catalyst by modifying with promoters such as Fe,[75, 76], Co,[76] Zn,[77-79] Ga,[80] W, [61, 81, 82] B,[77] Re,[83] Ag,[84] Pt,[85] Rh,[85, 86] Pd,[86] and Ru.[87] Concisely, the product formation rate (benzene) and the CH_4 conversion were marginally increased on the 1% wt. Fe and Co-modified 3% wt. Mo/HZSM-5. Recently, much focus has been given to add co-reactants along with methane, such as methanol.[55, 79, 88] However, in all these studies, the definitive establishment of structure-stability relationship is still pending

The Mo/zeolite catalyst is bifunctional with the contribution of both Mo sites and Brønsted acid sites making them suitable for MDA reaction.[89-91] Methane is activated over nano-crystalline Mo sites, which are responsible for the formation of CH_x species. These species then dimerize C_2H_y oligomerize on the Brønsted acid sites (BAS) of the zeolite to yield benzene toluene and p xylene. Most authors believe that ethylene as an intermediate during the aromatization reaction[90, 91] primarily producing benzene (the main aromatic product),p- xylene, naphthalene and toluene as

other aromatics and C_2 hydrocarbons such as ethylene and ethane are also produced during the reaction as shown in Figure 9 and Figure 10.

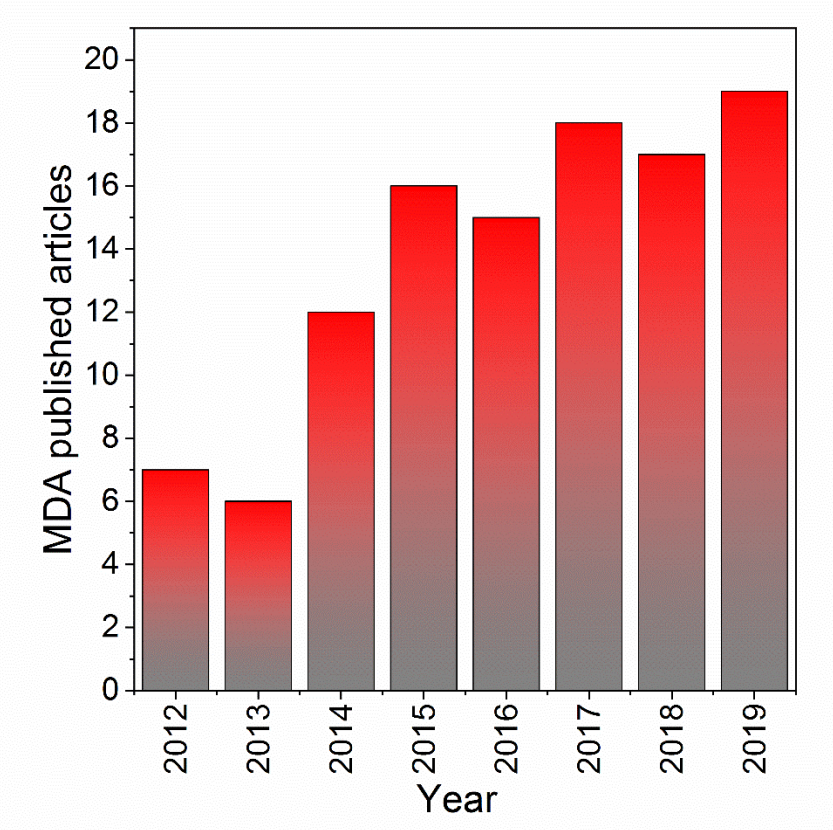

Figure 11. MDA publications since 2012. Search terms- MDA, Methane dehydroaromatization, methane to aromatics, Source: Google scholar.

Moreover, during 1993-2000, several studies were published on MDA, but due to the deficiencies in thorough characterization of the materials, the research articles went down afterward to merely 8-10. Nevertheless, lately, due to advancements in the materials characterization backed up with computational data, the number of literature is growing since Figure 11 and been focusing on looking for other materials that can convert methane into aromatics.

1.4. Aromatic hydrocarbons and it's market

In today's scenario, about 90% of petroleum products are derived from petrochemicals, also known as building blocks, they are: ethylene, propylene, and butadiene (as olefins), benzene, toluene and para-xylene (BTX aromatics) and methanol.[92] Amongst these, ethylene is the most demanded followed by propylene

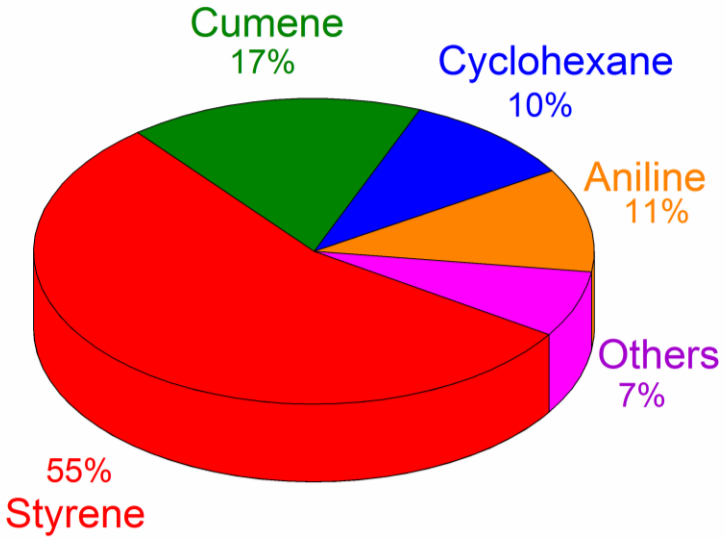

Figure 12. Global demand for benzene by applications in 2018. Source: The changing dynamics of global benzene supply

The most important aromatic is benzene. The global benzene demand is primarily directed by two major intermediates products, ethylbenzene and other being cumene. Additionally, ethylbenzene was the highly demanded chemical in 2014, nearly 50% of global demand goes to produce styrene monomer mainly (Figure 12**)**.

Aromatics hydrocarbons market

1. Global Benzene market: USD 111.1 billion by 2026

Source: https://www.marketwatch.com/press-release/benzene-market---global-industry-analysis-size-share-growth-trends-and-forecast-2018-to-2026-2019-05-23

2. Global benzene market to reach 56,304 thousand tons by the end of 2023

Source: https://www.businesswire.com/news/home/20181126005417/en/2018-Global-Benzene-Market-Forecasts-2023--

3. Global Benzene market: USD 81.02 billion by 2022

Source: https://www.marketresearchfuture.com/reports/para-xylene-market-2278

4. Global P xylene production 5.5 million tons in 2017

Source: https://www.marketresearchfuture.com/reports/para-xylene-market-2278

5. Global toluene market USD 35.9 billion by 2024, in 2018 it was USD 27.3 billion

Source: https://www.prnewswire.com/news-releases/global-toluene-market-was-valued-a--27-3-billion-in-2018-and-is-projected-to-reach--35-9-billion-by-2024--300846374.html

6. Global toluene production 34,112 thousand tones by 2023.

Source:https://www.businesswire.com/news/home/20181126005432/en/Global-Toluene-Market---Outlook-2023--

Chapter 2: Material synthesis and experimental methodology

2.1 Two-dimensional metal carbides (MXenes)

MXene materials are a family of two-dimensional transition metal carbides or nitrides with unique properties for various applications due to their layered hexagonal structure and versatile chemical composition, facile functionalization, and tunable layer thickness.[93, 94,95] MXenes are named according to their graphene-like morphology with a $M_{n+1}X_nT_x$ general chemical formula, where M is an early transition metal, X is carbon and/or nitrogen, T indicates various surface terminations, n is the number of layers, and *x* is the number of surface functional groups per unit formula as shown in Figure 13 and Figure 14.[93]

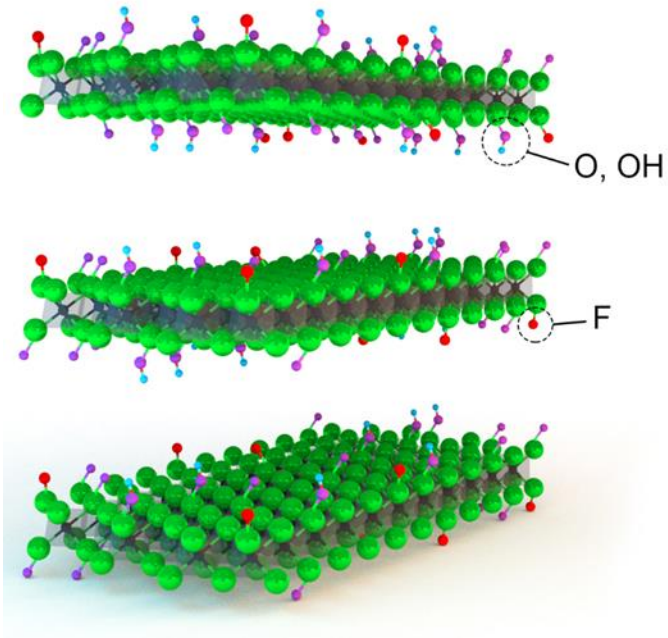

Figure 13. Schematic representation of multilayered V_2CT_x MXene with various terminal functional groups.

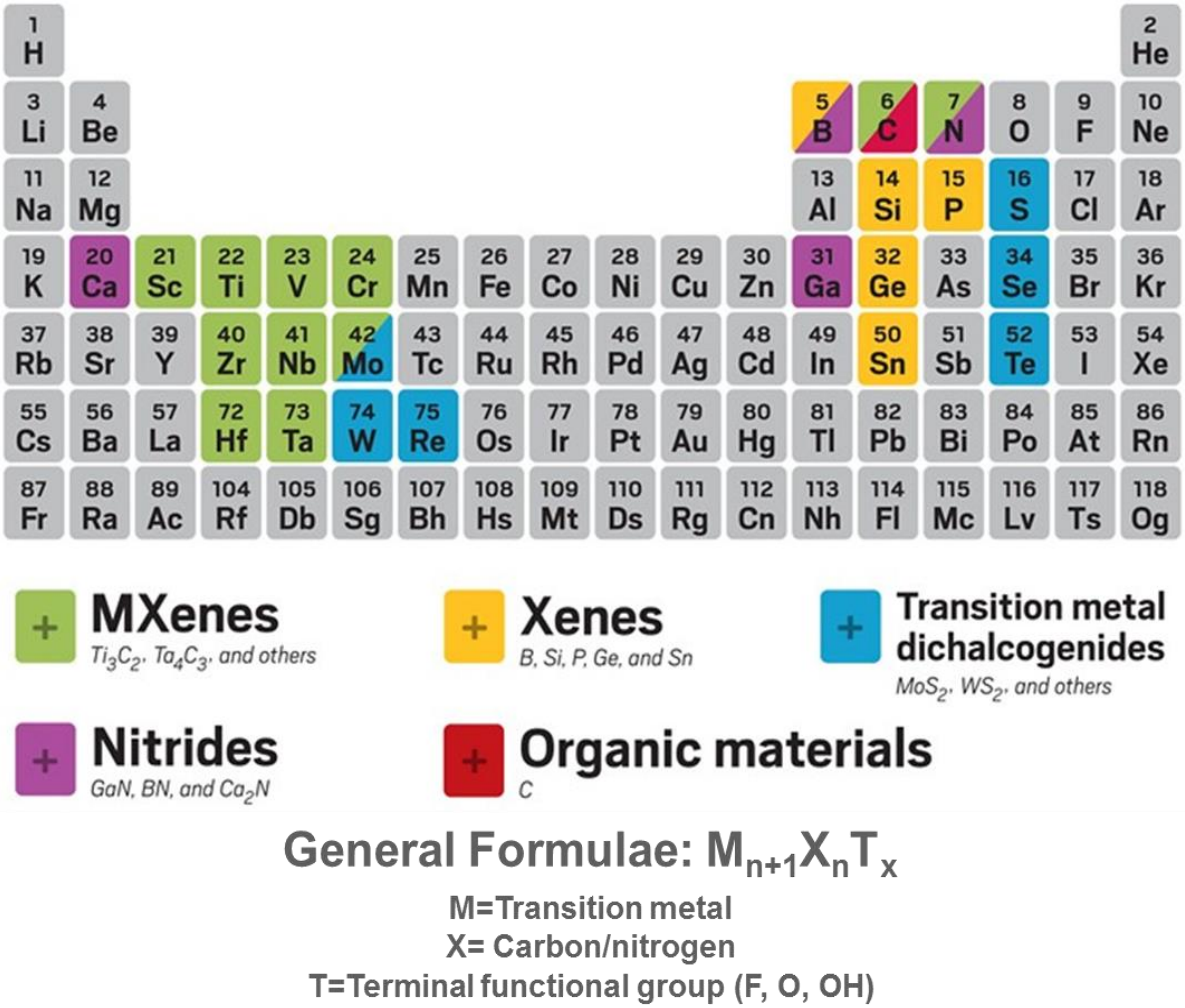

Figure 14. Schematic representation of MXene from the periodic table. Source: c&en: 2D materials go beyond graphene. Mitch Jacoby, 2017.

The precursor to prepare MXene materials is a mixture of an early transitional metal with aluminum and graphite powder called the MAX phase ($M_{n+1}AX_n$). The multilayered MXene structure is obtained by selectively etching metal atoms from MAX phases at specific conditions, leading to the removal of A-layer elements (eventually, elements from the group 13 or 14 in the periodic table, although typically aluminum).[94] To date, about twenty different MXenes have been synthesized, and many others have been theoretically predicted.[93, 95] The physiochemical

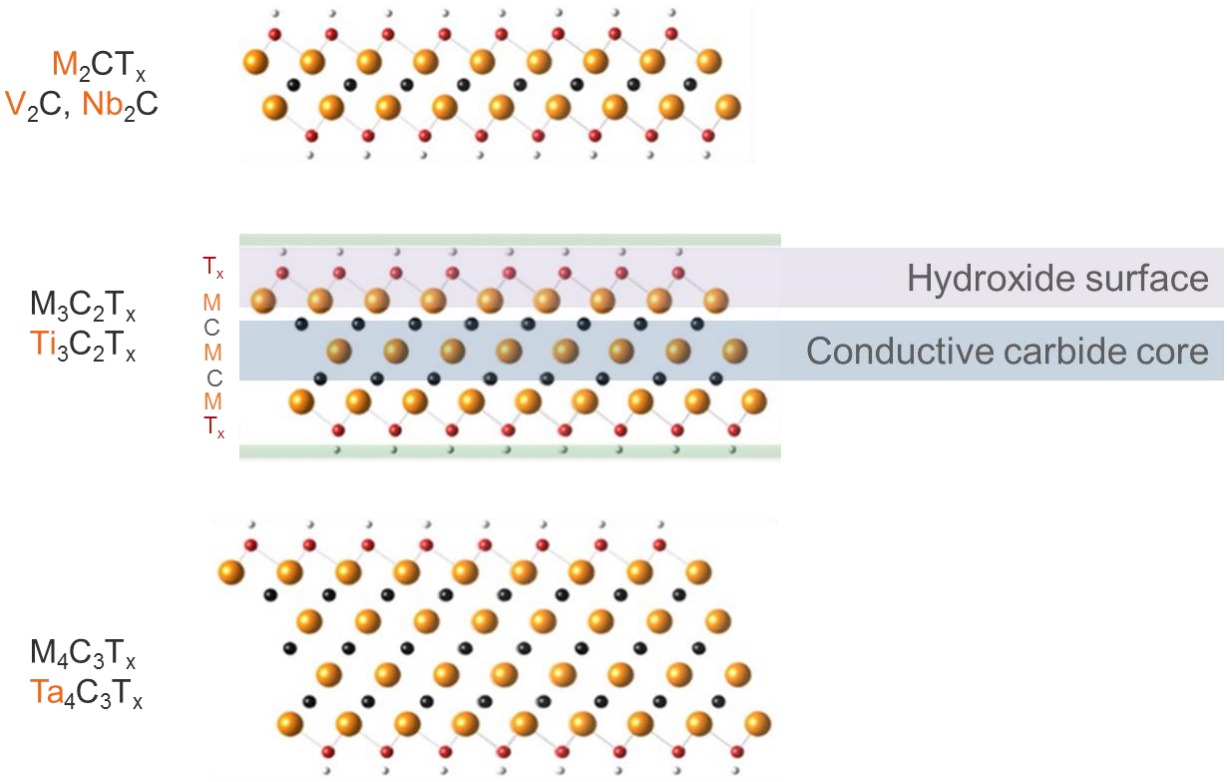

Figure 15. Types of MXenes according to the amount of metal ion.[93, 95]

Properties of these promising materials primarily depend on their composition and surface terminations (such as -F, -OH, and/or -O), which can be controlled to synthesize materials with distinguished properties to expand the application of MXenes in various fields.[96, 97] There are three major types of MXenes: M_2CT_x, $M_3C_2T_x$, and $M_4C_3T_x$.

The most common materials in M_2CT_x are the V_2CT_x and Nb_2CT_x, while the other common materials in other categories are shown in Figure 15. Apart from these categories, there can be mixed metal carbides having two different metals in the structure. Up to now, MXenes have been primarily and extensively developed as an electrode material for batteries and supercapacitors due to their exceptional electrical conductivity.[95] A detailed representation of the transformation of various MAX phases into respective MXenes can be found in Figure 16.

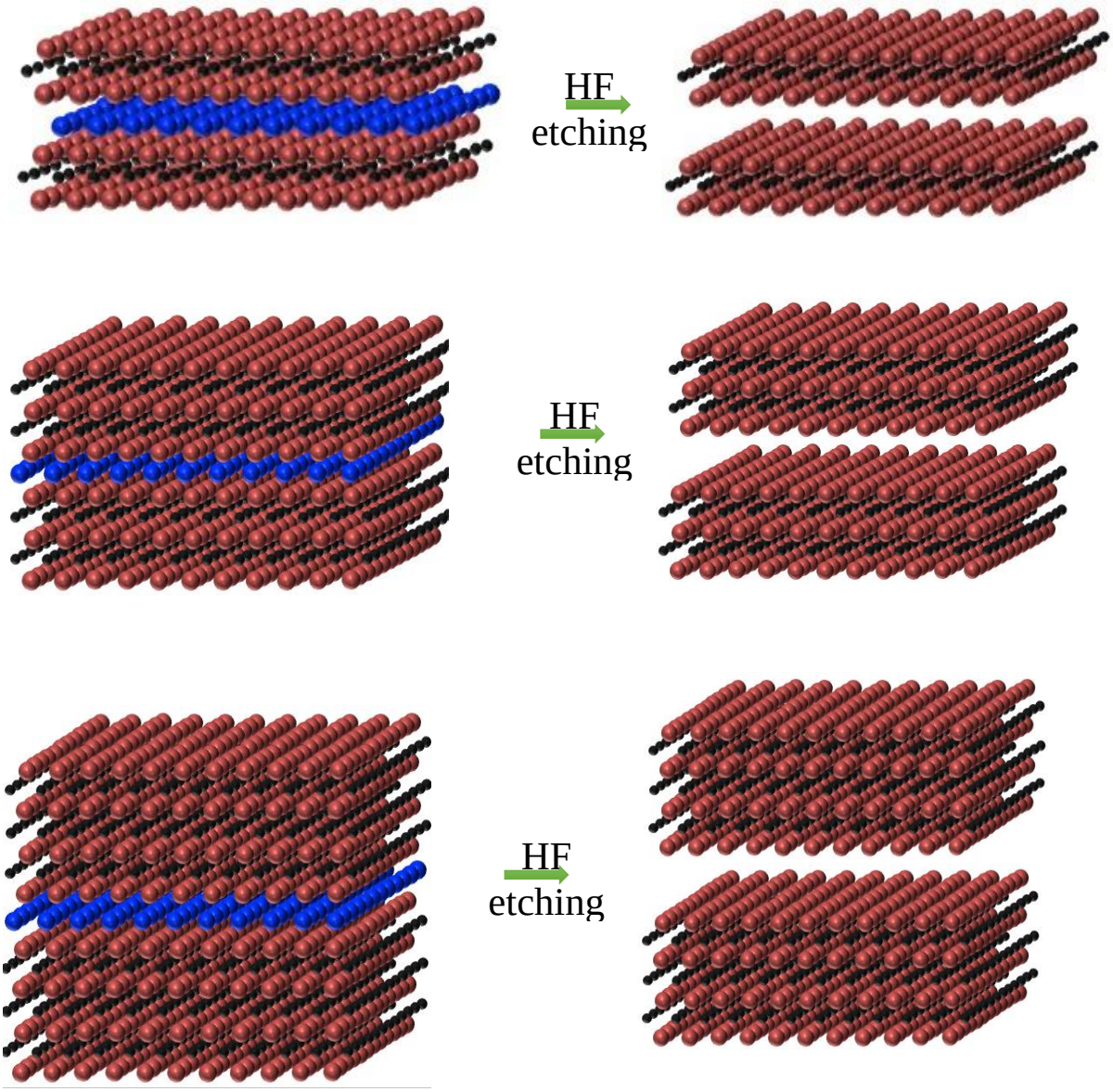

Figure 16. Schematic representation of different types of MAX phase transformation into MXenes after etching.

2.1.1 Synthesis of V_2AlC MAX phase

The synthesized V_2AlC MAX and V_2CT_x MXene phase were provided by Dr Armin VahidMohammadi and Dr Majid Beidaghi from Materials Engineering Department, Auburn University.

To synthesize V_2AlC, vanadium powder (99.5%, 325 mesh, Alfa Aesar), aluminum powder (99.5%, 325 mesh, Alfa Aesar), and graphite powder (99%, 325 mesh, Alfa Aesar) were mixed in a 2:1.3:1 weight ratio and ball-milled using zirconia balls for 18 h. Then the mixture was sintered at 1500 °C with a heating rate of 3 °C/min for 4 h under flowing argon atmosphere. The synthesized MAX phases were crushed, milled, and sieved through a 400 mesh to obtain powders with an average particle size of ~32 μm.

2.1.2 Synthesis of V_2CT_x MXene

V_2AlC MAX phase was treated with 48-50% concentrated hydrofluoric acid (ACS grade, BDH) in a ratio of 1g powder to 20 mL etchant for 92 h at room temperature while being stirred with a Teflon-coated magnetic bar at 200 rpm. For more details, the detailed procedure can be found elsewhere.[98-100] The etched powder was then washed several times using DI water and centrifuged at 3500 rpm for about 5 minutes until the pH of the supernatant was higher than four. The MXene powder was then filtered using a Celgard porous membrane, rinsed with DI water and absolute ethanol, collected, and dried under vacuum for 24h. The schematic for the transformation of the MAX phase into MXenes can be observed in Figure 17.

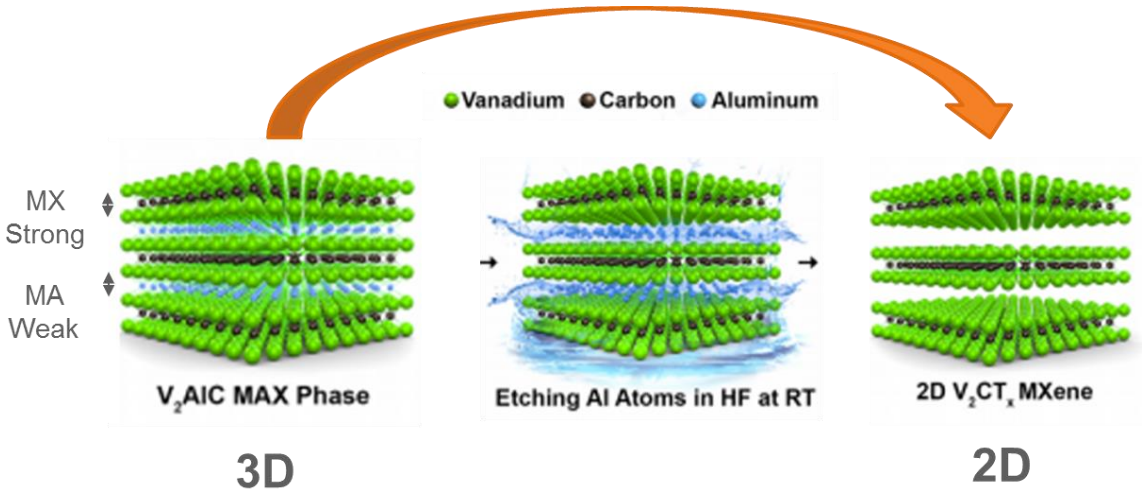

Figure 17. The synthesis of 2D V_2CT_x from its parent 3D V_2AlC MAX phase.[98]

2.1.3 MXenes as thermochemical catalysts

Recently, MXenes have started to gain consideration in photochemical, electrochemical, and thermochemical applications due to the presence of surface functional groups.[97, 101-103]

MXenes have also been studied for catalytic applications at relatively high temperatures (~550^{0}C), i.e., in the water gas shift (WGS) reaction[102, 104], ethylbenzene dehydrogenation[103], propane dehydrogenation[105], methane activation[106], and CO_2 activation[107]. However, to the best of our knowledge, MXenes have not been reported as catalysts for reactions at higher temperatures ($\geq$600^{0}C) with a highly concentrated feedstock that includes an oxidant under a long time on stream.

2.2 Zeolites

Zeolites were first introduced by a Swedish mineralogist in the year 1756, where he revealed leakage of water when the material was exposed to heat. He named those materials as zeolites. [108] However, due to the revolutionary work of Barrer and Milton during 1948-1955, synthetic zeolites were made. In 1962 synthetic faujasites such as zeolites X and Y were first utilized in the fluid cracking unit (FCC) at an industrial to process heavy petroleum fractions, one of the most important chemical processes worldwide. [109]

Zeolites are crystalline aluminosilicates materials having a three-dimensional structural framework composed of tetrahedra of SiO_4 and AlO_4 that are linked together by sharing their oxygen atoms. [109, 110] The bonding through one oxygen atom between two aluminum atoms is dictated by the Löwensteing's rule [111]. Each AlO_4 tetrahedron in the zeolite framework carries a unit negative charge. The framework structure encompasses intra-crystalline channels, channel intersections, and cages with dimensions from 0.2 to 1 nm. Inside these channels/inter-connected

voids are present the small cations/protons and water molecules that compensate the overall structure negative charge. [109, 112] Zeolites are represented by the empirical formula:

$M_{2/n}O \cdot Al_2O_3 \cdot ySiO_2 \cdot wH_2O$

Where "M" represents the exchangeable cationic ion, (group I or II ions), though other metal, non-metal and organic cations can also be used to compensate for the negative framework charge, 'n' is the cation valence, 'y' is ≥ 2 as Al3+ does not occupy adjacent tetrahedral sites and 'w' represents the H_2O contained in the voids spaces inside the zeolite framework [112]. The cations (normally Na^+ ions) are very mobile and normally experience ion exchange. Moreover, the H_2O trapped inside the pores can be desorbed when heating is applied without damaging the crystalline structure. The intra-crystalline channels can be either one or two or three dimensional. The channel diameter will determine the ability of the material as a molecular sieve.[112] Zeolites are classified according to the number of member rings (MR) of their channels/pores. [112]

1) *Small pore zeolites*: 8 MR, pore diameters of 3 to 4.5 Å ferrierite, chabazite).
2) *Medium pore zeolites*: 10 MR, diameters of 4.5 to 6 Å (ZSM-5/11, MCM-22).
3) *Large pore zeolites*: 12 MR, pore diameters of 6 to 8 Å (Beta, Mordenite, Y).
4) *Extra-large pore zeolites*: 14 MR, pore diameters up to 10 Å (UTD-1, CIT-5).

The zeolites are materials with networks of well-defined micropores that acts as a reaction channel. The activity and selectivity towards desirables of these channels increase/decrease with the introduction of active sites such as metal ions. Zeolites prove to be useful catalysts over a wide range of applications, ranging from acid-base catalysis to redox catalysis. Zeolites exhibits following properties such as [110] high surface area, pores or channels with molecular dimensions,

high adsorption capacity, separation of reactant/products, electronic properties of the active sites can be modified, the molecules can be pre-activated when they are inside the pores by strong electric fields and molecular confinement.

Zeolites display significant properties such as their surface acidity, which is directly related to the distribution of Brønsted acid sites (BAS) and the Lewis acid sites (LAS). The BAS is bridging hydroxyl groups that consist of a proton and framework oxygen from an AlO_4 tetrahedron, and the LAS are formed from the Brønsted acid sites dehydroxylation after heat treatment ($\geq$ 500 ºC) with water splitting. Consequently, the BAS is related to the framework aluminum (tetrahedral). Additionally, the three types of shape selectivity possessed by the zeolites can be categorized as [109, 110]

1) *Reactant shape selectivity*: the capability of reactant molecules to penetration inside the channels is facilitated or prevented.
2) *Product shape selectivity*: the diffusion of the small product molecule is facilitated, whereas the diffusivity of bulky products (greater than the pore size) is greatly reduced.
3) *Restricted transition state shape selectivity*: the cavity of the zeolite allows a specific geometrical arrangement/orientation of the reactants/products, allowing the selective formation of a specific intermediate transient product, leading to higher selectivity's towards the desired product.

2.2.1 Synthesis of Metal-ZSM-5

Incipient wetness impregnation method

The Supported metal oxide/zeolite sorbents are prepared via incipient wetness impregnation (Figure 18), followed by drying and calcination in flowing air. In short, metal acetates solutions of desired molarity are prepared by dissolving metal salt in de-ionized water. The metal acetate

solutions are then impregnated on support, such as SiO_2, and ZSM-5 depending on the supports pore volume. The impregnated samples are then dried overnight for 12h at 110 °C, followed by calcination in the air for 2-5 h at 500-550 °C.

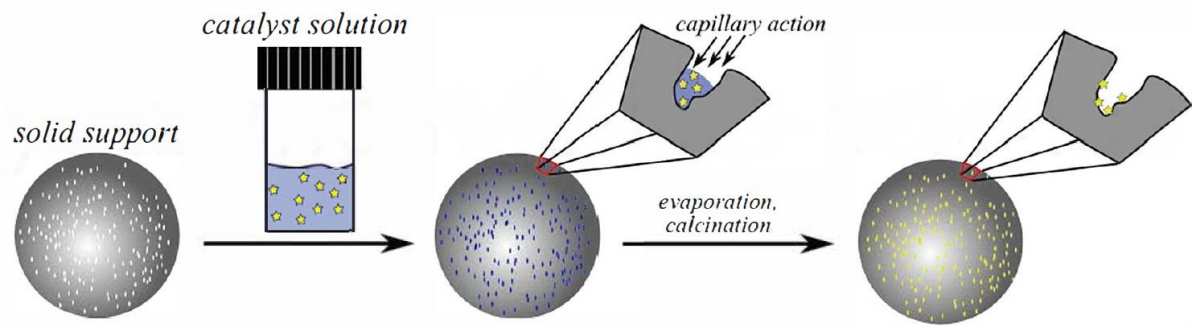

Figure 18. Incipient wetness impregnation methodology. Source: wordpress.com/tag/wetness.

2.2.2 Synthesis of 6wt%Mo on ZSM-5

The 6 wt.% Mo/ZSM-5 catalyst was prepared employing incipient wetness impregnation using ammonium heptamolybdate $(NH_4)6Mo_7O_{24}.4H_2O$ (Alfa Aesar, 99.9%) and ZSM-5 zeolite, CBV 2314 (Zeolyst Internatonal) having a Si/Al ratio of 23. The catalyst after impregnation was dried overnight at room temperature and further ramped to 120^0C at 1^0C/min with a hold time of 5 h. Subsequently, the catalyst was calcined in flowing air (Airgas, UHP grade) by ramping to 500^0C at 1^0C/min with a total hold time of 2 h

2.2.3 Synthesis of 5wt%Ni on ZSM-5

The preparation of Ni/ZSM was done by adopting a published procedure.[113] Briefly the H-ZSM-5 (Si/Al=23) was impregnated with Nickel Nitrate (Alfa Aesar) using incipient wetness impregnation (Ni 5 wt. %), dried for 12h at 110°C in oven followed by calcination at 550 °C with a ramp rate of 1 °C/min for 2h in furnace. The catalyst was further pelletized and sieved at a particle size between 425 and 500 µm for the DRM test.

2.3 Experimental methodology

2.3.1 Reactor setup and gas analysis

A custom-made reaction set up (Figure 19) equipped with five electronic GE50A MKS mass flow controllers, heating controllers, heated lines from the reactor's outlet to the gas chromatograph's (GC) inlet, a thermolyne 21100 tubular furnace which provide a well-defined isothermal heating zone of about 120 mm length, a custom-made liquid saturator isothermally heated with a chiller (VWR MX07R-20-V11B) when liquid vapors are needed, a pressure gauge prior to the reactor inlet, and an on-line Agilent 7890B GC equipped with three Agilent columns (HayeSep A, MolSieve, and DB-1), a flame ionization detector (FID) and a thermal conductivity detector (TCD). The steady-state catalytic measurements (for DRM and MDA) were performed at ambient pressure using a stainless-steel fixed bed reactor with an internal diameter and total length of 6 mm and 450 mm, respectively (Figure 20). The pristine powder catalyst was pelletized and sieved at a particle size between 425 and 500 μm.

The TCD measures changes in the thermal conductivity of the gaseous effluent passing through the column and compares it to a reference gas. Usually, nearly all compounds have a thermal conductivity value lower than H_2 or He (the most common reference and carrier gases). Both gases must be the same and when pass through the column its thermal conductivity is reduced, and a detectable signal is generated. The FID detector operates based on the detection of ions formed during the combustion of organic gaseous components inside the column by the hydrogen flame. The generation of these ions is directly proportional to the number of organic species in the gaseous effluent passing through the GC.

The reactions were carried out at specified temperatures and inlet flow of CO_2 (Airgas, UHP grade), CH_4 (Airgas, UHP grade), O_2 (Airgas, UHP grade) H_2 (Airgas, UHP grade) and N_2 (Airgas,

UHP grade) at various gas hourly space velocity (GHSV) ranging from 2,400 to 12,000 $ml g_{cat}^{-1} h^{-1}$. The quantification of the Hydrogen (H_2), Carbon dioxide (CO_2), Nitrogen (N_2), Carbon monoxide (CO) and methane (CH_4) was performed using the areas obtained by TCD, whereas hydrocarbon was performed by using the areas obtained by FID.

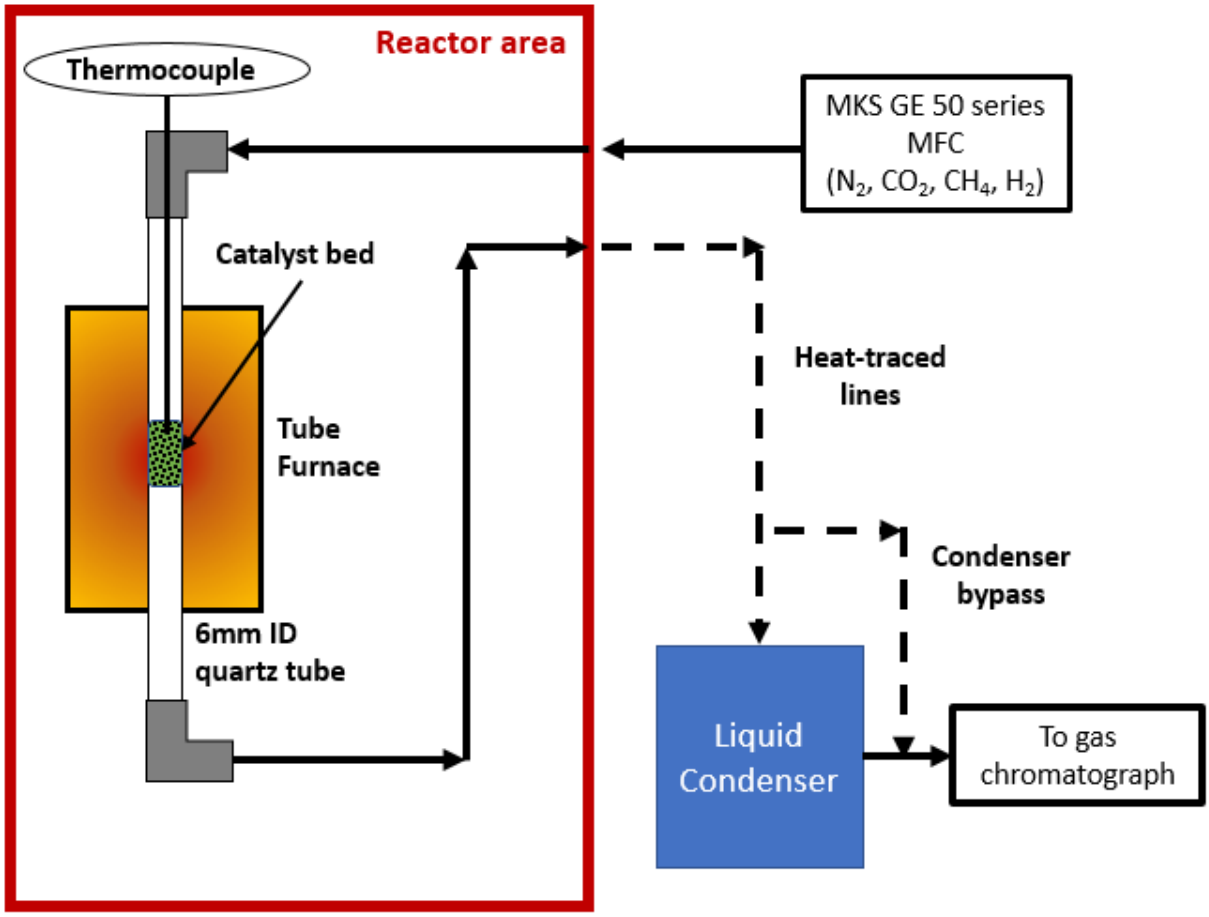

Figure 19. Schematic representation of the reaction setup. See the real picture in Appendix A1.

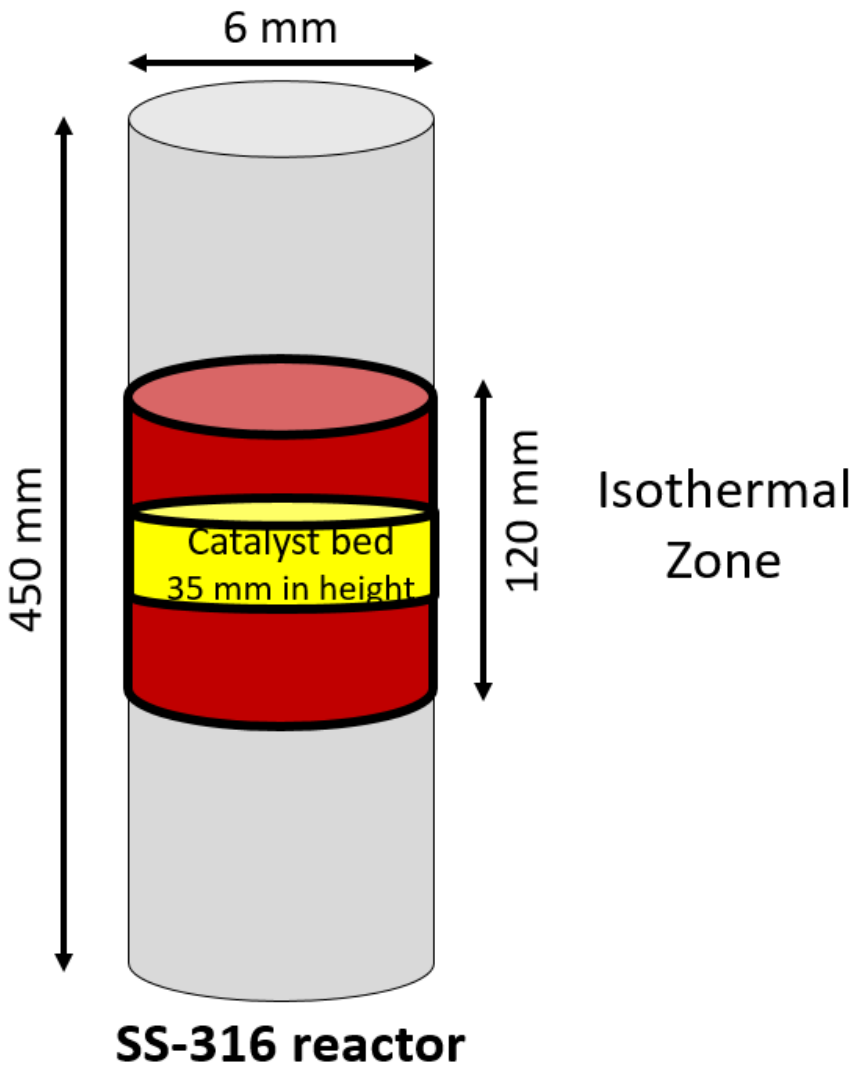

Figure 20. Schematic of SS-316 reactor used to study the DRM and MDA reactions.

The quantification of the gases was done by developing the calibration curves for the individual gases (Figure *21*). The individual gases (H_2, CO_2, CH_4, CO) were individually mixed with N_2, in various proportions (1,3,5,10,15,20,25,30,35,40,45,50,55,60,65,70,75,80,90, and 95%). For each concentration, 5 values were recorded, and the calibration curve was plotted with the average of the 5 values for each concentration.

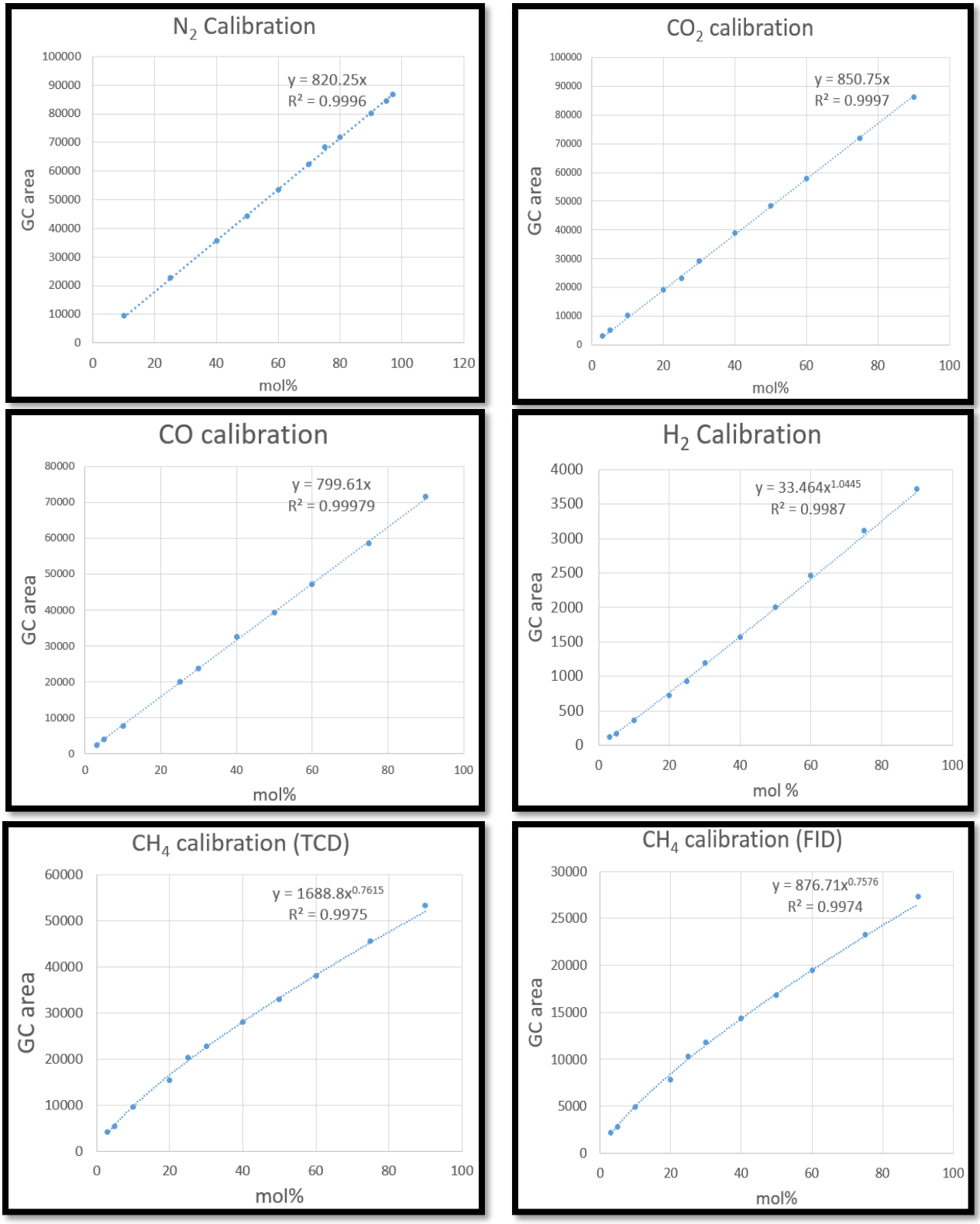

Figure 21. Calibration of different gases in FID and TCD for quantification.

The operating parameters for the FID and TCD are shown below in Table 1

Parameters	Values
Heater set point	300°C
Air flow	400 mL/min
H_2 fuel flow	30 mL/min
Makeup He flow	10 mL/min
Carrier gas flow	0.39327 mL/min
Split	10:1
Column	Agilent 122-1063 DB-1
Hold time	9.735 min
Pressure	9.3339 psi
Oven temperature	30°C
Hold time	10-30 min
TCD heater temperature	250°C
TCD reference gas flow (He)	10 mL/min
TCD make up He flow	5 mL/min

Table 1. FID and TCD operating parameters for the DRM reaction. For schematic representation see Appendix A2.

Further, *in-situ* Raman spectroscopy studies were performed using a Renishaw InVia Qontor Raman Spectrometer equipped with 785, 532, and 405 nm solid-state lasers, 5, 20, 50, and 100x objectives, and a MS 20 Encoded Stage. *In-situ* Raman studies were performed by coupling a Linkam CCR-1000 cell to the Raman microscope. Figure 22 and Figure 23. The LiveTrack feature of the Qontor version of the InVia Raman Microscope was used to maintain the sample in focus and, therefore, more accurately correlate changes in the intensity of the Raman signals with

specific chemical reactions as a function of time. The accumulation of Raman spectra was obtained under isothermal conditions. For the dehydration measurements, gases coming out of the Linkam cell were analyzed using a MKS Cirrus2 Mass Spectrometer. For the *In-situ*/*Operando* experiments, the Linkam CCR-1000 was used. To hold samples an alumina crucible of dimensions 5.5 x 7 mm was employed. Gaseous reactants flow from top to the bottom of the catalyst. A porous ceramic cloth supports the pelletized catalyst inside the crucible and allows the passage of gases to the mass spectrometer. The location of the thermocouple is along the periphery of the sample holder and at the same height where the sample is positioned. Technical details on the CCR-1000 cell can be found in the Linkam's homepage: http://www.linkam.co.uk/ccr1000-specifications/

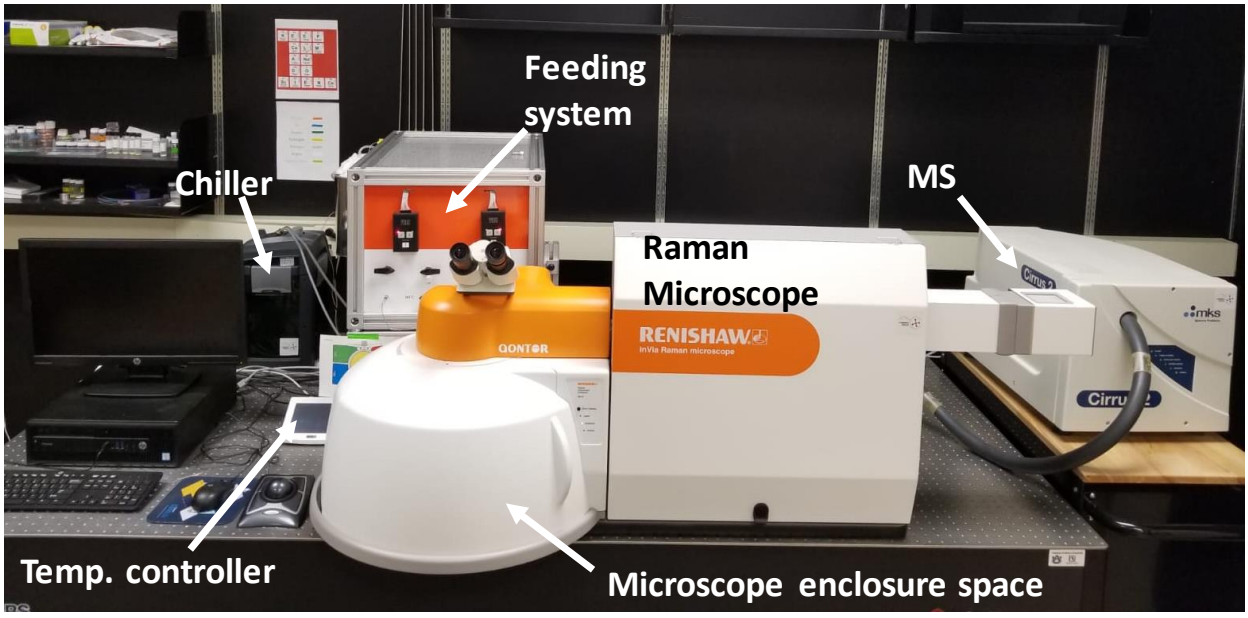

Figure 22. Schematic of the *operando* Raman setup with different components: gas feeding system, Raman microscope, mass spectrometer, Linkam cell chiller and temperature controller, and computer with Raman (Wire5.2) and MS (Process Eye) software.

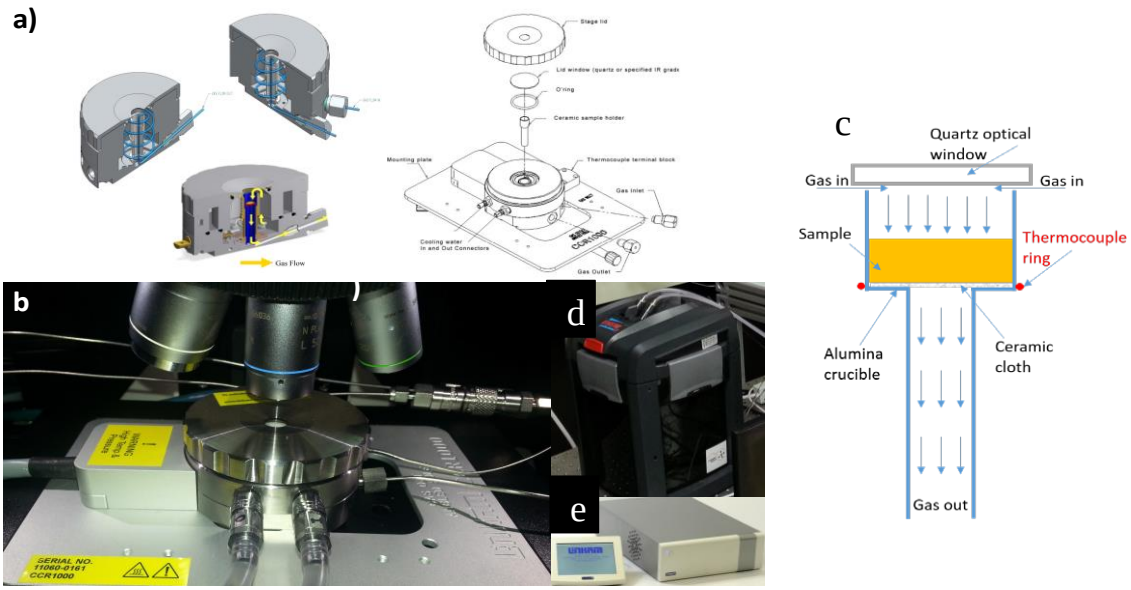

Figure 23. Schematic representation of the Linkam CCR-1000 cell. (a) detailed schematic representation of cell, (b) real image of cell, (c) details of crucible, (d) chiller for cooling the cell and (e) temperature controller for cell. Source: http://www.linkam.co.uk/ccr1000-specifications/

The isotopic labeling experiments were conducted using 99% $^{13}CO_2$ (Cambridge Isotope Laboratories Inc CLM-185-5) and $^{13}CH_4$ (Cambridge Isotope Laboratories Inc CLM-429-PK). These experiments were conducted to prove the reaction mechanism undergoing DRM reaction.

Figure 24

Figure 24. Isotopic labelled gases (a) $^{13}CO_2$ and (b) $^{13}CH_4$ for mechanistic steady-state DRM reaction studies from Cambridge Laboratories Inc, California.

Definition of calculations

$$\mathrm{CH_4\ Conversion\ (\%)} = \frac{CH_4 Converted\ (mol)}{CH_4\ input\ (mol)} * 100$$

$$\mathrm{CO_2\ Conversion\ (\%)} = \frac{\mathrm{CO_2} Converted\ (mol)}{\mathrm{CO_2}\ input\ (mol)} * 100$$

$$\frac{\mathrm{H_2}}{\mathrm{CO}}\mathrm{ratio} = \frac{\mathrm{H_2}\ produced\ (mol/min)}{CO\ produced\ (mol/min)}$$

$$\mathrm{CO\ formation\ rates} = \frac{CO\ produced\ (mol/min)}{Amount\ of\ catalyst\ (g)} * 100$$

$$\mathrm{CH_4}\ \ conversion\ rate = \frac{\mathrm{CH_4\ converted}\ (\frac{\mathrm{mol}}{\mathrm{min}})}{\mathrm{Amount\ of\ catalyst\ (g)}}$$

$$\mathrm{CO_2}\ conversion\ rate = \frac{\mathrm{CO_2\ converted}\ (\frac{\mathrm{mol}}{\mathrm{min}})}{\mathrm{Moles\ of\ metal\ (mol)}}$$

2.4 Overview of catalyst characterization techniques

Numerous characterization techniques such as bulk sensitive and surface sensitive techniques have been employed in the work; all these are described below.

2.4.1 Surface area determination by nitrogen physisorption

Nitrogen physisorption is the most used technique to characterize solid catalysts as it provides information regarding the porosity and the specific surface area of solid materials Figure 25. For surface area evaluation of a solid from a single isotherm, nitrogen is the most suitable adsorption agent. For surface area determination alone, argon provides an alternative to the commonly used nitrogen gas, but argon cannot be used at temperatures around -196 °C for the estimation of pore size distribution. If the specific surface is relatively low (less than $5m^2\ g^{-1}$) krypton, also at ~77K, offers the possibility of higher precision in the actual measurement of the adsorption-desorption trajectory, but not necessarily higher accuracy, than that obtained with N_2 or Ar. In biomass-based samples usually, CO_2 is used as an adsorbate to measure the surface area more accurately as compared to N_2.[114]

Figure 25. NOVA nitrogen physisorption equipment for the determination of surface area.

2.4.2 X-ray diffraction

X-ray diffraction (XRD) is a well establish and one of the most useful bulk characterization techniques to obtain structural information related to crystalline solids (Figure 26). The fundamentals of XRD can be found elsewhere[115] When the incident X-rays interact with the materials, a diffraction pattern is obtained, which is a fingerprint for that specific material. XRD is the elastic scattering of photons by the atoms (from the catalyst) in a periodic lattice, producing constructive interference. The photon scattering follows the Bragg relation

$$2d\sin\Theta=n\lambda$$

Where λ is the wavelength of the X-rays, d is the distance between two lattice planes, Θ is the angle between the incoming X-rays and the normal to the reflecting lattice plane and n is the integer naming the order of the reflection.[115]

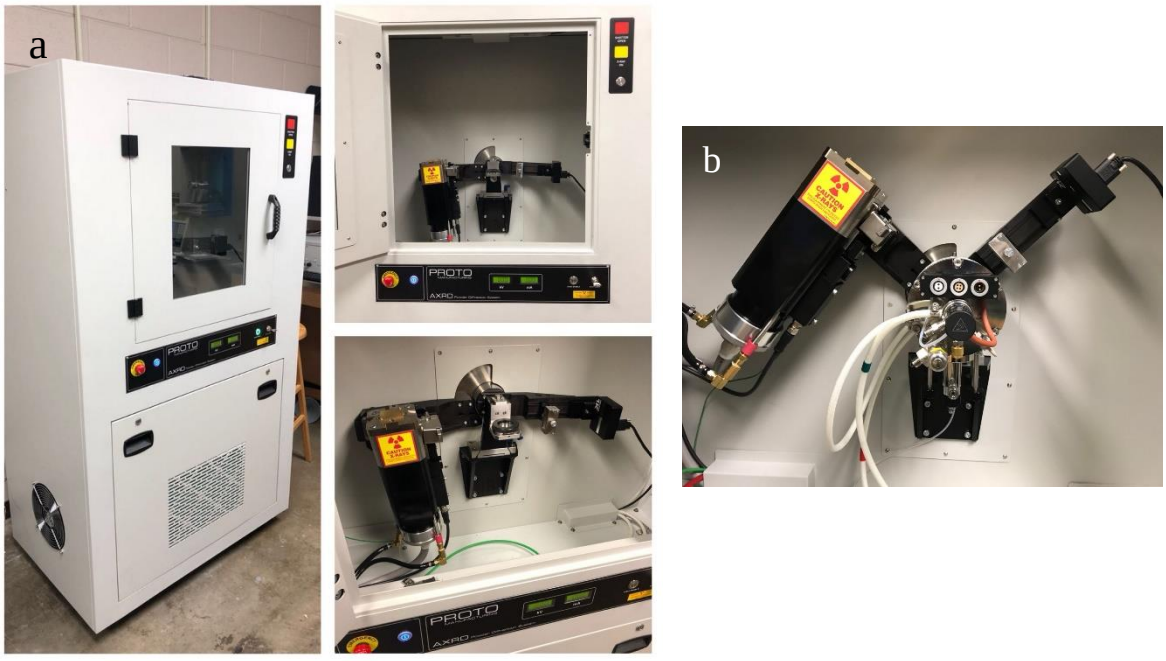

Figure 26. (a) XRD diffractometer to analyze the crystal structure of the catalyst, (b) equipped with an XRK-900 (Anton par) *in-situ* cell.

2.4.3 X-ray photoelectron spectroscopy

X-ray photoelectron spectroscopy (XPS) is a surface-sensitive quantitative spectroscopic technique that can measure the elemental composition, empirical formula, chemical state and electronic state of the elements that are present in the catalyst. Usually, the XPS spectra are acquired by irradiating the catalyst with a beam of X-rays and concurrently measuring the kinetic energy and number of electrons that escape from the top 0-10 nm of the catalyst surface. Conditions required to take XPS measurements require high vacuum ($P \sim 10^{-8}$ millibar) or ultra-high vacuum (UHV; $P < 10^{-9}$ millibar). The XPS measurements were conducted by Mingyang Chi from Dr Bruce Tatarchuk's lab Auburn University, and by Theodore O. Agbi from Dr Ive Herman's group at University of Wisconsin, Madison.

2.4.4 Raman spectroscopy

Raman spectroscopy is a technique to determine vibrational modes of molecules.[116] Raman spectroscopy is commonly used in material science to provide a structural fingerprint through which specific molecules can be identified and characterized. The incident laser interacts with molecular vibrations, phonons or other excitations in the system, this causes the energy of laser photons to shift up or down. This shift in the energy of the photons is specific to the material and gives information about the molecular vibrational modes present in the system. Figure 27

Figure 27. In via Raman spectrometer with Qontor technology for the analysis of vibrational modes present in the material.

2.4.5 Scanning electron microscopy

Scanning electron microscopy (SEM) is one of the types of electron microscopy that generates images of materials by scanning the whole surface with the focused beam of incident electrons beam. The incident electrons beam interacts with atoms in the material (catalyst) and produces signals that include information related to the surface topography and even the composition of the material (catalyst). The incident electron beam is typically scanned in a typical scan pattern known as 'raster scan pattern' and generates a signal to produce an image of the material (catalyst).

SEM analysis were conducted using JEOL JSM-7000F SEM equipped with an EDS detector, at Materials Engineering Department, Auburn University

2.4.6 Temperature programmed studies

Temperature programmed studies are often conducted to characterize heterogeneous catalysts. These studies evidence the behavior of the sample as s function of temperature under a specific gaseous environment. Such studies include a temperature-programmed reduction (TPR), temperature-programmed oxidation (TPO), temperature-programmed desorption (TPD), thermogravimetric analysis (TGA), etc. TPD studies were conducted on Quantachrome Autosorb IQ machine at Biosystems Engineering, Auburn University in Dr Sushil Adhikari's lab.

Chapter 3: Insights into the Thermal and Chemical Stability of Multilayered V_2CT_x MXene

Abstract

We report on the thermal stability of multilayered V_2CT_x MXene under different atmospheres by combining *in-situ* Raman Spectroscopy with *ex-situ* X-ray Diffraction (XRD), X-ray Photoelectron Spectroscopy (XPS), and Scanning Electron Microscopy (SEM) in order to elucidate and monitor molecular, electronic, and structural changes of both the surface and bulk of the V_2CT_x MXene which has recently received much attention. The MXene samples were heated up to 600 °C under inert (N_2), oxidative (CO_2, air), and reductive (H_2) environments with similar conditions. *In-situ* Raman showed that the V=O vibration for two-dimensional vanadia is preserved up to 600 °C under N_2, while its intensity reduces under H_2. When heated above 300 °C under either CO_2 or air, V_2CT_x slightly oxidizes or transform into V_2O_5, respectively. Furthermore, SEM revealed the persistence of an accordion-like layered structure for the MXene under N_2 and H_2, while under CO_2 and air, the layered structure collapses and form VO_2 (V^{4+}) and V_2O_5 (V^{5+}) crystals, respectively. XPS reveals that, regardless of the gas, surface V species oxidize above 300 °C during the dehydration process. Finally, we demonstrated that the partial dehydration of V_2CT_x results in the partial oxidation of the material, and the total dehydration is achieved once 700 ^{0}C is reached. We believe that our methodology is a unique alternative to tune the dehydration, oxidation, and properties of V_2CT_x, which allows for the expansion of MXenes' applications.

3.1 Introduction

Since their discovery in 2011,[117], two-dimensional (2D) metal carbides and nitrides (MXenes) have been extensively studied for various applications.[95, 118, 119] We envision to expand the application's portfolio of V_2CT_x, especially at high temperatures, to areas such as heterogeneous catalysis and/or sensors. In order to do so, new insights on the thermal structure-stability relationships of MXenes are necessary, especially bearing in mind that within the same material, both the chemical and structural properties of the surface and bulk are typically different. Therefore, the utilization of surface/bulk sensitive techniques, especially those allowing *in-situ* studies, are highly desired to meticulously study the physicochemical properties of V_2CT_x, and the expanding family of MXene materials in general. The formula for MXenes is $M_{n+1}X_nT_x$, where M is an early transition metal, X is carbon and/or nitrogen, T indicates various surface terminations, n=1, 2 or 3, and x is the number of surface groups per unit formula.[93] To date, about 20 different MXenes have been synthesized, and many others have been predicted theoretically.[95, 118] The physiochemical properties of these materials primarily depend on their composition and surface terminations (such as F, OH, and/or O), which can be controlled to produce materials with unique properties for specific applications.[95-120] MXenes are produced through selective etching of MAX phases, a family of hexagonal layered ternary carbides and nitrides (with a general formula of $M_{n+1}AX_n$).[93] The synthesis process allows the selective removal of A layered elements (group 13 or 14 elements, i.e., Al) from the structure of MAX phases (i.e., V_2AlC) and the formation of 2D MXenes.[94]

2D MXenes have shown unique electronic, mechanical, and optical properties[121] that render them as promising materials for applications such as gas sensors,[122, 123] water purification,[124] energy storage,[98, 125-127] biosensors,[128] hydrogen, and oxygen evolution,[94, 95, 129, 130] and catalysis.[95, 131-134]

Particularly V_2CT_x MXene has recently received considerable attention for charge storage applications in lithium-ion and multivalent-ion batteries.[99],[28,98] Up to now, the combination of e*x-situ* Raman, X-ray diffraction (XRD), X-ray Photoelectron Spectroscopy (XPS), and Scanning Electron Microscopy (SEM) have been extensively used to characterize the molecular and bulk (crystalline) structure of MXenes, primarily for $Ti_3C_2T_x$.[94, 117, 118, 121, 125, 129, 135-144] In addition, a few *in-situ* studies have also been performed using XRD[145] and Raman spectroscopy[146] to examine the structure $Ti_3C_2T_x$. Similarly, V_2CT_x has been characterized mainly using *ex-situ* XRD, XPS, and SEM,[93, 98, 147-150], and more recently, Champagne *et al*[151] evaluated computationally and experimentally the Raman spectra of V_2CT_x under ambient conditions.

To the best of our knowledge, *in-situ* characterization of the surface and bulk structure of V_2CT_x has not yet been performed before, especially under different environments and at temperatures above 25 °C. Therefore, we understand that there are still important insights on the structure-activity-stability relationships of V_2CT_x and MXenes, in general, to be discovered, discussed, and clarified. As it has been stated in previous studies related to MXenes,[95, 135, 136, 139, 152] their structural stability depends on the chemical environment and the experimental conditions.[95] For instance, *ex-situ* XRD shows that the $Ti_3C_2T_x$ structure is stable at 800-1200 °C under argon [135, 136, 139, 153] although, as suggested by Anasori *et al.*,[95] this still needs to be confirmed by *in-situ* XRD or Raman spectroscopy. In a different study conducted by Zhang *et al.*,[152] *ex-situ* Raman and XRD indicate that Nb_2CT_x oxidizes at 800 °C under CO_2. Nevertheless, a fundamental relationship between the surface and bulk structure with the reactivity of MXenes in operation and under real conditions (*in-situ*) still needs to be studied in order to design and prepare MXenes with tunable properties for high temperature applications, such as thermo-catalysis.

Herein, we report on the chemical and thermal stability of V_2CT_x up to 600 °C using *in-situ* Raman spectroscopy, together with *ex-situ* XPS, XRD, and SEM to monitor changes in the surface and the bulk physicochemical properties under different environments (N_2, Air, CO_2, and H_2). By combining *ex-situ* and *in-situ* studies, we demonstrate that the surface transforms differently as compared to the bulk structure as a function of temperature and environment. We primarily concentrate our study on V_2CT_x to identify *i)* the molecular structure of surface species, due to anticipated thermo-catalytic applications of this material, *ii)* the structural changes during the dehydration process, and *iii)* the optimal conditions where the layered structure is preserved. We aim to foster both V_2CT_x and MXenes in general as potential thermo-catalysts, beyond their already proved electro-catalytic applications. Recently, the water gas shift (WGS) reaction at 300 °C and the dehydrogenation of ethylbenzene at 550 °C were experimentally evaluated using Nb_2CT_x and $Ti_3C_2T_x$ MXenes, respectively.[134,103] These reported thermo-catalytic applications validate the importance of our study on establishing qualitative, and soon also quantitative,[154] structure-reactivity relationships for MXenes.

3.2 Materials characterization techniques.

3.2.1 XRD and SEM analysis

The structure of the synthesized MXene powder was characterized using a Bruker X-ray diffractometer with 40 kV and 40 mA Cu Kα radiation in using 0.2 sec/step. Around 20 mg of sample was loaded in the small cavity of the sample holder and pressed using a glass slide. Cross-section morphologies were obtained using a JEOL JSM-7000F scanning electron microscope.

3.2.2 Raman spectroscopy

Raman spectroscopy studies were performed using a Renishaw InVia Qontor Raman Spectrometer equipped with 785, 532, and 405 nm solid-state lasers, 5, 20, 50, and 100x objectives, and a MS

20 Encoded Stage. *In-situ* Raman studies were performed by coupling a Linkam CCR-1000 cell to the Raman microscope. The LiveTrack feature of the Qontor version of the InVia Raman Microscope was used to maintain the sample in focus and, therefore, more accurately correlate changes in the intensity of the Raman signals with specific chemical reactions as a function of time. For *in-situ* Raman studies, the samples were treated under inert, reducing, and oxidizing atmospheres using UHP gases in all cases. The various gases were introduced into the Linkam cell at a gas hourly space velocity (GHSV) of 36,000 mL $gm^{-1}hr^{-1}$. All measurements were taken with the 405 nm laser, 2400 L mm^{-1} grating, 50x long-distance objective, and, using 40 seconds of exposure time, 50% of power, and 40 accumulations. The behavior of the material under various atmospheres at different temperatures was recorded between 25 to 600 °C at a heating rate of 10 °C min^{-1}. The accumulation of Raman spectra was obtained under isothermal conditions. For the dehydration measurements, gases coming out of the Linkam cell were analyzed using a MKS Cirrus2 Mass Spectrometer.

3.2.3 X-ray photoelectron spectroscopy (XPS)

XPS data were collected by AXIS Ultra DLD (delay lines detector) X-ray photoelectron spectrometer (XPS) from Kratos Analytical Ltd. The end station consisted of a fast entry load lock, sample treatment chamber (STC), and a sample analysis chamber (SAC). Treated MXene samples were analyzed in SAC under 10^{-9} Torr. A monochromatic Al Kα X-ray source was used as the photon source. High-resolution spectra were obtained for C1s, O1s, and V2p using passing energy of 20 eV. The binding energy shifts due to surface charging were corrected using the C1s level at 284.6 eV. Core level peaks of O1s were deconvoluted by using Gaussian-Lorenzian (20%) peaks.

3.3 Results and discussion

In order to circumvent batch effects, about 2.5 grams of the same sample from the same batch was used for this study. Batch effects were considered very important for the present study because of the preparation of V_2CT_x. We noticed that a certain amount of residual carbon impurities is also formed along with the MXene phase due to the over-etching of the transition metals. As known, such surface carbonaceous deposits influence the material's thermal and chemical properties to a certain extent, and therefore we decided to use the same batch of MXene material for this study. Moreover, residual carbon complicates the Raman characterization of the VO_x species within the MXene, which is also one of the goals of this study. This is due to the stronger Raman scattering of carbon (D and G Raman peaks at 1351 and 1592 cm^{-1}, respectively). A series of Raman spectra from various batches is shown in Figure 28.

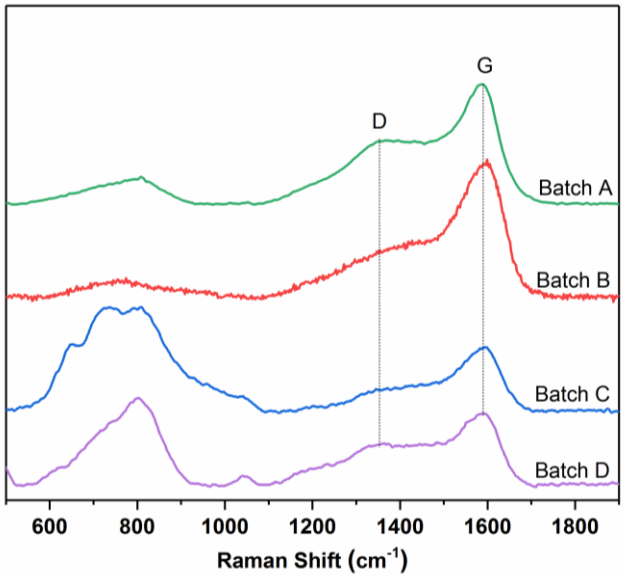

Figure 28. Raman spectra for various batches of V_2CT_X MXene showing a different amount of carbon on the surface. For the present study, batch D was selected.

3.3.1 As prepared V_2CT_x before the test

The transformation of the V_2AlC MAX phase into the V_2CT_x MXene phase is confirmed by various techniques, as shown in Figure *29*. The XRD spectra depicted in Figure *29* a shows a peak

around 2θ of 8.58° which is assigned to the (0002) plane of V_2CT_x MXene.[93, 95, 98, 143, 147-150] Importantly, the position of this peak tends to slightly shift depending on the amount of confined water that intercalates in between the MXene layers,[99] which in turn may change with varying the synthesis conditions. The small peaks around 2θ of 13.5° and 41.5° indicate the presence of a small amount of unreacted crystalline V_2AlC MAX phase (JCPDS No. 29-0101), consistent with previous reports.[7] This small amount of unreacted MAX phase appears in almost all MXenes synthesized by HF etching, and since it has a more ordered structures compared to the produced MXene, their XRD peaks are relatively sharp.[93, 99] Nevertheless, during our SEM studies, almost no MAX particles (similar to before treatment powders) were observed. This indicates that first, the amount of the unreacted particles is very low, and second, the observed sharp XRD peaks most probably originate from partially etched MXene particles, which still contain Al. In addition, SEM shows the formation of the typical accordion-like multilayered MXenes structure of V_2CT_x (Figure 29 b). The SEM image of V_2AlC MAX is shown in Figure 30**.**

After confirming the successful synthesis of V_2CT_x MXene, *in-situ* Raman studies were performed to gain information about the molecular structure of the surface species. Figure 29 c shows the Raman spectra for the V_2AlC MAX phase and V_2CT_x MXene. The sharp Raman vibrations observed in the V_2AlC MAX phase transform into broader peaks when it is converted into V_2CT_x MXene. Champagne *et al.* suggest that this might happen due to the large interlayer spacing in the MXene phase.[151] The V_2AlC MAX exhibits characteristic Raman peaks at 158, 239, 258, and 360 cm^{-1}.[151, 155, 156] The Raman vibration at 158 and 239 cm^{-1} (E_{2g}) represent in-plane vibration of V and Al atoms, while the vibrations at 258 cm^{-1} (E_{1g}) and 360 cm^{1} (A_{1g}) corresponds to the in-plane and out-of-plane vibration of V atoms.[151]

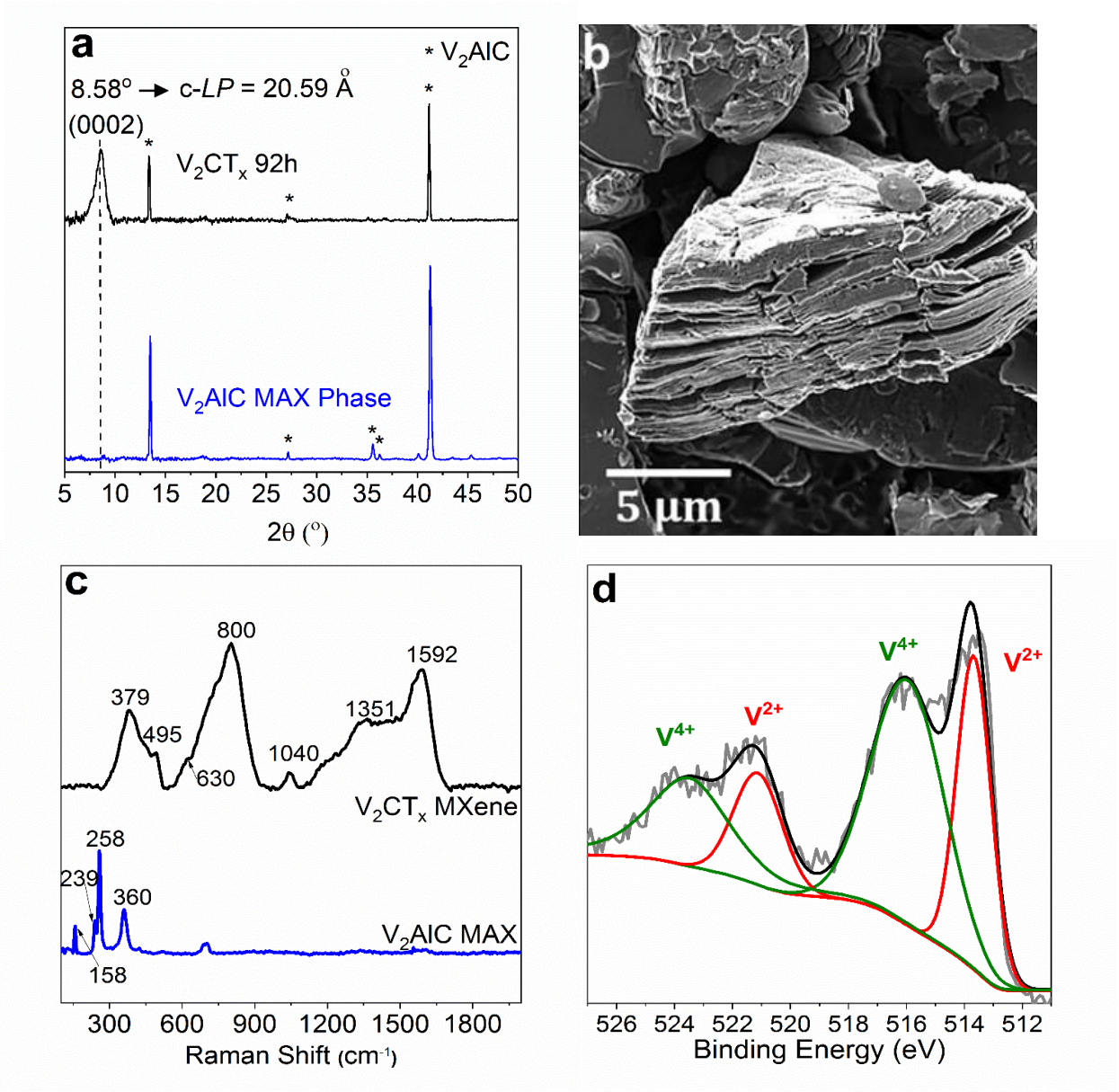

Figure 29. *Ex-situ* (a) XRD pattern of V_2CT_x MXene, the asterisk (*) denotes an unreacted MAX phase (b) SEM image of V_2CT_x MXene. (c) *In-situ* Raman spectra (405 nm) for as prepared V_2CT_x MXene and V_2AlC MAX phase, and (d) *ex-situ* XPS spectra of V2p region for bare V_2CT_x MXene.

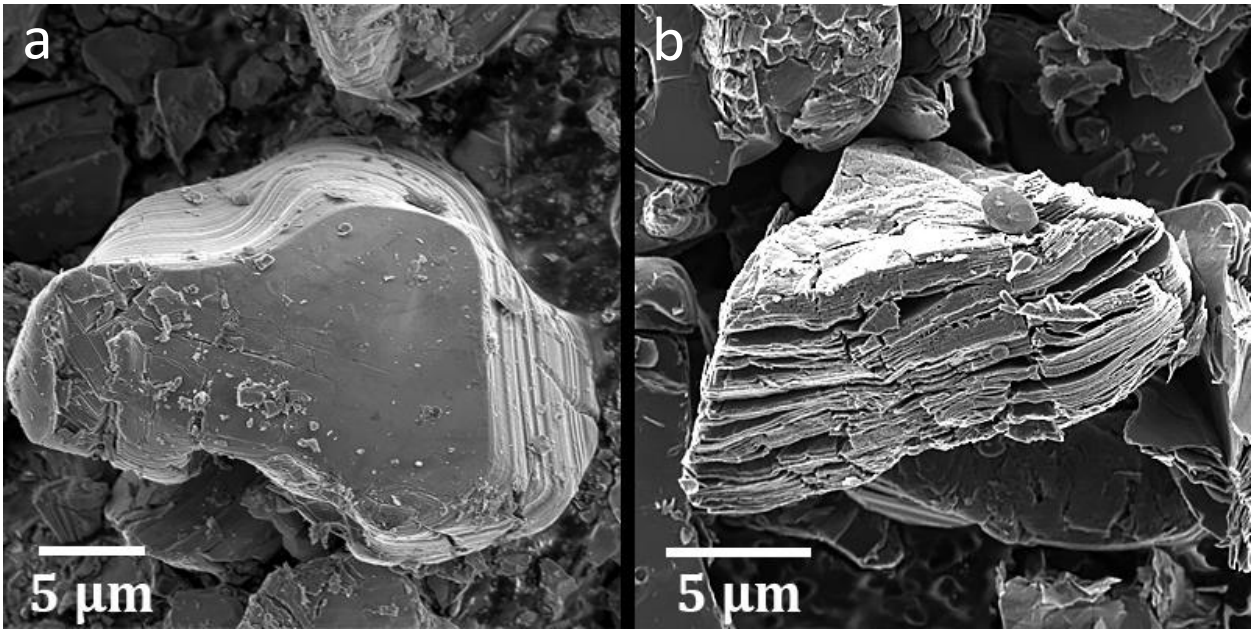

Figure 30. SEM image of (a) V_2AlC MAX phase and (b) V_2CT_x MXene phase.

On the other hand, V_2CT_x exhibits Raman peaks at 379, 495, and 630 $cm^{-1,}$ which are close to those vibrations calculated elsewhere.[151] We attribute the Raman vibration around 379 cm^{-1} to A_{1g} (out of plane vibrations of V atoms) mode of V_2C systems, while the Raman vibrations around 495 cm^{-1} to E_g (in-plane vibrations of V atoms) mode of $V_2C(OH)_2$ species. [151, 157] The presence of Raman peak in between 400 and 550 cm^{-1} is indicative of terminated V_2CT_x systems, and the peak around 630 cm^{-1} corresponds to the presence of mixed heterogeneous terminal functionalities (O, F, OH).[151] We performed our Raman study up to longer Raman shift (3000 cm^{-1}) and, therefore, we observed additional peaks. We assign the Raman peak at 800 cm^{-1} to V_2C MXene with terminal functionalities (F, OH), which typically appear below 750 cm^{-1} for V_2C MXene without fluorine and/or hydroxyl terminations.[151] This shift has also been reported for other MXenes.[158]

In addition, we observed a Raman peak at 1040 cm^{-1} attributed to the vanadyl (V=O) stretching for two-dimensional surface VO_x species.[159-162] This Raman V=O vibration corroborates for the first time the two-dimensional nature of VO_x species within the material (typically verified by

XRD and SEM). On the other hand, the Raman signals at 1351 and 1592 cm^{-1} are assigned to amorphous (D band) and graphitic (G band) carbon, respectively.[135, 163, 164] These carbon signals appear due to the over-etching of some MXene particles, which leads to the formation of carbon. It should be noted that previous studies on the complete etching of aluminum atoms from MAX phases also show the formation of mostly amorphous carbon with some graphitic regions.[165]

The XPS spectrum for V2p is shown in Figure 29 d. The deconvolution of the V2p region shows the presence of vanadium as V^{2+}(~513.3 eV)and V^{4+} (~516.3 eV), as reported in previous studies.[98] The peak at ~513.3 eV (V^{2+}) shows the presence of unreacted V_2AlC MAX phase and also the contribution from the V-C peak overlap at the same binding energy (~513.3 eV). Therefore, the peak is more pronounced, considering the strong metal carbide interaction. The peak around ~516.3 eV (V^{4+}) is attributed to the existence of a monolayer of vanadium oxide on the surface of vanadium carbide,[98,99], which corroborates the above-mentioned XRD and Raman results. The XPS spectra for C1s and O1s can be found in Figure 31. The C 1s region shows the presence of V-C (~282.2 eV), C-C (~284.8 eV), C-OH (~285.9 eV), and C=O (~288.3 eV), while the O 1s region shows the presence of VO_x (~530 eV), C-V-O_x (~531.2 eV), C-V-$(OH)_x$ (~532 eV) and H_2O_{ads} (~532.2 eV), which we will use for discussion of the V_2CT_x MXene material when subjected to different chemical atmospheres. The C-V-O_x (~531.2 eV), C-V-$(OH)_x$ (~532 eV) and H_2O_{ads} (~532.2 eV) species comprise the majority fraction (~75%) in the O 1s region. The remaining is in the form of mixed vanadium oxide (VO_x) species, which is primarily resulting from surface oxidation. The surface organic contaminants (OR) of COO and C-O contribute in this region, thus overlapping and obscuring other peaks. [166]

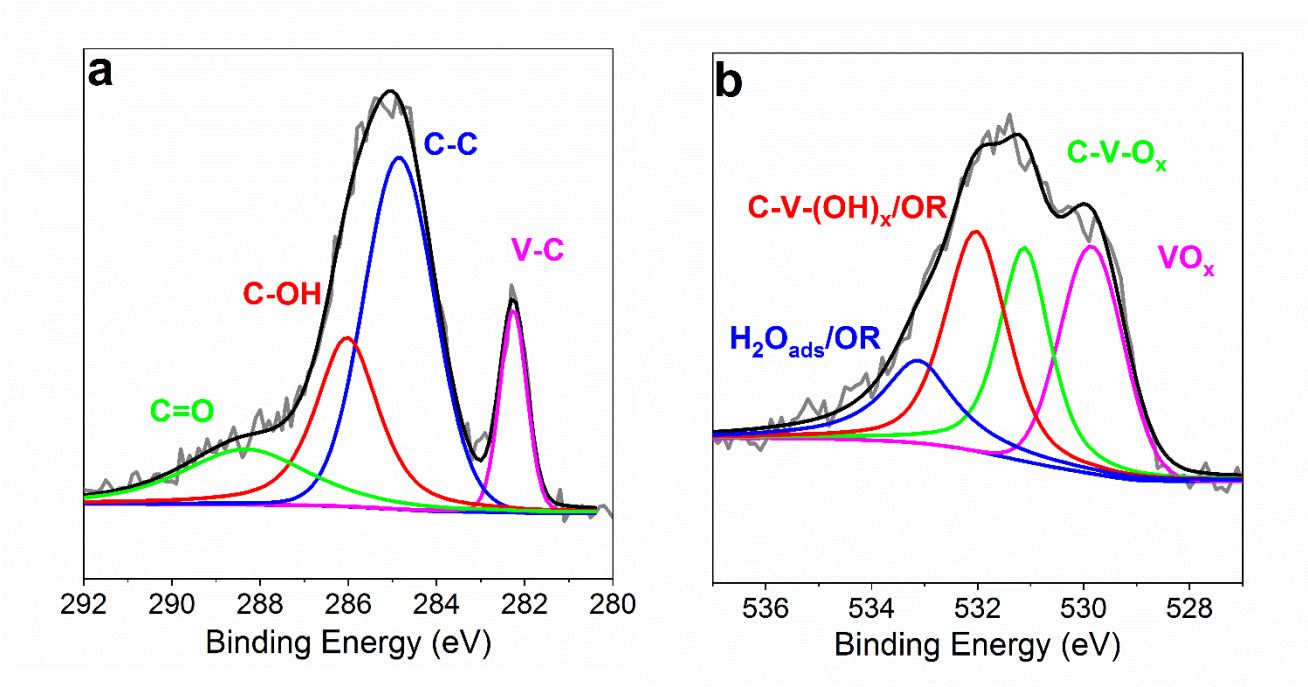

Figure 31. XPS spectra of (a) C1s region and (b) O1s region for the bare V_2CT_x MXene. Surface charging was corrected using the C1s level at 284.8 eV. OR stands for organic compounds due to atmospheric surface contaminations.

3.3.2 Nitrogen treated V_2CT_x MXene

To determine the thermal stability of V_2CT_x, we exposed it to nitrogen up to 600 °C. As shown in Figure 32a, the intensity of the Raman signals at 800 (carbide phase) and 1040 cm^{-1} (2D V=O) present in the prepared material remain constant as a function of temperature, proving the thermal stability of V_2CT_x. However, the surface of the material slightly oxidizes at 600 °C, as evidenced by the Raman vibration at 450 cm [1.] Xie *et al.* computationally calculated the activation barriers for dehydration of MXenes and explored the effect of drying temperature on the surface structure.[167] The dehydration follows Reaction 1, which evidences the change in the surface of MXenes during the dehydration process: [167]

$$Mn_{+1}X_n\,(OH)_2 \rightarrow M_{n+1}X_nO + H_2O \qquad (1)$$

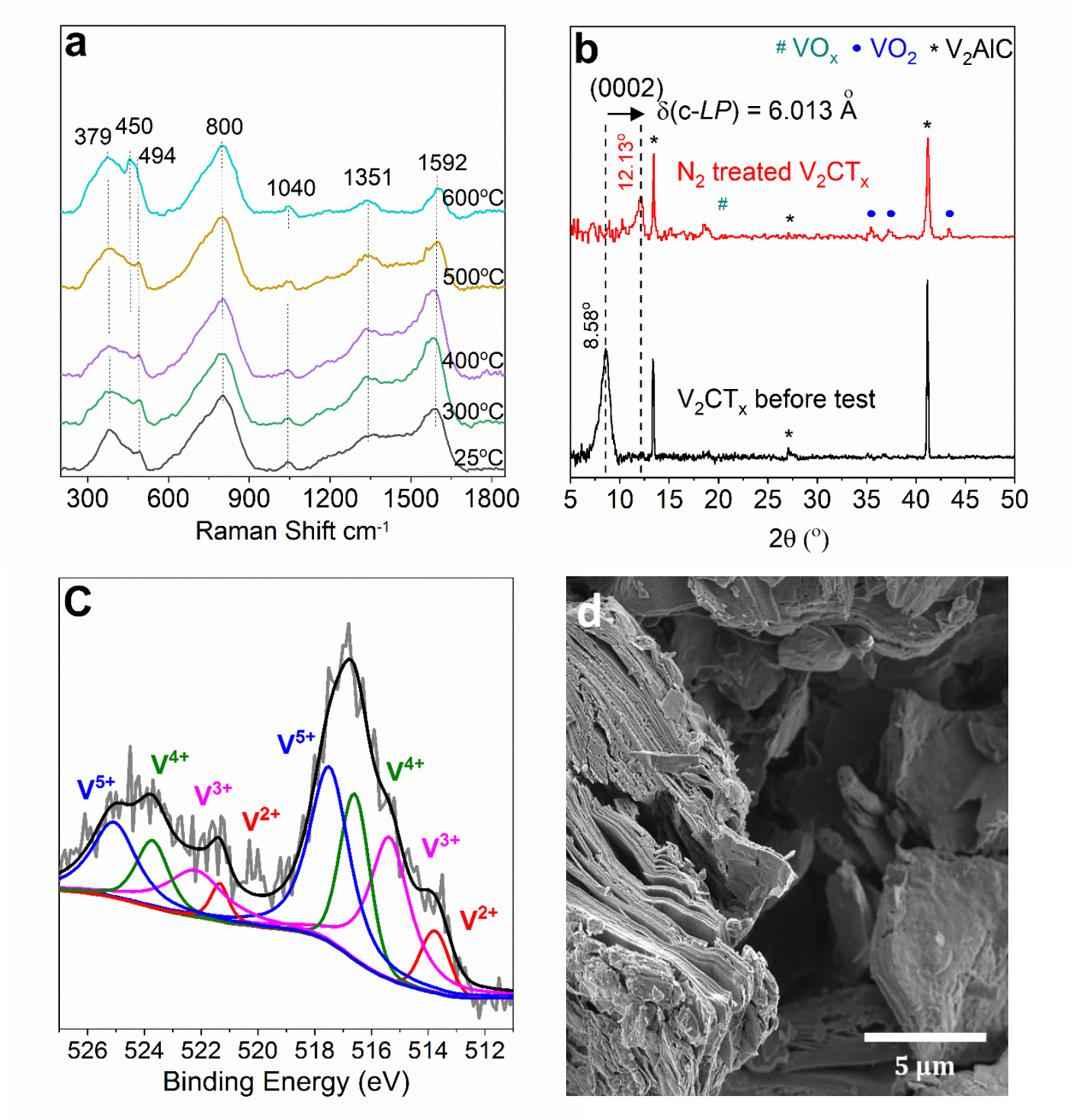

Figure 32. N_2-treated V_2CT_x MXene at 600°C, (a) *In-situ* Raman spectra (405 nm), *ex-situ* (b) XRD diffractogram, (c) XPS spectra of V2p region, and (d) SEM micrograph.

.

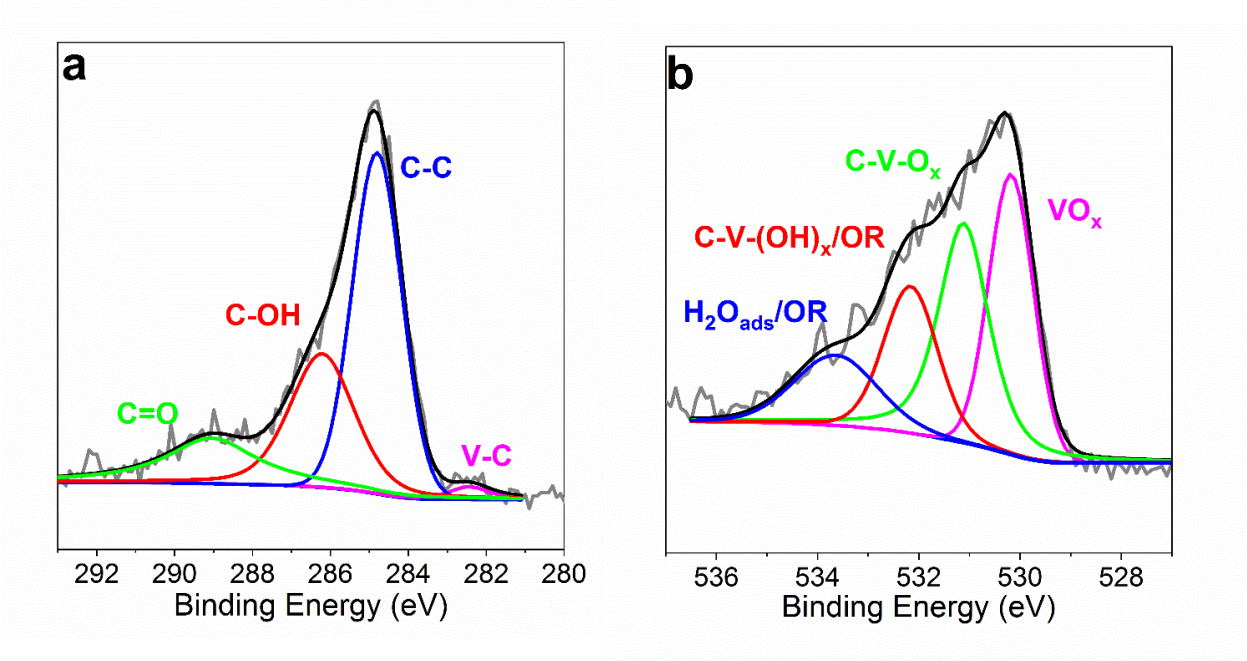

Figure 33. XPS spectra of (a) C1s region and (b) O1s region for the V_2CT_x MXene treated under nitrogen at 600°C Surface charging were corrected using the C1s level at 284.8 eV. OR stands for organic compounds due to atmospheric surface contaminations.

Importantly, we don't find a consensus on the reliable assignment for the Raman vibrations for V_2C with different terminations (F, OH, O). [151, 157] Thus, we ascribe the Raman vibration 450 cm^{-1} to the formation of V_2CO_x species resulting from dehydration of V_2CT_x at high temperature (Reaction 1). The decrease in the intensity of Raman peaks at 1351 (sp^3 amorphous carbon) and 1592 cm^{-1} (sp^2 graphitic carbon) above 500 °C, indicates the gasification of the residual carbon ($C + H_2O \rightarrow CO + H_2$) formed due to over-etching of V_2CT_x as a product of its reaction with structural water.

In addition, XRD shows a comparison of the as-prepared and N_2-treated V_2CT_x at 600 °C (Figure 32b). We attributed the shift of the MXene (0002) peak from 8.58 ° to 12.13 ° due to a decrease in the *c*-LP as a result of the removal of water trapped in-between the layers (dehydration). The formation of small diffraction peaks characteristic for VO_2 (V^{4+}) crystals, confirms the slight peripheral oxidation of material during the dehydration process.

XPS analysis of the V2p region (Figure 32c**)** reveals the presence of V^{5+} (~517 eV) and V^{3+} (~515.6 eV) along with V^{2+} (~513.3 eV) and V^{4+} (516.3 eV) which were present in the as-prepared material, indicating the oxidation of some V^{2+} and V^{4+} species to V^{3+} and V^{5+} species. The presence of V^{5+} species on the outermost layer(s) after the N_2-treatment up to 600 °C, is due to the above-mentioned slight oxidation of the surface vanadium species. The comparison of N_2-treated and the as-prepared V_2CT_x, using the C1s and O1s XPS spectra, is shown in Figure 33. The C1s XPS spectrum shows the presence of the V-C (~282.2 eV), C-C (~284.8 eV), C-OH (~285.9 eV), and C=O (~288.3 eV), with a slight decrease in V-C peak. While the O1s spectrum shows the increase in C-V-O_x (~531.2 eV) and C-V-$(OH)_x$ (~532 eV) peak intensity, signaling the minuscule oxidation of the V_2CT_x MXene surface.

Finally, SEM-micrograph evidences the persistence of the layered structure of V_2CT_x after the N_2-treatment at 600 °C **(**Figure 32d**)**. In summary, the bulk structure of V_2CT_x is stable under nitrogen up to 600 °C, while the surface slightly oxides by reacting with the trapped water during the dehydration process.

3.3.3 Carbon dioxide treated V_2CT_x MXene

Figure 34 shows the surface and bulk transformation of V_2CT_x MXene under CO_2 at 600 °C. *In-situ* Raman spectroscopy (Figure 34a) reveals that as opposed to its behavior under the nitrogen atmosphere, V_2CT_x oxidizes above 300 °C under this mild oxidant gas. First, additional Raman peaks appear at 235, and 332 cm^{-1}, which are assigned to VO_x species, particularly peak around 235 cm^{-1} corresponds to lattice motion involving V-V bonds while around 332 cm^{-1} correspond to the vibrational motion of V-O bonds. [168-171] Second, the Raman peak at 800 cm^{-1} ascribed to

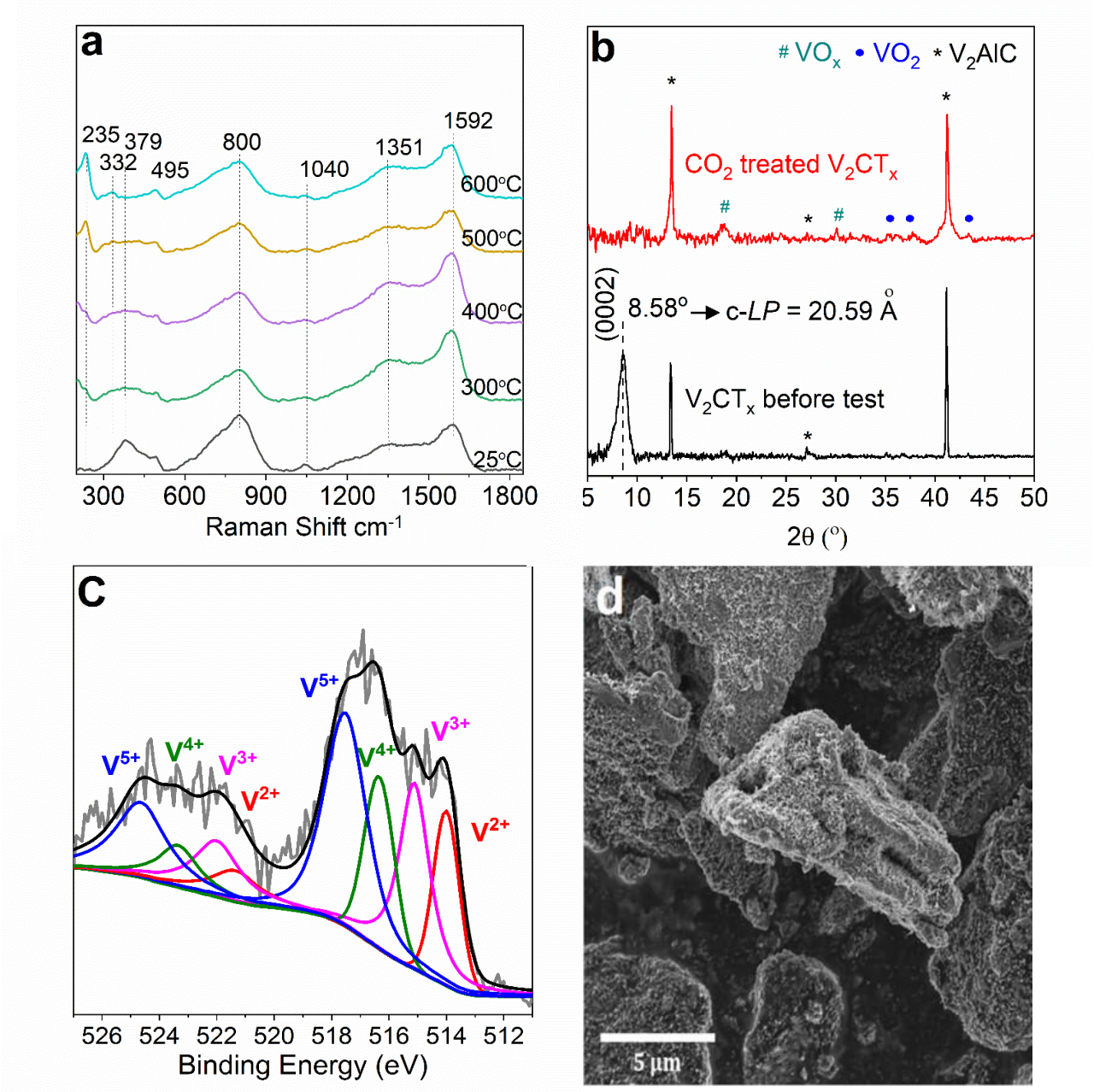

Figure 34. CO_2-treated V_2CT_x MXene at 600ºC, (a) *In-situ* Raman spectra (405 nm), *ex-situ* (b) XRD diffractogram, (c) XPS spectra of V2p region, and (d) SEM micrograph.

Vanadium carbide species decreases at temperatures above 400 °C, which does not happen under nitrogen. This indicates that CO_2 is responsible for this slight oxidation, instead of trapped water. XRD of the CO_2-treated V_2CT_x shows the disappearance of the MXene peak observed in the as-

prepared material around 2θ of 8.58° and the advent of a new peak around 2θ of 17.01° (Figure 34b). These peaks are assigned to a formation of VO_x species.[172, 173]

The diffractograms corroborate the slight oxidation of V_2CT_x observed during the *in-situ* Raman study (Figure 3a).

XPS analysis of the V2p region (Figure 34c) reveals the presence of V^{5+} (~518 eV) and V^{3+} (~515.6 eV), along with V^{4+} and V^{2+} that are originally present in the as-prepared material. This validates the slight surface oxidation of the material due to the presence of CO_2. However, comparing the above-described *in-situ* Raman and *ex-situ* XRD results, the V_2CT_x surface oxidizes differently to its bulk. The oxidation of the surface is also proven by the decrease in relative intensity in the XPS spectra of the V-C signal at 282.6 eV and the increase in the VO_x (~530 eV), C-V-O_x (~531.2 eV) signals in the O1s region Figure 35.

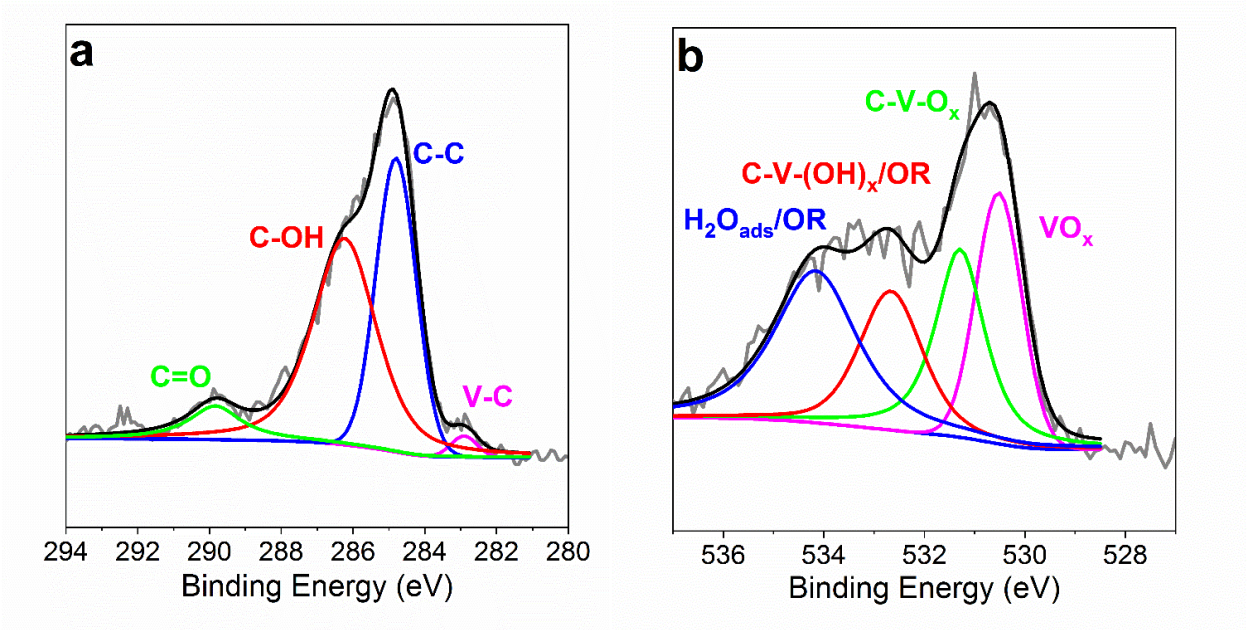

Figure 35.XPS spectra of (a) C1s region and (b) O1s region for the V_2CT_x MXene treated under Carbon dioxide at 600°C. Surface charging was corrected using the C1s level at 284.8 eV. OR stands for organic compounds due to atmospheric surface contaminations.

Finally, SEM studies reveal the formation of homogeneously distributed oxide nanocrystals on the MXene's surface after CO_2-treatment at 600 °C (Figure 34d). The mild oxidation of the surface and bulk structure of V_2CT_x may favor its electrochemical properties as has already been reported for CO_2-treated Nb_2CT_x MXenes.[152] In addition, SEM reveals the collapse of the layered structure of V_2CT_x, supporting our XRD results.

3.3.4 Air treated V_2CT_x MXene

Figure 36 shows the data for V_2CT_X MXene after air-treatment up to 600 °C. *In-situ* Raman (Figure 36a) shows the oxidation of V_2CT_X into bulk V_2O_5 around 400 °C as evidenced by *i)* the characteristic V_2O_5 peaks at 294, 480, 520, and 696 cm^{-1},[30, 36-37, 39] *ii)* the shift of the 1040 cm^{-1} peak assigned to the stretching of two-dimensional vanadyl (V=O) species [161, 174] to 995 cm^{-1}, which now corresponds to the stretching of V=O for V_2O_5 particles (
Figure 37)[175, 176] and the disappearance of the peaks at 800, 1351, and 1592 cm^{-1} assigned to the vanadium carbide phase, amorphous sp^3 carbon, and graphitic sp^2 carbon respectively. [40-43]
Additionally, the emergence of sharp XRD peaks around 2θ of 15.4°, 20.3°, 21.75°, 26.17°, 31.0°, 32.4°, 33.36°, 34.32°, 41.32°, and 42.0° (JCPDS No. 41-1426) reveals the oxidation of V_2CT_x into V_2O_5 (Figure 36b). This severe oxidation further leads to the destruction of the layered MXene's structure, as shown by the absence of the XRD peak at 2θ of 8.58°. The remaining MAX phase within the MXene material also oxidizes as evidenced by the disappearance of the XRD peak at 2θ of 13.5° while the peak at 41.5°remarkably decreases. For clarification, the XRD spectra of oxidized V_2CT_x MXene and bulk V_2O_5 can be found in the (Figure 38).

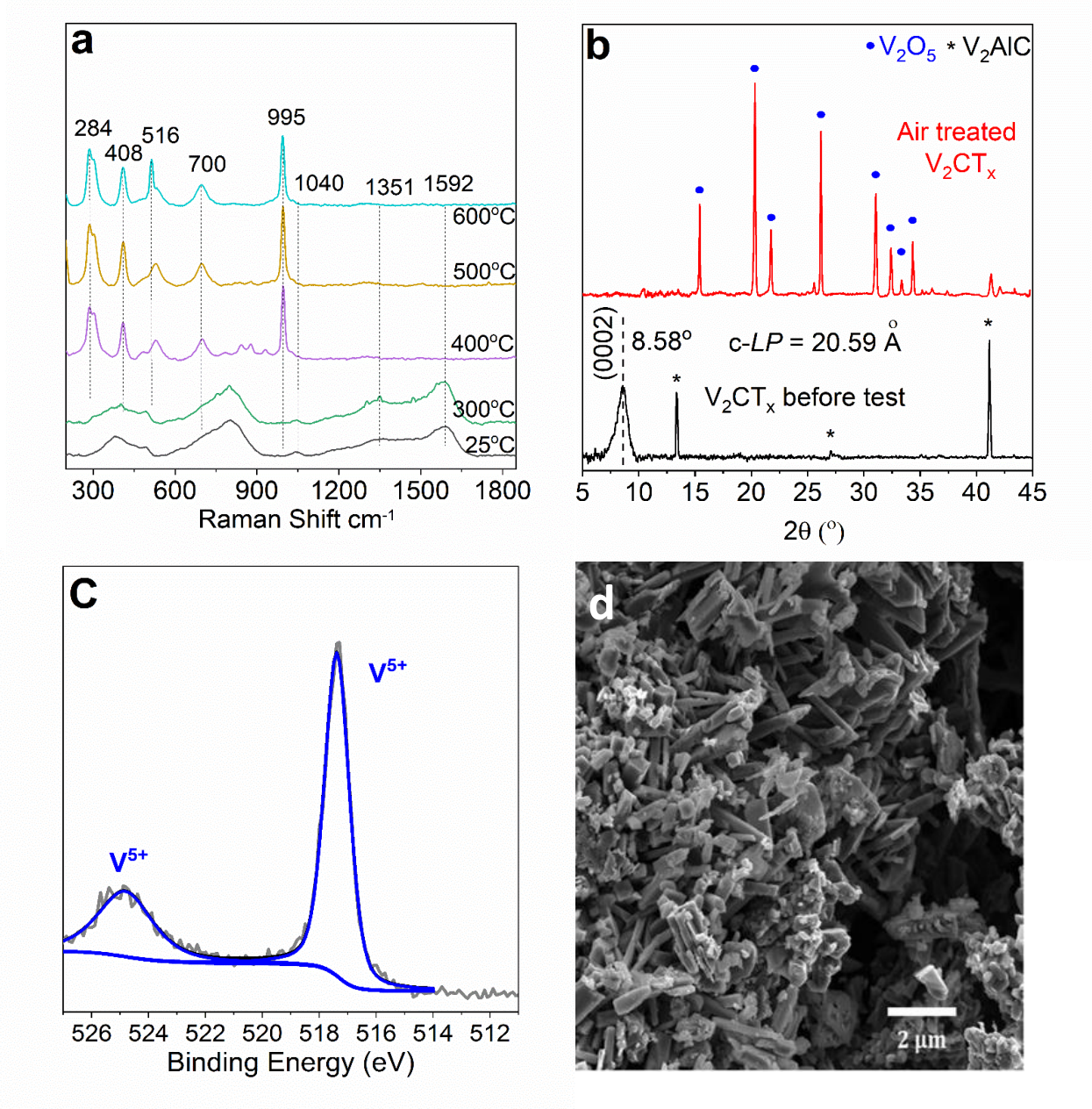

Figure 36. Air-treated V_2CT_x MXene at 600°C, (a) *In-situ* Raman spectra (405 nm), *ex-situ* (b) XRD diffractogram, (c) XPS spectra of V2p region, and (d) SEM micrograph.

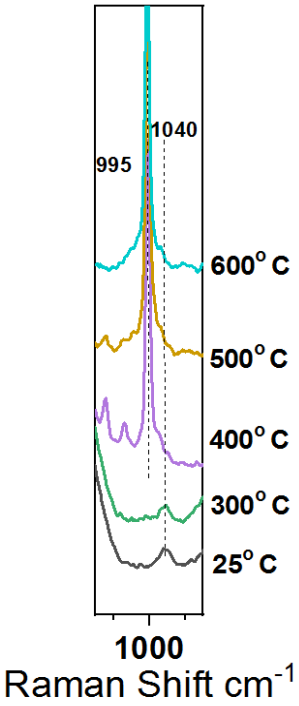

Figure 37. *In-situ* Raman spectra of air treated V_2CT_x MXene. Surface V=O (vanadyl) shift to 995 cm^{-1} from 1040 cm^{-1} as a function of temperature.

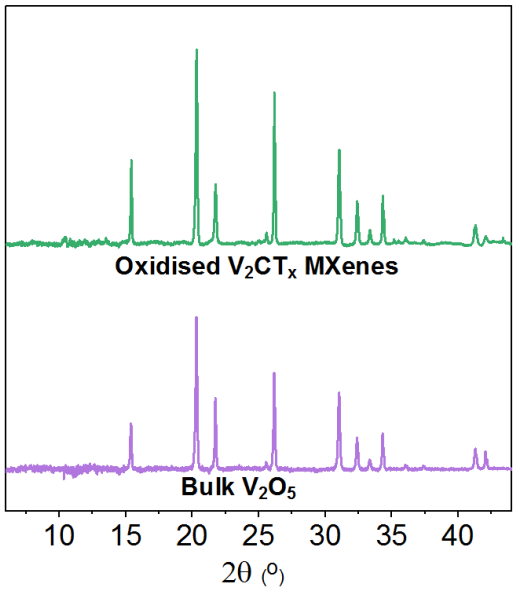

Figure 38. XRD diffractogram of commercial bulk V_2O_5 and V_2CT_x MXene after treating under air. (JCPDS No. 41-1426).

XPS analysis of the V2p region (Figure 36c) shows a completely oxidized V_2CT_x surface. Vanadium is present primarily as V^{5+} (~517 eV), resulting from the oxidation of V^{2+} (513.3 eV) and V^{4+} (516.3 eV) present in the as-prepared material (Figure 29d). Additionally, the XPS spectra for C1s and the O1s (Figure 39**)** show the disappearance of the V-C peak (~282.6 eV) and the increase in the VO_x species (~530 eV), respectively.

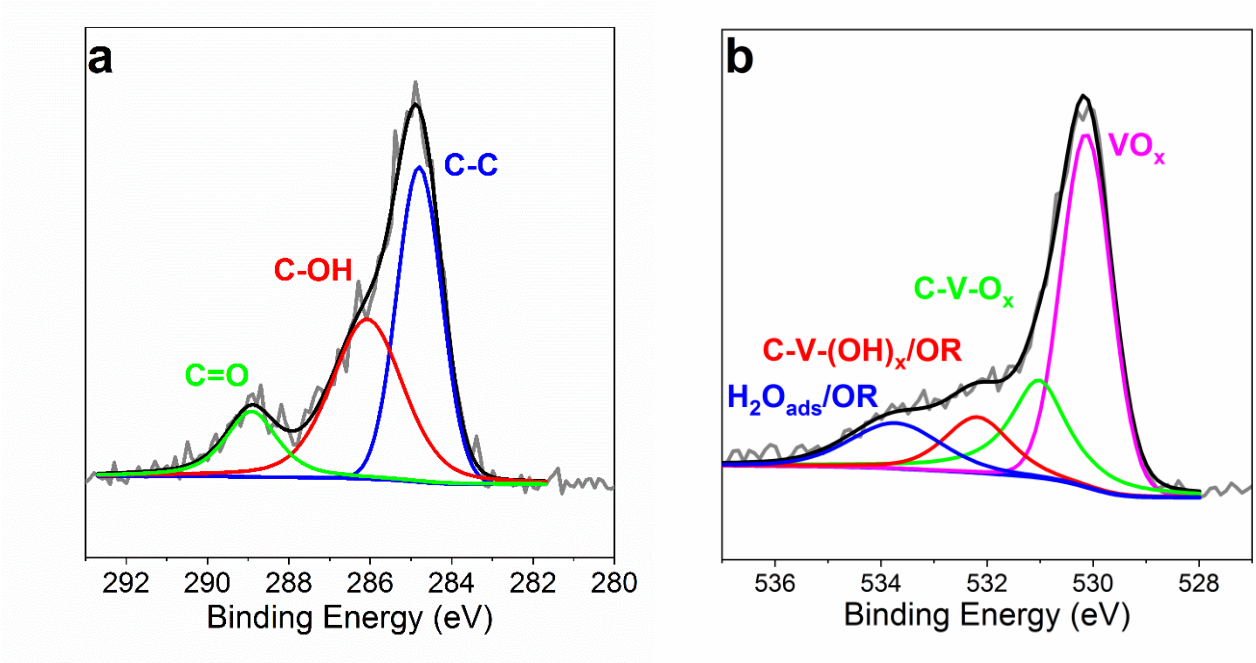

Figure 39. XPS spectra of (a) C1s region and (b) O1s region for the V_2CT_x MXene treated under air at 600°C. Surface charging was corrected using the C1s level at 284.8 eV. OR stands for organic compounds due to atmospheric surface contaminations.

Complimentary, SEM was performed to further investigate the structure of the air treated V_2CT_X MXene at high temperature. The micrograph shows the complete destruction of the layered MXenes structure and the formation of oxide crystals (Figure 36d). These crystals are similar in appearance when compared to the bulk V_2O_5.[177]; thus, the SEM study further substantiates the Raman, XRD, and XPS results discussed above. Similar results were reported for $Ti_3C_2T_x$ MXene, and a mechanism for its oxidation as a function of temperature was suggested.[135]

3.3.5 Hydrogen treated V_2CT_x MXene

As shown in Figure 40a, the decrease in the Raman peaks at 379 and 495 cm^{-1} attributed to A_{1g} (out of plane vibrations of V atoms) mode of V_2C systems and E_g (in-plane vibrations of V atoms) mode of $V_2C(OH)_2$ species [151, 157] and in the peak at 1040 cm^{-1} attributed to the stretching of two-dimensional surface vanadyl[175, 176] indicates that reduction of surface vanadium oxide species occurs in the H_2-treated V_2CT_x. Interestingly, the vanadyl Raman peak at 1040 cm^{-1} does not reduce fully, even after 7 hours under reduction, as has been reported for supported two-dimensional vanadium oxide.[178, 179] For clarification, *in-situ* Raman spectra highlighting the reduction of the vanadyl group is depicted in Figure 41.

The Raman peak at 1592 cm^{-1} assigned to the G carbon band increases as a function of temperature under hydrogen atmosphere (Figure 42). The rise in intensity of the G band can be attributed to the loss of surface terminal groups, mainly O and F, from the surface of V_2CT_x, exposing the carbon. Similar observations were reported for Ti_2CT_x and Nb_2CT_x MXenes when they were treated under a hydrogen environment.[134, 137]

As shown by XRD (Figure 40b), the MXene peak (0002) for V_2CT_x is no longer observed after reducing the material up to 600 °C. This can be attributed to the removal of water molecules, thus reducing the d-spacing and resulting in the disappearance of MXene peak as the orientation needed for the Bragg's diffraction cannot be formed. Insights on the chemical composition of the surface of the H_2-treated V_2CT_x at 600 °C were gained using XPS (Figure 40C). The deconvolution of the V2p region of the XPS spectra shows the presence of V^{2+} (~513.3 eV), V^{3+} (~515.8 eV), and V^{4+} (~516.3 eV), primarily evincing the reduction of the MXene under high-temperature hydrogen environment.

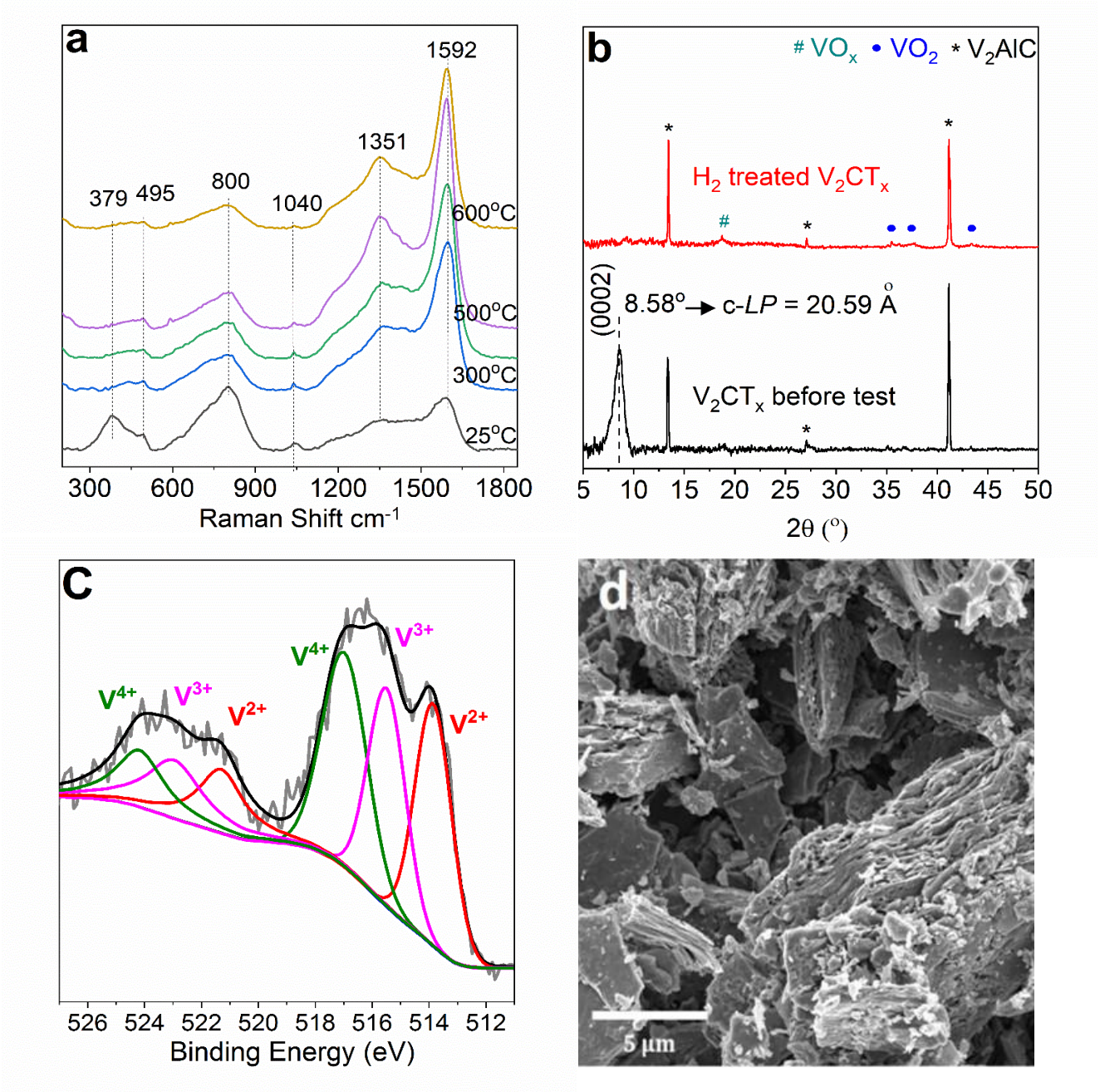

Figure 40. Hydrogen-treated V_2CT_x MXene at 600°C, (a) *In-situ* Raman spectra (405 nm), *ex-situ* (b) XRD diffractogram, (c) XPS spectra of V2p region, and (d) SEM micrograph.

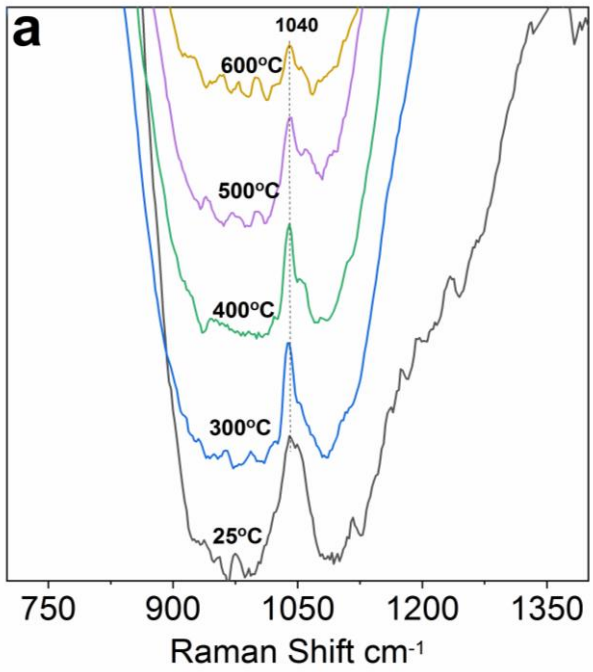

Figure 41. *In-situ* Raman spectra of hydrogen treated V_2CT_x MXene. Surface V=O (vanadyl) as a function of temperature under the H_2 environment.

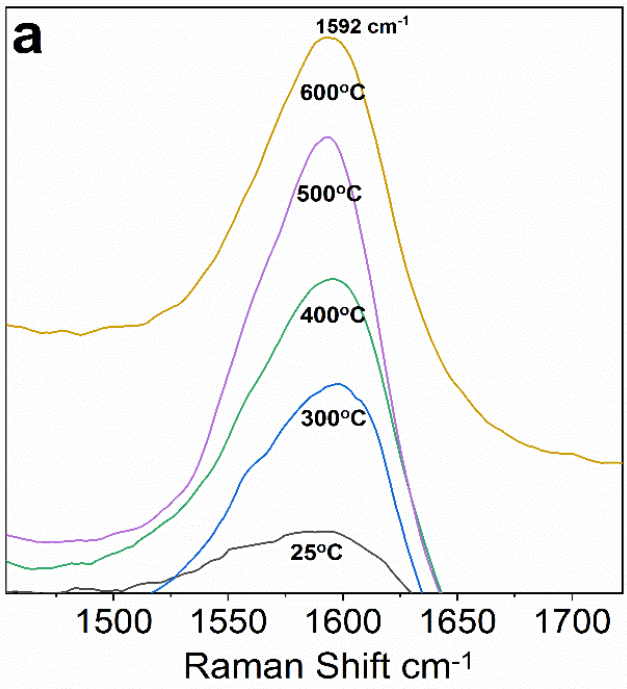

Figure 42. *In-situ* Raman spectra of hydrogen treated V_2CT_x MXene. G carbon signals increase as a function of temperature under the H_2 environment.

The C1s region still shows the persistence of pronounced V-C (~282.2 eV) peak, thereby indicating the presence of strong metal carbide interaction at the surface (Figure 43). Finally, the SEM micrograph (Figure 40d) reveals the presence of a layered morphology, but with a different structure. Based on the analysis conducted, it can be corroborated that the MXene peak (0002) is no longer observed, but the layered structure is maintained to a certain degree. The loss of the MXene peak (0002) and the difference in the structure is primarily due to the removal of water molecules. Importantly, even after the loss of the MXene peak (0002), the layered structure remains to a certain extent after reducing the V_2CT_x for about 7 hours up to 600 °C.

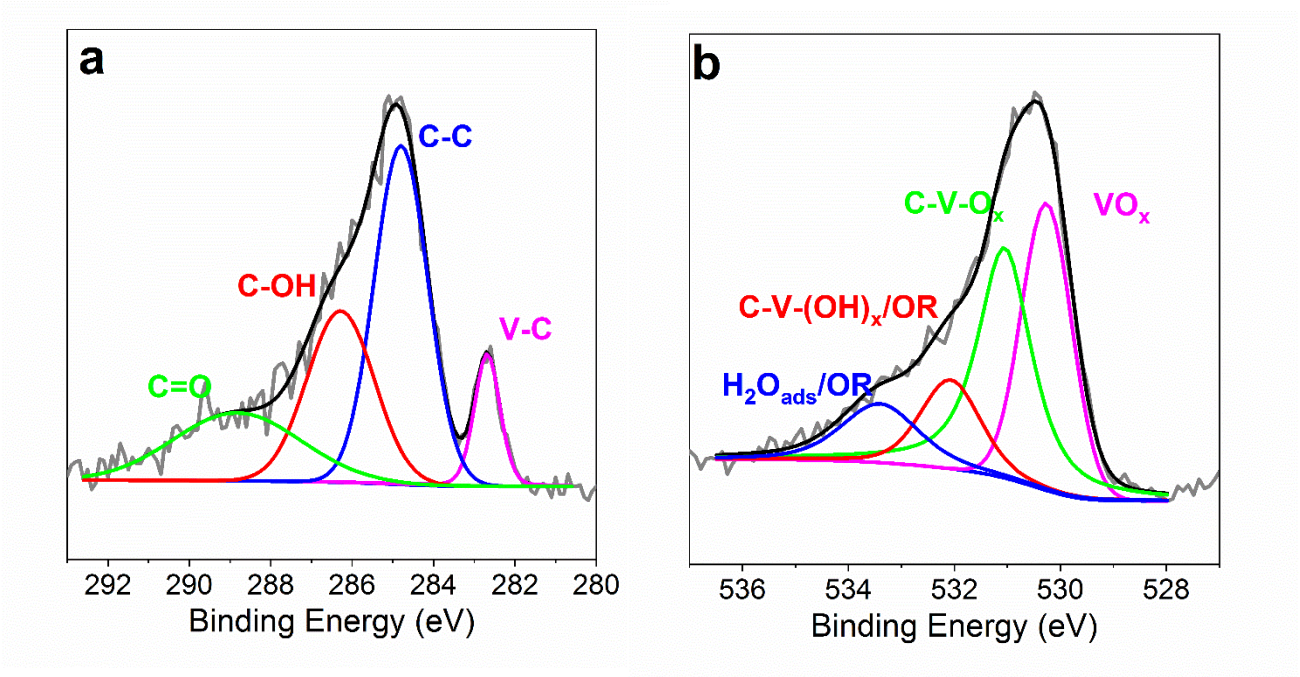

Figure 43. XPS spectra of (a) C1s region and (b) O1s region for the V_2CT_x MXene treated under hydrogen at 600°C. Surface charging was corrected using the C1s level at 284.8 eV. OR stands for organic compounds due to atmospheric surface contaminations.

In summary, our data show that the first chemical and structural transformation of the material from raising the temperature occurs due to the release of the water trapped within the V_2CT_x structure. *In-situ* Raman reveals that this dehydration process initiates the partial oxidation of the

surface and decreases the distance between the MXene layers above 400 °C. Furthermore, we reveal more insights into the dehydration process of V_2CT_x, as shown in Figure 44**.** It is important to elucidate and understand how water is confined within the MXene material to choose the optimal conditions for dehydration. Multilayered MXenes retain a significant amount of water from the existence of hydroxyl groups on the surface, and the void volume formed due to the presence of weak hydrogen bonds and van der Waals forces.[180, 181]

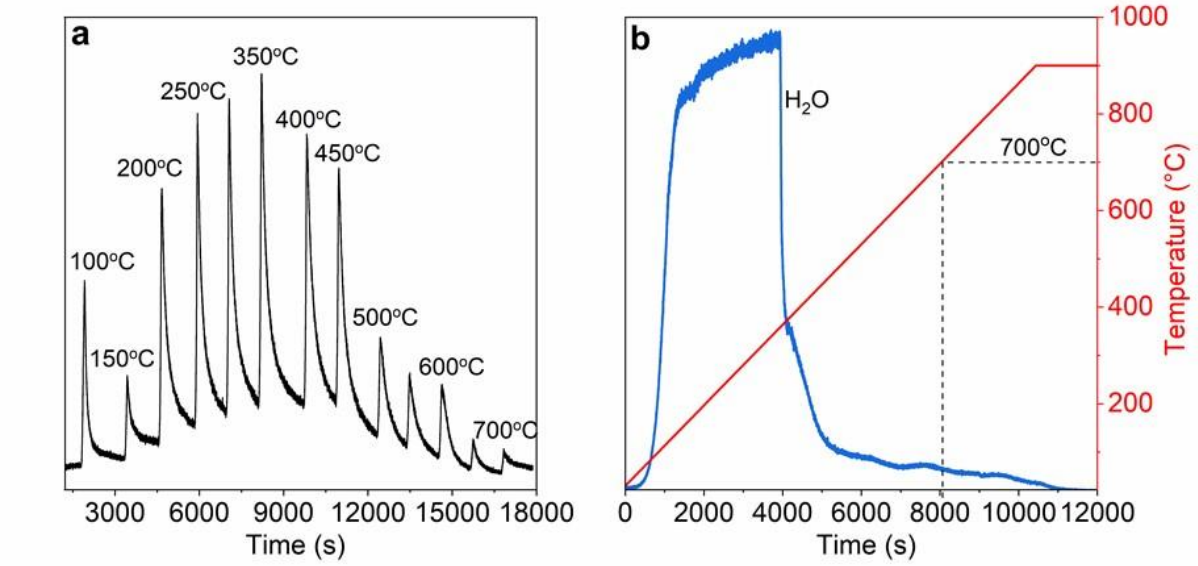

Figure 44. Dehydration of V_2CT_x MXene in (a) 50 °C increments per step up to 700 °C (b) and continuous heating @ 10 °C min^{-1} up to 900 °C.

.

The water adsorbed/trapped between the layers influences the properties of MXenes as it does in other 2D materials such as graphene.[181] When the material is heated up in steps-mode under nitrogen (Figure 44a), water is released as "*packets*", suggesting that either the water is confined in different compartments within the layered structure or interacting differently with the MXene surface. We hypothesize that the water released up to 150 °C (Figure 44a) represents the adsorbed water on the external surface, while the water trapped in-between the layers start to desorb above 200 ^{0}C.

The water-solid interaction gets stronger, primarily due to the presence of nanoconfined water,[182] therefore more energy is needed to desorb. Most of the water present in V_2CT_x is desorbed once reaching 500 ^{0}C (Figure 44a); however, the total dehydration is achieved at about 700 ^{0}C, as also shown in Figure 44b. Finally, the partial dehydration of V_2CT_x results in the partial oxidation of the material. Thus, the utilization of V_2CT_x at temperatures between 500 to 700 ^{0}C, despite maintaining the multilayered structure, will inevitably lead to the partial oxidation of the material. We believe that our methodology is a unique alternative to tune the dehydration, oxidation, and properties of V_2CTx, which allows for the expansion of MXenes' applications.

3.4 Conclusions

We provide new insights into the chemical and thermal stability of multilayered V_2CT_x MXene under inert, oxidizing, and reducing environments at various temperatures. Based on our results obtained from *in-situ* Raman and *ex-situ* XRD, XPS, and SEM, we listed the most relevant observations as follow:

N_2-treated V_2CT_x:

- The bulk layered structure of the V_2CT_x is stable up to 600 °C, although the surface of the material suffers minor oxidation by reacting with the water intrinsically contained within the structure of the as-prepared material.
- The c-LP decreases due to the dehydration of the material, but the layered structure remains intact.

CO_2-treated V_2CT_x:

- The material oxidizes above 300 °C, forming a mixture of VO_x species.
- The bulk layered structure collapses.

Air-treated V_2CT_x:

- The material transforms into bulk V_2O_5 with complete desertion of the characteristic layered structure above 300 °C.

H_2-treated V_2CT_x:

- The bulk layered structure is maintained to a certain degree, although the MXene peak (0002) disappears due to the removal of water molecules.
- The surface VO_x species are reduced.
- Terminal functional groups (OH, O, and F) get removed above 300 °C.

Our results indicate that at higher temperatures, the trapped water within the layered structure of the material inevitably burns the residual carbon and slightly oxidizes the V_2CT_x surface (above 400 °C), no matter the environment. This limits the utilization of V_2CT_x for high-temperature applications, especially when the carbide species, instead of oxi-carbide, are rather needed. However, one can adjust the oxidation degree of the material by tuning the dehydration temperature considering the fact that the water-solid interaction varies depending on the location of the water (trapped water). We foresee that when working at lower temperatures, and especially under reducing atmospheres, V_2CT_x will exhibit unprecedented thermo-catalytic properties. Additionally, the collapse of the MXene structure and the formation of different surface/bulk oxide and oxi-carbide species foster V_2CT_x and MXenes in general as a potential precursor for new bulk V_2O_5 and/or $V_xO_yC_z$ (oxi-carbide) catalysts. In our on-going studies, we are using the chemical and thermal properties of V_2CT_x presented in this work to select the optimal reaction conditions to perform various industrially attractive thermo-catalytic reactions. An important challenge we identified in this study is the irreversibility of the destruction and/or oxidation of the layered (accordion-type) structure. In order to broaden the applications of MXenes, especially at higher

temperatures and under oxidizing atmospheres, we might both enhance the stability of these materials towards oxidation and, more importantly, we need to develop methodologies to synthesize MAX phase and, therefore, MXene phase starting from a collapsed/oxidized material.

Chapter 4: Insights into the Genesis of a Selective and Coke-Resistant MXene-based Catalyst for the Dry Reforming of Methane

Abstract

We report the use of a multilayered vanadium carbide MXene (*m*-V_2CT_x) as a precursor for a robust oxy-carbide catalyst to convert CH_4 and CO_2 into *syngas* via dry reforming of methane (DRM). The *in-situ* generated V_2O_3-V_8C_7/*m*-V_2CT_x catalyst undergoes a *redox* (oxidation-carburization) mechanism that results in an attractive reactivity, selectivity (H_2/CO ratio close to unity) and unprecedented stability (negligible formation of coke). The oxy-carbide species (V_2O_3 and V_8C_7) growing *in-situ* under reaction conditions decorate the layers of *m*-V_2CT_x and provide better utilization of V sites in a way that the resulting V_2O_3-V_8C_7/*m*-V_2CT_x catalyst exhibits four times higher activity than its bulk counterparts, V_2AlC MAX phase and commercial vanadium carbide (VC). These kinetic findings combined with spectroscopy, microscopy, and isotopic labeling experiments reveal that while dehydrating the pristine *m*-V_2CT_x, a new oxy-carbide (V_2O_3-V_8C_7/*m*-V_2CT_x) material is produced which oxidizes further in the presence of CO_2 to generate additional V_2O_3 nanocrystals on the surface and in-between the multilayered structure. These oxide particles are further carburized *in-situ* by reacting with CH_4 and transforming into V_8C_7 nanocrystals. This study provides kinetic, structural, and mechanistic insights into the genesis of *m*-V_2CT_x as a selective and coke-resistant catalyst for DRM. We foresee *m*-V_2CT_x, and MXenes in general, as promising precursors, supports, and/or catalysts for various other catalytic applications at relatively high temperatures (≥ 500ºC).

4.1 Introduction

MXenes are a class of layered two-dimensional (2D) transition metal carbides and nitrides, which have garnered tremendous attention in the last decade due to their structure, thermal, and chemical stability, as well as their versatile chemical composition.[93, 95, 99, 103, 117, 119, 183] Multilayered-MXenes (*m*-MXenes) are named by their graphene-like morphology, in accordance with the $M_{n+1}X_nT_x$ general chemical formula (*n* can be 1, 2, 3 or 4), where *M* is an early transition metal, *X* is carbon and/or nitrogen, *T* indicates various surface terminations (O^-, ^-OH, F^-), and *x* is the number of surface functional groups per unit formula, (Figure 45).[95, 184-186] The precursors used for the synthesis of MXenes are a family of ternary carbides and nitrides called MAX phases (with a general formula of $M_{n+1}AX_n$, where A is a group 13 or 14 elements such as Al). The *m*-MXene structure is obtained by selectively etching A-layer metal atoms from the MAX phases structure (A = Si, Al, Ga).[93-95, 99, 102, 105, 117, 129, 187]

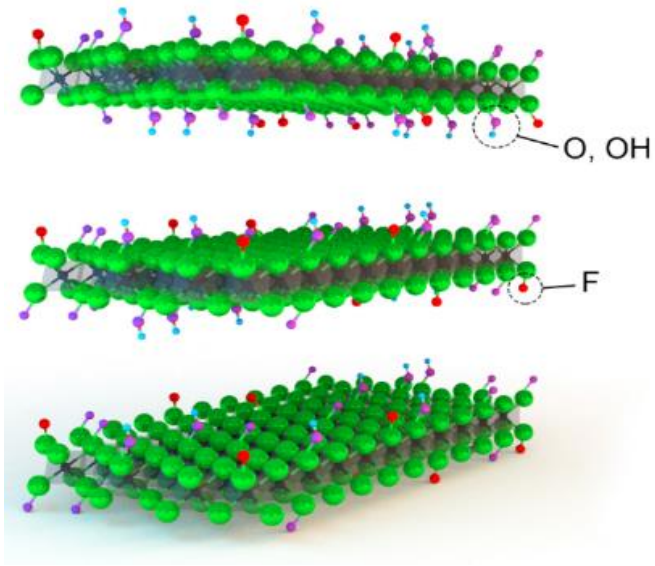

Figure 45. Schematic representation of *m*-V_2CT_x MXene with various terminal functional groups.

MXenes have found applications in diverse fields such as energy storage and conversion,[188, 189] photocatalysis,[143] water deionization,[190] electromagnetic interference shielding,[191] gas-sensing,[123] bio-sensing,[192] cancer theranostics,[193] and tissue engineering.[194] Recently, MXenes have also been studied for catalytic applications at relatively high temperatures (~550^{0}C), i.e., in the water gas shift (WGS) reaction,[102, 104] ethylbenzene dehydrogenation,[103] propane dehydrogenation,[105] methane activation[106], and CO_2 activation.[107] However, to the best of our knowledge, MXenes-based catalysts have not been reported for reactions involving more severe conditions such as higher temperatures ($\geq$ 600 ^{0}C) and highly concentrated oxidants (40 % CO_2).

In a previous study, we demonstrated that the multilayered structure of V_2CT_x MXene persists up to certain extent under inert (N_2) and reducing (H_2) environments, partially oxidizes (V_2CT_x decorated with V_2O_3) in the presence of CO_2, and undergoes total oxidation in the presence of air (V_2CT_x transform into bulk V_2O_5).[183] Nevertheless, the genesis of *m*-V_2CT_x onto the optimal surface and bulk structure for DRM (reaction 1) relies on repetitively compensate the mild oxidation of the material with a consecutive carburization reaction.

$$CH_4 + CO_2 \rightleftarrows 2CO + 2H_2 \qquad \Delta H^0_{298K} = 247 \text{ kJ mol}^{-1} \qquad (1)$$

Currently, CH_4 is industrially converted into *syngas* via steam reforming (SMR), while dry reforming (DRM), bi-reforming (BIM), auto-thermal reforming (ATR), and partial oxidation (PO_x) are still at the research stage.[18] DRM provides a 1:1 ratio of H_2/CO, which is practical for the production of specialty chemicals (e.g., oxo-synthesis)[195] and other liquid fuels via the Fischer-Tropsch process.[19, 20, 196-204] Both Pt and Ni-based catalysts are among the most studied materials for DRM,[19, 26, 32, 196, 198, 201, 205] from which various drawbacks can be found in the literature. Primary, their inability to diminish the cracking of CH_4 (reaction 2), Boudouard (reaction 3), and reverse-water-gas-shift (RWGS) (reaction 4)[18] reactions are still challenges that need to be

addressed. Also, Pt/Ni sites tend to sinter, leading to a loss in activity. Alternatively, transition metal carbide catalysts have also been explored for DRM. These materials minimize the precipitation of amorphous and graphitic carbon (coke) but undergo undesired bulk oxidation.[40, 42, 50] Important advancements have been achieved when using both Pt, Ni, and/or carbide-based catalysts for DRM, but they are still far from industrial application.[36, 50, 206, 207] Therefore, we propose to use *m*-V_2CT_x MXene as a precursor material to prepare a selective, stable, and active catalyst for DRM.

$CH_4 \rightarrow C_{(s)} + 2H_2$ $\Delta H^0_{298K} = 75$ kJ mol^{-1} (2)

$2CO \rightarrow C_{(s)} + CO_2$ $\Delta H^0_{298K} = -172$ kJ mol^{-1} (3)

$CO_2 + H_2 \rightarrow CO + H_2O$ $\Delta H^0_{298K} = 41$ kJ mol^{-1} (4)

Our studies reveal that two-dimensional *m*-V_2CT_x MXene serves as a precursor and transforms into a V_2O_3-V_8C_7/*m*-V_2CT_x catalyst after exposure to DRM and carburization conditions. This new oxy-carbide material shows attractive activity for DRM, converting about 78% CH_4 and 82% CO_2 with CH_4 and CO_2 conversion rates of $153.4\ mmol_{CH_4} mol_V^{-1} min^{-1}$ and $178.2\ mmol_{CO_2} mol_V^{-1} min^{-1}$ respectively. These results are comparable to Ni-based catalysts and are about four times higher than its bulk counterparts V_2AlC MAX phase and VC. In addition, V_2O_3-V_8C_7/*m*-V_2CT_x also provides an attractive H_2/CO ratio of ~ 0.9 over 96-hour time-on-stream (TOS). This is attributed to the *in-situ redox* cycle involving the oxidation and carburization of *m*-V_2CT_x with CO_2 and CH_4, leading to the formation of V_2O_3/*m*-V_2CT_x and V_8C_7/*m*-V_2CT_x respectively. The cyclic transformation of these V_2O_3 and V_8C_7 nanocrystals hinders the formation and precipitation of solid carbon, providing unique stability and thereby maintaining the H_2/CO ratio close to unity. Importantly, these results contrast with the performance observed when carburizing bulk V_2O_5 ($V_2O_5 \rightarrow VC_x$) catalyst, which easily deactivates due to its overoxidation

with CO_2 (returning to V_2O_5).[40] Based on our kinetic, spectroscopy, and isotopic labeling experiments we propose the possible reaction mechanisms governing both the transformation of *m*-V_2CT_x MXene (precursor) into V_2O_3-V_8C_7/*m*-V_2CT_x (catalyst) and the *redox* mechanism for DRM when using this unique oxy-carbide catalyst. This study shows the genesis of *m*-V_2CT_x MXene as a promising catalyst precursor for DRM, which involves the *in-situ* transformation of *m*-V_2CT_x into a selective, coke-resistant, and stable V_2O_3-V_8C_7/*m*-V_2CT_x catalyst. Based on the results presented in this study and also considering our ongoing research, we envision an exponential growth in the application of both multilayered, delaminated, and supported MXenes for catalytic applications at relatively high temperatures (above 550^0C).

4.2 Material characterization techniques

4.2.1 XRD and SEM: The structure of the synthesized MXene powder was characterized using a Bruker X-ray diffractometer with 40 kV and 40 mA Cu Kα radiation in using 0.2 sec/step. Around 20 mg of sample was loaded in the small cavity of the sample holder and pressed using a glass slide. Micrographs showing the cross-section morphology of V_2CT_x were obtained using a JEOL JSM-7000F scanning electron microscope (SEM). The chemical composition was determined by the EDS method. EDS spectra of the samples were recorded by mapping a large area on a JEOL JSM-7000F SEM equipped with an EDS detector and at 30kV voltage beam.

4.2.2 Nitrogen physisorption: Nitrogen adsorption isotherm measurements were performed at 77K using a Quantachrome Nova1400 equipment (t-plot analysis). BET was measured up to three times for each sample to ensure an accurate determination of the metal coverage. Briefly, samples were outgassed at 473K for 3 hours prior to performing N_2 adsorption experiments. Specific surface area (BET) was estimated from the adsorption data in the relative pressure range from 0.05 to 0.2 using the Brunauer-Emmett-Teller method.

4.2.3 X-ray photoelectron spectroscopy: XPS measurements were conducted on a Kratos Analytical Ltd. AXIS Ultra DLD (delay lines detector) X-ray photoelectron spectrometer (XPS) with a monochromatic Al Kα X-ray source (1486.6 eV). The end station consists of a fast entry load lock, a sample treatment chamber (STC) and a sample analysis chamber (SAC). The X-ray spot size is about 300×700 μm^2, and the angle between the sample holder and X-ray source is 35 degrees. Pass energy of 20 eV was used to measure the high-resolution spectra of V 2p, O 1s, and C 1s narrow scans. The observed binding energy shifts are due to surface charging were corrected by constraining the C 1S peak at 284.8 eV. Deconvolutions of the peaks using XPSPEAKS 4.1 software were conducted to obtain the relative atomic density for each species. Core level peaks were deconvoluted by fixing the binding energy at suggested values using Gaussian-Lorenzian (20%) method. The atomic sensitivity factors provided by the standard XPS handbook were used for the calculation. More details can be found elsewhere.[208]

4.2.4 Raman spectroscopy: Raman spectroscopy studies were performed on the fresh and spent catalyst using a Renishaw InVia Qontor Raman Spectrometer, for which details can be found elsewhere[209]. For all measurements, we used a 405 nm laser, 2400 L mm^{-1} grating, 50x objective, 10 seconds of exposure time, 1% of power, and 10 spectrum accumulations.

4.3 Catalytic Testing

The steady-state DRM catalytic measurements were performed at ambient pressure using a stainless-steel fixed bed reactor with an internal diameter and total length of 6 mm and 450 mm, respectively. The pristine powder catalyst was pelletized and sieved at a particle size between 425 and 500 μm. The catalytic tests were performed to minimize the heat and mass transfer limitations using the Carberry, Mears and Weisz-Prater criteria.[210, 211] A custom-made reaction set up equipped with multiple electronic GE50A MKS mass flow controllers, heating controllers, heated

lines from the reactor's outlet to the GC's inlet, a thermolyne 21100 tubular furnace which provides a well-defined isothermal heating zone of about 120 mm length, a liquid saturator isothermally heated with a chiller when liquid vapors are needed, a pressure gauge prior to the reactor inlet, and an on-line Agilent 7890B gas chromatograph (GC) equipped with three Agilent columns (HayeSep A, MolSieve, and DB-1), a flame ionization detector (FID) and a thermal conductivity detector (TCD). All the reactions were carried out at 800 °C with inlet flow ratios of 40% CO_2 (Airgas, UHP grade) and 40% CH_4 (Airgas, UHP grade) balance N_2 (Airgas, UHP grade) at 16 ml/min total flow rate, and the gas hourly space velocity (GHSV) was maintained at 4800 $ml\,g_{cat}^{-1}h^{-1}$. Prior performing the kinetics the V_2CT_x was *in-situ* dehydrated completely using inert gas till 800°C, following the learnings from previous studies.[183] [157] The Ni-based catalyst was *in-situ* reduced from room temperature to 700°C under H_2 flow and kept for 1h, followed by the DRM at 800°C. The quantification of the Hydrogen (H_2), Carbon dioxide (CO_2), Nitrogen (N_2), Carbon monoxide (CO) and methane (CH_4) was performed using the areas obtained by TCD, whereas hydrocarbon was performed by using the areas obtained by FID. The detailed graphical representation of stability test can be obtained in the Figure 46.

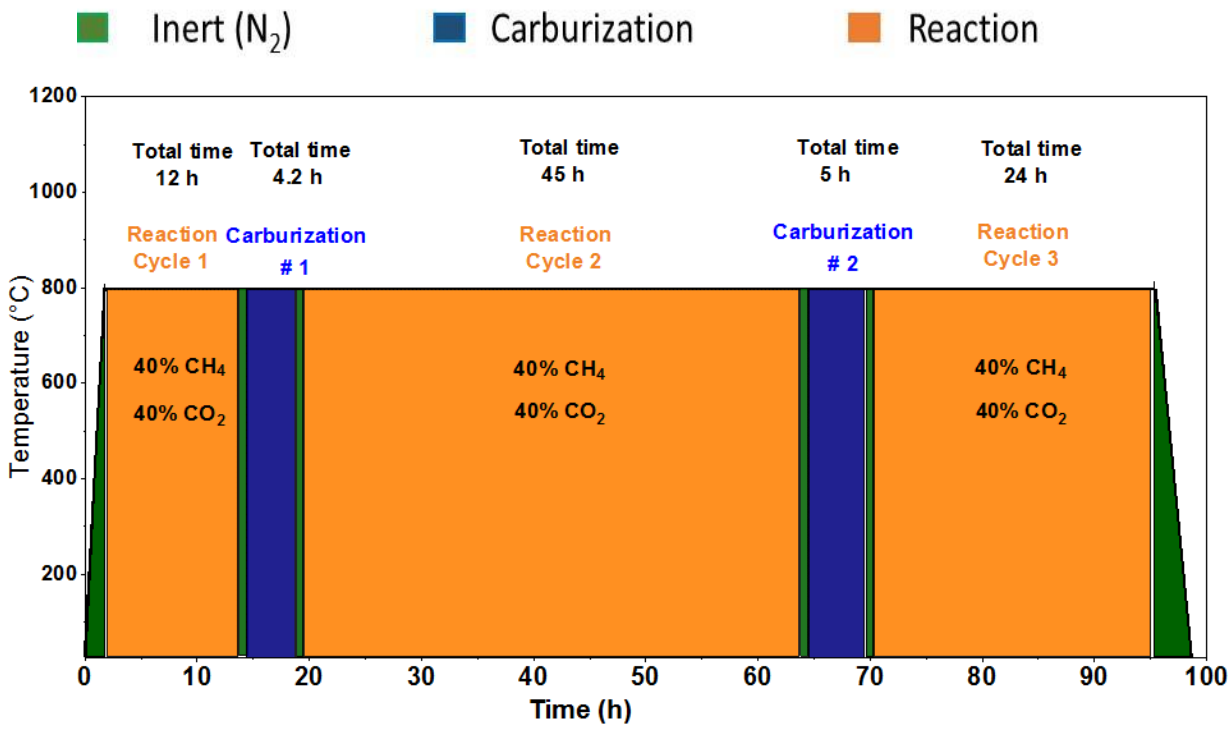

Figure 46. Graphical representation of various steps performed during the 96-hour stability test over V_2O_3-V_8C_7/*m*-V_2CT_x during DRM.

4.4 Isotopic labeled experiments

Isotopic labeled experiments were performed using $^{13}CO_2$ (Cambridge Isotope Laboratories, Inc. 99.98%) and $^{13}CH_4$ (Cambridge Isotope Laboratories, Inc. 99.98%). Briefly, the *m*-V_2CT_x MXene was heated/dried under inert to 800°C, followed by passing the reaction mixture 40% $^{12}CO_2$ and 40% $^{12}CH_4$ balance N_2 (Airgas, UHP grade) at 16 ml/min total flow rate, and the same gas hourly space velocity (GHSV) was maintained at 4800 $ml g_{cat}^{-1} h^{-1}$. After attaining steady state, the labeled $^{13}CO_2$ gas was introduced with $^{12}CH_4$ and the evolution of reaction products coming out of the reactor were analyzed using an MKS Cirrus2 mass spectrometer, while in a separated experiment, the $^{12}CO_2$ gas was introduced with $^{13}CH_4$. The carburization step was performed using 20% CH_4 and 80% H_2 at 800°C and progress was monitored by tracking CO and H_2O as the product of carburization. Blank experiments at different GHSV (2400, 4800, 12000 $ml g_{cat}^{-1} h^{-1}$.)

using pure quartz wool and temperatures (800 and 1000 ^{0}C) were conducted showing a negligible contribution of gas-phase reactions.

4.5 Results and discussion

The precursor, V_2AlC MAX phase, shows its typical morphology analogous to a tightly stacked un-exfoliated graphite as observed in Figure 47a.[98, 183] After the HF treatment (see experimental section), the tightly stacked layers transform to loosen accordion-like morphology with stacked layers well separated from each other due to the etching of Al atoms from the MAX phase (Figure 47b).[98, 183] The XRD diffractogram for bulk V_2AlC and two-dimensional *m*-V_2CT_x are depicted in Figure 47c. A characteristic peak at 2θ of 8.32^{o} assigned to the (0002) plane for *m*-V_2CT_x is present together with the traces of unreacted V_2AlC MAX phase (sharp peaks at 2θ of 13.5^{o} and 41.5^{o}).[98, 183] The average Al/V ratio obtained for the etched sample using EDS analysis on weigh basis is 0.054, evidencing traces of Al in the prepared MXene sample (Table 2). Except for the etching of Ti_3AlC_2 MAX phase that yields almost completely to $Ti_3C_2T_x$ MXene, [93, 212] the selective etching process applied to the rest of MAX phases to synthesize MXenes still lacks total control, thus resulting in different end results (i.e. ratio of conversion, amount of the unreacted MAX phase precursor, quality of the 2D MXene sheets, surface composition, stability).

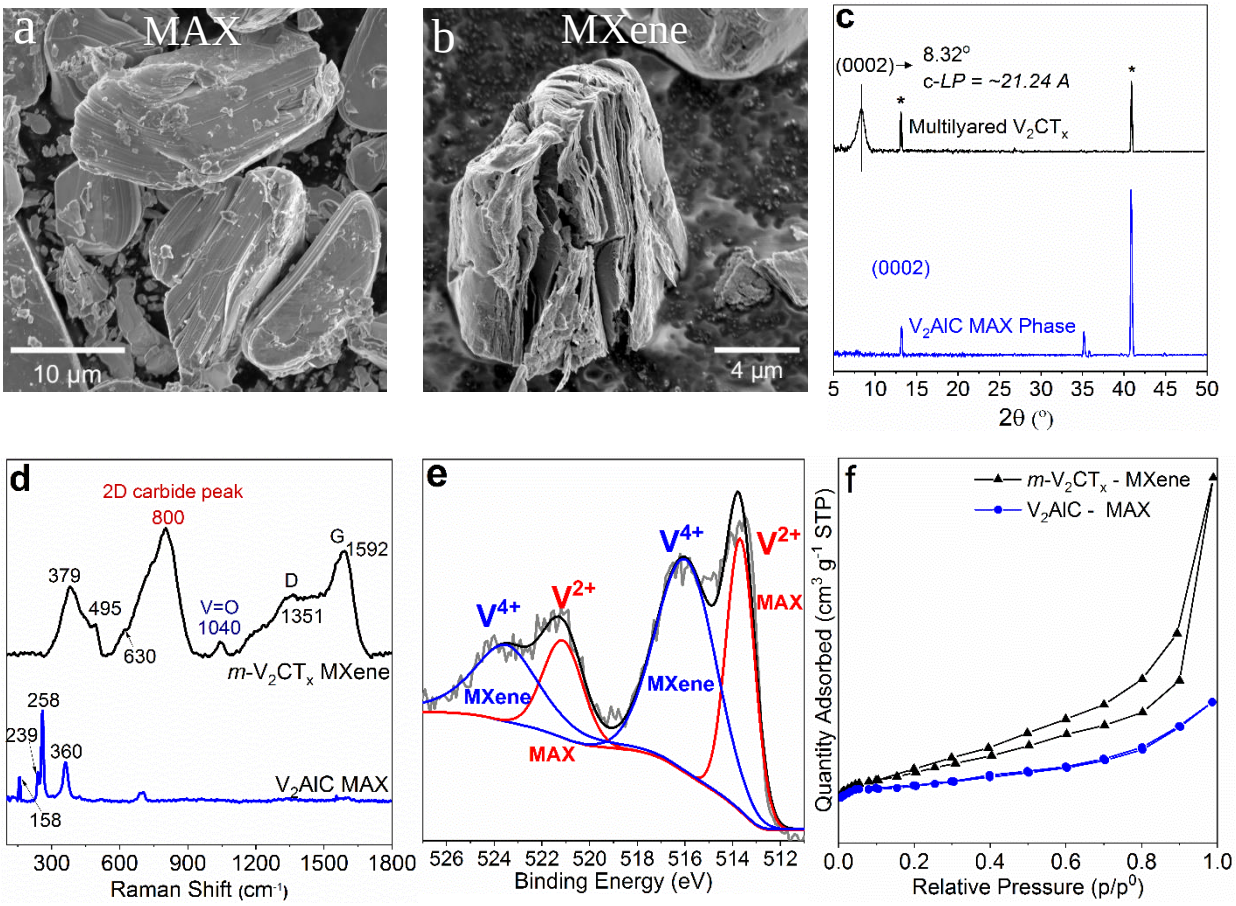

Figure 47. SEM micrograph of pristine (a) V_2AlC MAX phase and (b) *m*-V_2CT_x MXene. (c) XRD diffractogram of the V_2AlC MAX phase and the *m*-V_2CT_x MXene. Asterisk (*) indicates an unreacted MAX phase which matches with the crystallography information file JCPDS No. 29-0101. (d) Raman spectra of the V_2AlC MAX phase and the *m*-V_2CT_x MXene. (e) XPS V2p spectra of as-prepared *m*-V_2CT_x MXene. (f) Adsorption-desorption isotherms for *m*-V_2CT_x MXene (SA=10.25 m^2/g) and V_2AlC MAX phase (SA=1.50 m^2/g). SA=Surface area.

Sample	Element weight % content				Moles of V
	V	C	O	Al	
VC	51.84	21.25	26.24	-	0.00240
V_2AlC Max	45.73	15.95	30.05	8.3	0.00176
V_2O_3-V_8C_7/*m*-V_2CT_x	37.94	33.67	26.34	2.05	0.00145

Table 2. Surface composition of spent VC, V_2AlC Max and V_2O_3-V_8C_7/*m*-V_2CT_x by EDS analysis.

The purity of the MXene phase is typically evidenced from the weakening and disappearance of the sharp peaks related to MAX phases and appearance of broad peaks related to basal planes of MXenes.[93] Until now, a pure V_2CT_x MXene phase has not be obtained by etching of V_2AlC.[98, 99, 213, 214] Importantly, unreacted MAX phase appears in almost all MXenes synthesized by HF etching because achieving a total removal of Al atoms usually also results in the undesired removal of the transition metal (e.g. V in this case),[98] resulting in the formation of carbide-derived carbon (CDCs) materials.[215, 216]

The transformation of the V_2AlC MAX into *m*-V_2CT_x MXene phase is also corroborated by Raman spectroscopy (Figure 47d). While the V_2AlC MAX phase exhibits sharp characteristic Raman peaks at 158 (E_{2g}), 239 (E_{2g}), 258 (E_{1g}), and 360 (A_{1g}) cm^{-1}, [151, 155, 156] broader Raman peaks are observed for *m*-V_2CT_x (379, 495, 630, 800, 1040, 1351, 1592 cm^{-1}). The broad Raman peaks for MXenes are ascribed to the large interlayer spacing,[151] and the assignment of all Raman vibrations for *m*-V_2CT_x can be found in our previous work.[183] The changes on the surface of the material are tracked by XPS (Figure 47e). The peak at ~513.3 eV (V^{2+}) evidences both the presence of unreacted V_2AlC MAX phase and V-C from the C1s region, which overlap at the same binding energy, thus making this peak more prominent.[183] The peak at ~ 516.3 eV (V^{4+}) is attributed to the existence of a monolayer of vanadium oxide on the surface of vanadium carbide.[98] Details of the deconvoluted C1s and O1s region can be found in Figure 31. The N_2-physisorption study of *m*-V_2CT_x shows an H3-type adsorption-desorption trajectory with a hysteresis loop (P/P_0 = 0.5-1.0) distinctive for macroporous and layered materials (Figure 47f).[103] The hysteresis for *m*-V_2CT_x is more distinct compared to the V_2AlC (MAX phase) corroborating the presence of a layered structure, thus complementing our results.

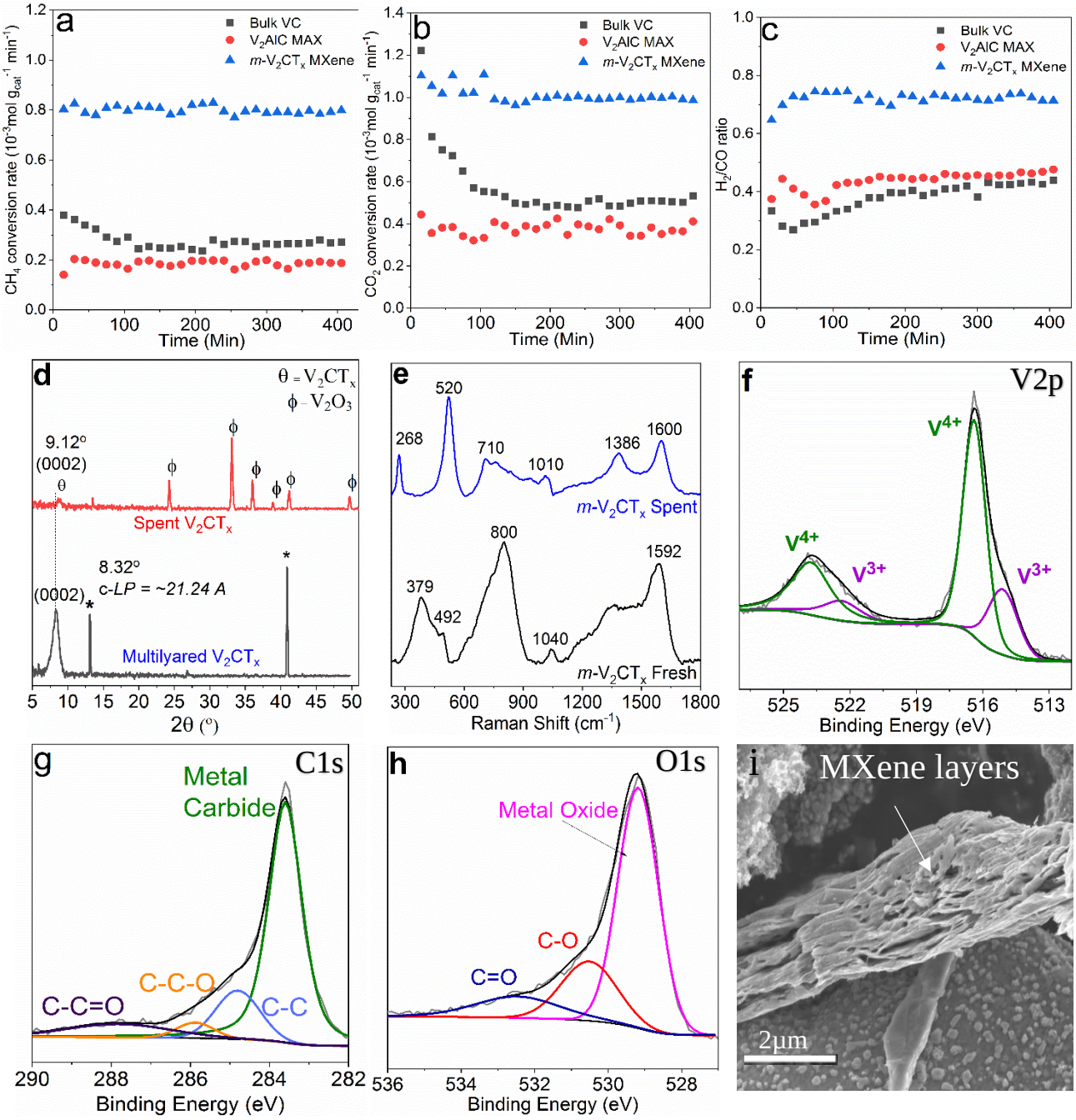

Figure 48. (a) CH_4 and (b) CO_2 conversion rates (c) H_2/CO ratio for V_2O_3-V_8C_7/*m*-V_2CT_x MXene and bulk VC and V_2AlC MAX phase. (d) XRD, (e) Raman, (f-h) XPS, and (i) SEM image of the spent V_2O_3-V_8C_7/*m*-V_2CT_x MXene catalyst. Catalyst mass = 0.2 g, TOS = 400 min, T= 800 ºC, P= 1 atm, 40% CH_4 and 40% CO_2, 20%N_2.

4.5.1 Steady-state kinetics

The catalytic performance in DRM and post-reaction characterization of two-dimensional *m*-V_2CT_x and it's three-dimensional (bulk) counterparts, VC and V_2AlC MAX are depicted in Figure 48. The catalysts were heated under N_2 up to 800 ^{0}C followed by the DRM tests. Notably, when the *m*-V_2CT_x MXene is heated under inert atmosphere (N_2, Ar) to high temperatures (> 400 ^{0}C), its surface partially oxidizes by reacting with H_2O trapped in between the layers and forming V_2O_3 nanocrystals, while some *m*-V_2CT_x gets transformed to V_8C_7 thereby resulting in an oxy-carbide V_2O_3-V_8C_7/*m*-V_2CT_x material.[157, 183] All tested materials show comparatively good stability for 420 minutes TOS under DRM conditions (Figure 48a-c), although V_2O_3-V_8C_7/*m*-V_2CT_x shows conversion rates ($0.81\ mmol_{CH_4} g_{cat}^{-1} min^{-1}$ and $0.97\ mmol_{CO_2} g_{cat}^{-1} min^{-1}$) that are about twice higher than its bulk counterparts when normalized per gram of catalyst and comparable to Ni-based catalysts.

This superior selectivity in combination with sustained stability under highly concentrated feedstock (40%CH_4, 40%CO_2, 20%N_2) and a low gas hourly space velocity (GHSV) of 4800 $ml g_{cat}^{-1} h^{-1}$, identifies this specific MXene as a promising precursor to obtain a robust catalyst for DRM. However, *ex-situ* XRD studies (Figure 48d) reveal significant structural changes after performing DRM at 800 ^{0}C. Some of the *m*-V_2CT_x phase can still be observed (see a small peak at 2θ of 9.12^o). This peak shifts to a slightly higher angle due to the decrease in lattice parameter (*c*-LP) as a result of the dehydration at high temperature. This also has been observed in other MXenes ($Ti_3C_2T_x$, Nb_2CT_x, Mo_2CT_x).[99, 157, 183, 217-219] In addition, the appearance of sharp peaks at 2θ of 24.3^o, 33.1^o, 36.01^o, 38.9^o, 41.2^o, 49.7^o, and 54.03^o are a fingerprint for the formation of V_2O_3 crystallites within the bulk *m*-V_2CT_x structure. The disappearance of the MAX phase peaks can be

attributed to thermal etching as reported elsewhere.[93, 95] The XRD diffractogram and Raman spectra for the spent V_2AlC and bulk VC can be found in Figure 49

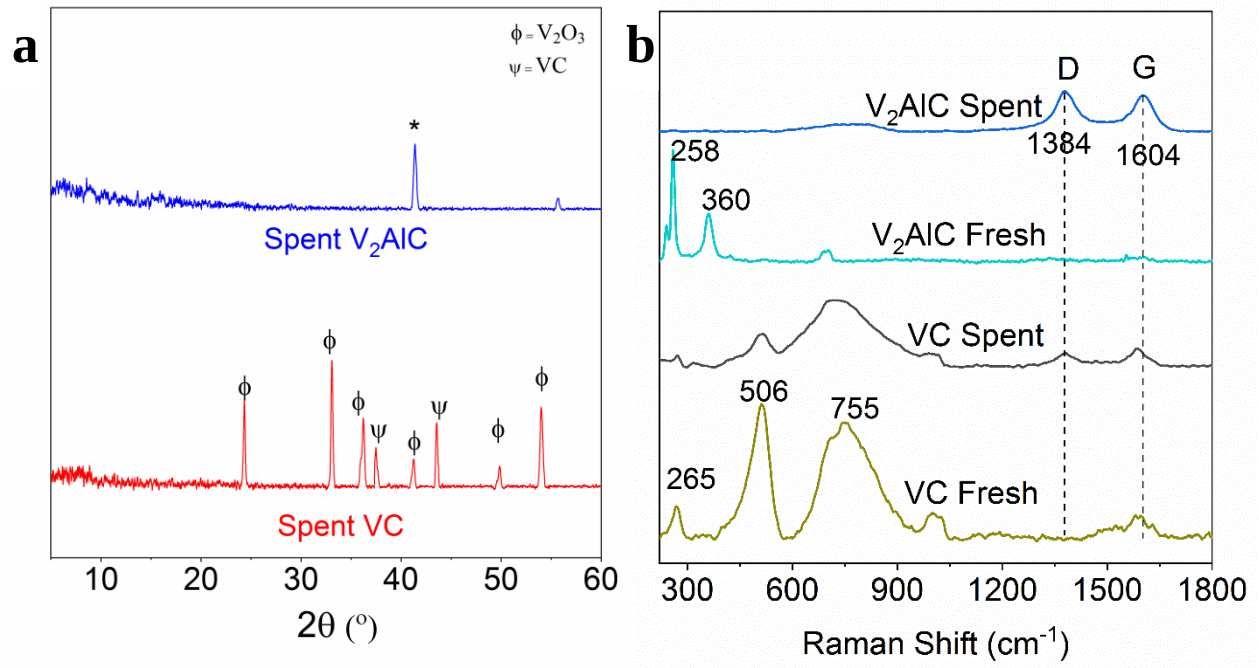

Figure 49. (a) XRD diffractogram of spent V_2AlC MAX phase and bulk VC. (b) Raman spectra of fresh and spent V_2AlC MAX phase and bulk VC.

The spent VC (bulk) exhibits VC/V_2O_3 peaks (Figure 49a), indicating the bulk oxidation of the material was taking place. This bulk oxidation can be due to the strong binding of the oxygen species formed during the dissociative adsorption of CO_2. The observed higher levels of initial conversion for CO_2 as compared to CH_4 can be attributed to the RWGS and/or to the rapid oxidation of the carbide phase at the onset of the reaction. Furthermore, looking at the H_2/CO ratio (0.4 for VC) it is reasonable to believe that the bulk VC favors both RWGS and bulk oxidation under the DRM conditions compared to the V_2O_3-V_8C_7/*m*-V_2CT_x. Raman shows very similar spectra for bulk VC prior to and after reaction (Figure 49b). The V_2AlC MAX phase did not show any sign of oxidation (Figure 49a) via XRD. The Raman for the V_2AlC MAX phase shows the

emergence of amorphous and graphitic carbon (D & G bands) resulted from methane decomposition. Such carbonaceous species scatter most of the light, thus weakening the Raman vibrations from the MAX phase.

Raman spectroscopy confirms the formation of V_2O_3 together with V_8C_7 species at the surface of *m*-V_2CT_x after DRM at 800 ^{0}C (Figure 48e). Both the emergence of the Raman peaks at 268, 710 and 1010 cm^{-1} and the disappearance of the 2D-carbide Raman peak at 800 cm^{-1} corroborate the formation of V_2O_3 particles on the surface.[220] Additionally, the presence of Raman signals at 520, 1386, and 1600 cm^{-1} signifies the simultaneous existence of V_8C_7 on the surface. Thus, under DRM conditions *m*-V_2CT_x transforms into V_2O_3-V_8C_7/*m*-V_2CT_x. The surface of the spent *m*-V_2CT_x was also studied by XPS (Figure 48f-h). The V2p, O1s, and C1s region show the emergence of V^{3+} (515.2 eV) as well as an increase in the metal-oxide signal (531 eV) and metal carbide (282.2 eV) signal, respectively. Likewise, XPS confirms the formation of oxy-carbide species on the spent material. Finally, the growth of small particles on the surface of *m*-V_2CT_x and its multilayered structure is evidenced by SEM (Figure 48i). By combining these various characterization techniques one can show the ability of *m*-V_2CT_x to transform into a unique V_2O_3-V_8C_7/*m*-V_2CT_x catalyst for DRM.

4.5.2 Stability test

To further validate the stability of V_2O_3-V_8C_7/*m*-V_2CT_x, we performed DRM for about 96 hours on stream (Figure 50a) and an improvement in the conversion of the reactants and the H_2/CO ratio is observed. The CH_4 and CO_2 conversion stabilizes at ~78% and ~82% respectively, while the H_2/CO ratio remains at 0.9 with the conversion rate for CH_4 and CO_2 of 1.0 $mmol_{CH_4} g_{cat}^{-1} min^{-1}$ and 1.3 $mmol_{CO_2} g_{cat}^{-1} min^{-1}$ respectively. XRD confirms the presence of oxy-carbide crystals

(V_2O_3, VO_2, V_8C_7 on *m*-V_2CT_x) while Raman spectroscopy evidences the presence of a carbide phase on the external surfaces (Figure 50b-c).

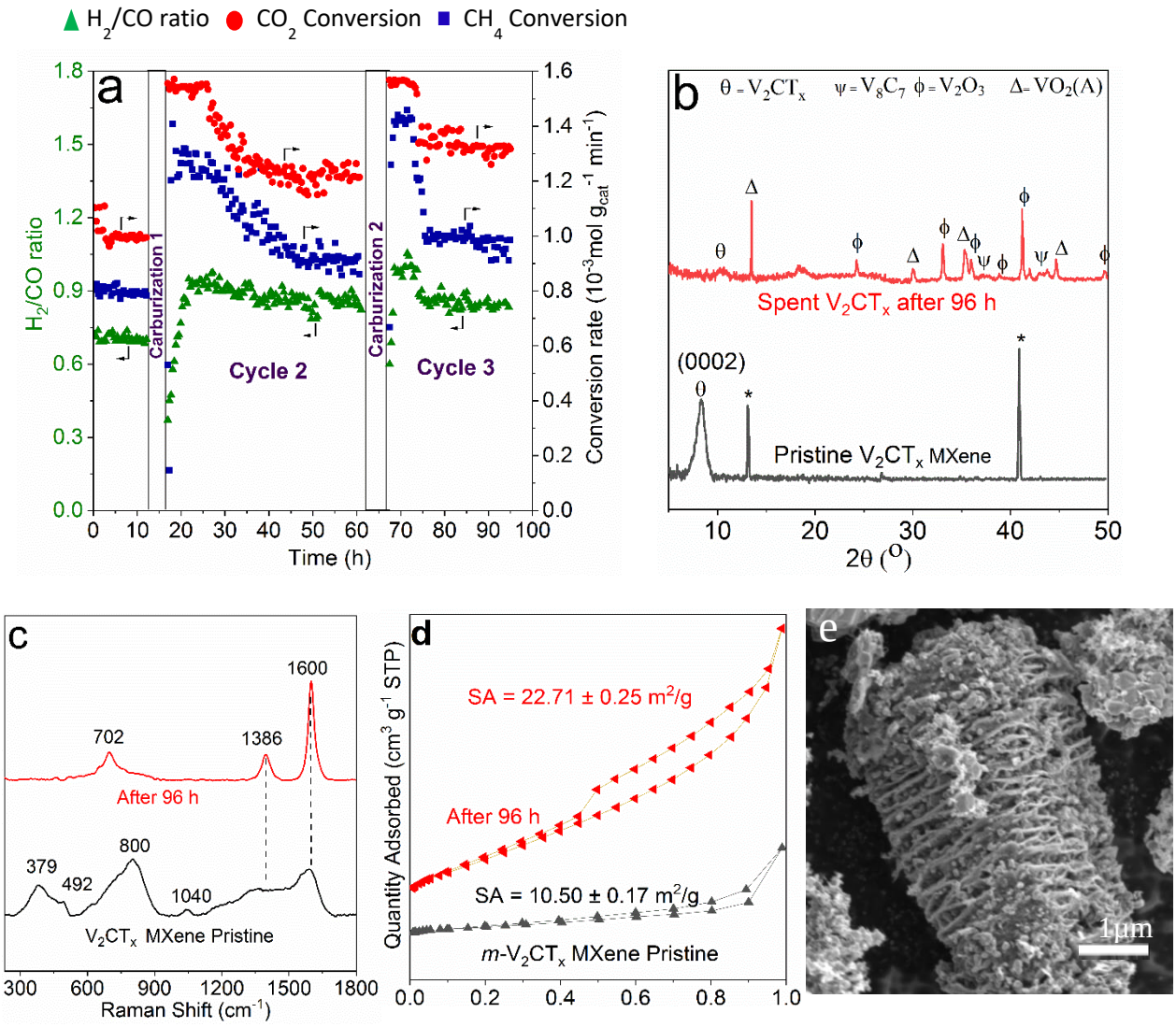

Figure 50. (a) CH_4 and CO_2 conversion activity and H_2/CO ratio of V_2O_3-V_8C_7/*m*-V_2CT_x MXene phase for 96 hours. Reaction conditions: 0.2 g catalyst *T*= 800 ºC, *P*= 1 atm, 40% CH_4 and 40% CO_2 (balance N_2). (b) XRD of the 96 hours tested V_2O_3-V_8C_7/*m*-V_2CT_x MXene catalyst (asterisk in unreacted MAX phase). (c) Raman spectra showing the formation of carbide on the surface. (d) N_2 physisorption of spent MXene showing the presence of a hysteresis loop. (e) Layered morphology still intact after DRM reaction additionally showing the presence of oxide and carbide nanocrystals decorated in between the MXene layers.

The SEM image (Figure 50e) of the catalyst before and after DRM did not reveal any significant change of the multilayered structure. This was additionally corroborated by the presence of H3-curve on the N_2-physisorption plot (Figure 50d). During the carburization step to convert V_2O_3 into V_8C_7 amorphous coke is also generated. Thus, a larger amount of CO_2 is consumed during the initial stage of DRM for burning such carbonaceous spices (Figure 50a). It can thus be established that after the initial activation a certain quantity of V_2O_3 and V_8C_7 nanocrystals must be generated to show sufficient catalytic performance. Furthermore, a certain induction time is needed to form these nanoparticles – such a hypothesis has already been reported by Baktash et.al. for nickel oxide nanoparticles.[221]

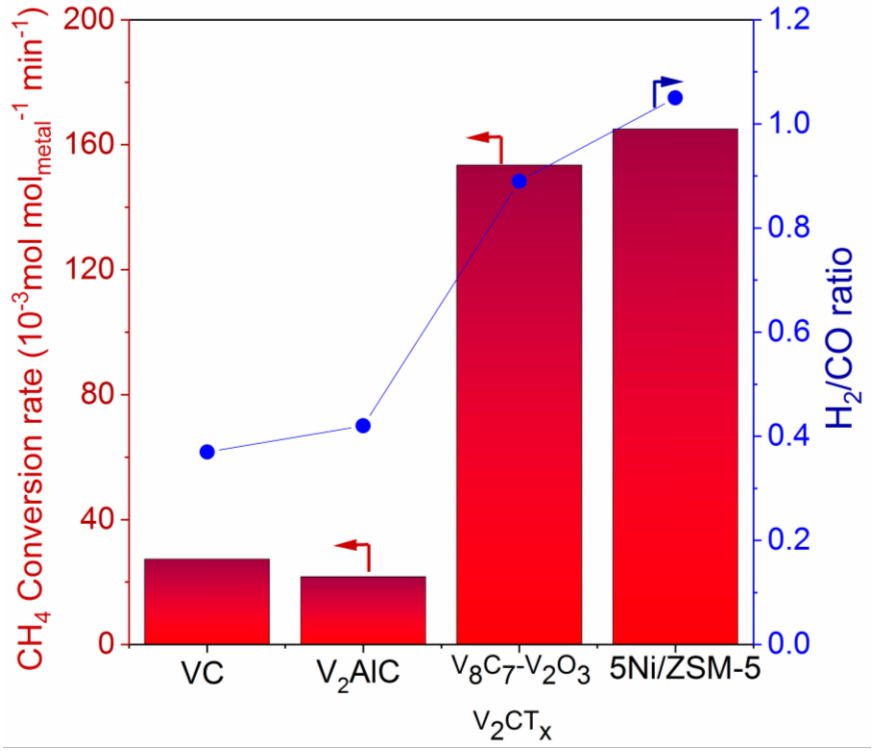

Figure 51. CH_4 conversion and H_2/CO ratio comparison for VC, V_2AlC, V_2O_3-V_8C_7/*m*-V_2CT_x MXene, and 5Ni/ZSM-5 after achieving steady-state at GHSV of 4800 $ml g_{cat}^{-1} h^{-1}$.. T= 800 ºC, P= 1 atm, 40% CH_4, 40% CO_2 and 20% N_2.

A comparison of CH_4 conversion rates when normalized by the surface moles of V basis shows striking differences as observed in Figure 51. The moles of V were calculated by mapping a large area of the catalyst during EDS analysis (Table 2). While the Bulk VC and V_2AlC MAX phases showed lower activity and selectivity towards the H_2/CO ratio, V_2O_3-V_8C_7/*m*-V_2CT_x shows a distinctive performance. The two-dimensional multilayered nature of the catalyst facilitates the exposure of a higher amount of V sites/particles eventually with intrinsic chemical potentials due to their size, morphology, and confinement (in between the layers). This results in a unique performance when compared with the bulk counterparts. The V_2O_3-V_8C_7/*m*-V_2CT_x shows a CH_4 consumption rate of $153.4\ mmol_{CH_4} mol_V^{-1} min^{-1}$, while the VC and V_2AlC shows a CH_4 consumption rate of $27.3\ mmol_{CH_4} mol_V^{-1} min^{-1}$ and $21.7\ mmol_{CH_4} mol_V^{-1} min^{-1}$ respectively. Moreover, when the rate is compared with Ni-based catalysts supported on ZSM-5, it shows a comparable performance ($165.2\ mmol_{CH_4} mol_{Ni}^{-1} min^{-1}$). However, as time proceeds for the Ni based catalysts the H_2/CO ratio increases above the unity signifying the formation of coke, whereas the V_2O_3-V_8C_7/*m*-V_2CT_x provides a stable H_2/CO ratio of 0.9 over 96 h TOS. The rates were also normalized on the overall surface area basis and compared with Ni-based catalysts (Figure 52), where the CH_4 consumption rate for V_2O_3-V_8C_7/*m*-V_2CT_x and Ni/ZSM-5 is $72.3\ \mu mol_{CH_4}\ m^{-2} min^{-1}$ and $0.97\ \mu mol_{CH_4}\ m^{-2} min^{-1}$, respectively.

The CH_4 conversion normalized with respect to the surface area of the catalyst (Figure 52a) yields striking differences as the surface area of the V_2CT_x Supported oxy-carbide catalyst is 10.5 m^2/g while for the Ni-based system is 295 m^2/g, thus showing higher rates in case of the oxy-carbide. The steady-state conversions of CH_4 and CO_2 for the V_2O_3-V_8C_7/*m*-V_2CT_x and the Ni-based catalysts are comparable (Figure 52b-d). The H_2/CO ratio for the Ni-based catalysts increases as TOS, signifying the excess cracking of methane thereby generating more H_2 and indicating that

the catalyst is coking, while for the V_2O_3-V_8C_7/*m*-V_2CT_x oxy-carbide, the H_2/CO ratio remains constant, signaling that there is no coking and a stable ratio is obtained over TOS. As seen for the oxy-carbide, the CO_2 conversions are higher as compared to CH_4 conversion, while for the Ni-based systems the CH_4 conversion is higher than the CO_2 conversion, thus strengthening the hypothesis about coking over the Ni-based systems

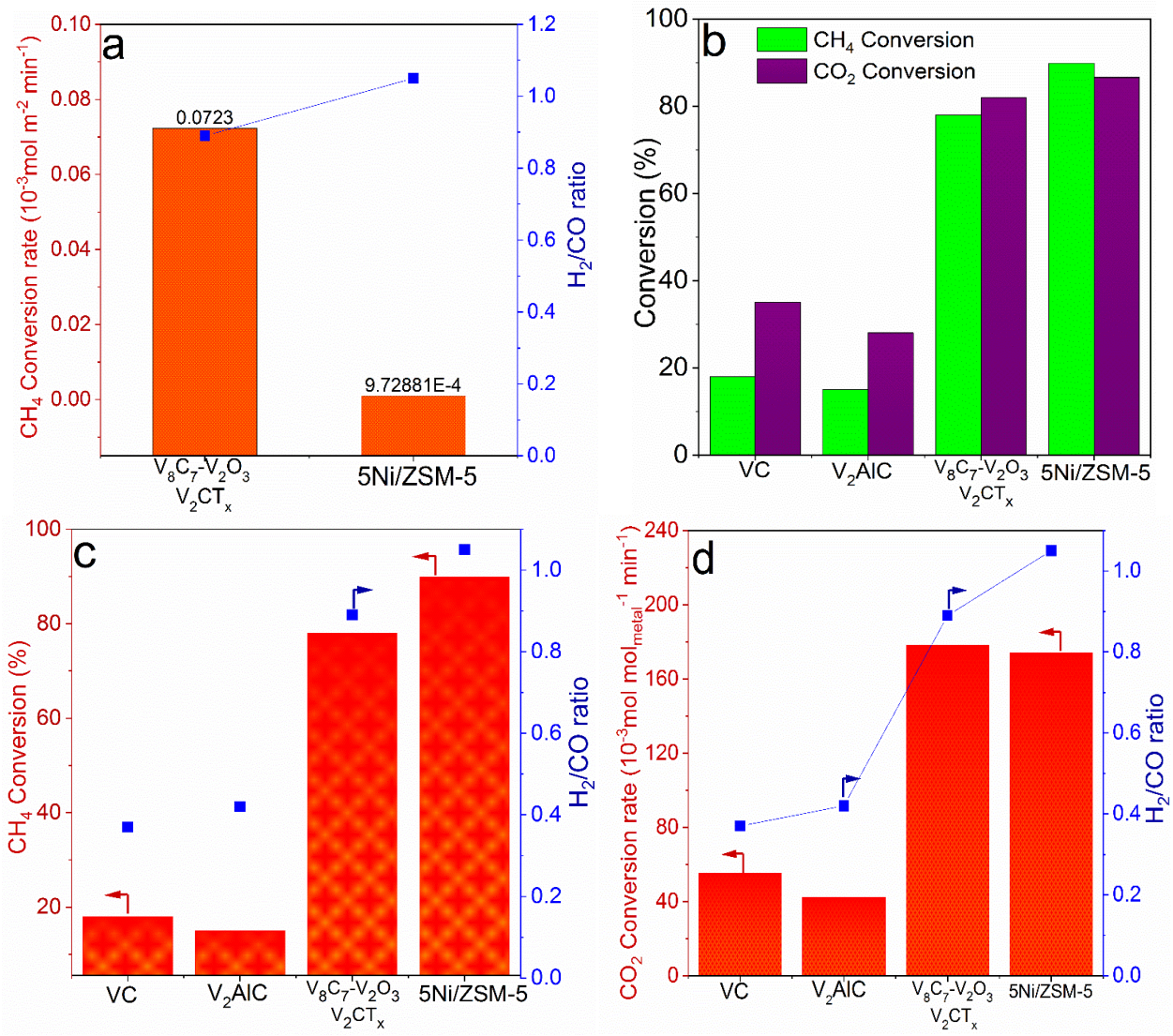

Figure 52. Conversion rates normalized with respect to the surface area of the catalyst after attaining a steady state. (a) CH_4 conversion rates, (b-d) CH_4 - CO_2 conversion and H_2/CO ratio for different catalysts. (metal = V and Ni).

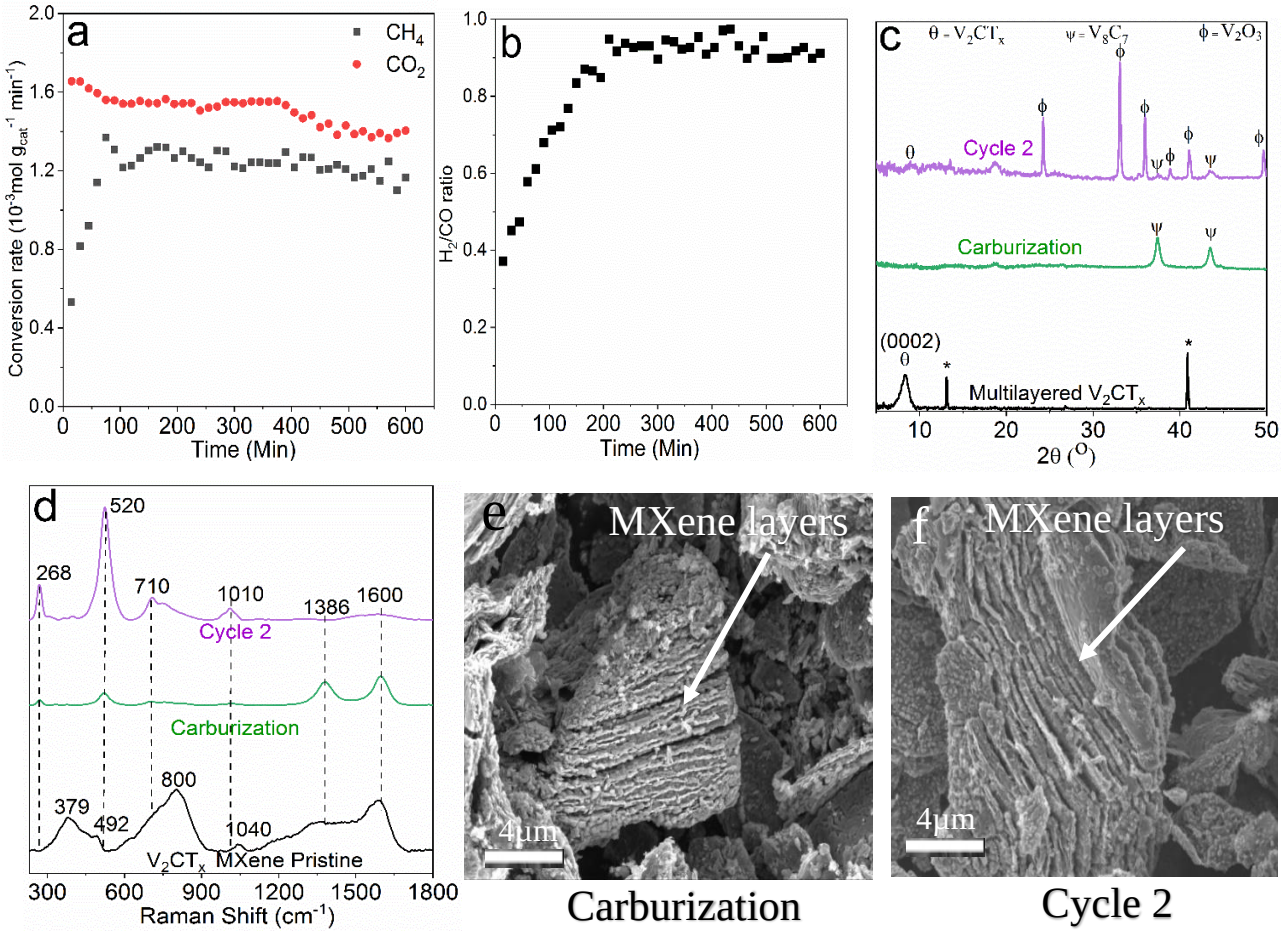

Figure 53. (a) CH_4 and CO_2 conversion (b) H_2/CO ratio for V_2O_3-V_8C_7/*m*-V_2CT_x MXene after carburization. (c) XRD, (d) Raman, and (e-f) SEM image of the fresh, carburized and spent V_2O_3-V_8C_7/*m*-V_2CT_x MXene catalyst. Catalyst mass = 0.2 g, TOS = 400 min, T= 800 ºC, P= 1 atm, 40% CH_4, 40% CO_2 and 20% N_2.

Further kinetic insights were obtained by studying the influence of carburization after the first DRM catalytic cycle (Figure 53a-b). The carburization (20% CH_4 and 80% H_2) of V_2O_3-V_8C_7/*m*-V_2CT_x was monitored by tracking CO as the product of carburization (Figure 54). Indeed, the carburization resulted in the transformation of V_2O_3-V_8C_7/*m*-V_2CT_x into V_8C_7/*m*-V_2CT_x which is evidenced by the sole presence of characteristic XRD and Raman peaks for V_8C_7, nevertheless, the multilayered structure was maintained to a certain degree (Figure 53c-e).

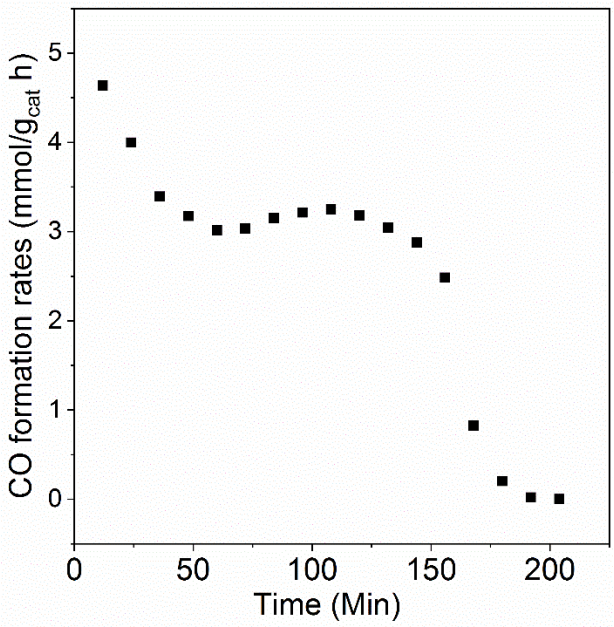

Figure 54. CO formation rates during the re-carburization of V_2O_3-V_8C_7/*m*-V_2CT_x MXene. Conditions: 20% CH_4 (Rest H_2), T= 800 ºC.

Rietveld refinement shows that the total oxide and carbide species within the spent material are about ~65% and ~35%, respectively (Figure 53c). After carburization, the kinetic experiments were conducted (Figure 53a-b) to monitor catalytic performance and an initial increase in activity was observed, similar to the one reported in Figure 50a, with a conversion rate of 1.21 $mmol_{CH_4}g_{cat}^{-1}min^{-1}$ and 1.47 $mmol_{CO_2}g_{cat}^{-1}min^{-1}$. After the second DRM catalytic cycle, characterization of the spent V_2O_3-V_8C_7/*m*-V_2CT_x catalyst revealed the simultaneous presence of V_8C_7 and V_2O_3 along with the multilayered morphology as evidenced by XRD (Figure 53c), Raman (Figure 53d), and SEM (Figure 53f) respectively. The N_2-physisorption data for the spent catalyst can be found in Figure 55. The N_2 adsorption-desorption profile shows a typical H3 type of porosity for all the samples

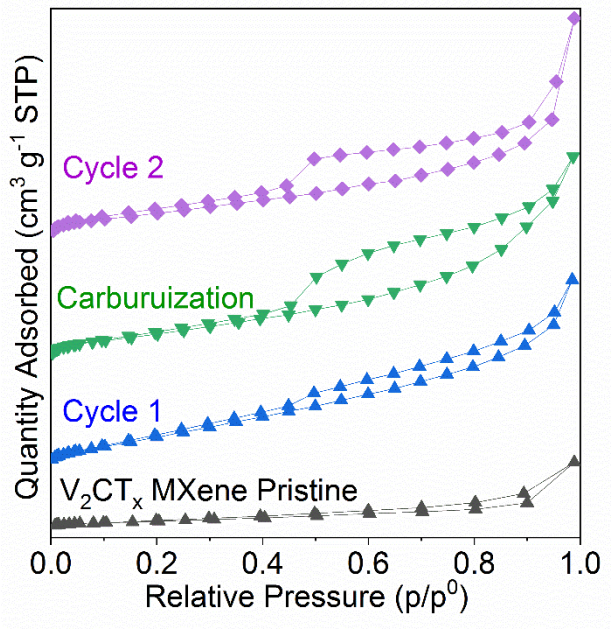

Figure 55. N_2 adsorption and desorption profiles for the spent catalyst after cycle 1, carburization and cycle2. The surface area of pristine *m*-V_2CT_x is 10.50 m^2/g, while after cycle 1 and cycle 2 it increases to 20.04 and 22.71 m^2/g respectively.

The results presented in Figure 53 further indicates that new potential active sites (V_2O_3-V_8C_7) are created after exposure of *m*-V_2CT_x to CO_2 and CH_4 at elevated temperatures (800°C) when an optimum 1:1 molar ratio of reactants is fed. As a result, the pristine *m*-V_2CT_x needs to be initially exposed to DRM cycle followed by a carburization process to consequently obtain an unprecedented oxy-carbide catalyst. This dynamic and complex process occurs as follows: firstly, the multilayered structure of the pristine *m*-V_2CT_x remains to some degree (confirmed by SEM and N_2 physisorption); secondly, such layers are decorated with V_2O_3 and V_8C_7 nanoparticles located both in-between the layers and on the surface (corroborated by Raman, XRD, and SEM). These findings provide valuable insight into the potential reaction mechanism taking place for DRM with *m*-V_2CT_x and the reasons for the observed superior performance of V_2O_3-V_8C_7/*m*-V_2CT_x. It is reasonable to hypothesize that the *in-situ* generation of V_2O_3 and V_8C_7 nanocrystals

between the layered structure are driving the DRM reaction and the *m*-V_2CT_x MXene structure serves as the precursor to generate and disperse these oxides (V_2O_3) and carbide (V_8C_7) crystals on *m*-V_2CT_x. This new V_2O_3-V_8C_7/*m*-V_2CT_x material maximizes the utilization of active and selective V sites. These sites now exist as V_2O_3 and V_8C_7 particles with high stability against sintering and undergo *in-situ redox* reactions, which simultaneously passivate the bulk overoxidation of the carbide *m*-V_2CT_x phase. Therefore, this new oxy-carbide catalyst addresses the major challenges observed when using bulk oxides and carbides as catalysts for DRM. In addition, we carburized both V_2O_3 and V_2O_5 bulk materials and then performed DRM, observing a relatively poor performance compared to V_2O_3-V_8C_7/*m*-V_2CT_x, especially in terms of stability. This is also corroborated elsewhere.[40]

4.5.3 Effect of GHSV

Next, we evaluated the effect of various GHSV (2,800 – 12,000 $ml g_{cat}^{-1} h^{-1}$ at different temperatures (800 - 1000°C) to approach equilibrium conversions and validate the stability of the material. (Figure 56, Figure 57 and Figure 58). Note that the reactant conversion and the H_2/CO ratio at higher GHSV (12,000 $ml g_{cat}^{-1} h^{-1}$) and at 800 °C, exhibits lower H_2/CO ratio, which is due to the simultaneous occurrence of reverse-water-gas-shift under such conditions.

Two separate experiments were performed at GHSV of 2400 mL/(g_{cat}.h) at 800 and 1000 ºC (Figure 56) In both cases, equilibrium conversion is reached and the H_2/CO ratio close to unity was recorded. The stable reactant conversion and *syngas* ratio at these severe conditions corroborates the good stability of V_2O_3-V_8C_7/*m*-V_2CT_x.

An additional experiment was also performed at GHSV of 4800 mL/(g_{cat}.h) at 1000 ºC and the equilibrium conversion is reached with an optimal H_2/CO ratio close to unity. Once again, we corroborate the stability of the material. (Figure 57)

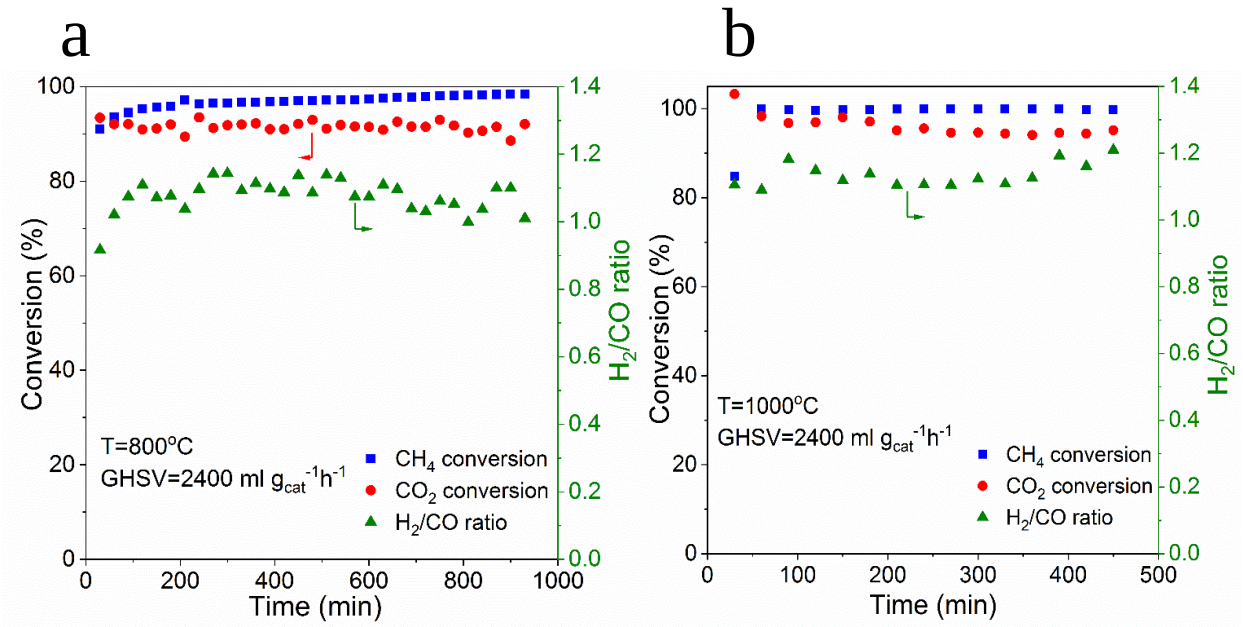

Figure 56. CH_4 and CO_2 conversion and H_2/CO ratio of V_2O_3-V_8C_7/*m*-V_2CT_x under (a) GHSV 2400 ml $g_{cat}^{-1}h^{-1}$ at T= 800 ºC (b) GHSV 2400 ml $g_{cat}^{-1}h^{-1}$ at T= 1000 ºC. Reaction conditions: 0.2 gm catalyst, P= 1 atm, CH_4=40%, CO_2=40%, N_2=20%.

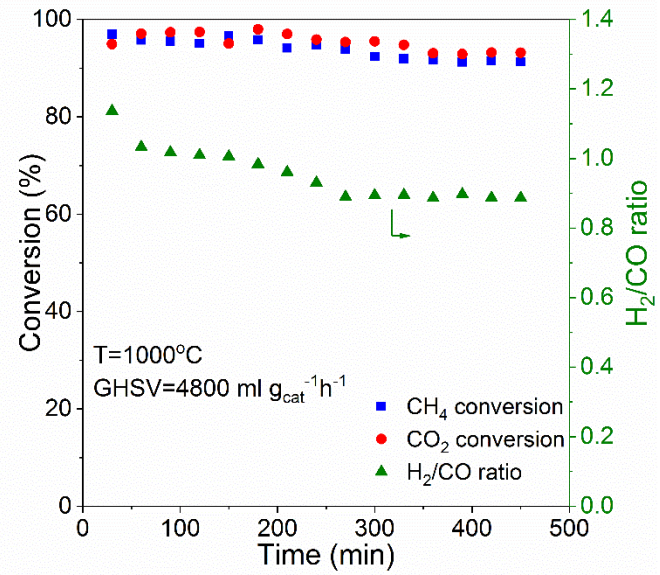

Figure 57. CH_4 and CO_2 conversion and H_2/CO ratio of V_2O_3-V_8C_7/*m*-V_2CT_x under GHSV 4800 ml $g_{cat}^{-1}h^{-1}$ at T= 800 ºC. Reaction conditions: 0.2 gm catalyst, P= 1 atm, CH_4=40%, CO_2=40%, N_2=20%.

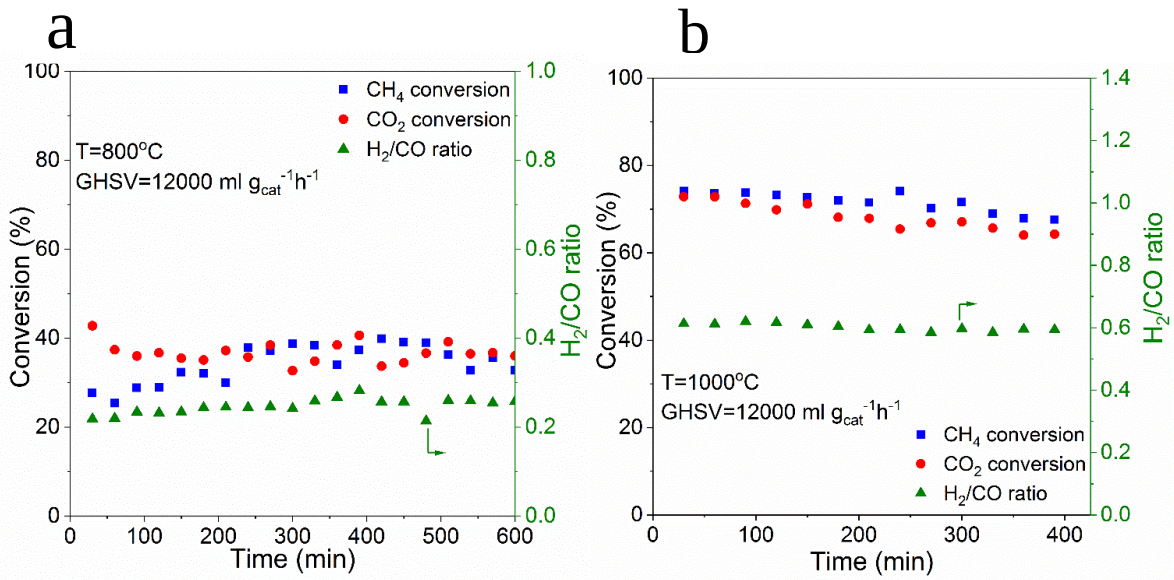

Figure 58. CH_4 and CO_2 conversion and H_2/CO ratio of V_2O_3-V_8C_7/*m*-V_2CT_x under (a) GHSV 12000 ml $g_{cat}^{-1}h^{-1}$ at T= 800 ºC (b) GHSV 12000 ml $g_{cat}^{-1}h^{-1}$ at T= 1000 ºC. Reaction conditions: 0.2 gm catalyst, P= 1 atm, CH_4=40%, CO_2=40%, N_2=20%.

Two separate experiments were performed at GHSV of 12000 mL/(g_{cat}.h) at 800 and 1000 ºC (Figure 58). In both cases, the reactants' conversion and H_2/CO ratio were stable. As the temperature rises to 1000ºC, the conversion and the H_2/CO ratio increases and remains stable. A lower H_2/CO ratio indicates a contribution from RWGS at such conditions. The catalyst under high GHSV (12000 ml $g_{cat}^{-1}h^{-1)}$ at 800 ºC is not that active and selective when compared to its performance at lower GHSV (2800 and 4800 ml $g_{cat}^{-1}h^{-1}$). This suggests that at shorter contact times the CH_4 and CO_2 dissociation proceeds at a slower rate and RWGS dominates at such conditions.

4.5.4 Effect of reactant concentration

Next, the effect of different reactant concentrations (oxidant lean and rich conditions) on the DRM kinetics over V_2O_3-V_8C_7/*m*-V_2CT_x was also investigated (Figure 59). The oxidant lean condition caused the precipitation of large amounts of coke, clogging the reactor. However, oxidant rich conditions led to deeper oxidation of the V_2O_3-V_8C_7/*m*-V_2CT_x MXene to V_2O_3/*m*-V_2CT_x (Figure

60). This behavior clearly signals that an optimum ratio (1:1) between the CH_4 and CO_2 needs to be maintained in the feed stream to facilitate the optimum activity-stability, and a H_2/CO ratio close to unity.

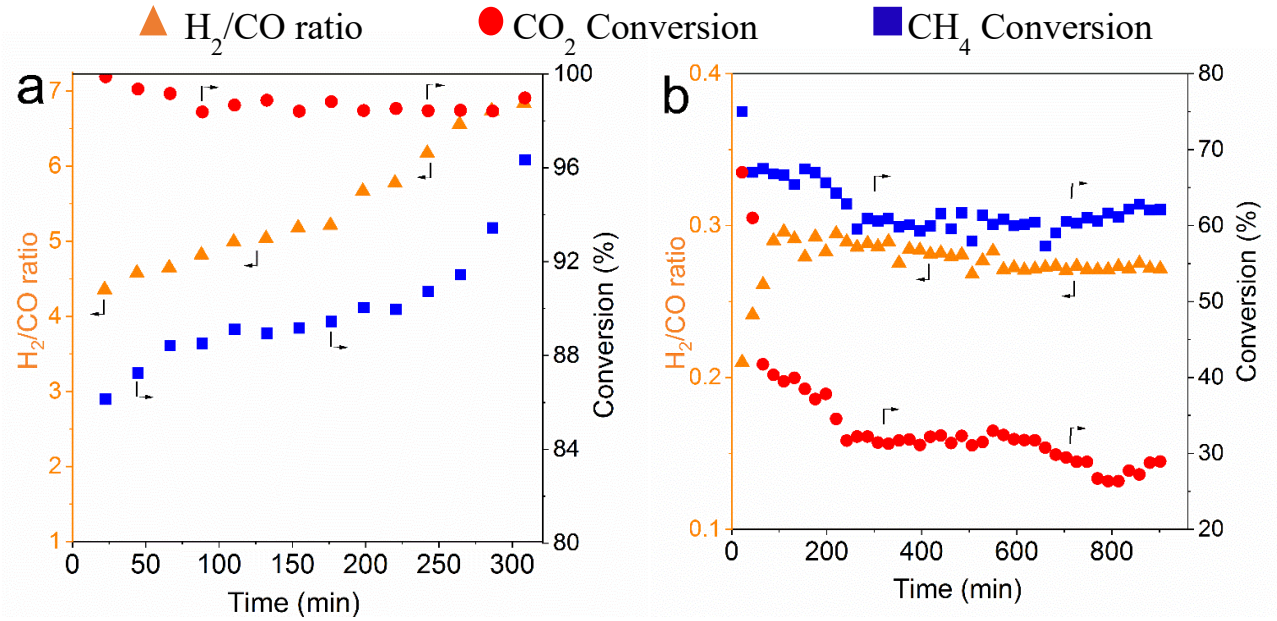

Figure 59. CH_4 and CO_2 conversion and H_2/CO ratio of V_2O_3-V_8C_7/*m*-V_2CT_x under (a) oxidant lean conditions, (b) Oxidant rich conditions. Reaction conditions: 0.2 gm catalyst T= 800 ºC, P= 1 atm, for oxidant lean 70% CH_4 and 20% CO_2 (rest inert) and for oxidant rich 20% CH_4 and 70% CO_2 (rest inert)

Two separate experiments were performed, where in the first case, (oxidant rich condition) inlet CO_2 to CH_4 ratio was maintained at 0.7, while for the second experiment (oxidant lean conditions), the CH_4 to CO_2 ratio was maintained at 0.7. The activity of the V_2O_3-V_8C_7/*m*-V_2CT_x MXene under such diverse conditions can be found in Figure 59. Under the oxidant lean conditions, a substantial amount of coke was generated on the catalyst from the cracking of the methane, thereby accumulating a copious amount of coke on the catalyst surface and leading to the clogging of the reactor (Figure 60a and c). While under the oxidant rich conditions, the V_2O_3-V_8C_7/*m*-V_2CT_x MXene suffered oxidation, and the surface became decorated with tiny oxide crystals on the surface (Figure 60b). Figure 60c evidence the formation of carbon under 70% CH_4 concentration

while, the formation of V_2O_3 phase under 70% CO_2 concentration, evidencing the necessity of correct ratio of CO_2 and CH_4 under DRM

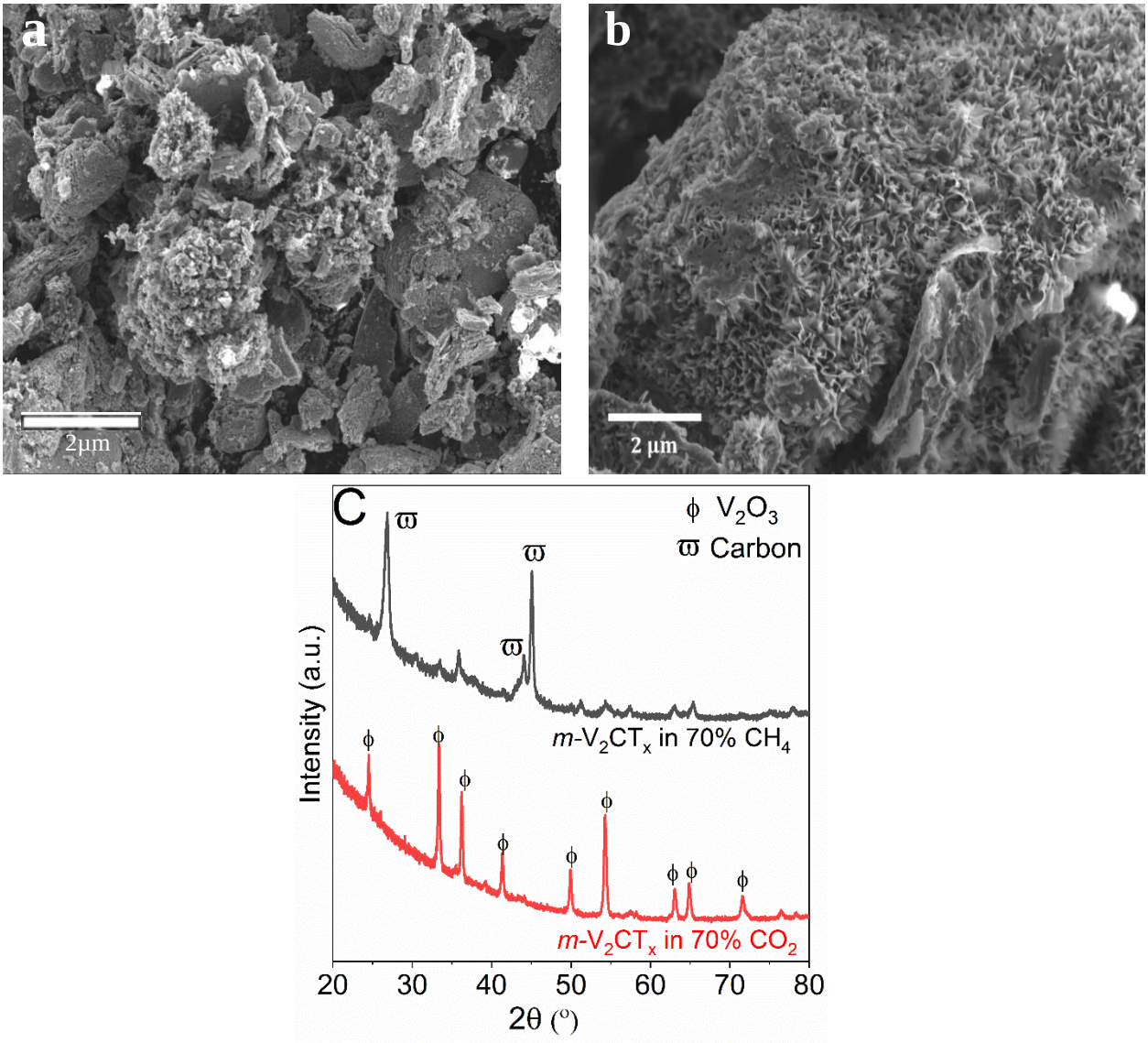

Figure 60. (a) SEM images of the V_2O_3-V_8C_7/*m*-V_2CT_x MXenes phase treated under oxidant lean conditions evidencing the deposition of coke on the surface. (b) Oxidant rich conditions, evidencing the destruction of layered structure and formation of tiny oxide crystals on the surface. (c) XRD pattern of the spent catalyst after the oxidant rich/lean test. Signifying the deposition of graphitic carbon under oxidant lean condition and transformation to V_2O_3 under oxidant rich condition. Reaction conditions: 0.2 gm catalyst T= 800 ºC, P= 1 atm, for oxidant lean 70% CH_4 and 20% CO_2 (rest inert) and for oxidant rich 20% CH_4 and 70% CO_2 (rest inert).

4.5.5 Isotopic labeling experiments

To validate our hypothesis about the operation of the V_2O_3-V_8C_7/*m*-V_2CT_x catalyst and to also corroborate our kinetic and spectroscopy findings, we combined steady-state kinetics with isotopic labeling experiments ($^{13}CO_2$ and $^{13}CH_4$). Figure 61a shows the DRM product distribution over pristine V_2O_3-V_8C_7/*m*-V_2CT_x, which matches with the steady-state kinetic data measured by GC (Figure 50a).

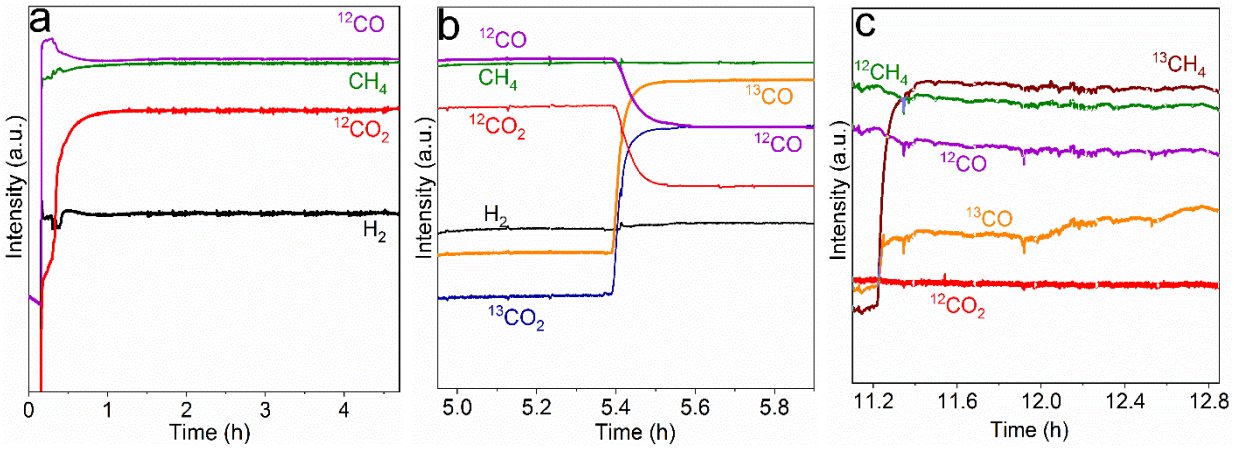

Figure 61. (a) Initial DRM reaction over pristine V_2O_3-V_8C_7/*m*-V_2CT_x for 5.5 hours. (b) First switching between the $^{12}CO_2$ and $^{13}CO_2$, demonstrating the prime source of CO. (c) "zoomed-in" plot of $^{12}CH_4$ switch to $^{13}CH_4$ during a separate DRM experiment, evidencing a gradual rise in ^{13}CO and fall in ^{12}CO signals. ($^{12}CH_4$ (m/z=16), $^{13}CH_4$ (m/z=17), $^{12}CO_2$ (m/z=44), $^{13}CO_2$ (m/z=45) Ar (m/z=40), ^{12}CO (m/z=28), ^{13}CO (m/z=29), H_2 (m/z=2).

Next, switching $^{12}CO_2$ to $^{13}CO_2$ reveals that CO is originated from both the oxidation of *m*-V_2CT_x with CO_2 and during the carburization of V_2O_3/*m*-V_2CT_x with CH_4, as evidenced by the formation of 69% of ^{13}CO and 31% of ^{12}CO (obtained from the MS-intensity ratios) (Figure 61b). Details can be found in Figure 62 and Figure 63.

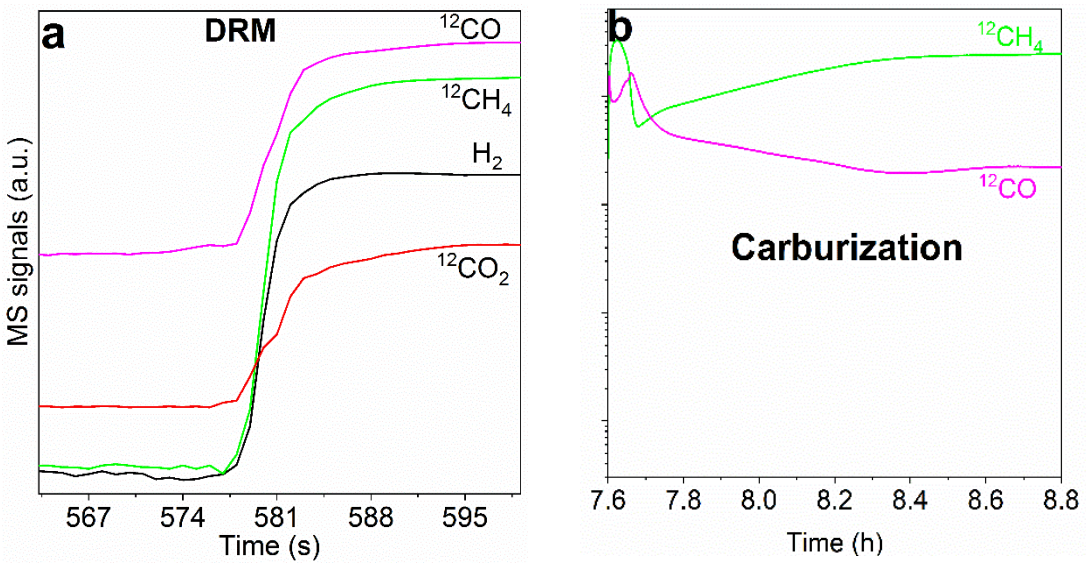

Figure 62. Results of isotopic $^{13}CO_2$ labelled experiments over V_2O_3-V_8C_7/*m*-V_2CT_x MXenes. (a) Initial DRM reaction after passing the reaction mixture at 800^0C over V_2O_3-V_8C_7/*m*-V_2CT_x. (b) Carburization step after running the DRM for 5.5 hours. CO is the product during carburization.

The isotopic labeling experiments were performed utilizing the same methodology employed under the steady-state kinetic experiments. The *m*-V_2CT_x MXene was heated under N_2 till the reaction temperature and 1:1 ratio of $^{12}CH_4$ and $^{12}CO_2$ were passed at 800^0C. The products of the reaction were tracked using a mass spectrometer (Figure 62a). After the steady-state was achieved, the $^{12}CO_2$ was replaced with $^{13}CO_2$ and the reaction was continued. The product CO with ^{12}C and ^{13}C as the carbon source was detected. After the reaction, the catalyst was carburized using methane (20%) and hydrogen (rest) (Figure 62b). After carburization, the DRM reaction was progressed to verify the increase in activity of the catalyst after carburization and positive results were obtained. Similar switching between ^{12} CO_2 and $^{13}CO_2$ was performed 4 times to verify the source of carbon in CO (Figure 63).

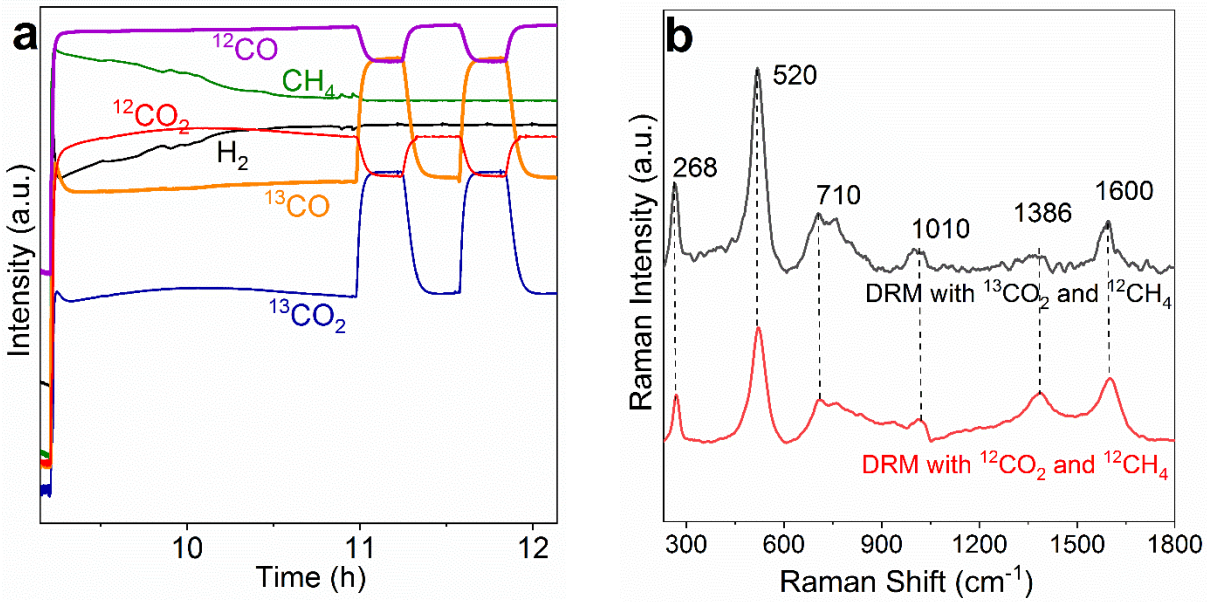

Figure 63. (a) DRM kinetics over the carburized V_2O_3-V_8C_7/m-V_2CT_x catalyst, followed by periodic switching between $^{12}CO_2$ and $^{13}CO_2$ to validate the proposed hypothesis. ($^{12}CH_4$ (m/z=16), $^{13}CH_4$ (m/z=17), $^{12}CO_2$ (m/z=44), $^{13}CO_2$ (m/z=45) Ar (m/z=40), ^{12}CO (m/z=28), ^{13}CO (m/z=29), H_2 (m/z=2). (b) Raman of spent V_2O_3-V_8C_7/*m*-V_2CT_x catalyst after performing DRM using $^{12}CH_4$ and $^{13}CO_2$, no significant changes are observed in the spectra when comparing to spent V_2O_3-V_8C_7/*m*-V_2CT_x catalyst after DRM with $^{12}CH_4$ and $^{12}CO_2$. This indicates that there is no incorporation of C from CO_2 into the structure.

To further show that carbon from the V_8C_7 particles supported on *m*-V_2CT_x participates in the DRM reaction, we also performed isotopic labeled $^{13}CH_4$/$^{12}CO_2$ experiments. Wherein, after attaining steady-state conditions, we switch from $^{12}CH_4$ to labelled $^{13}CH_4$ and follow the evolution of ^{13}CO and ^{12}CO. A continuous gradual rise in the ^{13}CO signal and a gradual drop in ^{12}CO signals are observed (Figure 61c), indicating the replacement of ^{12}C from the V_8C_7 particles with ^{13}C (Figure 64 and Figure 65). To reinforce this observation, we conducted the DRM reaction with $^{13}CH_4$ for about 2 h and the spent V_2O_3-V_8C_7/*m*-V_2CT_x catalyst was then oxidized with air at 800 $^{\circ}C$.

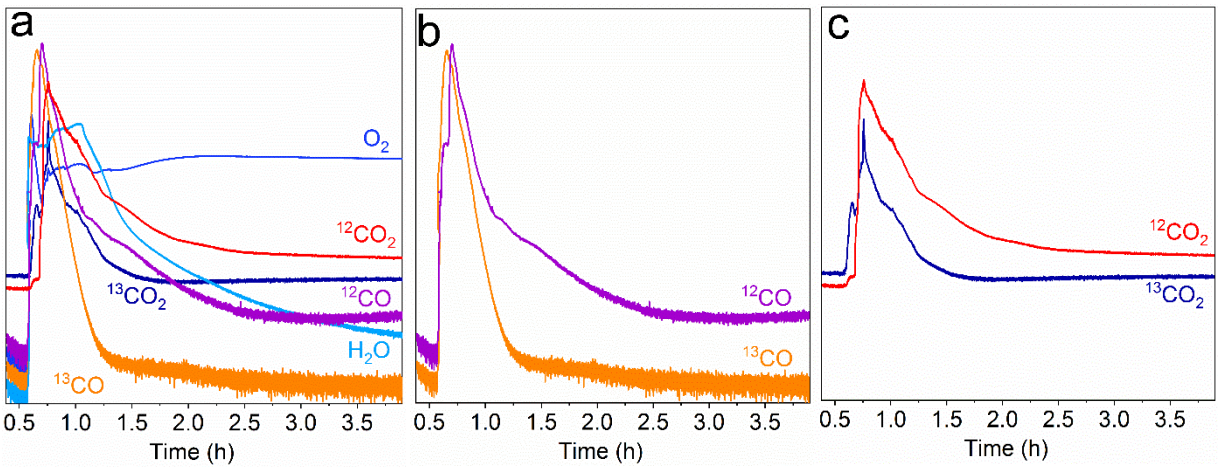

Figure 64. (a) Oxidation products from the spent V_2O_3-V_8C_7/*m*-V_2CT_x after performing DRM with $^{13}CH_4$ and $^{12}CO_2$. (b) Evolution of ^{13}CO and ^{12}CO (c) $^{13}CO_2$ and $^{12}CO_2$ during the oxidation process. Oxidation conditions: 21% O_2 and 79% Ar, T=800^{0}C.

After performing DRM with $^{12}CH_4$ and $^{12}CO_2$, the feed was switched to isotopic labeled $^{13}CH_4$ and $^{12}CO_2$. The reaction was continued for 2 hours. After the reaction was stopped the feed was switched to Ar and the system was flushed for 30 minutes. After flushing the system, air (21% O_2 and 79% Ar) was introduced and combustion products were tracked. Evolution of products was tracked following the atomic mass (O_2 (m/z=32), $^{12}CO_2$ (m/z=44), $^{13}CO_2$ (m/z=45), Ar (m/z=40), ^{12}CO (m/z=28), ^{13}CO (m/z=29), H_2O(m/z=18). Figure 64a. shows the magnitude of all the combustion products. Figure 64b evidences the evolution of ^{12}CO and ^{13}CO, while the Figure 64c. shows the evolution of $^{12}CO_2$ and $^{13}CO_2$. It is evident that the $^{12}CO_2$ evolution is a bit delayed, and its evolution starts with a small hump, which can be due to the burning of a small amount of amorphous coke deposited on the surface. The $^{13}CO_2$ evolution dominates initially as compared to $^{13}CO_2$, which can be due to the burning of $V_8{}^{13}C_7$ nanoparticles on the surface (which primarily contains ^{13}C in their structure), followed by the combustion of the support *m*-V_2CT_x, which primarily contains ^{12}C in its structure.

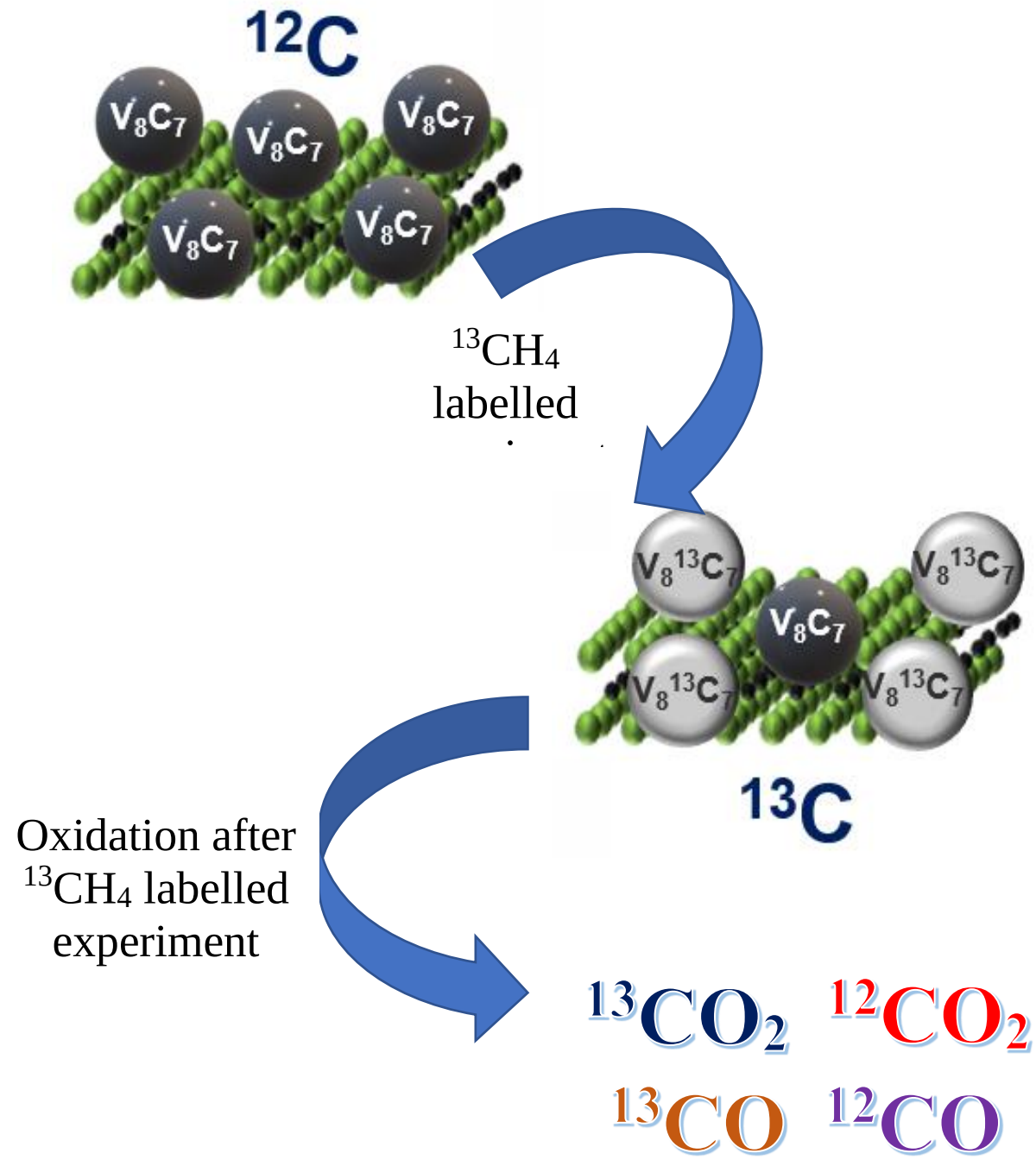

Figure 65. Schematic representation showing the oxidation products from the spent V_2O_3-V_8C_7/*m*-V_2CT_x after performing DRM with $^{13}CH_4$ and $^{12}CO_2$. (b) Evolution of ^{13}CO and ^{12}CO (c) $^{13}CO_2$ and $^{12}CO_2$ during the oxidation process. Oxidation conditions: 21% O_2 and 79% Ar, T=800^{0}C.

The combustion products (Figure 64 and Figure 65) contain a significant amount of ^{13}C along with ^{12}C products. This confirms that the carburization of V_2O_3 crystals forms V_8C_7 particles instead of cracking methane into hydrogen and amorphous/graphitic carbon, which is the typical operation-mode for most of the reported catalysts for DRM. The above-mentioned isotopic labeled experiments evidence the unique operation mode of the originated selective, coke-resistant, reactive, and self-healing V_2O_3-V_8C_7/*m*-V_2CT_x catalyst.

The presented kinetic and spectroscopic data complemented by isotopic labeling experiments confirm that *m*-V_2CT_x serves as a precursor for *in-situ* generation of V_2O_3 and V_8C_7 nanocrystals during DRM. Currently, there is no consensus in the literature about the reaction mechanism for DRM.[50] Based on our experimental findings; we propose that, initially, when heated to 800 ^0C under inert gas, the *m*-V_2CT_x partially oxidizes. During this ramp-up, the trapped water within the layers yields V_2O_3 particles, while some of the MXene transforms into V_8C_7 particles (initiation reaction in Figure 66).[157] Then, the V_8C_7/*m*-V_2CT_x is oxidized with CO_2 to form V_2O_3/*m*-V_2CT_x and yielding CO (oxidation reaction in Figure 66) followed by recarburization of V_2O_3/*m*-V_2CT_x with CH_4 to form V_8C_7/*m*-V_2CT_x (reduction reaction in Figure 66). Consequently, an oxy-carbide V_2O_3-V_8C_7/*m*-V_2CT_x catalyst is created that converts CO_2 and CH_4 and selectively produces *syngas* with a H_2/CO ratio close to unity (overall reaction in Figure 66).

Because coking is suppressed up to a certain extent when using transition metal carbide-based catalysts,[40, 42] these materials primarily deactivate because of overoxidation under DRM conditions. Brungs *et al.*,[40] suggested that running the DRM reaction at high temperature when using metal carbide catalysts leads to catalyst stabilization because re-carburization becomes thermodynamically favorable. Therefore, the oxidation reaction now competes with the

carburization reaction resulting in a less severe oxidized material, especially when using CH_4 and CO_2 as feedstock.

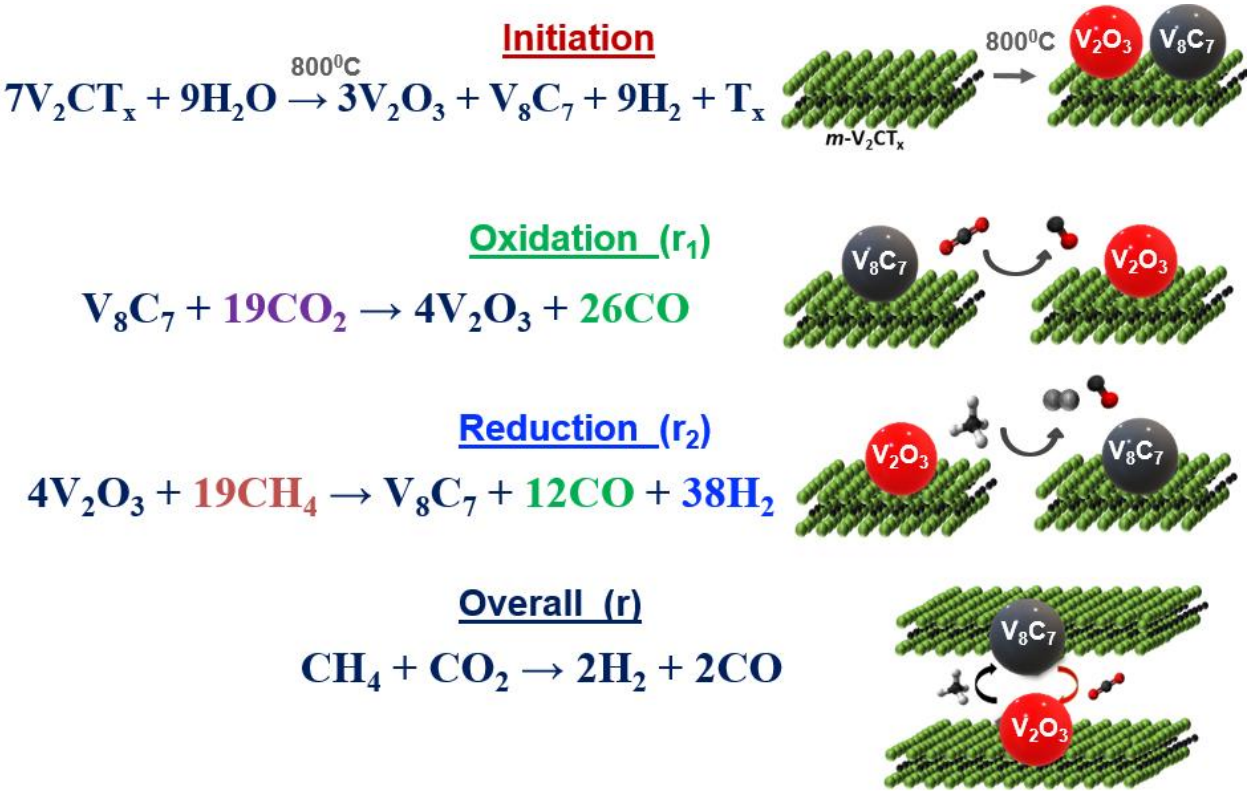

Figure 66. Proposed DRM mechanism when using *m*-V_2CT_x MXene as a precursor highlighting the transformation of V_8C_7 into V_2O_3 nanoparticles in-between the layers and on the surface via an *in-situ* redox mechanism.

Our results demonstrate that the active V_2O_3-V_8C_7/*m*-V_2CT_x material is highly selective and stable for DRM despite the presence of a mild oxidant, CO_2. This is because at 800 ºC, the carburization of vanadium oxide becomes thermodynamically favorable and, therefore, when using the conditions for this study (temperature, feed composition, concentration, reaction time, and residence time) we avoid an overoxidation of the *m*-V_2CT_x MXene into bulk V_2O_5 and, instead, we obtain an unprecedented layered oxy-carbide catalyst. Certainly, our conditions favor both the oxidation and carburization rates in similar extent, converting the CH_4 and CO_2 to *syngas* and

minimizing *i)* the formation of coke, *ii)* RGWS reaction, *iii)* overoxidation of the *m*-V_2CT_x phase, and *iv)* the overgrowth of the V_2O_3 and V_8C_7 particles.

Interestingly, V_2O_3-V_8C_7/*m*-V_2CT_x exhibits better performance when compared to bulk VC. We attribute these differences to the structure of the involved carbide phases since *m*-V_2CT_x is a hexagonal structure (hcp) acting as a precursor to form V_2O_3-V_8C_7/*m*-V_2CT_x, while bulk VC is a face-centered structure (fcc). Our ongoing research is focused on gaining additional fundamental insight into the dynamics of the carbide species when exposed to various oxidants and diverse conditions. We are tuning the surface composition of different MXenes and their ability to selectively activate specific chemical bonds (e.g. C-H, C-C, C-O) at relatively high temperatures.

4.6 Conclusions

A two-dimensional transition metal carbide, *m*-V_2CT_x MXene was prepared by selective chemical etching of the V_2AlC MAX phase using HF solution and was *in-situ* transformed into V_2O_3-V_8C_7/*m*-V_2CT_x. This unique V_2O_3-V_8C_7/*m*-V_2CT_x catalyst is selective (produces H_2/CO ratio close to unity by lessening methane cracking, Boudoudard, and RWGS reactions), stable (avoids coke formation and severe bulk oxidation), and active (converts about 78% CH_4 and 82% CO_2) for DRM with CH_4 conversion rates comparable to Ni-base catalyst ($153.4\ mmol_{CH_4} mol_V^{-1} min^{-1}$) and also more than four times higher than its bulk counterparts (bulk VC and the V_2AlC MAX phase). The main aspects to highlight from this promising precursor *m*-V_2CT_x MXene are the H_2/CO ratio close to unity, the negligible formation of solid carbon, and unprecedented stability. This optimal DRM catalytic performance is achieved when V_2O_3-V_8C_7/*m*-V_2CT_x is treated with an equimolar CH_4 and CO_2 mixture at 800 ^{0}C for about 7 hours (GHSV = 4800 $ml g_{cat}^{-1} h^{-1}$). Using both surface and bulk sensitive techniques is evidenced by the formation of an oxy-carbide phase, where the *m*-V_2CT_x structure remains, up to a certain extent, and serves as a precursor of and

support for V_2O_3-V_8C_7 nanocrystal. However, these initial conditions are not ideal to entirely carburize V_2O_3 particles into V_8C_7. Therefore, a further carburization process (20% CH_4 and 80% H_2) to convert V_2O_3/*m*-V_2CT_x into V_8C_7/*m*-V_2CT_x is needed. Next, this new V_8C_7/*m*-V_2CT_x material is exposed to DRM conditions yielding V_2O_3-V_8C_7/*m*-V_2CT_x, which shows an attractive performance for DRM with unprecedented stability (negligible coke formation). This coke-resistant catalyst follows an *in-situ redox* mechanism where V_2O_3 transforms into V_8C_7 and *vice versa.* This *redox* mechanism is corroborated by combining kinetics and isotopic labeled studies. As a result, we state that *m*-V_2CT_x acts as a precursor to *in-situ* generate a new MXene-based catalyst for DRM, V_2O_3-V_8C_7/*m*-V_2CT_x. We foresee that the severe conditions used in this study will catch the attention of the heterogeneous catalysis community and the chemical/energy industry to consider the utilization of *m*-V_2CT_x, and other MXenes, as a precursor, catalyst, and/or support for DRM, and even for other important catalytic reactions demanding relatively high temperatures.

Chapter 5: Multilayered Two-Dimensional V_2CT_x MXene for Methane Dehydroaromatization

Abstract

We report a thermally stable multilayered two-dimensional vanadium carbide (V_2CT_x) MXene catalyst for the direct conversion of methane (CH_4) into benzene (C_6H_6). The multilayered carbide structure shows state-of-the-art CH_4 conversion 11.8% with a C_6H_6 formation rate of 1.9 mmol $g_{cat}^{-1}h^{-1}$ (4.84% C_6H_6 yield) at 700 ^{0}C, which is comparable to the benchmark Mo/ZSM-5 catalyst. The structure-activity relationship was explored by numerous characterization techniques including *in-situ/operando* Raman-MS, *ex-situ* X-ray diffraction (XRD), scanning electron microscopy (SEM), X-ray photoelectron spectroscopy (XPS), and ammonia temperature-programmed desorption (NH_3-TPD). This work provides a new platform to design and explore multilayered two-dimensional catalysts demonstrating confinement effect to convert CH_4 into $*C_2H_3$ intermediates which further oligomerizes inside multilayered structures producing C_6H_6 as a final product.

5.1 Introduction

Multilayered MXenes are a relatively new family of two-dimensional (2D) metal carbides and nitrides.[95, 130] They are named by their graphene-like morphology, in accordance with the general chemical formula $M_{n+1}X_nT_x$, where *n* can be 1,2, or 3, *M* is an early transition metal, *X* is carbon and/or nitrogen, *T* indicates various surface terminations ($^-$OH, O^- and F^-), which depend on the preparation method, and *x* is the number of surface functional groups per unit formula (Figure 67).[117]

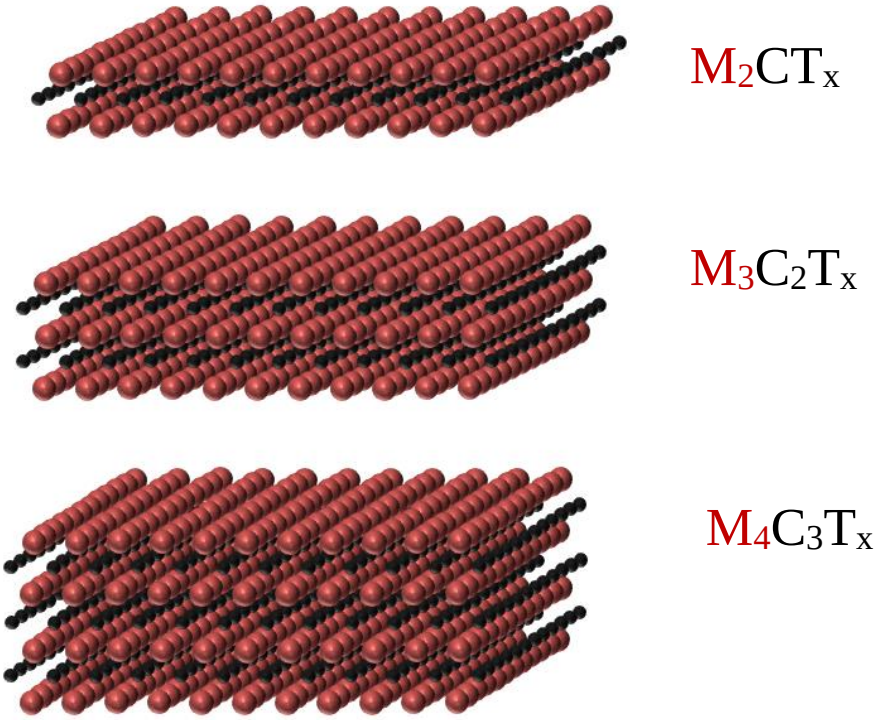

Figure 67. Schematic representation of different types of MXenes. M- Transition metal, C-Carbon, T-Terminal groups.

Already, about 20 different MXenes have been synthesized, while the properties of several have been theoretically predicted.[95, 118] Their potential and attractiveness reside on both their unique electronic and mechanical properties, and the bonding between interlayers which exhibits a combination of ionic, metallic, and covalent character.[95, 99, 222]

Only a few studies have been reported on the catalytic activity of MXenes at relatively high temperatures, such as the ammonia perchlorate decomposition,[95, 131] water gas shift reaction,[102] ethylbenzene dehydrogenation,[103] and propane dehydrogenation.[105] Based on the good thermal and chemical stability of *m*-V_2CT_x, especially under inert and reducing atmospheres,[183] we decided to further explore the catalytic properties of this material for the production of liquid aromatics via methane dehydroaromatization (MDA). Recently, it was reported, *m*-V_2CT_x as an active, selective

and coke-resistant catalyst for the dry reforming of methane at 800 ^{0}C. where an *in-situ redox* mechanism was proposed that demonstrates the catalytic attractiveness of MXenes for reactions where deactivation by carbon deposition is still a present issue. Taking advantage and simultaneously combining the *i)* structure of multilayered MXenes, that eventually provides the confinement effect that has been proposed as responsible to enhance the selectivity toward aromatics when using zeolites,[4, 56, 57, 223] *ii)* the oxy-carbide species coexisting on the surface of MXenes,[120] and *iii)* the relatively good thermal and structural stability of *m*-V_2CT_x under various conditions,[183] paved the path to study the MDA reaction over this promising *m*-V_2CT_x MXene catalyst (Reaction 1).

$$6CH_4 \rightleftarrows C_6H_6 + 9H_2 \qquad (1) \qquad \Delta H^0_{298K} = 434 \text{ kJ mol}^{-1}$$

The MDA reaction has gained interest essentially due to *i)* the ever-growing demand of aromatics, *ii)* the lack of on-purpose technologies for the production of aromatics, driven by the recent trends of using shale gas as feedstocks in cracker units,[4, 224-226] and *iii)* the notable discrepancies in the literature regarding the nature of active site(s) and the possible reaction mechanism when using the benchmark Mo/ZSM-5 catalysts.[227] The MDA process is far from industrial implementation due to stability-related issues as a result of various reasons such as *i)* rapid catalyst deactivation caused by carbonaceous deposits obstructing the catalytically active sites,[228] *ii)* extraction of framework Al species above 700^{0}C,[223, 224] *iii)* migration of the active site (Mo species) from internal to external framework in zeolites,[224] *iv)* rapid increase in graphitic-amorphous carbon over TOS demanding severe regeneration processes,[229] and *v)* the lack of consensus about the nature of active sites whether they are oxidic (MoO_x), carbidic (MoC_x) and/or oxy-carbidic (MoC_xO_y).[227]

5.2 Results and discussion

Herein, we report the use of *m*-V_2CT_x MXene as an active, selective, and potentially regenerable catalyst for MDA. We synthesize *m*-V_2CT_x by selectively etching Al from the corresponding precursor, so-called MAX phase (V_2AlC), using hydrofluoric acid (Figure 68).[98, 183, 230]

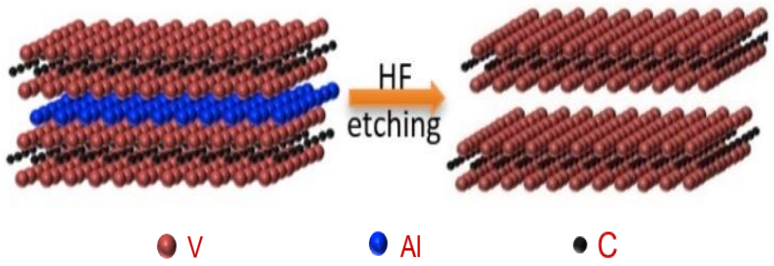

Figure 68. Schematic representation of the V_2AlC MAX phase transformation into V_2CT_x MXene after HF treatment.

In line with the literature, we carried out the MDA reaction at 700^{0}C using 50 mol% of both methane (CH_4) and inert, primarily producing benzene and hydrogen.[231] As stated in various studies using the benchmarked Mo/ZSM-5 catalyst, the first step in MDA reaction involves the carburization of the catalyst,[4, 232, 233] wherein the molybdenum oxide, anchored in the internal framework of the zeolite, is converted to carbide/oxy-carbide, which then acts as the active site for converting methane.[56, 223, 224, 227, 234] Initially, C-H bond activation occurs inside the channels of ZSM-5 forming methyl radicals, that subsequently dimerize forming C2 species and further undergoing oligomerization and cyclization over Bronsted acid sites to finally produce benzene (Figure 9).[57, 224]

Scanning electron microscopy (SEM) confirms the formation of *m*-V_2CT_x MXene (Figure 69b) after HF-treatment of the V_2AlC Max phase (Figure 69a). The precursor, V_2AlC, shows its typical morphology analogous to a tightly stacked un-exfoliated graphite as observed by scanning electron microscopy (SEM) (Figure 69a).[98, 183]

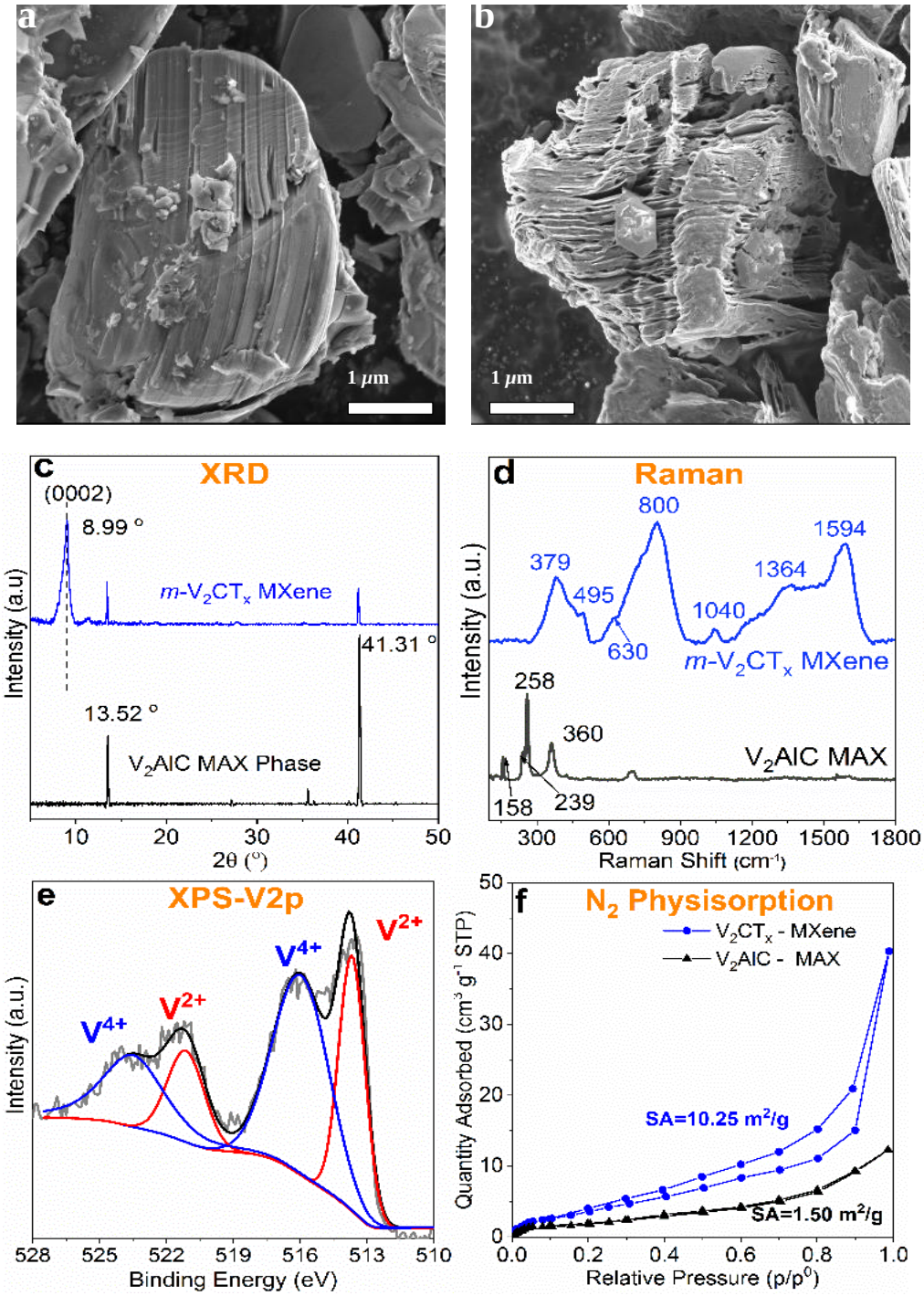

Figure 69. SEM micrograph of (a) V_2AlC MAX and (b) *m*-V_2CT_x MXene. (c-d) XRD diffractogram and Raman of V_2AlC MAX phase and the *m*-V_2CT_x MXene. (JCPDS No. 29-0101). (e) XPS V2p spectra of as-prepared *m*-V_2CT_x MXene. (f) N_2 physisorption of V_2AlC MAX and *m*-V_2CT_x MXene. SA=Surface Area.

Again, after the HF treatment, the tightly stacked layers transform to loosen accordion-like morphology with stacked layers well separated from each other due to the etching of Al atoms from the MAX phase (Figure 69b).[98, 183]Interestingly, the well-defined layered structure provides an interlamellar space of ~ 7.0 Å,[183] which is slightly larger than the kinetic diameter of benzene (~ 6.0 Å).[4, 231] These interlamellar spaces provide the confinement necessary for the oligomerization and cyclization of intermediates (C2 species) to then form benzene. X-ray diffraction (XRD) (Figure 69c) shows a characteristic peak at 2θ of 8.99° which corresponds to (0002) plane for *m*-V_2CT_x, along with traces of unreacted V_2AlC MAX phase (13.5° and 41.3°). The latter appears in almost all MXenes synthesized by HF etching, because more severe etching procedures lead to the extraction of V as well, resulting in forming carbide-derive-carbon (CDC) materials.[95, 183] The Raman spectra (Figure 69d) for the V_2AlC MAX phase exhibits sharp peaks at 158 (E_{2g}), 239 (E_{2g}), 258 (E_{1g}), and 360 (A_{1g}) cm^{-1},[151, 155, 156] while for the *m*-V_2CT_x exhibits broader peaks at 379, 495, 630, 800, 1040, 1364, and 1594 cm^{-1}. This broadening of peaks for *m*-V_2CT_x is attributed to the large interlayer spacing,[151] and the assignment of all the Raman vibrations can be found elsewhere.[183] Amongst the various vibrations, the Raman peak at 800 cm^{-1} corresponds to two-dimensional V_2CT_x MXene with terminal functional groups (F, OH),[151] which typically appears around 750 cm^{-1} for bulk VC carbide.[151] Also, we track the changes on the surface of *m*-V_2CT_x using X-ray photoelectron spectroscopy (XPS) (Figure 69e). The peak centered at ~513.3 eV (V^{2+}) evidences both the presence of unreacted V_2AlC MAX phase and the V-C phase from the V2p and C1s region, respectively. The peak centered at ~ 516.3 eV (V^{4+}) is attributed to the existence of a monolayer of vanadium oxide on the surface of vanadium carbide.[98] Details of the deconvoluted XPS spectra in the C1s and O1s region be found in Figure 31. The N_2-physisorption study (Figure 69f) of *m*-V_2CT_x shows a surface area of 10.25 m^2/g and H3-type

adsorption-desorption trajectory with a hysteresis loop (P/P_0 = 0.5-1.0) distinctive for macroporous and layered materials.[103] While the V_2AlC (MAX phase) has a surface area of 1.50 m^2/g and no porosity.

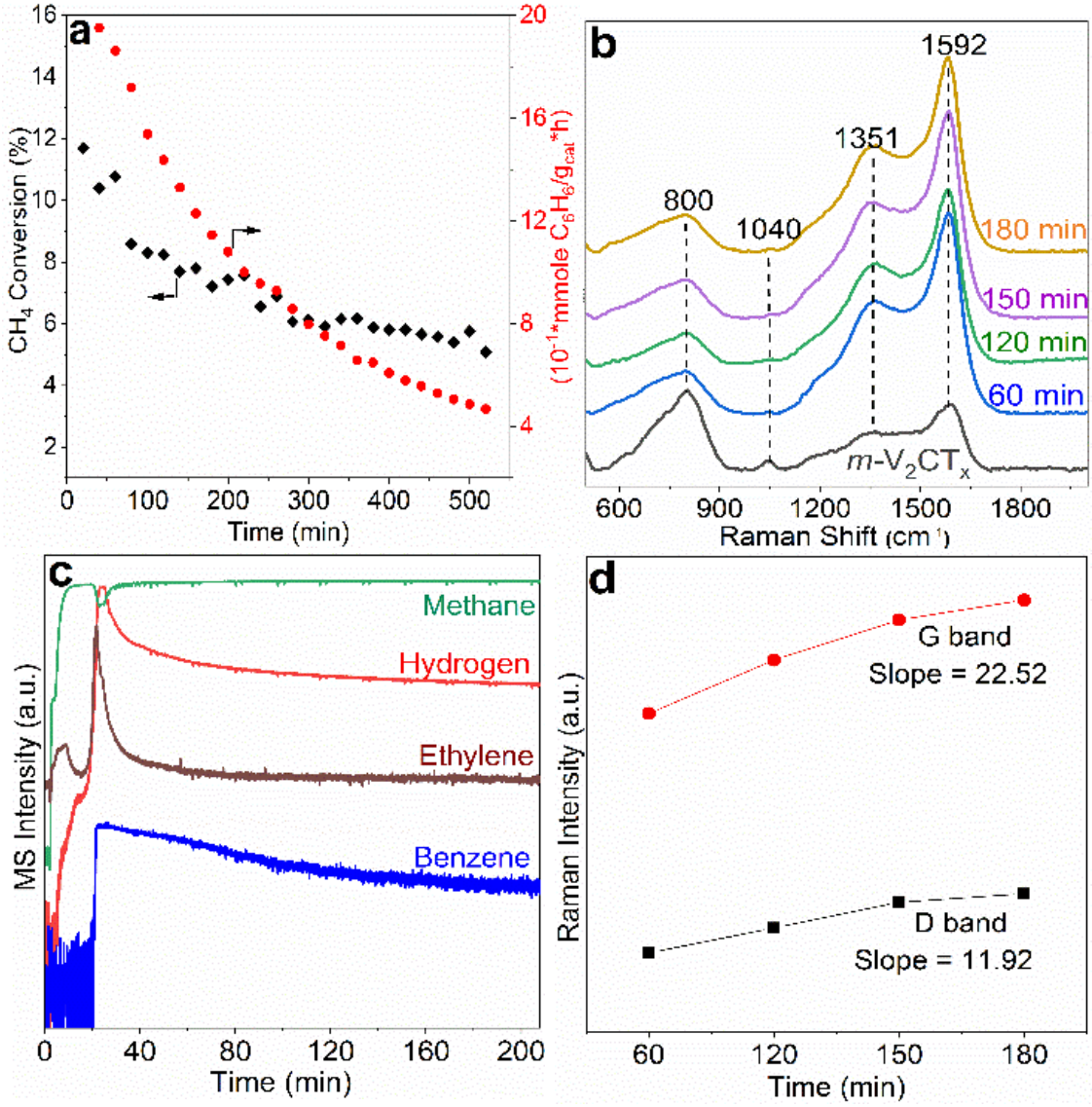

Figure 70. (a) CH_4 conversion and C_6H_6 formation rates over *m*-V_2CT_x MXene. (b-c) *Operando* Raman -MS plot (d) Relative rate of D (1351 cm^{-1}) and G (1592 cm^{-1}) carbon formation as a function of TOS at 700 ^0C.

5.2.1 steady-state kinetics

After confirming the formation of *m*-V_2CT_x, we explored its catalytic activity in MDA under industrially attractive conditions and specifically focused on benzene formation (Figure 70). As shown in Figure 70a, the rate of formation of C_6H_6 initially has a maximum formation rate of 1.9 mmol C_6H_6/g_{cat}.h at 11.8 % CH_4 conversion, which decreases as a function of time up to 0.4 mmol C_6H_6/g_{cat}.h in about ten hours. Similar deactivation trend is observed when using Mo/ZSM-5 catalyst (Figure 71), although with higher magnitude (2.3 to 1.1 mmol C_6H_6/g_{cat}.h within seven hours). The C_6H_6 yield for both catalysts can be found in Figure 72

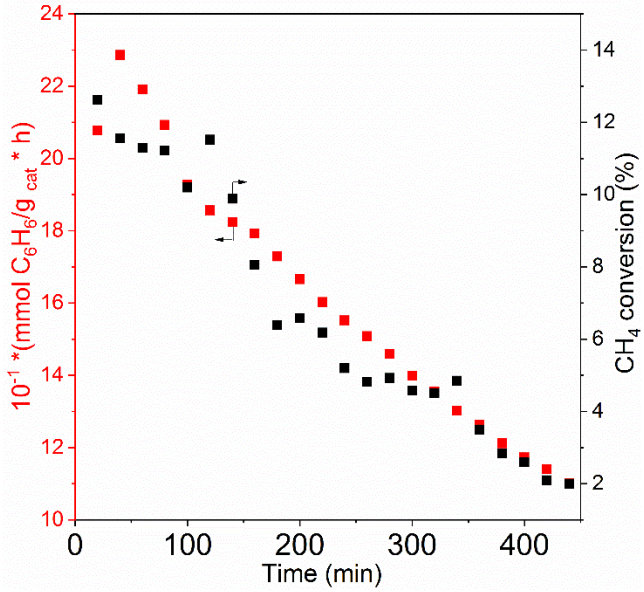

Figure 71. CH_4 conversion and C_6H_6 formation rates over 6Mo/ZSM-5 catalysts. Catalyst mass 0.2g, T=700°C, CH_4= 50%.

The C_6H_6 yield for the MXene (4.84%) is comparable to 6Mo/ZSM-5 (5.76%) around 12% CH_4 conversion (Figure 72). The MXene exhibits ~42% C_6H_6 selectivity against 6Mo/ZSM-5 catalyst which exhibits ~50% C_6H_6 selectivity. Such selectivity has already been reported for Mo/ZSM-5 catalysts around 12% CH_4 conversions.[57] Such a comparable catalytic performance highlights the potential of multilayered two-dimensional MXene for MDA reaction.

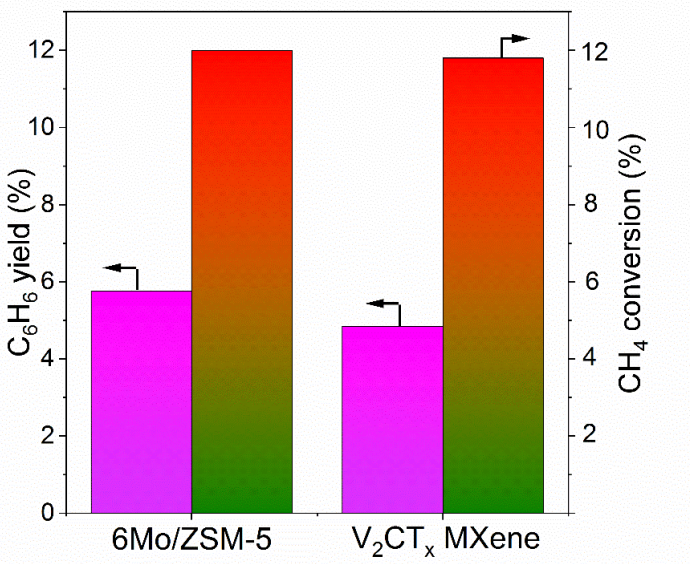

Figure 72. Initial C_6H_6 yield and CH_4 conversion for the 6Mo/ZSM-5 and V_2CT_x MXene catalyst. Catalyst mass 0.2g, T=700°C, CH_4= 50%.

On the other hand, the V_2AlC MAX phase exhibits no reactivity in MDA (Figure 73), thus proving the need for confinement to produce benzene.[4]

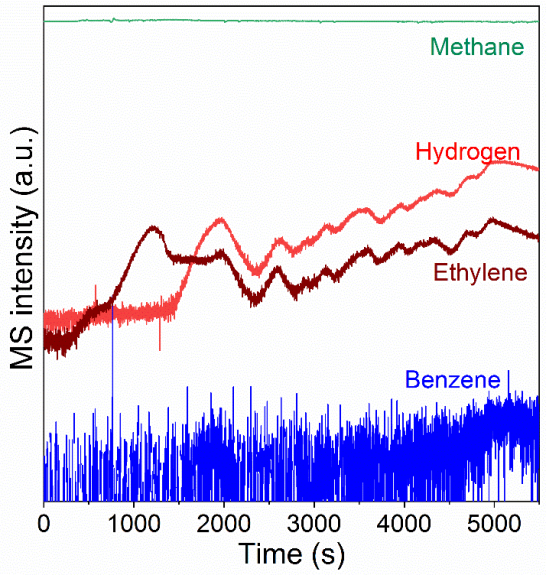

Figure 73. CH_4 conversion over the V_2AlC MAX phase catalyst. No benzene formation observed, Catalyst mass 0.2g, T=700°C, CH_4= 50%.

The V_2AlC Max phase was explored for MDA reaction (Figure 73), where after heating the material under inert (Ar) till 700°C, was subjected to 50% CH_4. Ethylene and hydrogen were recorded on a mass spectrometer, and no appreciable amount of C_6H_6 could be recorded. Thus, signaling the importance of multilayered structure for the aromatization of intermediate ethylene species to form C_6H_6.

5.2.2 *Operando* Raman spectroscopy

Operando Raman spectroscopy, evidence *i)* the presence of the 2D structure of *m*-V_2CT_x (peaks at 800 cm^{-1} and 1040 cm^{-1} assigned to 2D-VC and 2D-V=O,[183] respectively) (Figure 70b), *ii)* the formation of C_2H_4 and H_2 as the initial products followed by the formation of C_6H_6 (Figure 70c), and *iii)* the development of solid amorphous and graphitic carbon on the surface (eventually in between the layers) of *m*-V_2CT_x (Figure 70b&d). Such carbonaceous species limit the accessibility of CH_4 inside the channels, explaining the deactivation. As the reaction proceeds, the amount of C_6H_6 starts to decrease (Figure 70 a and c), which coincides with the rise of D/G carbon Raman peaks (Figure 70b). The D-carbon peak corresponds to the sp^3 amorphous carbon while the G-carbon peak is attributed to the sp^2 graphitic carbon.[183] The gradual drop in C_6H_6 can be attributed to precipitation of carbon (amorphous and graphitic) in between the layers, thereby blocking the active sites and ultimately reducing the activity of the catalyst. Figure 70c clearly shows that the formation of coke starts right from the onset of MDA reaction as the C_6H_6 and H_2 signals start to decrease.

5.2.3 Spent catalyst characterization

SEM, XRD, and XPS were performed on the spent material to further explore the deactivation process. The SEM micrographs still show up to the certain extent the multilayered structure of the material (Figure 74a), while XRD reveals that the (0002) MXene peak remarkably decreases (noise

level) and shift to a slightly higher angle (Figure 74b). The almost disappearance of this specific diffraction peak can be attributed to the deposition of carbon between the layers, while its shift is primarily due to a decrease in the lattice parameter because of dehydration.[183]

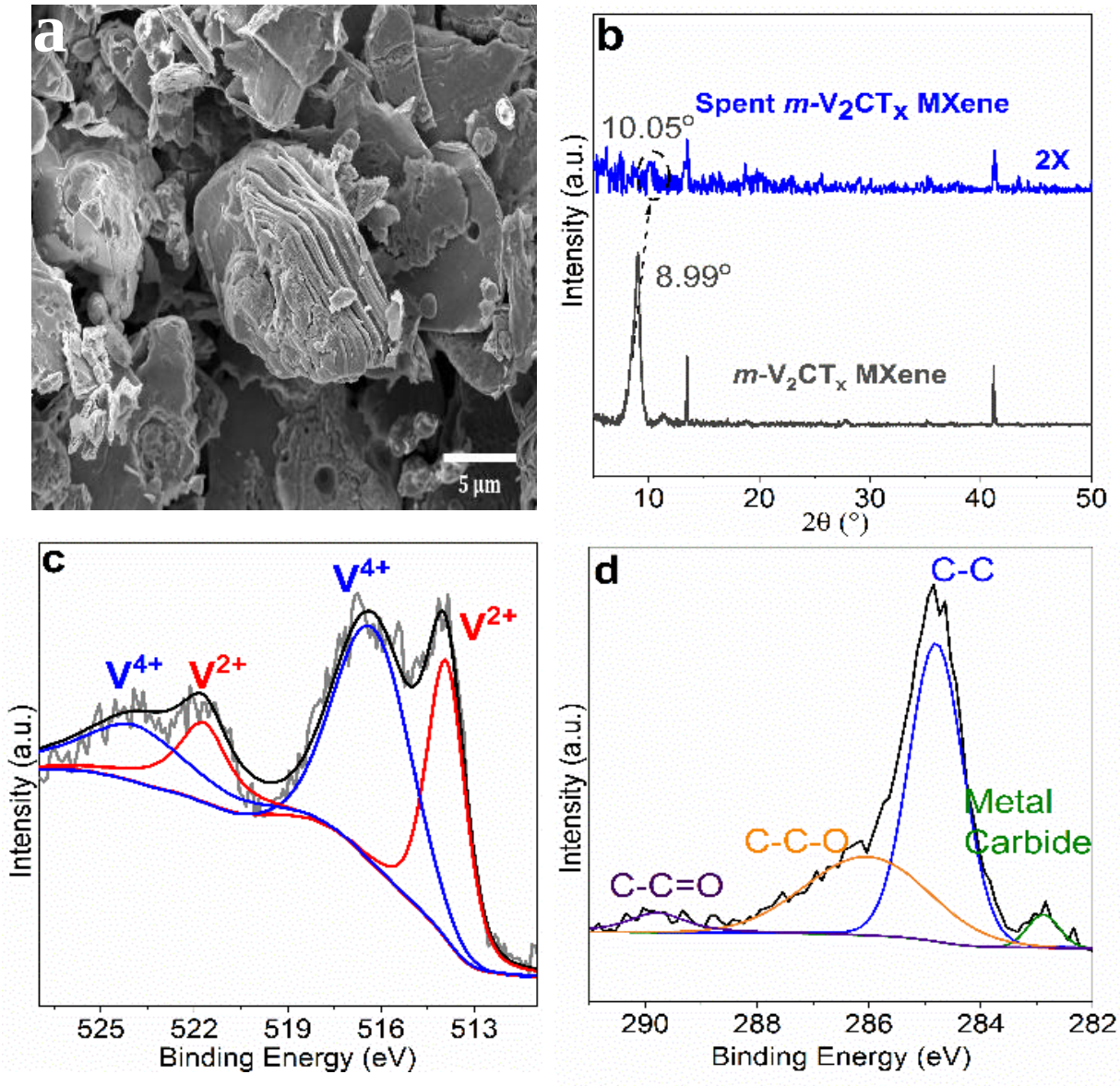

Figure 74. (a) SEM, (b) XRD, and XPS of spent *m*-V_2CT_x MXene, evidencing the excellent structural and thermal stability.

Finally, the V2p (Figure 74c) XPS spectra shows the presence of 516.3 eV (V^{4+}) and ~513.3 eV (V^{2+}) peaks, similar to Figure 69e. Additionally, the C1s spectra (Figure 74d) shows prominent C-

C (~284.8 eV) along with V-C (~282.2 eV) peaks. The C-C (~284.8 eV) peak increases relative to V-C (~282.2 eV), confirming the deposition of carbon on the surface. The N_2 physisorption profile for the spent catalyst can be found in Figure 75.

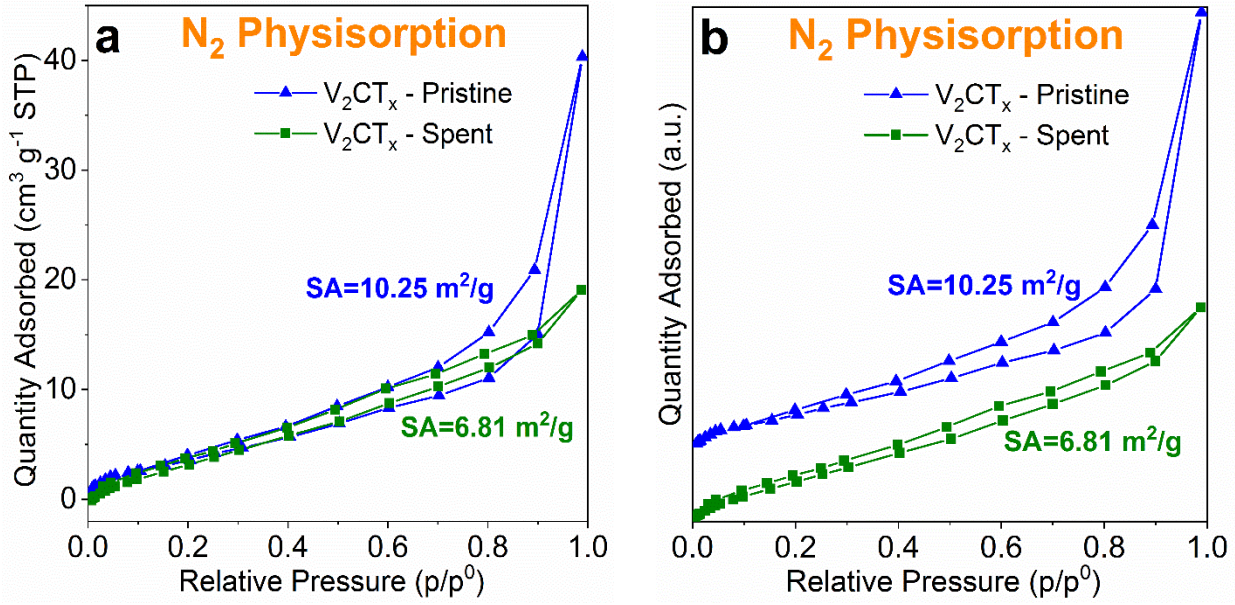

Figure 75. (a) N_2 physisorption data for the pristine and the spent V_2CT_x MXene. (b) separated adsorption-desorption profiles.

The spent V_2CT_x MXene after MDA reaction exhibits a similar H3 type adsorption-desorption trajectory. It is evident that the surface area decreases (by 33%) and the relative quantity of N_2 adsorption at the highest p/po decreases. These results demonstrate that the multilayered structure is still intact to a certain degree and the decrease in surface area is typically due to the deposition of coke in between and on the surface of the catalyst thus reducing the accessibility of N_2 inside the multilayered structure.

5.2.4 Proposed reaction mechanism

As for Mo/ZSM-5 catalyst,[4, 56, 57, 223, 224, 227] we propose that first the CH_4 is activated over metal (V-C) sites of *m*-V_2CT_x MXene, thereby forming CH_x species, which further undergoes oligomerization and dimerization through a series of gas-phase reactions in between the interlayers

yielding C_6H_6, C_2H_4 and H_2. (Figure 76). Methyl and ethyl oligomerization primarily occurring in the gas phase to yield benzene have already been reported when using Fe©SiO2 catalysts.[225]

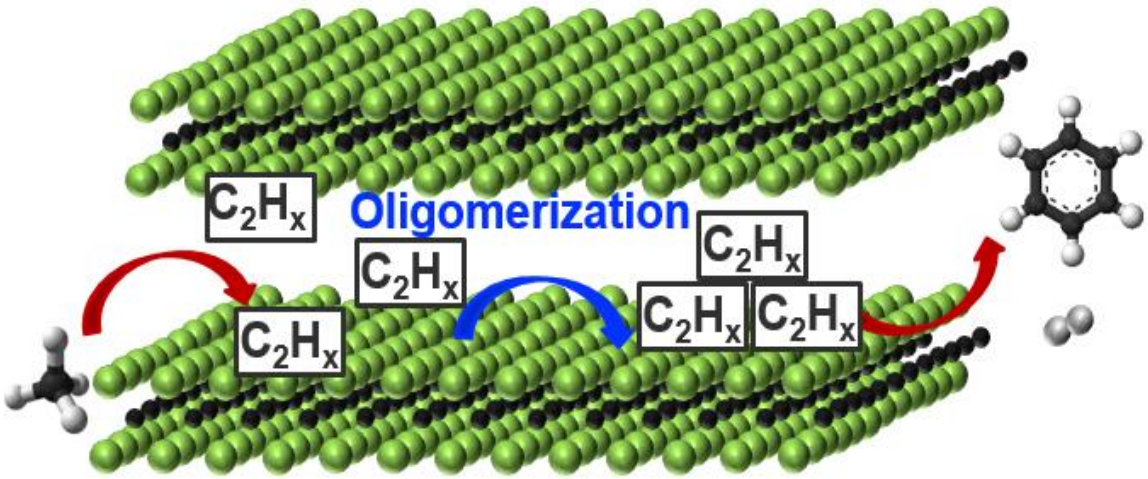

Figure 76. MDA reaction scheme over *m*-V_2CT_x MXene forming C_6H_6 and H_2 as the main reaction products.

However, the need for (weak) Lewis acid sites to catalyze the oligomerization of C2 species to form benzene has been also proposed.[84] *m*-V_2CT_x contains less, but still some, Lewis and Brönsted sites when compared to Mo/ZSM-5 (Figure 77). Such acidity can be attributed to the presence of terminal functional groups (e.g. OH and O^-) and/or due to unreacted MAX Phase within the MXene. At this point, we cannot conclusively state that solely the proposed gas-phase mechanism for MDA occurring in a confinement environment is taking place when using *m*-V_2CT_x, because it also contains acid sites, which might significantly contribute during the oligomerization of the ethyl radicals (*C_2H_3) to form benzene as proposed when using zeolite-based catalysts.[4, 57, 224]

6Mo/ZSM-5 and V_2CT_x were compared and analyzed after NH_3 TPD. The acid sites have been classified as weak (<573K), moderate (573-723K) and strong (>723K) acid peaks.[235] It is believed that for the Mo/ZSM-5, the intermediate ethylene species are aromatized over the strong (Bronsted) acid sites. So apart from the contribution from gas-phase reactions, the effect of acidity

coming from V_2CT_x MXene cannot be neglected. So, acidity exhibited from the MXene might also contribute to the aromatization.

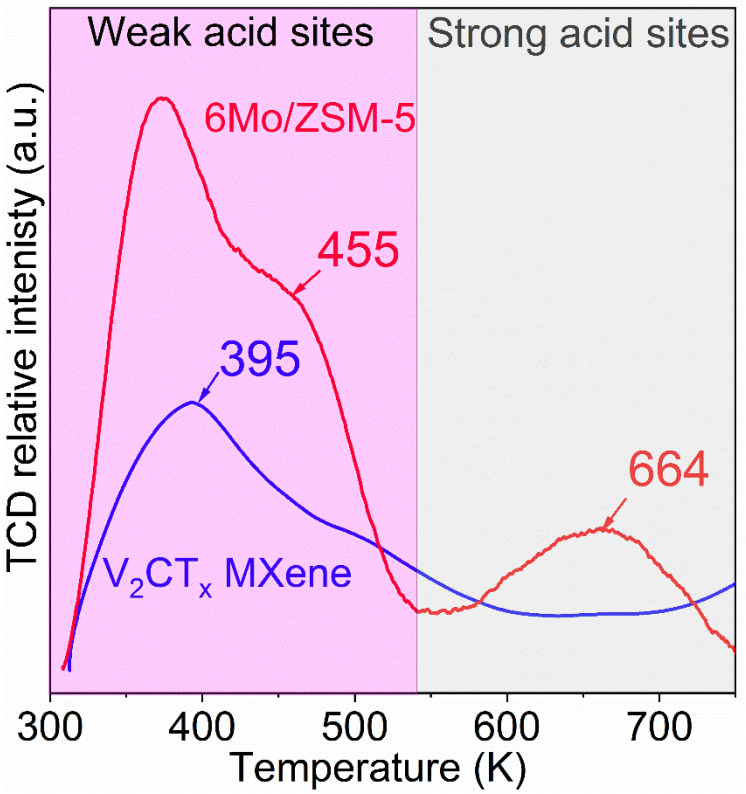

Figure 77. NH_3- TPD profiles for the Mo/ZSM-5 (red) and V_2CT_x MXene (blue).

5.3 Conclusions

In summary, it is shown that *m*-V_2CT_x MXene catalyzes the formation of benzene via MDA at 700^0C with a maximum formation rate of 1.9 mmol $C_6H_6/g_{cat}.h$ (4.84% C_6H_6 yield), which is comparable to state-of-the-art Mo/ZSM-5 catalysts (2.3 mmol $C_6H_6/g_{cat}.h$). It can be expected that this catalytic performance potentially encourages the heterogeneous catalysis community to explore the ever-growing family of MXenes in the upgrading of natural gas. The interesting properties observed by *in-situ/operando* Raman, *ex-situ* XRD, XPS and SEM for the pristine and spent *m*-V_2CT_x MXene, corroborate the remarkable and attractive stability of this material when comparing to metal-containing zeolite catalysts, which typically suffer from structural changes due

to, for instance, the expulsion of aluminum ions from the zeolite lattice forming both octahedral non-framework aluminum ion and $Al_2(MoO4)_3$.[4, 224] However, *m*-V_2CT also deactivates due to the deposition of amorphous/graphitic carbon, which remains as one of the challenges for potential industrial application. The regeneration protocol required to remove carbon from spent catalysts becomes an issue when using transition metal carbides materials because of their total-bulk oxidation.

Ongoing research on the use of MXenes for catalytic applications at relatively high temperatures (>400 ^{0}C) has resulted in developing a protocol to remove carbonaceous species and avoiding total-bulk oxidation of the layered carbide phase (Figure 66). Playing with various regeneration protocols, tuning the acidity of *m*-V_2CT_x, controlling the interlayer distance, and testing other MXenes phases are the follow-up strategies we are currently working on to gain new insights into the genesis of an alternative, suitable, and regenerable no-zeolite catalyst for MDA. Furthermore, since scaling-up the synthesis of MXenes is still an issue, primarily due to the high exothermicity of the process and the use of strong acids such as HF, researchers are currently applying a factorial experimental design to increase the production per batch without altering the intrinsic material structure and properties.

There are over twenty different MXenes that have been synthesized so far, with different and tunable structures, properties, and surface terminations, which we envision are going to broaden the applicability of MXenes either as catalyst precursors, catalysts, or catalyst supports for suitable catalytic reactions.

Chapter 6: How Controlling Pretreatment Affects the Catalytic Performance of Mo/ZSM-5 in Methane Dehydroaromatization

Abstract

Shape-selective molybdenum (Mo) containing zeolites are promising catalysts for the direct conversion of natural gas into aromatics via methane dehydroaromatization (MDA). We believe that to advance in addressing the disagreements encountered in literature, primarily those related to the structure of the active Mo-site(s) and the reaction mechanism governing MDA; we need better control over the numerous variables participating in this reaction. The complexity of this process relies on the fact that such variables influence both each individual step and the process as a whole, the *i)* pretreatment, *ii)* carburization, *iii)* reaction, and *iv)* regeneration steps operating when performing MDA. Therefore, we intend to minimize uncertainty and determine the key conditions affecting the desired performance by varying only the reacting gas and the temperature in the pretreatment step while maintaining constant all the other variables during the MDA process. Among the various pretreatment methods tested, we found that reducing the catalyst at 500 ^{0}C before the carburization step increases the rate of both methane consumption and benzene formation, which can be attributed to a greater amount of Mo-carbide species generated from Mo-oxyhydride intermediates. Therefore, we further analyzed the reduced-carburized Mo/ZSM-5 via *Operando* Raman-MS and reactivity studies. In this study, we investigated the influence of the gas-type and temperature during the pretreatment of the pristine material, which can be then used as a benchmark to continue studying the influence of the other variables during the pretreatment, carburization, reaction, and regeneration steps. We use the activity, selectivity, and stability of Mo/ZSM-5 in MDA to validate the impact of our approach and correlate such catalytic insights with the structural changes in the material.

6.1 Introduction

The challenge of converting methane (CH_4), the most abundant component in natural gas, into transportable chemicals and fuels has been incited by other evolving industrial developments, such as rapidly rising hydrogen demand and a global shortage in aromatics caused by shifting the refinery targets towards light olefins [225]. In an era of depleting natural resources, the conversion of methane into valuable products is not only economically attractive but also reduces the greenhouse gas emissions that ultimately result in improved quality of life [57].

At present, an indirect and direct route are the two catalytic approaches currently considered to convert methane. The indirect route involves the formation of *syngas*, which is then subsequently converted to valuable chemicals such as alkanes, alkenes, alcohols, gasoline, and dimethyl ether via Fischer-Tropsch or via methanol to hydrocarbon processes [4, 236]. This indirect route operates industrially but is very costly and energy intensive. On the other hand, the direct route involves processes such as oxidative coupling of methane (OCM) and dehydroaromatization (MDA), which are more economically attractive and environmental-friendly [4]. Despite decades of research, the OCM process still experiences poor selectivity/productivity towards ethylene, delaying its potential application at large scale [225]. Whereas, the MDA process experiences stability issues due to both undesired changes in the catalyst structure [4, 55, 56, 73, 90, 224, 227, 229, 237-246] and the precipitation of solid carbon (coke) [247] [4, 56, 57, 224, 225, 227, 248] under reaction conditions. The MDA reaction has recently gained interest primarily due to *i)* the ever-growing demand of aromatics [106], *ii)* the lack of on-purpose technologies to produce aromatics, especially benzene, toluene and xylenes (BTXs), propelled by the shift of shale gas as feedstocks into the cracker units [4, 224-226], and *iii)* the significant discrepancies in the literature regarding the nature of active site(s) and the possible reaction mechanism when using the benchmark Mo/ZSM-5 catalysts [227].

It has been reported that Mo species inside the ZSM-5 framework activates CH_4 forming CH_x species, which then undergo dimerization yielding C_2H_y that subsequently oligomerizes on the remaining and confined Brönsted acid sites (BAS) forming aromatics (Figure 78) [225, 227]. There is still no consensus on the nature of the active species catalyzing the MDA reaction.

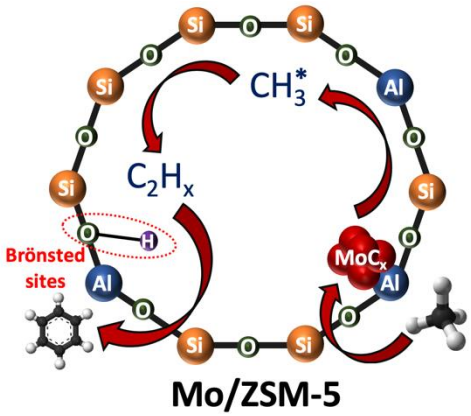

Figure 78 Proposed MDA reaction mechanisms showing the formation of methyl radicals in the MoCx sites and the oligomerization of C2Hx species on the remaining Brönsted acid sites (BAS) when using Mo/ZSM-5 catalysts.

The debate is centered primarily on whether the active species are oxide (MoO_x), carbide (MoC_x), and/or oxy-carbide (MoC_xO_y), and if they are originated either from $(MoO_2)^{2+}$ monomers or from $(Mo_2O_5)^{2+}$ dimers [227]. However, there is an agreement that the Mo-sites located in the internal framework of ZSM-5 are active while the Mo residing on the external surface is inactive [56, 223, 231, 249].

Aiming to improve the activity in MDA, various studies focused either on support effects or the use of promoters. For instance, MCM-22 [250], ITQ-2 [69], HZRP-1 [251] FSM-16 [64], SiO_2, Al_2O_3 [64], HMCM-22 [65], HMCM-36 [66], HMCM-49 [67], HMCM-56 [68], ITQ-2 [69], ITQ-13[70], IM-5 [71], and TNU-9 [72] have been used as supports, whereas Pt [85], Cu [252], Fe [236], V [253], Ni [254], Ga [255], Co [254] have been used as promoters. It was found that promoting Mo/ZSM-5 with Fe relatively improves stability [57], although we believe that there is room for further improvements. Aiming to improve the

performance of Mo/ZSM-5 in MDA, we primarily focus on identifying the processes and the most relevant variables to eventually decode the complexity of this reaction. We recognized that four individual processes are integrated to perform MDA, which are *i)* pretreatment, *ii)* carburization, *iii)* reaction, and *iv*) regeneration (Table 3). It has been reported that the pretreatment of the pristine catalyst influences the catalytic activity of Mo/ZSM-5 in MDA [57] [256]. However, these studies were performed *ex-situ* (originated carbide material is exposed to air while transferring to the MDA reactor) which in our view complicates an accurate determination of the surface species desired to produce the desired MoC_x phase. Moreover, we also noticed in literature that when varying the pretreatment conditions to improve the performance and compare with other studies, the variables, such as temperature, feed-composition, residence time, and others were not normalized while performing the carburization, reaction and regeneration steps. To gain insights from this complex combination of processes and variables, we believe that a factorial design of experiments is required to determine the key variables influencing the performance of Mo/ZSM-5 and advance in the fundamental understanding of the MDA process. Furthermore, other studies are focused on the *in-situ* removal of H_2 to improve the MDA performance [257-259]. For instance, membrane technologies [257] and the use of zirconium (Zr) as a selective hydrogen absorbent [260] has been proposed to enhance the conversion of methane.

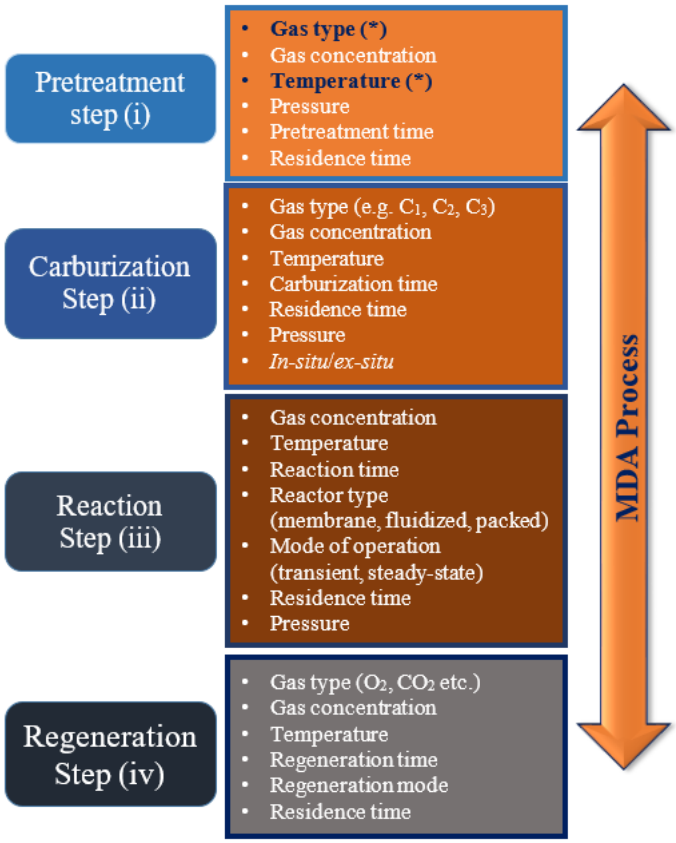

Table 3 Process steps and operational variables operating when performing MDA. (*) Variables that were varied in this study while maintaining constant the others.

In this current study, we investigate the structure of Mo-species confined inside ZSM-5 using Operando Raman-Mass spectroscopy, X-ray diffraction (XRD), X-ray photoelectron spectroscopy (XPS), thermogravimetric analysis (TGA), and temperature-programmed reduction (TPR). First, we validate the position of the MoO_x species within the ZSM-5 framework in the pristine catalyst using *in-situ* Raman spectroscopy. Then, various pretreatment experiments were performed, varying both the gas and the temperature based on the lessons learned from literature. By maintaining constant the conditions during the carburization and reaction steps, we found that reducing Mo/ZSM-5 at 500 ^{0}C enhances the rate of methane consumption (~ 1.2 *m*molCH_4 mol_{Mo}^{-1} s^{-1}) and benzene formation (~ 2.4 *m*molC_6H_6 mol_{Mo}^{-1} s^{-1}). We suggest that this is due to the

formation of a greater amount of MoC_x species after carburizing the reduced material. Finally, *operando* Raman and stability studies of the reduced material confirm that the initial structure of the catalysts (MoO_x/ZSM-5) is restored. After investigating the first parameter of a "home-made" factorial experimental design, our ongoing studies are focused on using the reduced material to then *in-situ* modify the variables in the carburization step (temperature, gas type, and composition, reaction time, residence time) while maintaining the same conditions during the reaction and the regeneration steps. When completing this approach, we envision to have sufficient data on the structure and reactivity of Mo/ZSM-5 that can be more accurately and easily compared.

6.2 Experimental and material characterization techniques

6.2.1 Catalyst preparation

The 6 wt.% Mo/ZSM-5 catalyst was prepared employing incipient wetness impregnation using ammonium heptamolybdate $(NH_4)6Mo_7O_{24}.4H_2O$ (Alfa Aesar, 99.9%) and ZSM-5 zeolite, CBV 2314 (Zeolyst Internatonal) having a Si/Al ratio of 23. The catalyst after impregnation was dried overnight at room temperature and further ramped to 120^0C at 1^0C/min with a hold time of 5 h. Subsequently the catalyst was calcined in flowing air (Airgas, UHP grade) by ramping to 500^0C at 1^0C/min with a total hold time of 2 h.

6.2.2 X-ray diffraction

The structure of the synthesized Mo/ZSM-5 catalyst was characterized using a Proto X-ray diffractometer with 40 kV and 40 mA Cu Kα radiation in using 0.2 sec/step. Around 20 mg of sample was loaded in the small cavity of the sample holder and pressed using a glass slide

6.2.3 Nitrogen physisorption

Nitrogen adsorption isotherm measurements were performed at 77K using a Quantachrome Nova1400 equipment (t-plot analysis). BET was measured up to three times for each sample to ensure an accurate determination of the metal coverage. Briefly, samples were outgassed at 473K for 12 hours prior to performing N_2 adsorption experiments. Specific surface area (BET) was estimated from the adsorption data in the relative pressure range from 0.05 to 0.3 using the Brunauer-Emmett-Teller method.

6.2.4 X-ray photoelectron spectroscopy

XPS data were collected by AXIS Ultra DLD (delay lines detector) X-ray photoelectron spectrometer (XPS) from Kratos Analytical Ltd. The end station consisted of a fast entry load lock, sample treatment chamber (STC), and a sample analysis chamber (SAC). Treated MXene samples were analyzed in SAC under 10^{-9} Torr. A monochromatic Al Kα X-ray source was used as the photon source. High-resolution spectra were obtained for C1s and Mo3d using passing energy of 20 eV. The binding energy shifts due to surface charging were corrected using the C1s level at 284.6 eV. Core level peaks of O1s were deconvoluted by using Gaussian-Lorenzian (20%) peaks.

6.2.5 *Operando* Raman spectroscopy

Operando Raman spectroscopy was performed using a Renishaw InVia Qontor Raman Spectrometer equipped with 785, 532, and 405 nm solid-state lasers, 5, 20, 50, and 100x objectives, and a MS 20 Encoded Stage. *Operando* Raman studies were performed by coupling a Linkam CCR-1000 cell to MKS Cirrus2 Mass Spectrometer. The LiveTrack feature of the Qontor version of the InVia Raman Microscope was used to maintain the sample in focus and, therefore, more accurately correlate changes in the intensity of the Raman signals with specific chemical reactions as a function of time. For *operando* Raman studies, the sample was pretreated under reducing atmospheres using UHP gases. The reaction mixture (50% CH_4 and 50% N_2) was introduced into

the Linkam cell at a gas hourly space velocity (GHSV) of 4,800 mL g^{-1} hr^{-1}. All measurements were taken with the 405 nm laser, 2400 L mm^{-1} grating, 50x long-distance objective, and, using 10 seconds of exposure time, 50% of power, and 5 accumulations. The accumulation of Raman spectra was obtained under isothermal conditions and was ensured that the spot does not burn off due to the power of the laser, details can be found elsewhere.[183, 209]

To obtain the Raman spectra of calcined 6 wt.% Mo/ZSM-5, the catalyst (~60 mg) was loaded in a temperature-programmed Linkam CCR-1000 cell equipped with the quartz window and sealed with O rings. The catalyst was dehydrated following the procedure reported elsewhere. [224] Briefly, the sample was ramped at 1^0C/min to 500^0C with a hold time of 1 h in 30 sccm flow of 10 mol% O_2 (Airgas, UHP grade). After cooling the cell to 50^0C, the Raman spectra were collected.

6.2.6 Temperature programmed reduction

The reducibility of the catalyst was studied by hydrogen temperature-programmed reduction (H_2-TPR) in an Autosorb iQ Quantachrome instrument. Approximately 0.1 g was introduced in a quartz cell and the cell was flushed using 10 cm^3/min of Ar for 40 min at room temperature. The TPR experiments were performed using 10 vol% H_2/Ar at a flow rate of 50 cm^3/min. The consumption of H_2 was monitored using the thermal conductivity detector (TCD).

6.2.7 Thermogravimetric analysis (TGA)

The coke accumulation in the spent catalyst was analyzed using thermogravimetric analysis (TGA) (Shimadzu Scientific Instruments). The loaded TG cell was kept in dry air for ~30 min and was ramped at 10^0C/min from room temperature to 800^0C. The weight loss was used to determine the amount of coke content after the MDA reaction.

6.3 Catalytic testing

The steady-state MDA catalytic measurements were performed at ambient pressure using a stainless-steel fixed bed reactor with an internal diameter and total length of 6 mm and 450 mm, respectively. The pristine powder catalyst was pelletized and sieved at a particle size between 425 and 500 µm. A custom-made reaction set up equipped with multiple electronic GE50A MKS mass flow controllers, heating controllers, heated lines from the reactor's outlet to the GC's inlet, a Thermolyne 21100 tubular furnace which provide a isothermal heating zone of about 120 mm length, a liquid saturator isothermally heated with a chiller when liquid vapors are needed, a pressure gauge prior to the reactor inlet, and an on-line Agilent 7890B gas chromatograph (GC) equipped with three Agilent columns (HayeSep A, MolSieve, and DB-1), a flame ionization detector (FID) and a thermal conductivity detector (TCD). All the reactions were carried out at 900 K with inlet flow ratios of 50% CH_4 and 50% N_2 at 16 ml/min total flow rate, and the gas hourly space velocity (GHSV) was maintained at 4800 mL $g_{cat}^{-1} \cdot h^{-1}$. The quantification of hydrogen (H_2), nitrogen (N_2) and methane (CH_4) were done using the areas obtained by TCD, whereas hydrocarbon (C_6H_6 and CH_4) was done by using the areas obtained by FID. The duration of each GC analysis was about 20 minutes. Briefly, Method A: Oxidative pretreatment at 500^0C for 2 h; Method B: Oxidative pretreatment at 677^0C for 2 h; Method C: Reductive pretreatment at 500^0C for 2 h; Method D: Inert pretreatment till 677^0C; Method E: Heating under reaction mixture (50% CH_4 and 50% N_2). For all the pretreatment the catalyst was carburized at the reaction temperature i.e. 900K.

6.4 Results and discussions

6.4.1 catalyst characterization

The nature of MoO_x species on ZSM-5 was examined using *in-situ* Raman spectroscopy under dehydrated conditions Figure 79a). The absence of sharp signals from crystalline MoO_3 (996, and 815 cm^{-1}) and $Al_2(MoO_4)_3$ (1004 and 1045 cm^{-1}) signifies that molybdenum is completely

dispersed [224]. The sharp Raman peak at 993 cm^{-1} corresponds to the normal vibrational mode of $Mo(=O)_2^{2+}$ nanostructures anchored on double Al sites with two bridging framework O atoms, while the peak at 974 cm^{-1} corresponds to vibrational mode of $Mo(=O)_2(OH)^+$ nanostructures anchored on single Al sites on ZSM-5 framework [224]. The weak signals at 950 and 1029 cm^{-1} indicate the presence of some mono-oxo $(Si\text{-}O\text{-})_4Mo(=O)$ structures that are anchored on defect sites generated from Si or Al framework vacancies [224]. The absence of a peak at 984 cm^{-1} signifies the lack of $Mo(=O)_2$ dioxo species as $(Si\text{-}O\text{-})_2Mo(=O)_2$ on the external surface of ZSM-5, indicating that all the Mo-species are anchored in the internal framework [224]. Further, to understand the degree of reducibility of the Mo-species, H_2-TPR studiers were performed (Figure 79b). The H_2-TPR peaks between 200 and 400 ^0C are attributed to the reduction of amorphous polymolybdates, whereas the peaks between 400 and 600^0C correspond to the reduction of octahederaly coordinated Mo^{6+} species to Mo^{4+} species. Finally, the peaks above 600 ^0C represent the reduction of Mo^{4+} into metallic Mo^0 [239, 261, 262].

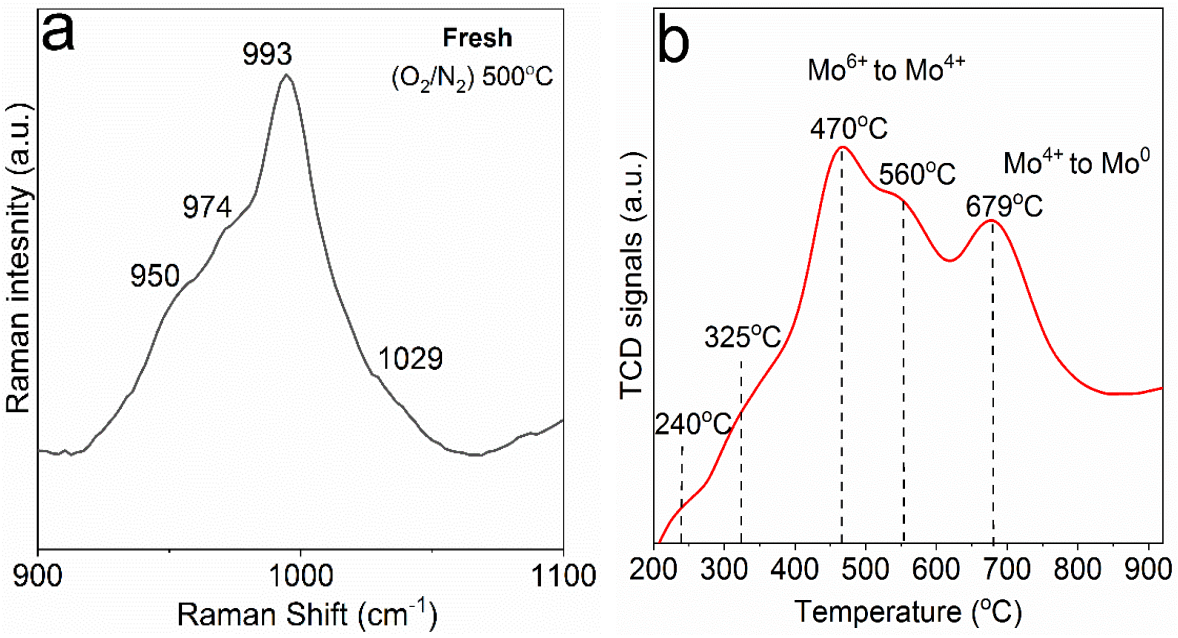

Figure 79 (a) In-situ Raman spectra (405 nm) and (b). H_2-TPR profile of fresh Mo/ZSM-5 catalyst under dehydrated conditions.

6.4.2 In situ Pretreatment and activity of 6% wt. Mo/ZSM-5

Treating the pristine MoO_x/ZSM-5 using different methodologies and then performing carburization and MDA reaction under similar conditions results in specific rates for methane consumption and benzene formation, as shown in Figure 80.

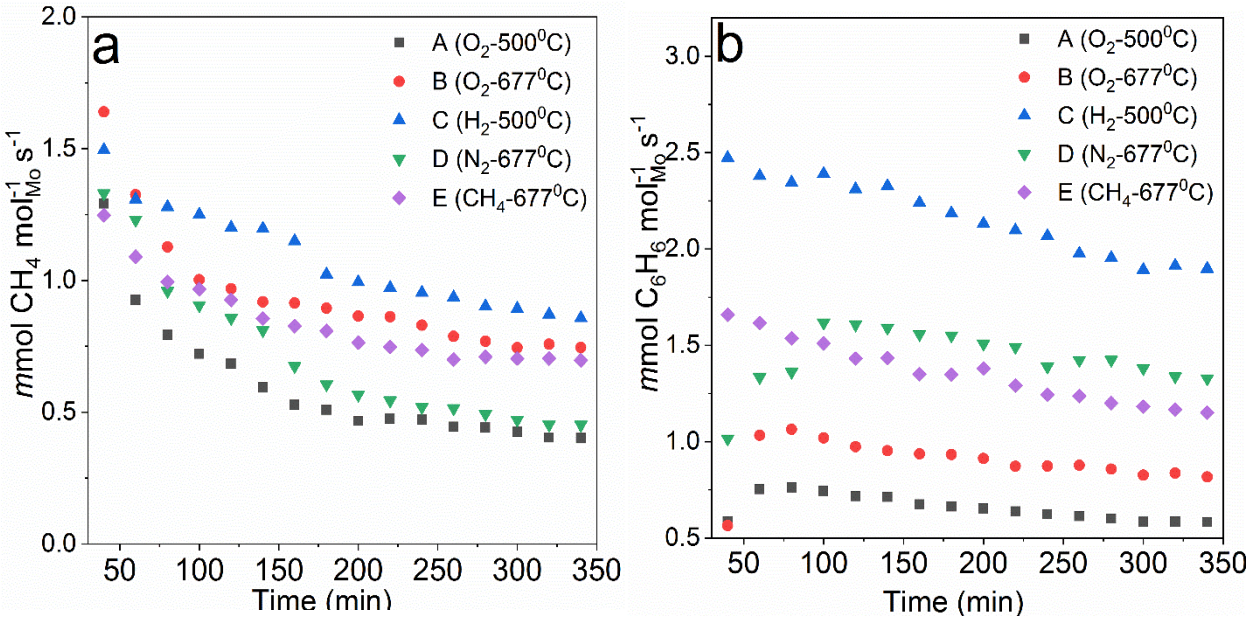

Figure 80 (a) Methane conversion and (b) benzene formation rates over 6 wt% Mo/ZSM-5 undergoing different pretreatment methods as a function of time. Pretreatment A: Oxidation at 500^{0}C for 2 h. Pretreatment B: Oxidation at 677^{0}C for 2 h. Pretreatment C: H_2 Reduction at 500^{0}C for 2 h. Pretreatment D: Inert till 677^{0}C. Pretreatment E: Heating under reaction mixture (50% CH_4 and 50% N_2)

Interestingly, the activity of the material does not change as much as the selectivity toward benzene when varying the pretreatment method. Reducing the pristine material for 2 hours at 500 ^{0}C with pure H_2 (method C) improves the rates for both methane consumption and benzene formation to ~ 1.2 *m*mol CH_4 mol_{Mo}^{-1} s^{-1} and ~ 2.4 *m*mol C_6H_6 mol_{Mo}^{-1} s^{-1}, respectively. This is due to the topotactic transformation of Mo species from the hexagonal close-packed (hcp) into the face-centered cubic (fcc) structure [263-269], where the latter (α-MoO_xC_y) is desired for MDA [263]. On

the other hand, the oxidation pretreatments show the lowest performance, especially for the formation of benzene. This is because when oxidizing at 500 ^{0}C (method A), Mo is present in its highest oxidation state (Mo^{6+}) [224], which primarily transforms into (hcp) β-MoO_xC_y during the carburization step [263]. While, pre-oxidation at 677 ^{0}C (method B) additionally leads to the expulsion of the Al sites from the ZSM-5 lattice, forming undesirable $Al_2(MoO_4)_3$. Indeed, a general finding is that the Mo/ZSM-5 is not stable under oxidative conditions [223]. The similar reactivity and selectivity observed when Mo/ZSM-5 is treated with N_2 and CH_4, which is not as attractive as when reducing the material, is because the carburization process will primarily form (hcp) β-MoO_xC_y [263]. A graphical representation of the above-mentioned structural transformations that Mo/HZM-5 undergoes under different pretreatment is depicted in Figure 82. The formation rates of benzene as a function of pretreatment follow the trend; reductive > inert > oxidative, which leads to the formation of α-MoO_xC_y, β-MoO_xC_y, and $Al_2(MoO_4)_3$, respectively. The benzene yields can be found in the Figure 81. In summary, these studies served to select the reductive pretreatment (method C) to further investigate the performance of α-MoO_xC_y/HZM-5 using *operando* Raman spectroscopy.

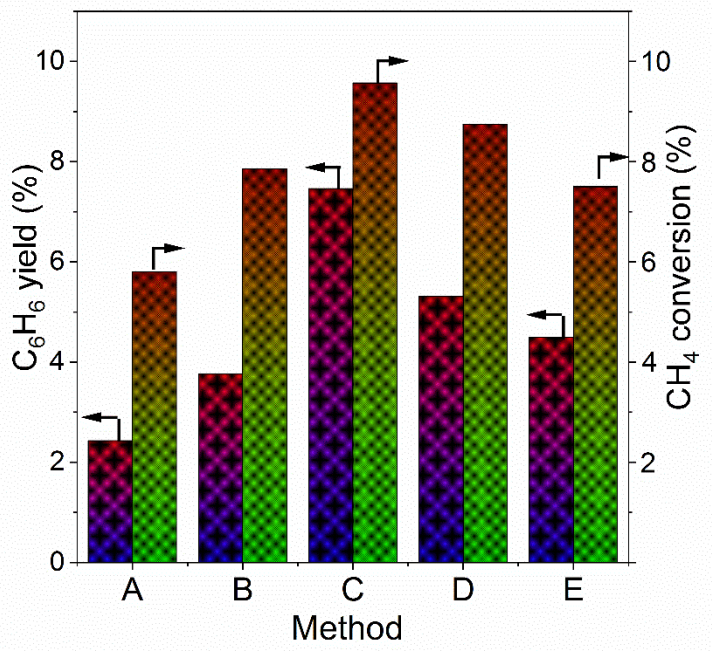

Figure 81. C_6H_6 yield and CH_4 conversion after 2 h TOS using different pretreatment methodology.

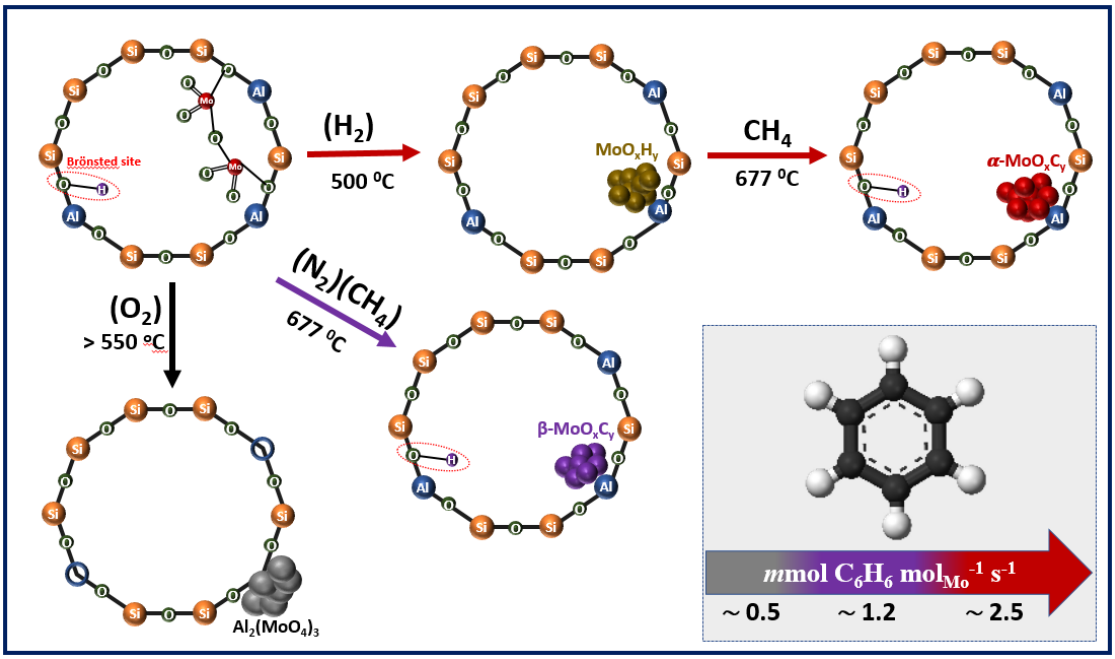

Figure 82 Graphical representation of the different pretreatments Mo/ZMS-5 undergoes prior to performing carburization and MDA reaction. The insert highlights the benzene formation rates as a function of Mo oxycarbide phase ($Al_2(MoO_4)_3$, β-MoO_xC_y, and α-MoO_xC_y.

6.4.3 Operando Raman Spectroscopy and stability of reduced 6% wt. Mo/ZSM-5

The dynamic changes in Mo nanostructures during the reductive pretreatment (method C), followed by carburization, MDA reaction, and regeneration steps, were tracked using *operando* Raman-MS (Figure 83). Upon reducing the catalyst with H_2 at 500^0C for 2 h, the sample was completely flushed using argon, to then raise the temperature up to 677^0C and perform the carburization with 50% CH_4. The formation of CO_2 almost immediately after adding CH_4 evidence the transformation of MoO_x into α-MoO_xC_y species [263], which ends in about 20 min (CO_2 formation terminates). Then, the initiation of the MDA reaction is evidenced by the formation of ethylene and benzene (Figure 83a). When reducing the pristine material, Raman spectroscopy shows the disappearance of the peak at 993 cm^{-1} (Figure 83b-*ii*), typically assigned to Mo sites anchored on dual Al sites inside the ZSM-5 framework (Figure 83b-*i*). As the reaction progresses, the rise of 1173, 1379, and 1593 cm^{-1} peaks indicate the formation of carbonaceous polyaromatic species, which also reveals the production of aromatic products (Figure 83b-*iii*) [224].

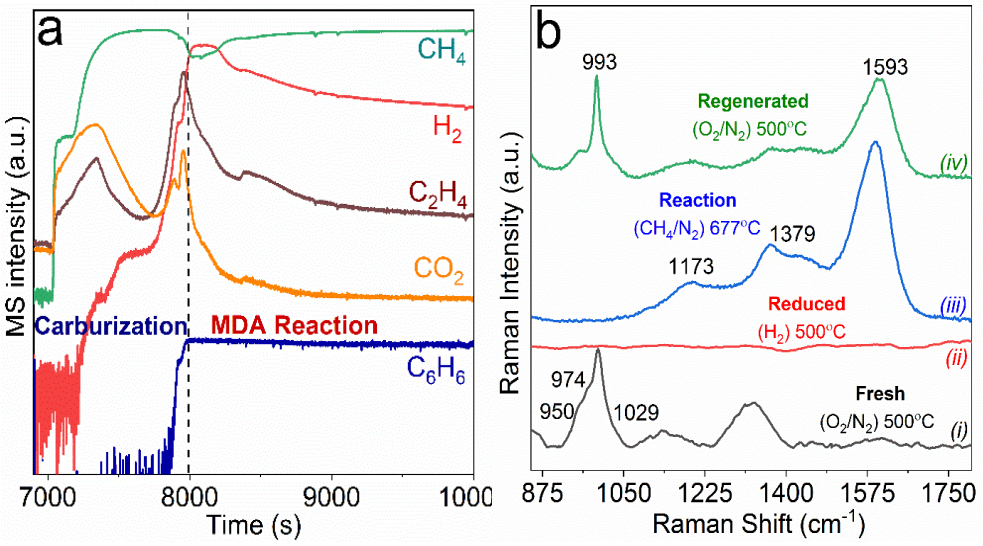

Figure 83. Simultaneous mass spectroscopy (a-b) operando Raman spectroscopy (405 nm) as a function of TOS for 6Mo/ZSM-5 catalyst under MDA conditions using reductive pretreatment (method C). (a) MS plot evidencing the formation of CO_2 during the carburization step, followed

by a rise in C_6H_6 signals. (b) Operando Raman plots of the catalyst under different stages of MDA cycle.

Finally, the catalyst was regenerated at 500^0C for 100 minutes after performing MDA for about six hours using the conditions reported by Gao et al. [224]. The rationality behind using this condition is to restrict the anchoring of Mo to dual Al sites, avoiding its migration to either single Al site or (external) Si. Interestingly, after regenerating the spent material (using 5 mol% O_2), the α-MoO_xC_y/ZSM-5 transforms back to dispersed (anchored on dual Al sites) Mo/ZSM-5, as evidenced by the reappearance of the prominent Raman peak at 993 cm^{-1} (Figure 83b-*iv*). The disappearance of the peak at 974 cm^{-1} after regeneration also signifies that Mo is primarily anchored to dual Al sites. Nevertheless, the formed polyaromatic carbonaceous species are not totally oxidized (peak at 1593 cm^{-1}) when the spent material is regenerated under this specific condition. This is in line with previous studies inferring the complexity of the MDA mechanism, where confined carbonaceous species are also essential to convert methane into aromatics [56]. Our Raman studies also suggest that the amount of such remaining carbonaceous species is low because the vibrations of Mo sites anchored to dual Al sites (993 cm^{-1}) and defects sites (950 and 1029 cm^{-1}) are still noticeable.

To evaluate the catalyst stability under reductive pretreatment, the α-MoO_xC_y/ZSM-5 catalyst formed after the reduction and carburization steps (steps *i* and *ii*), was exposed to MDA conditions for relatively long time-on-stream (~ 40 hours) including two regeneration steps (Figure 84a). The activity of the material remains the same after each regeneration step, corroborating the *operando* Raman findings about the transformation of α-MoO_xC_y into MoO_x species anchored in dual Al sites. Also, the similar deactivation trends for the three cycles depicted in Figure 84a evidences the reversibility of the changes in the catalyst structure when exposed to reduction, carburization,

and MDA conditions. Interestingly, although still decreasing as a function of time, a slight improvement in the benzene formation rate when comparing the fresh and regenerated catalyst (Figure 84b) validates the presence of primarily Mo anchored to dual Al sites (absence of Mo anchored to single Al sites), which is the desired precursor to produce α-MoO_xC_y species after performing

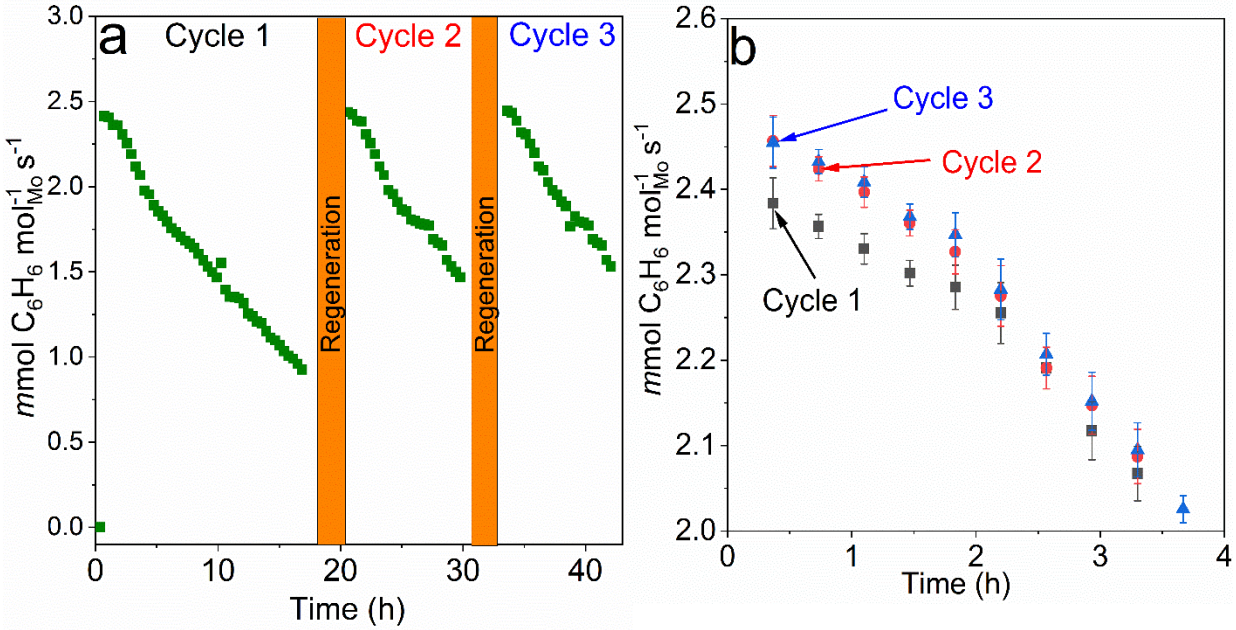

Figure 84 (a) Stability test of catalyst following reductive pretreatment (Method C) (b) benzene formation rates comparison for the fresh and regenerated catalyst evidencing the effect of regeneration time and conditions

reduction-pretreatment and carburization. Furthermore, the remaining confined carbonaceous species after the regeneration step also enhances the rate of formation of benzene [56], which after about 1.5 hours, decreases following a similar trend due to an increase in the amount of precipitated carbon. Therefore, a desired synergistic effect when having confined α-MoO_xC_y and an optimal amount of carbonaceous species enhance the rate of formation of benzene (Figure 85).

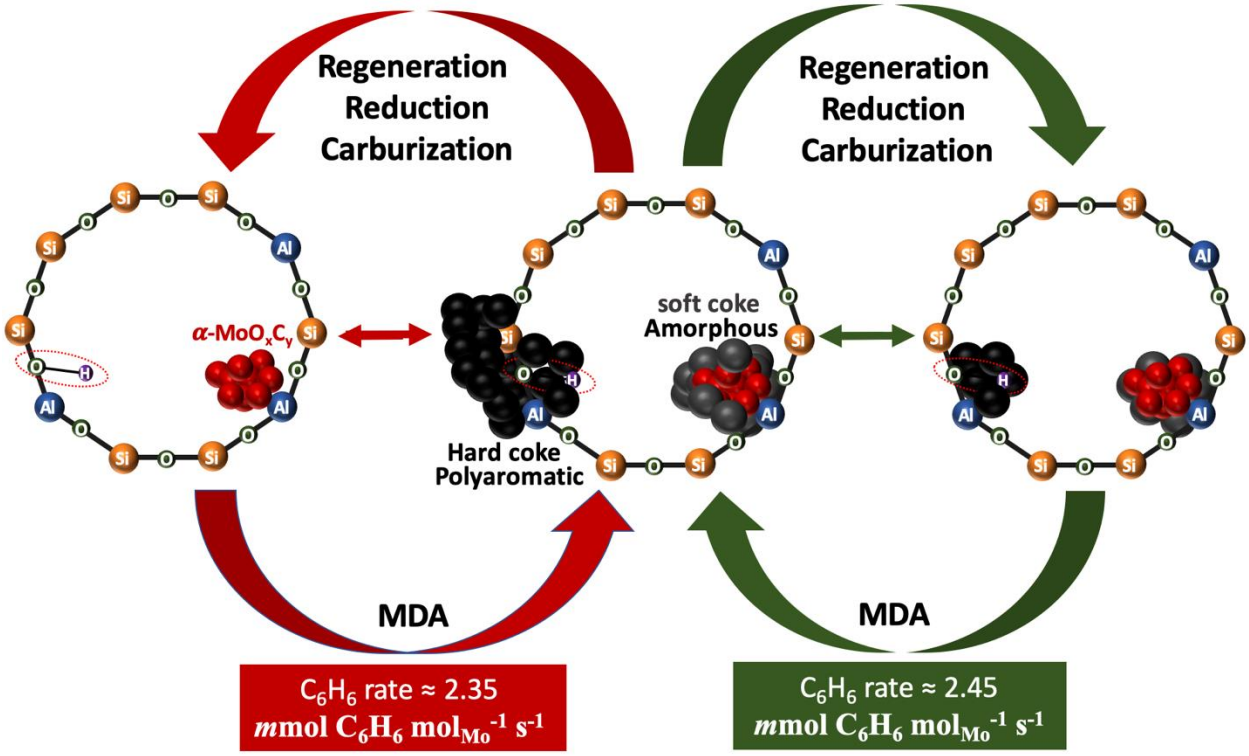

Figure 85 Schematic representation highlighting the importance of confined carbon species to enhance the benzene formation rate. Soft amorphous carbon growing on the Mo-carbide clusters and hard polyaromatic coke growing on BAS have been proposed elsewhere [256, 270, 271].

6.4.4 Structure-reactivity relationships for MDA over Mo/ZSM-5

The type and amount of carbonaceous species formed during the MDA reaction can either positively or negatively influence the performance. Therefore, we combine surface and bulk sensitive characterization techniques such as Raman spectroscopy, XPS, TGA, N_2-physisorption, and XRD to check the relative amount and type of carbonaceous species to eventually correlate with the activity.

No matter the pretreatment methodology, the formation of carbonaceous species during MDA is unavoidable as corroborated by the Raman peaks centered at 1173, 1379 (amorphous carbon, D band), and 1593 cm^{-1} (polyaromatic carbon, G band) (Figure 87a). However, the ratio between graphitic and amorphous carbon (I_g/I_d ratio) changes with pretreatment methodology. The

oxidative pretreatments (method A and B) have the smallest I_g/I_d ratio ~1 and the larger amount of amorphous carbon, which can be attributed to the migration of Mo sites from the internal to the external framework, resulting in the formation of amorphous-carbon over $Al_2(MoO_4)_3$ [256]. On the other hand, the reductive and inert pretreatments (methods C and D) show I_g/I_d higher than one, and because dealumination does not occur under these conditions, such a higher ratio is due to the generation of graphitic carbon over BAS within the ZSM-5 framework. While the largest I_g/I_d ratio (~ 5.7) is obtained when the catalyst is pretreated directly under reaction mixture (method E) due to favorable methane cracking rather than carburization when heating the catalyst.

TGA studies show a rise in weight while heating the spent material under air between 300 and 450^{0}C, indicating the oxidation of Mo-carbide to MoO_x species following reaction (1) [57, 272-274]. A subsequent loss in weight when raising the temperature from 450 to 750^{0}C indicates the burning of amorphous and/or graphitic carbon deposited on the catalyst (reaction 2) (Figure 86).

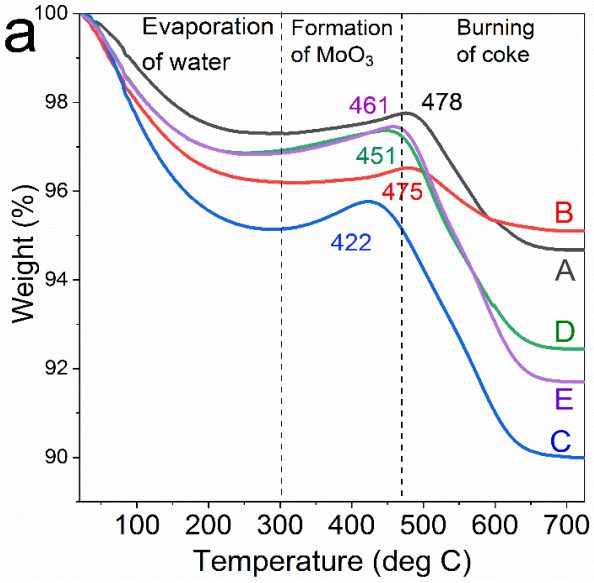

Figure 86 (a) TGA profiles evidencing the regions of weight gain and weight loss for the spent catalysts following different pretreatment methodology.

$$2Mo_2C + 7.5O_2 \rightarrow 4MoO_3 + CO_2 + CO \qquad (1)$$

$$C\ (coke) + O_2 \rightarrow CO_2 \qquad (2)$$

Figure 87b shows the correlation between Mo-carbide and amorphous/graphitic carbonaceous species with pretreatment method, after performing carburization and MDA reaction. The catalysts pretreated under oxidation conditions (methods A and B) produce less amount of both Mo-carbide and carbonaceous species, as compared to the inert and reductive pretreatments (methods C, D, and E). Interestingly, the reductive pretreatment (method C) shows the maximum rise in weight, indicating that MoO_xH_y intermediates generate a greater amount of Mo-carbide species, primarily α-MoO_xC_y. (reactions 3 and 4) [264, 265, 269].

$$MoO_3 + H_2 \rightarrow MoO_xH_y + H_2O \qquad (3)$$

$$MoO_xH_y + CH_4 \rightarrow \alpha\text{-}MoO_xC_y + H_2O + CO_2 \qquad (4)$$

This explains the better performance of this material since α-MoO_xC_y activates methane, which then couples into C2 species follow by its aromatization over BAS [263]. Among the various pretreatment methods, the reductive pretreatment shows that α-MoO_xC_y oxidizes at a lower temperature (Figure 86). This can be because of different Mo-oxycarbide species (α-MoO_xC_y, β-MoO_xC_y, $Al_2(MoO_4)_3$) or Mo-oxycarbide morphology (size, dispersion, shape, location) are generated depending on the pretreatment.

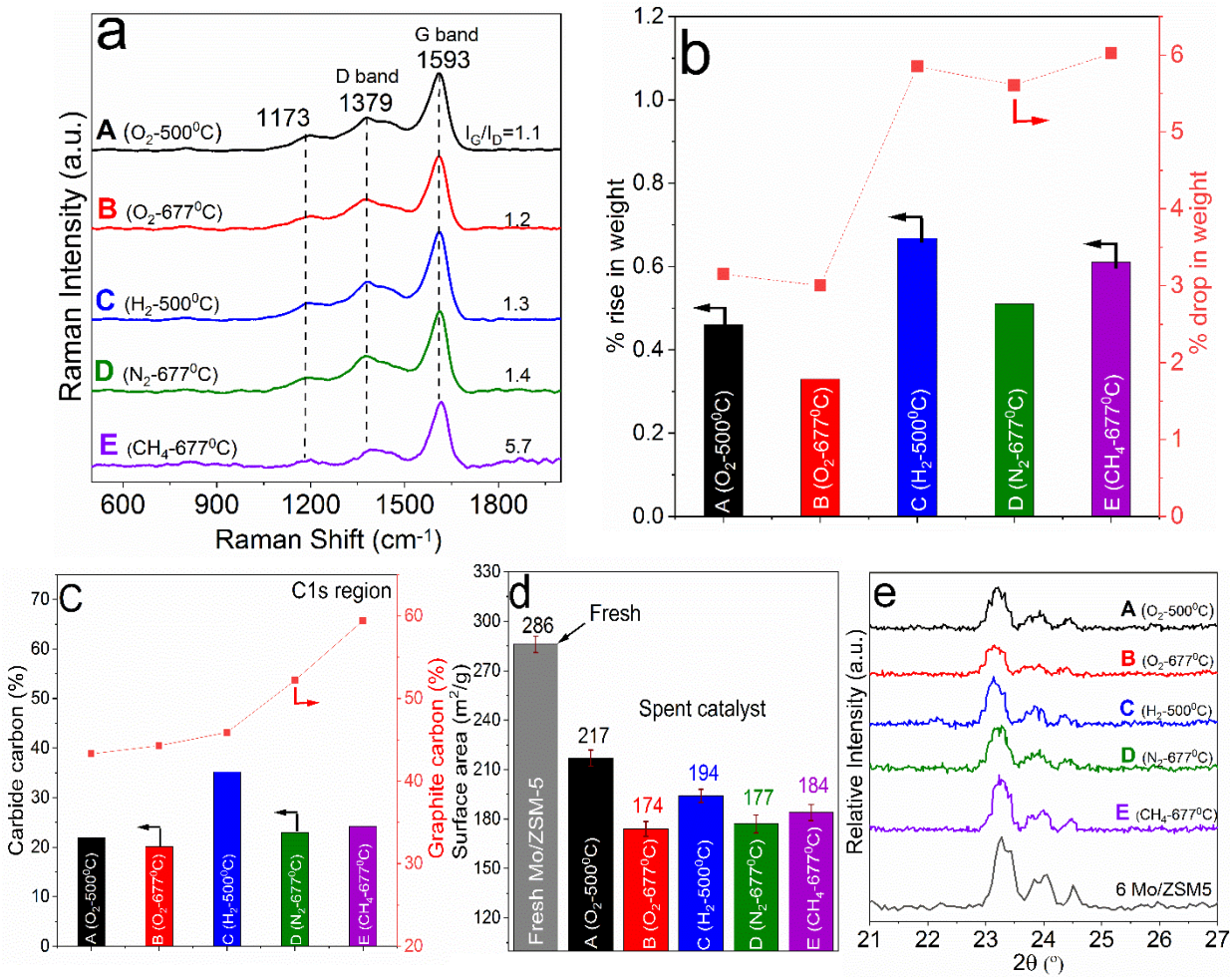

Figure 87 (a) Raman spectra (405nm), (b) TGA plot, (C) XPS spectra, (d) Surface area, and (e) XRD diffractogram of the spent catalyst following different pretreatment methodology.

X-ray photoelectron spectroscopy (XPS) provides insights to differentiate carbon as Mo-carbide and graphitic carbon (Figure 87c) [90, 275, 276]. Deconvolution of the C1s regions confirms that primarily two types of carbon species are present on the spent catalysts, *viz.* 284.6 eV for the graphitic carbon (C-C) and at 283.5 eV for the carbide carbon (Mo_2C) (Figure 88) [90, 91]. While the reductive pretreatment (method C) yields the maximum amount of carbide carbon (35.2%), so-called α-MoO_xC_y [263], the method E (24.2%), method D (22.9%), method A (21.9%) and method B (20.2%) yield β-MoO_xC_y [263]. This is in line with both the rise in the weight of the spent catalysts

observed in TGA studies (Figure 87b) and the higher formation rate of benzene. Furthermore, when observing the C1S XPS region (Figure 87c), the trend in the relative amount of graphitic carbon (284.6 eV) matches with the I_g/I_d ratio measured via Raman spectroscopy (Figure 87a) as a function of pretreatment methodology.

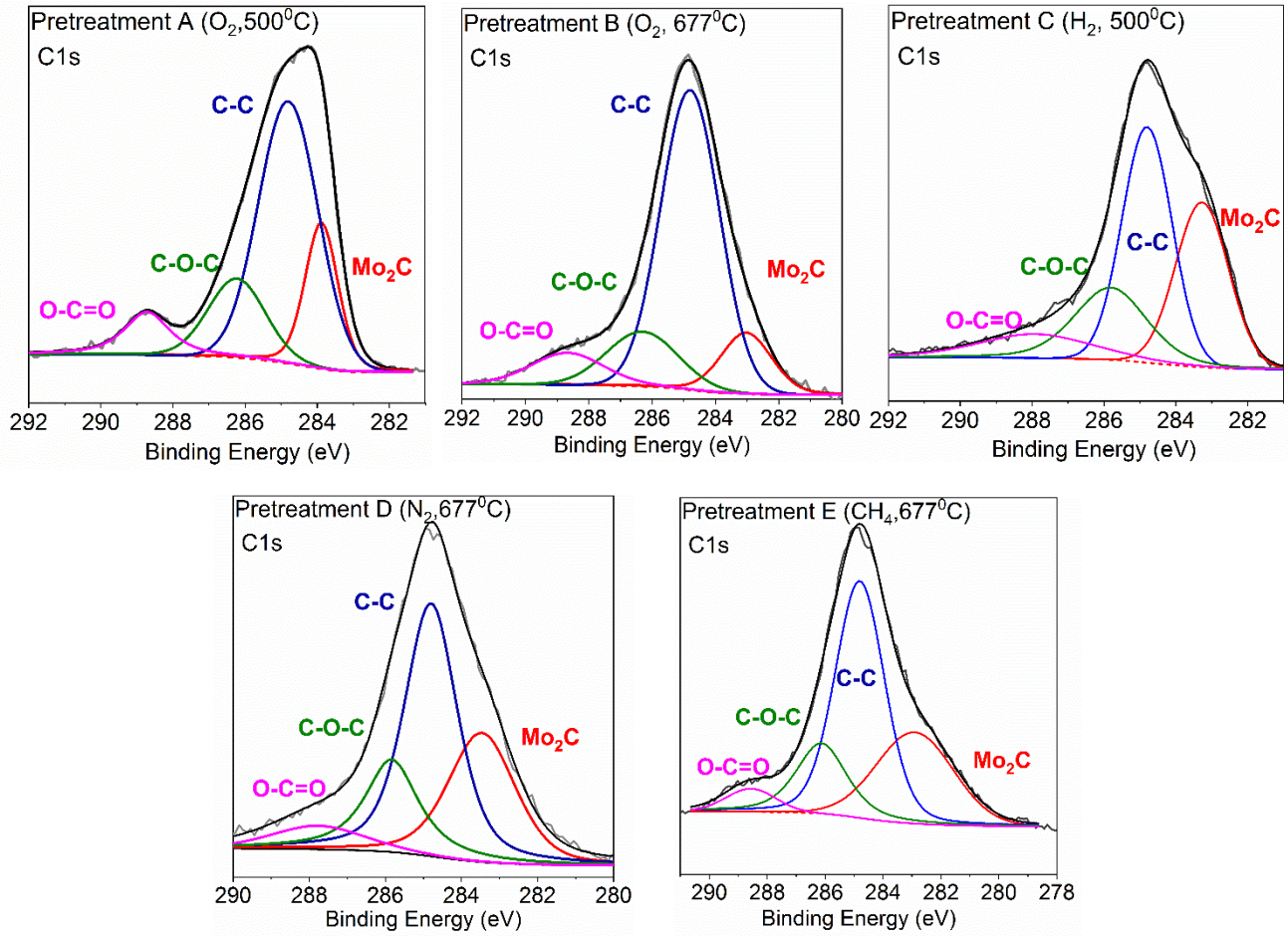

Figure 88 (a) XPS profiles evidencing the regions of carbide and graphite carbon for the spent catalysts following different pretreatment methodology.

Combining N_2-physisorption and XRD studies further correlate the catalytic activity with the structural changes in the catalyst (Figure 89). Regardless of the pretreatment, the surface area of the spent material decreases, primarily due to the formation of solid carbon within the external and internal framework of ZMS-5. While pretreatment A shows the smallest drop in the surface area (from 286 to 217 m^2/g (24%)) because the lower generation of solid carbon as depicted in Figure

87b, the pretreatment B shows the largest drop in surface are (from 286 to 174 m^2/g (~39%)), primarily due to structural damage caused by dealumination and formation of $Al_2(MoO_4)_3$ on the external framework. Interestingly, when reducing the pristine Mo/HZM-5 (method C), the surface area falls from 286 to 194 m^2/g (~30%), which is in agreement with reported studies [57] and also corroborates the formation of less amount of graphitic carbon deposited on the external framework (Figure 87c) [263]. The methods D and E show a similar drop in surface area as compared to method B, but herein the surface area is decreased primarily due to the deposition of graphitic carbon (blocking the pores) and not due to structural damage. Such a hypothesis is further corroborated by the higher percentage amount of graphitic carbon observed in XPS (Figure 87c).

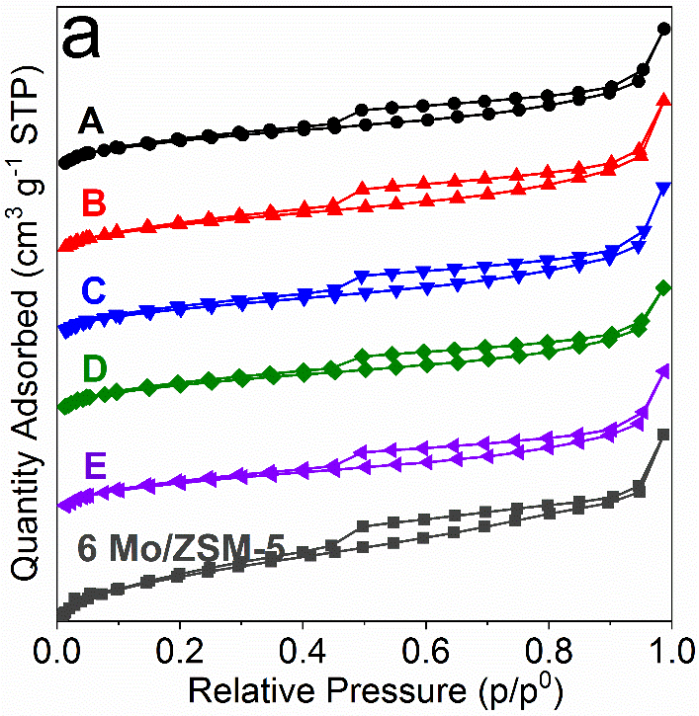

Figure 89 (a) Nitrogen adsorption-desorption profiles of fresh and spent catalysts following different pretreatment methodology.

All the spent catalysts exhibit diffraction peaks similar to the pristine Mo/ZSM-5 catalyst (Figure 87e), indicating the persistence of the ZSM-5 structure. However, a loss in crystallinity is observed

(peaks between 2θ of 23 and 25) under oxidative pretreatments at high temperatures (methods A and B) [223], which is in line with surface area (Figure 87d) and reactivity.

6.5 Conclusions

The direct conversion of remote natural gas into transportable liquid fuels and chemicals remains a daunting technological challenge, and the MDA process still appears to be an attractive and feasible alternative. The various steps (pretreatment, carburization, reaction, and regeneration) operating in the MDA process, which each of them inherently relies on the tuning of several variables (Table 1), evidences the complexity of this process. Herein, we found that the reduced state-of-the-art Mo/ZSM-5 catalyst shows a rate of benzene formation and methane consumption of ~ 2.4 *m*molC_6H_6 mol_{Mo}^{-1} s^{-1} (7.5 % C_6H_6 yield) and ~ 1.2 *m*molCH_4 mol_{Mo}^{-1} s^{-1} (9.6% CH_4 conversion), respectively. This performance is remarkably better when using other pretreatment protocols. The reduction pretreatment leads to a larger quantity of Mo-carbide species (α-MoO_xC_y) as corroborated by XPS and TGA studies. Future XAS studies will be carried out to investigate the geometrical and electronic structure of such α-MoO_xC_y species.

By combining kinetic and spectroscopic, we found that both the identity of Mo nanostructures and the carbonaceous deposits on the ZSM-5 catalyst influences the catalytic activity. First, it is crucial to control the anchoring of MoO_x primarily on dual Al sites residing inside the ZSM-5 internal framework, which under reductive pretreatment transform into MoO_xH_y, thereby generating a larger amount of α-MoO_xC_y during carburization, and secondly, a small amount of the confined carbonaceous species is also important to enhance the rate of formation of benzene. While identifying the parameters influencing the MDA reaction, we realized that the complexity of this process requires the implementation of a factorial experimental design that needs to be

complemented with *operando* characterization techniques to advance in the discovery of both optimal catalysts and reaction conditions to perform MDA at industrial scale.

Chapter 7: Conclusions, proof of concept, and recommendations for future studies

7.1 Conclusions from research

This dissertation extensively focuses on the designing, synthesis, and characterization of heterogeneous catalysts (especially 2D metal carbides) for developing structure-reactivity relationships when upgrading natural gas into valuable chemicals and fuels. Primarily in upgrading methane (CH_4), the most abundant component of natural gas into aromatics (benzene) and to *syngas* (CO and H_2). This work focuses on newly discovered two-dimensional multilayered vanadium carbides (V_2CT_x) MXene as a promising precursor, support, and/or catalyst for various other catalytic applications at relatively high temperatures (≥ 500ºC).

Insights related to the thermal and chemical stability of V_2CT_x MXene under different environments reveal that the multilayered structure persists up to certain extent under inert (N_2) and reducing (H_2) environments while observing partial oxidation (V_2CT_x decorated with V_2O_3) in the presence of CO_2 and undergoes total oxidation in the presence of air (V_2CT_x transform into V_2O_5). The results from this study were published in *RSC Nanoscale Journal (IF=6.97)* (*Nanoscale 11 (2019) 10716).*

Comprehending the performance of V_2CT_x MXene under different environments, V_2CT_x was investigated for catalytic applications, where such reducing and inert conditions exist. Further study was concentrated on the reactions which face challenges towards industrialization due to issues related to the catalyst stability and selectivity. The performance of V_2CT_x MXene for dry reforming of methane (DRM) and methane dehydro-aromatization (MDA), the two most important reactions which if industrialized would lead to the tremendous reduction in global energy footprints, as the current industrially process to produce these chemicals are very energy-intensive.

The state-of-the-art Ni and Pt-based catalysts to convert CH_4 via DRM are far from industrialization due to following concomitant reason: *(i)* rapid coke deposition over the active sites, *(ii)* involvement of regeneration step to burn up the carbonaceous deposits, and *(iii)* the sintering of the active metallic species as result of severs process conditions. Regarding MDA, the major challenges to address are related to the stability of the state-of-the-art Mo/ZSM-5 catalyst that undergoes irreversible structural changes under reaction conditions.

Under DRM conditions, it was revealed that the V_2CT_x MXene serves as a precursor to generating V_2O_3-V_8C_7/*m*-V_2CT_x material, which is highly active towards sintering and coking, the two major challenges which the state-of-the-art Ni-based catalyst faces until today. This study provides kinetic, structural, and mechanistic insights into the genesis of *m*-V_2CT_x MXene as a selective and coke-resistant catalyst converting about 78% CH_4 and 82% CO_2 with CH_4 and CO_2 conversion rates of $153.4\ mmol_{CH_4} mol_V^{-1} min^{-1}$ and $178.2\ mmol_{CO_2} mol_V^{-1} min^{-1}$ respectively. These results are comparable to Ni-based catalysts and are about four times higher than its bulk counterparts V_2AlC MAX phase and VC. This coke-resistant MXene-based catalyst follows an *in-situ redox* mechanism where V_2O_3 transforms into V_8C_7 and *vice versa.* This *redox* mechanism was corroborated by combining kinetics with isotopic labeled studies using $^{13}CH_4$ and $^{13}CO_2$. The research article related to this study are published in the prestigious high impact factor *ACS Catalysis Journal (IF=12.2).*

Additionally, it was also discovered that if we exploit the confined spaces found in the multilayered structure, important catalytic reactions could be executed, where the confinement effect is the key. MDA was analyzed with V_2CT_x MXene, a reaction that depends on confinement spaces provided by the state-of-the-art Mo containing zeolite-based catalysts. Our studies show that the V_2CT_x MXene can efficiently convert CH_4 into C_6H_6, with yields close to 5%. These results are already

online in *ChemCatChem journal (IF=4.5)* (*doi.org/10.1002/cctc.201902366)*, a very important journal in the field of catalysis. *This article was selected by the reviewers as a Highly Important Paper* and will be showcased in the Wiley Journal family as an important work in the field of catalysis

Apart from MXenes, we also focused on the state-of-the-art Mo-zeolite catalysts for MDA reaction The challenges to address the disagreement in the current literature about both the structure of the active Mo-site(s) and the reaction mechanism governing MDA is the lack of control over the numerous variables participating in this reaction. The complexity of this process relies on the fact that such variables influence, both individually and overall, the *i)* pretreatment, *ii)* carburization, *iii)* reaction and *iv)* regeneration steps. Therefore, in our work, we intend to minimize uncertainty and determine the key conditions affecting the desired performance by varying only the gas and the temperature in the pretreatment step while maintaining constant all the other variables during the MDA process. It was found that the pretreatment of the catalyst plays an important role in the catalytic activity of the catalyst. The results from this study are already submitted in and are under the peer review cycle.

The knowledge accumulated using V_2CT_x MXene catalysts, our group envision to further expand by developing metal oxide-based catalysts supported on silica. To prove the concept, supported vanadium catalyst on silica were prepared, and the carburization methodology was applied. The data generated to date shows that the knowledge which was produced from MXenes based catalysts is also applicable to other catalyst and further will be valuable in developing catalysts for industrially attractive reactions. Furthermore, a paper on “A review on the catalytic applications of MXenes” is being worked upon.

7.2 Proof of concept

The DRM mechanisms highlighted from the presented dissertation evidence that a mixture of V_2O_3 and V_8C_7 nanostructures supported over a MXene material are the active species responsible for an industrially attractive and stable performance. Moving ahead with this hypothesis and keeping in mind the mechanism described, it could be possible to design such systems over well-defined metal oxide supports such as SiO_2, Al_2O_3, ZrO_2, etc.

An extensive literature survey was conducted, and to the best of our knowledge, we could not find any paper which reported supported vanadium oxide as a catalyst for the DRM. So, our group is the first to explore the catalytic activity of supported vanadium oxide under DRM conditions. Since most of the DRM literature and advancements are focused on using noble metals and Ni-based catalysts. Furthermore, when the supported metal catalysts are used, usually they are reduced before performing any reaction. Less focus is stress towards carburizing the supported metal oxides. A couple of hand-full of literature demonstrates the use of carburized supported metal oxides.

Therefore, using these two approaches for the first time in the scientific experimental catalytic community, we prepared supported vanadium oxides over SiO_2, carburized it, and then performed DRM kinetics to support the learnings obtained when using V_2CT_x MXene as precursors for V_2O_3 and V_8C_7 nanostructures.

The preliminary data generated using supported vanadium catalysts proves the suggested DRM mechanism, and this knowledge will be beneficial in developing industrially attractive catalysts and to move the DRM process to the industrial scale.

7.2.1 Preparation of V/SiO_2 catalysts (4 and 10 wt.% V)

The silica (Cabot Cab-O-Sil HS-5) was impregnated with ammonium vanadium oxide (Alfa Aesar 99%) (NH_4VO_3) as a source of vanadium. To improve the dissolution of NH_4VO_3 in water, oxalic acid was added, and the mixture was stirred in a heating plate for 10 minutes. The homogenous solution was then impregnated with SiO_2. More details can be found elsewhere.[277] After impregnation, the catalyst was dried in over at 110°C for 12 hours, followed by calcination in a muffle furnace at 550°C for 3 hours in flowing air. The ramp rate was 1°C/min.

7.2.2 Fresh catalyst characterization by XRD and Raman

The prepared catalysts were characterized by bulk sensitive (XRD) and surface-sensitive characterization techniques (Raman spectroscopy). The XRD diffractogram for the fresh catalyst can be found in Figure 90. Note that the $4V/SiO_2$ does not show the presence of any peak on the diffractogram, while the $10V/SiO_2$ show some V_2O_5 peaks. This indicates that the $4V/SiO_2$ does not have any oxide particles, and vanadium is well dispersed.

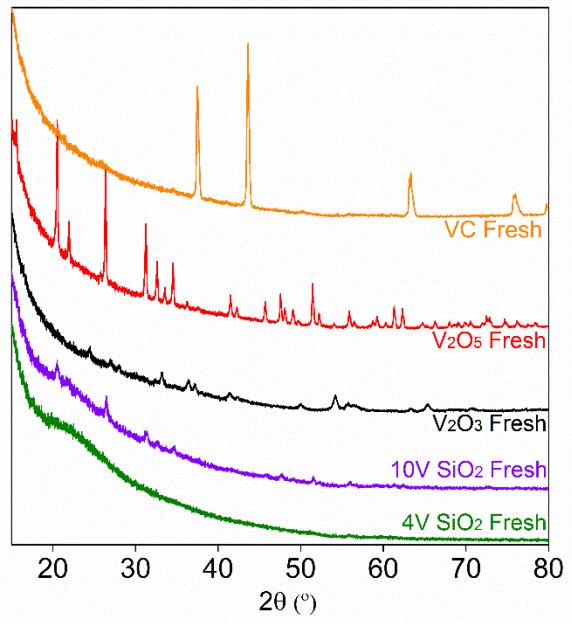

Figure 90. XRD diffractogram of the fresh catalysts ($4V/SiO_2$, $10V/SiO_2$, V_2O_3, and V_2O_5).

The Raman of the fresh catalysts was also performed to see the nature of vanadium species supported over SiO_2. Figure 91 evidences that the $4V/SiO_2$ has 2D vanadium species (Raman band at 1030 cm^{-1}), while the $10V/SiO_2$ has a mixture of 2D and 3D vanadium species (Raman band at 994 and 1030 cm^{-1}). The Raman vibration at 994cm^{-1} evidence that some V_2O_5 particles (3D vanadium) are also generated, thus corroborating the XRD data.

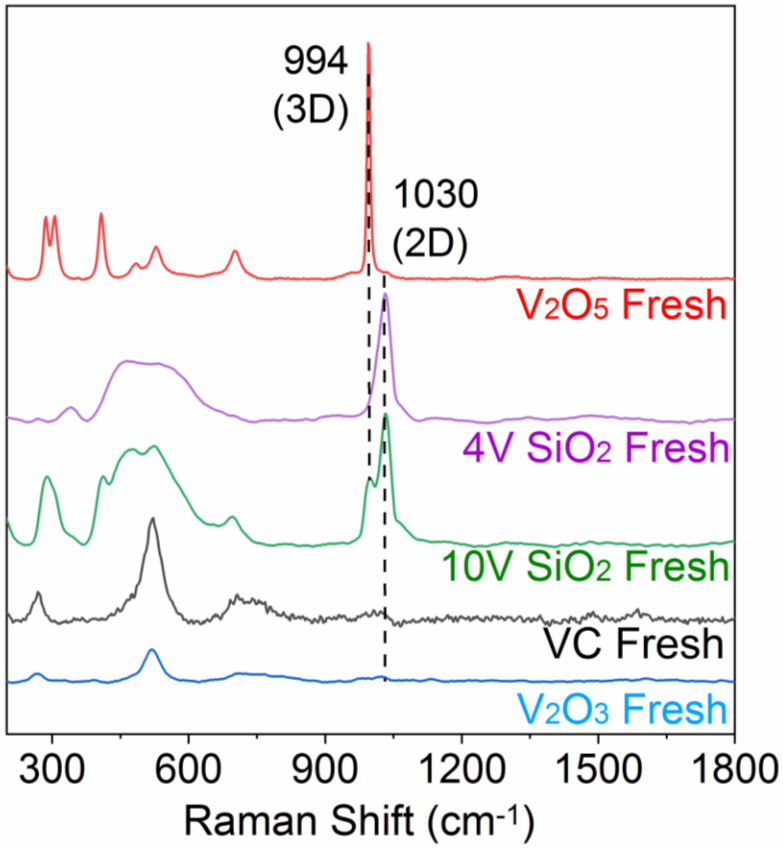

Figure 91. Raman spectra of fresh catalysts. $4V/SiO_2$ shows the vanadium as 2D nature while the $10V/SiO_2$ shows the vanadium as a mixture of 2D and 3D.

7.2.3 Steady-state kinetic testing

The catalyst after pelletizing was subjected to DRM test under the same conditions as described for the V_2CT_x MXene catalysts. For further comparison bulk, V_2O_3 and V_2O_5 were also evaluated

under similar conditions. The catalysts were heated under N_2 till 800°C and further carburized. After carburization, their performance in DRM was evaluated as shown in Figure 92. Apart from carburization, $4V/SiO_2$ was also reduced with H_2 to evaluate and compare the performance of the reduced catalyst. Usually, the supported transition metal oxide catalysts are first reduced to lower oxidation states and then utilized for the specific application.

All the catalysts were evaluated for the stability test, consisting of a carburization step in-between. It can be seen that during cycle 1, the CH_4 conversions for $4V/SiO_2$ and $10V/SiO_2$ are around 45% and 70% respectively, while the CO_2 conversion is also in similar magnitudes.

The H_2/CO ratio during cycle 1 is below 0.7 for both the catalysts. However, after performing the carburization of the catalysts, a significant gain in performance could be observed. The CH_4 and CO_2 conversion for both the catalysts reached close to equilibrium conversions, and the H_2/CO ratio stabilized at 1.0. Thus indicating that the carburization of the catalyst after cycle 1 generates structural changes in the catalyst structure, thereby improving the activity. The most significant gain was observed for the $4V/SiO_2$ catalyst. Further, the spent catalysts after each stage were analyzed using XRD and Raman spectroscopy. Separate catalytic tests were performed to get the state of the catalyst after every stage in the cycle. Thus the catalytic tests were conducted three times, and reproducible data could be generated.

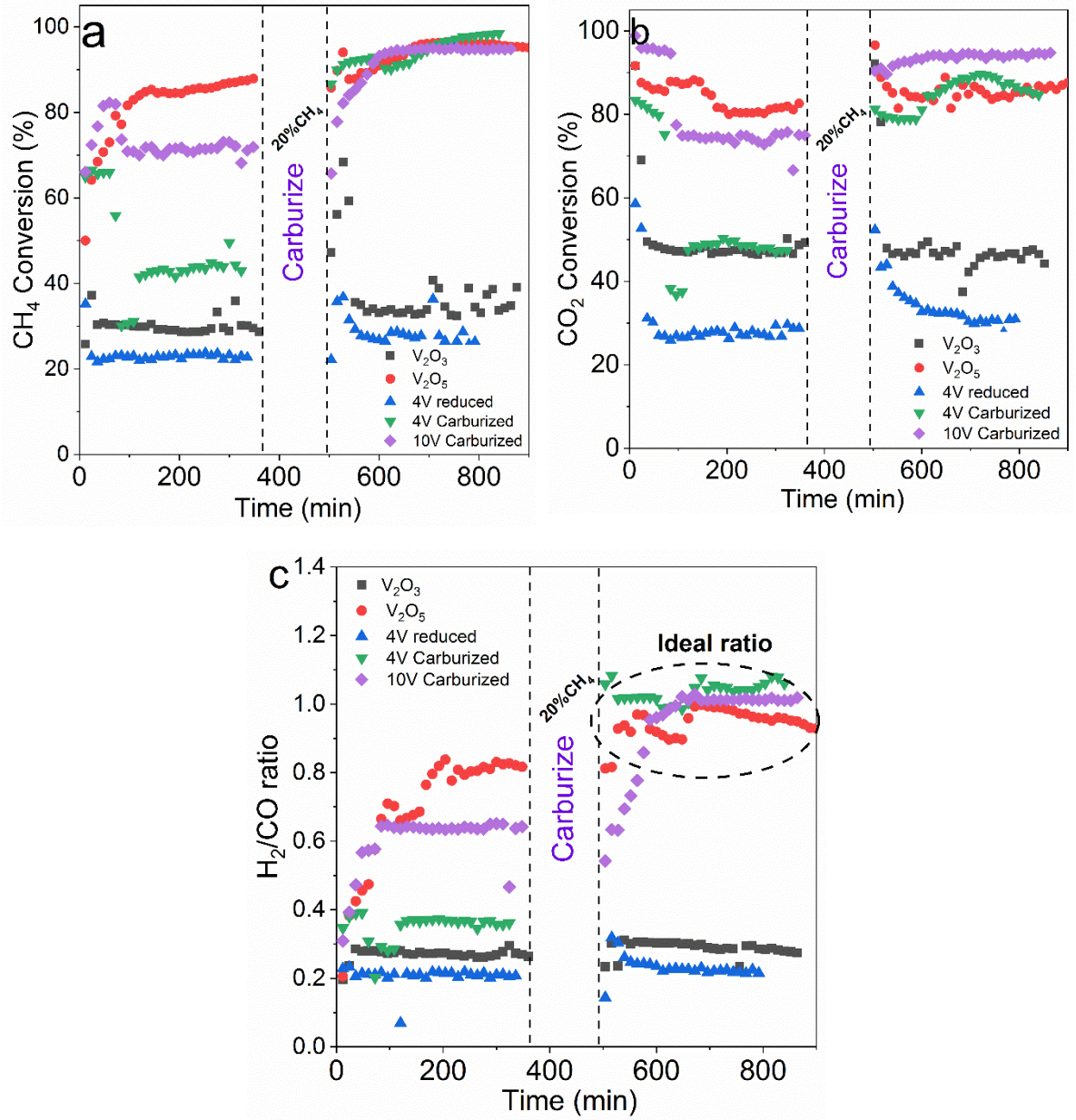

Figure 92. CH_4, CO_2 conversion, and H_2/CO ratio for the vanadium-based catalysts supported over SiO_2.

7.2.4 Spent catalyst characterization by XRD and Raman

To gain more insights into the observed gain in the catalytic performance, the catalysts after every stage of the catalytic cycle (cycle 1, carburization, and cycle 2) were evaluated to see the changes in the structure.

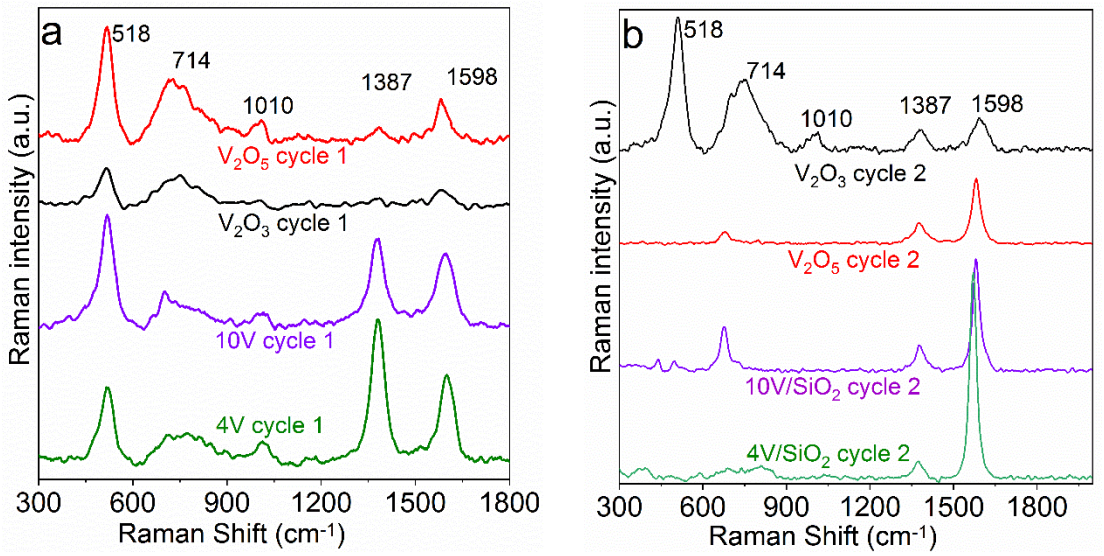

Figure 93. Raman spectra of the catalyst after DRM cycle 1 and cycle 2.

After the first catalytic cycle, all the catalysts were studied by XRD and Raman spectroscopy. Figure 93a and b show the Raman characterization of the catalyst after cycle 1 and cycle 2. In both, the spectra, the formation of oxide (1010 cm^{-1}) and carbide (714cm^{-1}) species can be observed. Further XRD after cycle 1 and 2 was analyzed and a striking difference was observed (Figure 94). The $4V/SiO_2$ catalyst does not show any peaks till cycle 1, but after carburizing it, there is evidence of V_8C_7 peaks, indicating that during the carburization step, the product water reacts with the 2D vanadium species and converts it to the 3D species (XRD detectable). These carbide species undergo DRM cycle and generate the mixture of oxide and carbide species while reacting with CH_4 and CO_2 during the DRM cycle 2. This is the reason why an increase in performance is observed after the carburization step.

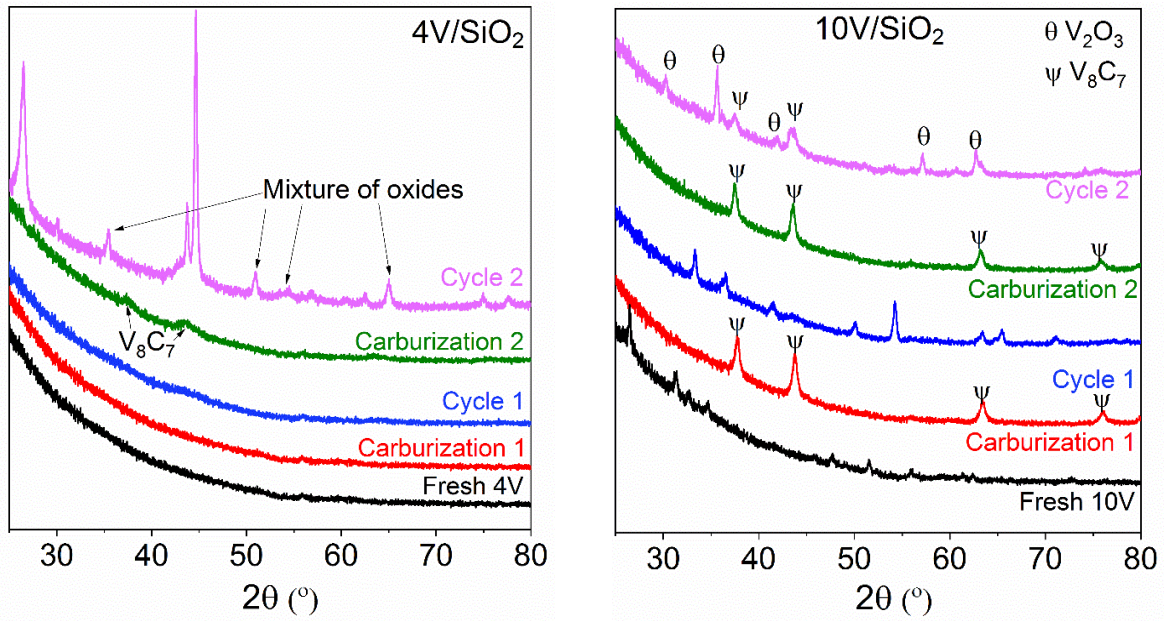

Figure 94. XRD comparison of $4V/SiO_2$ and $10V/SiO_2$ catalyst after every stage of DRM cycle.

Second, the 10V/SiO2 catalyst, which has particles of V_2O_5, transforms into V_2O_3 particles after cycle 1, which after the carburization step undergoes a complete transformation into V_8C_7 particles. These particles undergo DRM cycle 2 reacting with CH_4 and CO_2, thereby generating a mixture of V_2O_3 and V_8C_7 particles (XRD after cycle 2). This mixture of particles was not observed after cycle 1. Thus, evidence that the carburization step after cycle 1, generates significant structural changes in the material which results in enhanced catalytic performance.

This work is done in collaboration with Dr. Abhaya Datye from the University of New Mexico, Dr. Simon Bare from SLAC national synchrotron laboratory (Stanford) and Dr. Tej Choksi from the National University of Singapore. Dr. Datye is providing high angle annular dark field imaging with scanning transmission electron microscopy (HAADF-STEM) to study the structure of the oxide-carbide interface, Dr. Bare is providing the X-ray absorption techniques (XAS) which include, X-ray absorption near edge structure (XANES) to gain information into the local structure and Dr. Choksi will provide the computational calculations to support the proposed hypothesis.

7.3 Recommendations for future work

It has been demonstrated in this dissertation that the nanocrystals of V_2O_3 and V_8C_7 supported over any support such as MXene and SiO_2, results in an enhanced performance during the DRM cycle. This was the first time it has been reported in the scientific community about developing such a vanadium oxy-carbide interface for the dry reforming of methane. The initial foundation has been laid to conduct further research using these supported vanadium oxy-carbide interfaces. However, the experimentalists and the theoreticians working with this emerging family of two-dimensional materials should focus on tackling the following

7.3.1 Evaluating alternative, safe, robust, and acid-free pathways to exfoliate the MAX phase at large scales.

To date, MXenes are synthesized using HF as an etchant. HF is one of the most dangerous chemicals in terms of its effects on the environment and to humans. The HF etching process leads to an exothermic reaction, thereby generating a large quantity of heat and results in a large consumption of the solvent. Further research needs to focus on acid-free pathways such as employing ultrasonication to etch MAX phases. Other studies have shown that using the mechanochemical (MC) method, the etching can be made possible. [278] However, it is still in its preliminary stages.

7.3.2 **Gaining fundamental insights using other characterization techniques**

The changes in the local structure of the V_2CT_x MXene needs to be evaluated using *operando* X-ray absorption studies (XAS), such as X-ray absorption fine structure (EXAFS). Correlating the changes in the oxidation states with the kinetic data will lead to a better understanding and generating structure-reactivity relationships. Dr. Simon Bare from SLAC national laboratory, Stanford will be performing *operando* EXAFS studies to provide a better understanding of the

transformation of the V_2CT_x MXene into a robust and stable V_2O_3-V_8C_7/V_2CT_x Catalysts. Furthermore, Dr. Abhaya Datye from the University of New Mexico will be assisting with the high angle annular dark field imaging with scanning transmission electron microscopy (HAADF-STEM) to study the structure of the oxide-carbide interface at the nanometer scale.

7.3.3 Computational studies to back up the proposed reaction mechanism

Computational modeling and molecular simulations have significantly contributed to the progress of understanding the fundamentals of catalytic phenomenon These computation tools provide a versatile toolkit for studying and understanding the mechanistic details within a catalytic system. With the help of isotopic labeling experiments, catalyst characterization, and kinetic data, an *in-situ* redox mechanism has been proposed. To further understand the mechanistic details, Dr. Tej Choksi from the National University of Singapore along with Dr. Jeffrey Greeley from Purdue University will be assisting with the computational calculations Preliminary data has already been generated and is in line with the suggested proposed reaction mechanism.

7.3.4 Studying DRM using other well developed and characterized MXenes

Our studies on studying the thermal and chemical stability of V_2CT_x MXene has resulted in expanding the portfolio of this MXene for high-temperature applications. Bulk molybdenum carbide and niobium carbides have been used in DRM reactions. However, it would be interesting to evaluate the performance of Mo_2CT_x and Nb_2CT_x in DRM, although thermal and chemical stability needs to be performed beforehand. $Ti_3C_2T_x$ provides another alternative, as this MXene is well characterized and its chemical and thermal stabilities have already been reported. [279]

7.3.5 Utilizing the V_2CT_x for selective dehydrogenation of light alkanes

Our results demonstrate that the V_2CT_x Mxene are highly stable under reducing and inert conditions. Reactions such as dehydrogenation of ethane, propane, butane, pentane, hexane,

ethylbenzene to their respective olefins, etc can be performed over this MXene. $Ti_3C_2T_x$ have already been reported as an effective and efficient catalyst to convert ethylbenzene to styrene and are performing much better than the state-of-the-art catalyst for such reaction.[103]

7.3.6 Use of vanadium catalysts with different supports

Our study indicates that the vanadium supported over SiO_2 works as an efficient catalyst for the DRM reaction. Such a methodology can be extended to other supports such as Al_2O_3, ZrO_2, TiO_2, zeolites which after preparation will be carburized and evaluated for their performance. It is important to ensure and track the carburization step. As excessive carburization can lead to the generation of excess amorphous coke and the catalyst thereby blocking the reactor bed.

7.3.7 Use of membranes to remove the hydrogen to reduce the RWGS effect

The major drawback which the DRM reaction focuses is the simultaneous occurrence of reverse water gas shift reaction (RWGS). RWGS leads to a decrease in the H_2/CO ratio, as the generated H_2 gets consumed by the unreacted CO_2 and generates more CO, thereby reducing the H_2/CO ratio in *syngas*. However, this comes at the cost of the catalyst, as the byproduct of RWGS is H_2O, which can react with the catalyst and eventually lead to its failure. As most of the catalysts at such high temperature under the presence of H_2O suffer from poisoning thus leading to a reduction in activity and selectivity.[7] The water generated when using MXenes can lead to the oxidation of the carbide, thereby affecting its stability. H_2 separation membranes such as permselective palladium membranes can be utilized to remove the H_2 and control the H_2/CO ratio.

7.3.8 DRM process optimization using industrial COSORB units

The *syngas* with the H_2/CO ratio of unity generated during DRM process can be further be improved. CO removal from the generated *syngas* is an option to boost the H_2/CO ratio. To optimize this, an industrially tested process known as COSORB (CO absorption unit) can be

utilized along with DRM process. COSORB has already been extensively studied and is operational is commercial plants (http://www.msk.co.rs/en-GB/content/cid253/production). COSORB is an absorption -desorption process that uses a toluene-based solvent containing $CuAlCl_4$. The absorbed CO can be further be desorbed and can be utilized for other processes such as acetic acid production (reacting methanol and CO).

7.3.9 DRM process integration with alkane dehydrogenation units

The other pathway to boost the H_2/CO ratio is by integrating the DRM process with the alkane dehydrogenation units. The dehydrogenation of alkanes produces respective olefins, and H_2 is generated as a byproduct. This H_2 can be used as a makeup flow to boost H_2/CO ratios.

Appendix A1

Actual reactor setup, showing mass flow controllers, temperature controller, furnace, chiller, transfer line, and GC.

Appendix A2

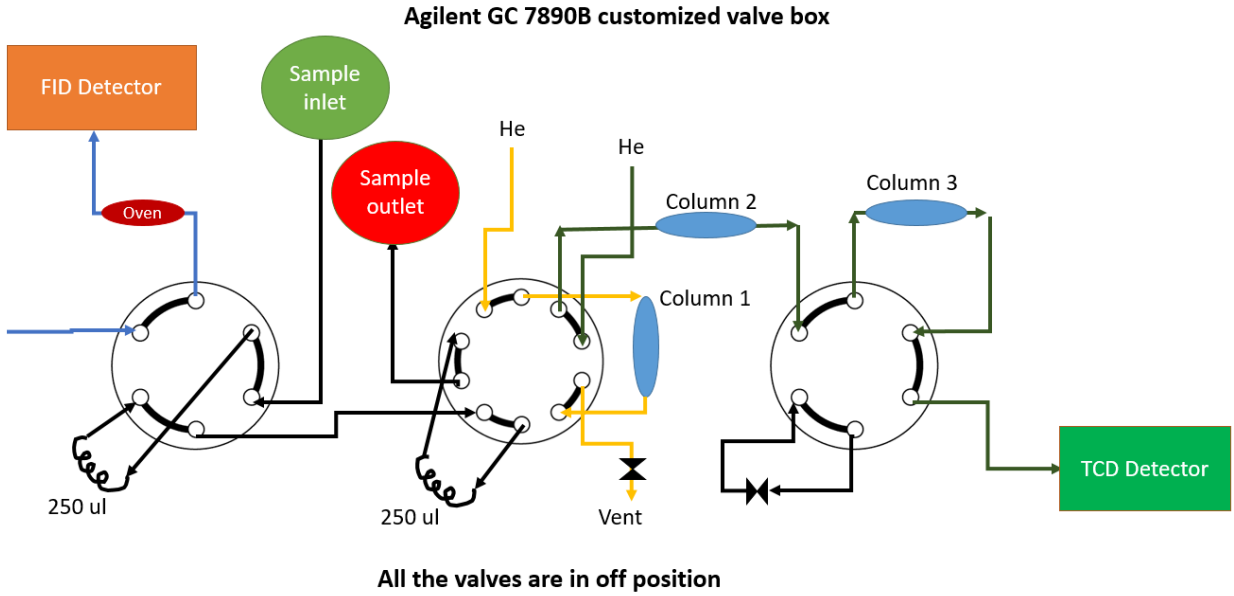

Customized valves box used inside the GC 7890B for quantification of hydrocarbons and permanent gases.

References

1. Capuano, L., International energy outlook 2018 (IEO2018). *US Energy Information Administration (EIA): Washington, DC, USA* **2018,** *2018*, 21.

2. Cole, W. J.; Frazier, A.; Das, P.; Mai, T. T.; Donohoo-Vallett, P. *2018 Standard Scenarios Report: A US Electricity Sector Outlook*; National Renewable Energy Lab.(NREL), Golden, CO (United States): 2018.

3. Center, B. P., Annual Energy Outlook 2020. **2020**.

4. Ma, S.; Guo, X.; Zhao, L.; Scott, S.; Bao, X., Recent progress in methane dehydroaromatization: From laboratory curiosities to promising technology. *Journal of Energy Chemistry* **2013,** *22* (1), 1-20.

5. González, R. Z. Intensification of methane dehydroaromatization process on catalytic reactors. 2017.

6. Suib, S. L., *New and future developments in catalysis: activation of carbon dioxide*. Newnes: 2013.

7. Porosoff, M. D.; Yan, B.; Chen, J. G., Catalytic reduction of CO 2 by H 2 for synthesis of CO, methanol and hydrocarbons: challenges and opportunities. *Energy & Environmental Science* **2016,** *9* (1), 62-73.

8. Khatib, H., IEA world energy outlook 2011—A comment. *Energy policy* **2012,** *48*, 737-743.

9. Ismagilov, Z. R.; Matus, E. V.; Tsikoza, L. T., Direct conversion of methane on Mo/ZSM-5 catalysts to produce benzene and hydrogen: achievements and perspectives. *Energy & Environmental Science* **2008,** *1* (5), 526-541.

10. Gao, K. Methane dehydro aromatization: thermodynamics, catalysts, kinetics and potential of membrane reactors. Otto-von-Guericke-Universität Magdeburg, 2015.

11. van der Hoeven, M.; Kobayashi, Y.; Diercks, R., Technology Roadmap: Energy and GHG Reductions in the Chemical Industry via Catalytic Processes. *International Energy Agency: Paris* **2013**, 56.

12. Birol, F., World energy outlook. *Paris: International Energy Agency* **2008,** *23* (4), 329.

13. Hansen, J.; Sato, M.; Ruedy, R.; Lo, K.; Lea, D. W.; Medina-Elizade, M., Global temperature change. *Proceedings of the National Academy of Sciences* **2006,** *103* (39), 14288-14293.

14. Knutson, T. R.; Tuleya, R. E., Impact of CO2-induced warming on simulated hurricane intensity and precipitation: Sensitivity to the choice of climate model and convective parameterization. *Journal of climate* **2004,** *17* (18), 3477-3495.

15. Dyrssen, D.; Turner, D.; Paul, J.; Pradier, C., Carbon Dioxide Chemistry: Environmental Issues. Athenaeum Press, Cambridge: 1994.

16. Sankaranarayanan, S.; Srinivasan, K., Carbon dioxide–a potential raw material for the production of fuel, fuel additives and bio-derived chemicals. **2012**.

17. Wilhelm, D.; Simbeck, D.; Karp, A.; Dickenson, R., Syngas production for gas-to-liquids applications: technologies, issues and outlook. *Fuel processing technology* **2001,** *71* (1-3), 139-148.

18. Hamzehlouia, S.; Jaffer, S. A.; Chaouki, J., Microwave heating-assisted catalytic dry reforming of methane to syngas. *Scientific reports* **2018,** *8* (1), 8940.

19. Ross, J. R., Natural gas reforming and CO2 mitigation. *Catalysis Today* **2005,** *100* (1-2), 151-158.

20. Inderwildi, O. R.; Jenkins, S. J.; King, D. A., Mechanistic studies of hydrocarbon combustion and synthesis on noble metals. *Angewandte Chemie International Edition* **2008,** *47* (28), 5253-5255.

21. Wang, S.; Lu, G.; Millar, G. J., Carbon dioxide reforming of methane to produce synthesis gas over metal-supported catalysts: state of the art. *Energy & fuels* **1996,** *10* (4), 896-904.

22. Mette, K.; Kühl, S.; Tarasov, A.; Willinger, M. G.; Kröhnert, J.; Wrabetz, S.; Trunschke, A.; Scherzer, M.; Girgsdies, F.; Düdder, H., High-temperature stable Ni nanoparticles for the dry reforming of methane. *ACS Catalysis* **2016,** *6* (10), 7238-7248.

23. Pakhare, D.; Spivey, J., A review of dry (CO 2) reforming of methane over noble metal catalysts. *Chemical Society Reviews* **2014,** *43* (22), 7813-7837.

24. Usman, M.; Daud, W. W.; Abbas, H. F., Dry reforming of methane: Influence of process parameters—A review. *Renewable and Sustainable Energy Reviews* **2015,** *45*, 710-744.

25. Aramouni, N. A. K.; Touma, J. G.; Tarboush, B. A.; Zeaiter, J.; Ahmad, M. N., Catalyst design for dry reforming of methane: Analysis review. *Renewable and Sustainable Energy Reviews* **2018,** *82*, 2570-2585.

26. Mohamedali, M.; Henni, A.; Ibrahim, H., Recent Advances in Supported Metal Catalysts for Syngas Production from Methane. *ChemEngineering* **2018,** *2* (1), 9.

27. Aramouni, N. A. K.; Touma, J. G.; Tarboush, B. A.; Zeaiter, J.; Ahmad, M. N., Catalyst design for dry reforming of methane: Analysis review. *Renewable and Sustainable Energy Reviews* **2017**.

28. Budiman, A. W.; Song, S.-H.; Chang, T.-S.; Shin, C.-H.; Choi, M.-J., Dry reforming of methane over cobalt catalysts: a literature review of catalyst development. *Catalysis Surveys from Asia* **2012,** *16* (4), 183-197.

29. Şener, A. N.; Günay, M. E.; Leba, A.; Yıldırım, R., Statistical review of dry reforming of methane literature using decision tree and artificial neural network analysis. *Catalysis Today* **2018,** *299*, 289-302.

30. Muraza, O.; Galadima, A., A review on coke management during dry reforming of methane. *International Journal of Energy Research* **2015,** *39* (9), 1196-1216.

31. Wang, Y.; Yao, L.; Wang, S.; Mao, D.; Hu, C., Low-temperature catalytic CO2 dry reforming of methane on Ni-based catalysts: a review. *Fuel Processing Technology* **2018,** *169*, 199-206.

32. Jang, W.-J.; Shim, J.-O.; Kim, H.-M.; Yoo, S.-Y.; Roh, H.-S., A review on dry reforming of methane in aspect of catalytic properties. *Catalysis Today* **2019,** *324*, 15-26.

33. Dębek, R.; Motak, M.; Grzybek, T.; Galvez, M. E.; Da Costa, P., A short review on the catalytic activity of hydrotalcite-derived materials for dry reforming of methane. *Catalysts* **2017,** *7* (1), 32.

34. Abdullah, B.; Ghani, N. A. A.; Vo, D.-V. N., Recent advances in dry reforming of methane over Ni-based catalysts. *Journal of Cleaner Production* **2017,** *162*, 170-185.

35. Bian, Z.; Das, S.; Wai, M. H.; Hongmanorom, P.; Kawi, S., A review on bimetallic nickel-based catalysts for CO2 reforming of methane. *ChemPhysChem* **2017,** *18* (22), 3117-3134.

36. Lavoie, J.-M., Review on dry reforming of methane, a potentially more environmentally-friendly approach to the increasing natural gas exploitation. *Frontiers in chemistry* **2014,** *2*, 81.

37. Abdulrasheed, A.; Jalil, A. A.; Gambo, Y.; Ibrahim, M.; Hambali, H. U.; Hamid, M. Y. S., A review on catalyst development for dry reforming of methane to syngas: Recent advances. *Renewable and Sustainable Energy Reviews* **2019,** *108*, 175-193.

38. Neiva, L.; Gama, L., A study on the characteristics of the reforming of methane: a review. *Brazilian Journal of Petroleum and Gas* **2010,** *4* (3).

39. Brungs, A. J.; York, A. P.; Claridge, J. B.; Márquez-Alvarez, C.; Green, M. L., Dry reforming of methane to synthesis gas over supported molybdenum carbide catalysts. *Catalysis Letters* **2000,** *70* (3-4), 117-122.

40. Brungs, A. J.; York, A. P.; Green, M. L., Comparison of the group V and VI transition metal carbides for methane dry reforming and thermodynamic prediction of their relative stabilities. *Catalysis letters* **1999,** *57* (1-2), 65-69.

41. Zhang, A.; Zhu, A.; Chen, B.; Zhang, S.; Au, C.; Shi, C., In-situ synthesis of nickel modified molybdenum carbide catalyst for dry reforming of methane. *Catalysis Communications* **2011,** *12* (9), 803-807.

42. Claridge, J. B.; York, A. P.; Brungs, A. J.; Marquez-Alvarez, C.; Sloan, J.; Tsang, S. C.; Green, M. L., New catalysts for the conversion of methane to synthesis gas: molybdenum and tungsten carbide. *Journal of Catalysis* **1998,** *180* (1), 85-100.

43. Shao, H.; Kugler, E. L.; Ma, W.; Dadyburjor, D. B., Effect of temperature on structure and performance of in-house cobalt− tungsten carbide catalyst for dry reforming of methane. *Industrial & engineering chemistry research* **2005,** *44* (14), 4914-4921.

44. LaMont, D. C.; Thomson, W. J., Dry reforming kinetics over a bulk molybdenum carbide catalyst. *Chemical engineering science* **2005,** *60* (13), 3553-3559.

45. Shi, C.; Zhang, A.; Li, X.; Zhang, S.; Zhu, A.; Ma, Y.; Au, C., Ni-modified Mo2C catalysts for methane dry reforming. *Applied Catalysis A: General* **2012,** *431*, 164-170.

46. Hirose, T.; Ozawa, Y.; Nagai, M., Preparation of a nickel molybdenum carbide catalyst and its activity in the dry reforming of methane. *Chinese journal of catalysis* **2011,** *32* (5), 771-776.

47. York, A.; Claridge, J.; Marquez-Alvarez, C.; Brungs, A.; Tsang, S.; Green, M., Synthesis of early transition metal carbides and their application for the reforming of methane to synthesis gas. In *Studies in Surface Science and Catalysis*, Elsevier: 1997; Vol. 110, pp 711-720.

48. York, A. P.; Claridge, J. B.; Brungs, A. J.; Tsang, S. C.; Green, M. L., Molybdenum and tungsten carbides as catalysts for the conversion ofmethane to synthesis gas using stoichiometric feedstocks. *Chemical Communications* **1997,** (1), 39-40.

49. Du, X.; France, L.; Kuznetsov, V.; Xiao, T.; Edwards, P.; AlMegren, H.; Bagabas, A., Dry reforming of methane over ZrO 2-supported Co–Mo carbide catalyst. *Applied Petrochemical Research* **2014,** *4* (1), 137-144.

50. Yao, Z.; Jiang, J.; Zhao, Y.; Luan, F.; Zhu, J.; Shi, Y.; Gao, H.; Wang, H., Insights into the deactivation mechanism of metal carbide catalysts for dry reforming of methane via comparison of nickel-modified molybdenum and tungsten carbides. *RSC Advances* **2016,** *6* (24), 19944-19951.

51. Cheng, J.; Huang, W., Effect of cobalt (nickel) content on the catalytic performance of molybdenum carbides in dry-methane reforming. *Fuel processing technology* **2010,** *91* (2), 185-193.

52. Guo, J.; Zhang, A.-J.; Zhu, A.-M.; Xu, Y.; Au, C.; Shi, C., A carbide catalyst effective for the dry reforming of methane at atmospheric pressure. In *Advances in CO2 conversion and utilization*, ACS Publications: 2010; pp 181-196.

53. Huang, J.; Huang, T.; Liu, L.; Huang, W.; Ma, R., Mo2C/SBA-15 Modified by Ni for the Dry Reforming of Methane. *Energy Sources, Part A: Recovery, Utilization, and Environmental Effects* **2011,** *33* (24), 2249-2256.

54. Ginsburg, J. M.; Piña, J.; El Solh, T.; De Lasa, H. I., Coke formation over a nickel catalyst under methane dry reforming conditions: thermodynamic and kinetic models. *Industrial & engineering chemistry research* **2005,** *44* (14), 4846-4854.

55. Liu, Y.; Li, D.; Wang, T.; Liu, Y.; Xu, T.; Zhang, Y., Efficient conversion of methane to aromatics by coupling methylation reaction. *ACS Catalysis* **2016,** *6* (8), 5366-5370.

56. Kosinov, N.; Wijpkema, A. S.; Uslamin, E.; Rohling, R.; Coumans, F. J.; Mezari, B.; Parastaev, A.; Poryvaev, A. S.; Fedin, M. V.; Pidko, E. A., Confined Carbon Mediating Dehydroaromatization of Methane over Mo/ZSM-5. *Angewandte Chemie International Edition* **2018,** *57* (4), 1016-1020.

57. Sridhar, A.; Rahman, M.; Khatib, S. J., Enhancement of Molybdenum/ZSM-5 Catalysts in Methane Aromatization by the Addition of Iron Promoters and by Reduction/Carburization Pretreatment. *ChemCatChem* **2018,** *10* (12), 2571-2583.

58. Kim, Y.-H.; Borry III, R. W.; Iglesia, E., Genesis of methane activation sites in Mo-exchanged H–ZSM-5 catalysts. *Microporous and Mesoporous Materials* **2000,** *35*, 495-509.

59. Li, S.; Ma, D.; Kan, Q.; Wu, P.; Peng, Y.; Zhang, C.; Li, M.; Fu, Y.; Shen, J.; Wu, T., Methane aromatization in the absence of oxygen over Mo/H [B] ZSM-5 catalysts. *Reaction Kinetics and Catalysis Letters* **2000,** *70* (2), 349-356.

60. Ding, W.; Li, S.; D Meitzner, G.; Iglesia, E., Methane conversion to aromatics on Mo/H-ZSM5: structure of molybdenum species in working catalysts. *The Journal of Physical Chemistry B* **2001,** *105* (2), 506-513.

61. Ding, W.; Meitzner, G. D.; Marler, D. O.; Iglesia, E., Synthesis, structural characterization, and catalytic properties of tungsten-exchanged H-ZSM5. *The Journal of Physical Chemistry B* **2001,** *105* (18), 3928-3936.

62. Mehdad, A.; Lobo, R. F., Ethane and ethylene aromatization on zinc-containing zeolites. *Catalysis Science & Technology* **2017,** *7* (16), 3562-3572.

63. Zhang, C.-L.; Li, S.; Yuan, Y.; Zhang, W.-X.; Wu, T.-H.; LIn, L.-W., Aromatization of methane in the absence of oxygen over Mo-based catalysts supported on different types of zeolites. *Catalysis letters* **1998,** *56* (4), 207-213.

64. Liu, S.; Wang, L.; Ohnishi, R.; Ichikawa, M., Bifunctional catalysis of Mo/HZSM-5 in the dehydroaromatization of methane to benzene and naphthalene XAFS/TG/DTA/MASS/FTIR characterization and supporting effects. *Journal of Catalysis* **1999,** *181* (2), 175-188.

65. Shu, Y.; Ma, D.; Xu, L.; Xu, Y.; Bao, X., Methane dehydro-aromatization over Mo/MCM-22 catalysts: a highly selective catalyst for the formation of benzene. *Catalysis Letters* **2000,** *70* (1-2), 67-73.

66. Wu, P.; Kan, Q.; Wang, D.; Xing, H.; Jia, M.; Wu, T., The synthesis of Mo/H-MCM-36 catalyst and its catalytic behavior in methane non-oxidative aromatization. *Catalysis Communications* **2005,** *6* (7), 449-454.

67. Wang, D.; Kan, Q.; Xu, N.; Wu, P.; Wu, T., Study on methane aromatization over MoO3/HMCM-49 catalyst. *Catalysis today* **2004,** *93*, 75-80.

68. Xing, H.; Zhang, Y.; Jia, M.; Wu, S.; Wang, H.; Guan, J.; Xu, L.; Wu, T.; Kan, Q., Detemplation with H2O2 and characterization of MCM-56. *Catalysis Communications* **2008,** *9* (2), 234-238.

69. Martínez, A.; Peris, E.; Sastre, G., Dehydroaromatization of methane under non-oxidative conditions over bifunctional Mo/ITQ-2 catalysts. *Catalysis today* **2005,** *107*, 676-684.

70. Xu, C.; Guan, J.; Wu, S.; Jia, M.; Wu, T.; Kan, Q., Catalytic performance of zeolite ITQ-13 with 9-and 10-member rings for methane dehydroaromation. *Reaction Kinetics, Mechanisms and Catalysis* **2010,** *99* (1), 193-199.

71. Liu, H.; Wu, S.; Guo, Y.; Shang, F.; Yu, X.; Ma, Y.; Xu, C.; Guan, J.; Kan, Q., Synthesis of Mo/IM-5 catalyst and its catalytic behavior in methane non-oxidative aromatization. *Fuel* **2011,** *90* (4), 1515-1521.

72. Liu, H.; Yang, S.; Wu, S.; Shang, F.; Yu, X.; Xu, C.; Guan, J.; Kan, Q., Synthesis of Mo/TNU-9 (TNU-9 Taejon National University No. 9) catalyst and its catalytic performance in methane non-oxidative aromatization. *Energy* **2011,** *36* (3), 1582-1589.

73. Weckhuysen, B. M.; Wang, D.; Rosynek, M. P.; Lunsford, J. H., Conversion of methane to benzene over transition metal ion ZSM-5 zeolites: I. Catalytic characterization. *Journal of catalysis* **1998,** *175* (2), 338-346.

74. Wang, L.; Ohnishi, R.; Ichikawa, M., Novel rhenium-based catalysts for dehydrocondensation of methane with CO/CO 2 towards ethylene and benzene. *Catalysis letters* **1999,** *62* (1), 29-33.

75. Ohnishi, R.; Liu, S.; Dong, Q.; Wang, L.; Ichikawa, M., Catalytic dehydrocondensation of methane with CO and CO2toward benzene and naphthalene on Mo/HZSM-5 and Fe/Co-modified Mo/HZSM-5. *Journal of Catalysis* **1999,** *182* (1), 92-103.

76. Xu, Y.; Wang, J.; Suzuki, Y.; Zhang, Z.-G., Effect of transition metal additives on the catalytic stability of Mo/HZSM-5 in the methane dehydroaromatization under periodic CH4–H2 switch operation at 1073 K. *Applied Catalysis A: General* **2011,** *409*, 181-193.

77. Liu, B.; Zhang, Y.; Liu, J.; Tian, M.; Zhang, F.; Au, C.; Cheung, A.-C., Characteristic and mechanism of methane dehydroaromatization over Zn-based/HZSM-5 catalysts under conditions of atmospheric pressure and supersonic jet expansion. *The Journal of Physical Chemistry C* **2011,** *115* (34), 16954-16962.

78. Luzgin, M. V.; Rogov, V. A.; Arzumanov, S. S.; Toktarev, A. V.; Stepanov, A. G.; Parmon, V. N., Understanding Methane Aromatization on a Zn-Modified High-Silica Zeolite. *Angewandte Chemie International Edition* **2008,** *47* (24), 4559-4562.

79. Majhi, S.; Dalai, A. K.; Pant, K. K., Methanol assisted methane conversion for higher hydrocarbon over bifunctional Zn-modified Mo/HZSM-5 catalyst. *Journal of Molecular Catalysis A: Chemical* **2015,** *398*, 368-375.

80. Ma, D.; Shu, Y.; Zhang, C.; Zhang, W.; Han, X.; Xu, Y.; Bao, X., Synthesis and characterization of galloaluminosilicate/gallosilicalite (MFI) and their evaluation in methane dehydro-aromatization. *Journal of Molecular Catalysis A: Chemical* **2001,** *168* (1-2), 139-146.

81. Amin, N., Dual effects of supported W catalysts for dehydroaromatization of methane in the absence of oxygen. *Catalysis Letters* **2005,** *102* (1-2), 69-78.

82. Kozlov, V.; Zaikovskii, V.; Vosmerikov, A.; Korobitsyna, L.; Echevskii, G., Active sites of the methane dehydroaromatization catalyst W-ZSM-5: An HRTEM study. *Kinetics and Catalysis* **2008,** *49* (1), 110-114.

83. Shu, Y.; Ohnishi, R.; Ichikawa, M., Improved methane dehydrocondensation reaction on HMCM-22 and HZSM-5 supported rhenium and molybdenum catalysts. *Applied Catalysis A: General* **2003,** *252* (2), 315-329.

84. Hsieh, M. F.; Zhou, Y.; Thirumalai, H.; Grabow, L. C.; Rimer, J. D., Silver-Promoted Dehydroaromatization of Ethylene over ZSM-5 Catalysts. *ChemCatChem* **2017,** *9* (9), 1675-1682.

85. Kojima, R.; Kikuchi, S.; Ma, H.; Bai, J.; Ichikawa, M., Promotion effects of Pt and Rh on catalytic performances of Mo/HZSM-5 and Mo/HMCM-22 in selective methane-to-benzene reaction. *Catalysis letters* **2006,** *110* (1-2), 15-21.

86. Aboul-Gheit, A. K.; Awadallah, A. E.; El-Kossy, S. M.; Mahmoud, A.-L. H., Effect of Pd or Ir on the catalytic performance of Mo/H-ZSM-5 during the non-oxidative conversion of natural gas to petrochemicals. *Journal of Natural Gas Chemistry* **2008,** *17* (4), 337-343.

87. Hassan, A.; Sayari, A., Highly active, selective and stable Mo/Ru-HZSM-5 catalysts for oxygen-free methane aromatization. *Applied Catalysis A: General* **2006,** *297* (2), 159-164.

88. Choudhary, V. R.; Mondal, K. C.; Mulla, S. A., Simultaneous Conversion of Methane and Methanol into Gasoline over Bifunctional Ga-, Zn-, In-, and/or Mo-Modified ZSM-5 Zeolites. *Angewandte Chemie* **2005,** *117* (28), 4455-4459.

89. Solymosi, F.; Erdöhelyi, A.; Szöke, A., Dehydrogenation of methane on supported molybdenum oxides. Formation of benzene from methane. *Catalysis Letters* **1995,** *32* (1-2), 43-53.

90. Wang, D.; Lunsford, J. H.; Rosynek, M. P., Characterization of a Mo/ZSM-5 catalyst for the conversion of methane to benzene. *Journal of Catalysis* **1997,** *169* (1), 347-358.

91. Solymosi, F.; Cserényi, J.; Szöke, A.; Bánsági, T.; Oszko, A., Aromatization of methane over supported and unsupported Mo-based catalysts. *Journal of Catalysis* **1997,** *165* (2), 150-161.

92. Aguilera, R. F., Production costs of global conventional and unconventional petroleum. *Energy Policy* **2014,** *64*, 134-140.

93. Naguib, M.; Mochalin, V. N.; Barsoum, M. W.; Gogotsi, Y., 25th anniversary article: MXenes: a new family of two-dimensional materials. *Advanced Materials* **2014,** *26* (7), 992-1005.

94. Naguib, M.; Mashtalir, O.; Carle, J.; Presser, V.; Lu, J.; Hultman, L.; Gogotsi, Y.; Barsoum, M. W., Two-Dimensional Transition Metal Carbides. *ACS Nano* **2012,** *6* (2), 1322-1331.

95. Anasori, B.; Lukatskaya, M. R.; Gogotsi, Y., 2D metal carbides and nitrides (MXenes) for energy storage. *Nature Reviews Materials* **2017,** *2* (2), 16098.

96. Magne, D.; Mauchamp, V.; Célérier, S.; Chartier, P.; Cabioc'h, T., Site-projected electronic structure of two-dimensional Ti 3 C 2 MXene: the role of the surface functionalization groups. *Physical Chemistry Chemical Physics* **2016,** *18* (45), 30946-30953.

97. Wen, Y.; Rufford, T. E.; Chen, X.; Li, N.; Lyu, M.; Dai, L.; Wang, L., Nitrogen-doped Ti3C2Tx MXene electrodes for high-performance supercapacitors. *Nano energy* **2017,** *38*, 368-376.

98. VahidMohammadi, A.; Hadjikhani, A.; Shahbazmohamadi, S.; Beidaghi, M., Two-Dimensional Vanadium Carbide (MXene) as a High-Capacity Cathode Material for Rechargeable Aluminum Batteries. *ACS Nano* **2017,** *11* (11), 11135-11144.

99. Naguib, M.; Halim, J.; Lu, J.; Cook, K. M.; Hultman, L.; Gogotsi, Y.; Barsoum, M. W., New two-dimensional niobium and vanadium carbides as promising materials for Li-ion batteries. *Journal of the American Chemical Society* **2013,** *135* (43), 15966-15969.

100. VahidMohammadi, A.; Mojtabavi, M.; Caffrey, N. M.; Wanunu, M.; Beidaghi, M., Assembling 2D MXenes into Highly Stable Pseudocapacitive Electrodes with High Power and Energy Densities. *Advanced Materials* **2019,** *31* (8), 1806931.

101. Ran, J.; Gao, G.; Li, F.-T.; Ma, T.-Y.; Du, A.; Qiao, S.-Z., Ti 3 C 2 MXene co-catalyst on metal sulfide photo-absorbers for enhanced visible-light photocatalytic hydrogen production. *Nature communications* **2017,** *8*, 13907.

102. Li, Z.; Cui, Y.; Wu, Z.; Milligan, C.; Zhou, L.; Mitchell, G.; Xu, B.; Shi, E.; Miller, J. T.; Ribeiro, F. H., Reactive metal–support interactions at moderate temperature in two-

dimensional niobium-carbide-supported platinum catalysts. *Nature Catalysis* **2018,** *1* (5), 349.

103. Diao, J.; Hu, M.; Lian, Z.; Li, Z.; Zhang, H.; Huang, F.; Li, B.; Wang, X.; Su, D. S.; Liu, H., Ti3C2Tx MXene Catalyzed Ethylbenzene Dehydrogenation: Active Sites and Mechanism Exploration from both Experimental and Theoretical Aspects. *ACS Catalysis* **2018,** *8* (11), 10051-10057.

104. Deeva, E. B.; Kurlov, A.; Abdala, P. M.; Lebedev, D.; Kim, S. M.; Gordon, C. P.; Tsoukalou, A.; Fedorov, A.; Müller, C. R., In situ XANES/XRD Study of the Structural Stability of Two-Dimensional Molybdenum Carbide Mo2CTx: Implications for the Catalytic Activity in the Water-Gas Shift Reaction. *Chemistry of Materials* **2019,** *31* (12), 4505-4513.

105. Li, Z.; Yu, L.; Milligan, C.; Ma, T.; Zhou, L.; Cui, Y.; Qi, Z.; Libretto, N.; Xu, B.; Luo, J., Two-dimensional transition metal carbides as supports for tuning the chemistry of catalytic nanoparticles. *Nature communications* **2018,** *9* (1), 5258.

106. Thakur, R.; Hoffman, M.; VahidMohammadi, A.; Smith, J.; Chi, M.; Tatarchuk, B.; Beidaghi, M.; Carrero, C., Multilayered Two-Dimensional V2CTx MXene for Methane Dehydroaromatization. *ChemCatChem*.

107. Morales-García, Á.; Fernández-Fernández, A.; Viñes, F.; Illas, F., CO 2 abatement using two-dimensional MXene carbides. *Journal of Materials Chemistry A* **2018,** *6* (8), 3381-3385.

108. Colella, C.; Gualtieri, A. F., Cronstedt's zeolite. *Microporous and Mesoporous Materials* **2007,** *105* (3), 213-221.

109. Weitkamp, J., Zeolites and catalysis. *Solid State Ionics* **2000,** *131* (1-2), 175-188.

110. Corma, A., State of the art and future challenges of zeolites as catalysts. *Journal of Catalysis* **2003,** *216* (1-2), 298-312.

111. Loewenstein, W., The distribution of aluminum in the tetrahedra of silicates and aluminates. *American Mineralogist: Journal of Earth and Planetary Materials* **1954,** *39* (1-2), 92-96.

112. Kulprathipanja, S., *Zeolites in industrial separation and catalysis*. John Wiley & Sons: 2010.

113. Moradi, G.; Khezeli, F.; Hemmati, H., Syngas production with dry reforming of methane over Ni/ZSM-5 catalysts. *Journal of Natural Gas Science and Engineering* **2016,** *33*, 657-665.

114. Sing, K. S., Physisorption of nitrogen by porous materials. *Journal of Porous Materials* **1995,** *2* (1), 5-8.

115. Hebbar, K. R., *Basics of X-ray diffraction and its applications*. IK International Publishing House Pvt. Limited: 2007.

116. Graves, P.; Gardiner, D., Practical raman spectroscopy. *Springer* **1989**.

117. Naguib, M.; Kurtoglu, M.; Presser, V.; Lu, J.; Niu, J.; Heon, M.; Hultman, L.; Gogotsi, Y.; Barsoum, M. W., Two-dimensional nanocrystals produced by exfoliation of Ti3AlC2. *Advanced Materials* **2011,** *23* (37), 4248-4253.

118. Zhu, J.; Ha, E.; Zhao, G.; Zhou, Y.; Huang, D.; Yue, G.; Hu, L.; Sun, N.; Wang, Y.; Lee, L. Y. S.; Xu, C.; Wong, K.-Y.; Astruc, D.; Zhao, P., Recent advance in MXenes: A promising 2D material for catalysis, sensor and chemical adsorption. *Coordination Chemistry Reviews* **2017,** *352*, 306-327.

119. Gogotsi, Y., *Nanomaterials handbook*. CRC press: 2006.

120. Anasori, B.; Xie, Y.; Beidaghi, M.; Lu, J.; Hosler, B. C.; Hultman, L.; Kent, P. R.; Gogotsi, Y.; Barsoum, M. W., Two-dimensional, ordered, double transition metals carbides (MXenes). *ACS nano* **2015,** *9* (10), 9507-9516.

121. Akuzum, B.; Maleski, K.; Anasori, B.; Lelyukh, P.; Alvarez, N. J.; Kumbur, E. C.; Gogotsi, Y., Rheological Characteristics of 2D Titanium Carbide (MXene) Dispersions: A Guide for Processing MXenes. *ACS nano* **2018,** *12* (3), 2685-2694.

122. Lee, E.; VahidMohammadi, A.; Prorok, B. C.; Yoon, Y. S.; Beidaghi, M.; Kim, D.-J., Room temperature gas sensing of two-dimensional titanium carbide (MXene). *ACS applied materials & interfaces* **2017,** *9* (42), 37184-37190.

123. Kim, S. J.; Koh, H.-J.; Ren, C. E.; Kwon, O.; Maleski, K.; Cho, S.-Y.; Anasori, B.; Kim, C.-K.; Choi, Y.-K.; Kim, J., Metallic Ti3C2T x MXene Gas Sensors with Ultrahigh Signal-to-Noise Ratio. *ACS nano* **2018,** *12* (2), 986-993.

124. Zhang, Q.; Teng, J.; Zou, G.; Peng, Q.; Du, Q.; Jiao, T.; Xiang, J., Efficient phosphate sequestration for water purification by unique sandwich-like MXene/magnetic iron oxide nanocomposites. *Nanoscale* **2016,** *8* (13), 7085-7093.

125. Peng, Y.-Y.; Akuzum, B.; Kurra, N.; Zhao, M.-Q.; Alhabeb, M.; Anasori, B.; Kumbur, E. C.; Alshareef, H. N.; Ger, M.-D.; Gogotsi, Y., All-MXene (2D titanium carbide) solid-state microsupercapacitors for on-chip energy storage. *Energy & Environmental Science* **2016,** *9* (9), 2847-2854.

126. Couly, C.; Alhabeb, M.; Van Aken, K. L.; Kurra, N.; Gomes, L.; Navarro-Suárez, A. M.; Anasori, B.; Alshareef, H. N.; Gogotsi, Y., Asymmetric Flexible MXene-Reduced Graphene Oxide Micro-Supercapacitor. *Advanced Electronic Materials* **2018,** *4* (1), 1700339.

127. VahidMohammadi, A.; Moncada, J.; Chen, H.; Kayali, E.; Orangi, J.; Carrero, C. A.; Beidaghi, M., Thick and freestanding MXene/PANI pseudocapacitive electrodes with ultrahigh specific capacitance. *Journal of Materials Chemistry A* **2018**.

128. Xu, B.; Zhu, M.; Zhang, W.; Zhen, X.; Pei, Z.; Xue, Q.; Zhi, C.; Shi, P., Ultrathin MXene-Micropattern-Based Field-Effect Transistor for Probing Neural Activity. *Advanced Materials* **2016,** *28* (17), 3333-3339.

129. Hong Ng, V. M.; Huang, H.; Zhou, K.; Lee, P. S.; Que, W.; Xu, J. Z.; Kong, L. B., Recent progress in layered transition metal carbides and/or nitrides (MXenes) and their composites: synthesis and applications. *Journal of Materials Chemistry A* **2017,** *5* (7), 3039-3068.

130. Choi, W.; Choudhary, N.; Han, G. H.; Park, J.; Akinwande, D.; Lee, Y. H., Recent development of two-dimensional transition metal dichalcogenides and their applications. *Materials Today* **2017,** *20* (3), 116-130.

131. Gao, Y.; Wang, L.; Li, Z.; Zhou, A.; Hu, Q.; Cao, X., Preparation of MXene-Cu2O nanocomposite and effect on thermal decomposition of ammonium perchlorate. *Solid State Sciences* **2014,** *35*, 62-65.

132. Azofra, L. M.; Li, N.; MacFarlane, D. R.; Sun, C., Promising prospects for 2D d 2–d 4 M 3 C 2 transition metal carbides (MXenes) in N 2 capture and conversion into ammonia. *Energy & Environmental Science* **2016,** *9* (8), 2545-2549.

133. Zhang, X.; Lei, J.; Wu, D.; Zhao, X.; Jing, Y.; Zhou, Z., A Ti-anchored Ti 2 CO 2 monolayer (MXene) as a single-atom catalyst for CO oxidation. *Journal of Materials Chemistry A* **2016,** *4* (13), 4871-4876.

134. Li, Z.; Cui, Y.; Wu, Z.; Milligan, C.; Zhou, L.; Mitchell, G.; Xu, B.; Shi, E.; Miller, J. T.; Ribeiro, F. H., Reactive metal–support interactions at moderate temperature in two-dimensional niobium-carbide-supported platinum catalysts. *Nature Catalysis* **2018**, 1.

135. Ghassemi, H.; Harlow, W.; Mashtalir, O.; Beidaghi, M.; Lukatskaya, M. R.; Gogotsi, Y.; Taheri, M. L., In situ environmental transmission electron microscopy study of oxidation of two-dimensional Ti 3 C 2 and formation of carbon-supported TiO 2. *Journal of Materials Chemistry A* **2014,** *2* (35), 14339-14343.

136. Lai, S.; Jeon, J.; Jang, S. K.; Xu, J.; Choi, Y. J.; Park, J.-H.; Hwang, E.; Lee, S., Surface group modification and carrier transport properties of layered transition metal carbides (Ti2CTx, T:–OH,–F and–O). *Nanoscale* **2015,** *7* (46), 19390-19396.

137. Rakhi, R.; Ahmed, B.; Hedhili, M. N.; Anjum, D. H.; Alshareef, H. N., Effect of postetch annealing gas composition on the structural and electrochemical properties of Ti2CT x MXene electrodes for supercapacitor applications. *Chemistry of Materials* **2015,** *27* (15), 5314-5323.

138. Wang, H.; Wu, Y.; Zhang, J.; Li, G.; Huang, H.; Zhang, X.; Jiang, Q., Enhancement of the electrical properties of MXene Ti3C2 nanosheets by post-treatments of alkalization and calcination. *Materials Letters* **2015,** *160*, 537-540.

139. Wang, K.; Zhou, Y.; Xu, W.; Huang, D.; Wang, Z.; Hong, M., Fabrication and thermal stability of two-dimensional carbide Ti3C2 nanosheets. *Ceramics International* **2016,** *42* (7), 8419-8424.

140. Cai, Y.; Shen, J.; Ge, G.; Zhang, Y.; Jin, W.; Huang, W.; Shao, J.; Yang, J.; Dong, X., Stretchable Ti3C2T x MXene/Carbon Nanotube Composite Based Strain Sensor with Ultrahigh Sensitivity and Tunable Sensing Range. *ACS nano* **2017**.

141. Feng, A.; Yu, Y.; Jiang, F.; Wang, Y.; Mi, L.; Yu, Y.; Song, L., Fabrication and thermal stability of NH4HF2-etched Ti3C2 MXene. *Ceramics International* **2017,** *43* (8), 6322-6328.

142. Khazaei, M.; Ranjbar, A.; Arai, M.; Sasaki, T.; Yunoki, S., Electronic properties and applications of MXenes: a theoretical review. *Journal of Materials Chemistry C* **2017,** *5* (10), 2488-2503.

143. Li, R.; Zhang, L.; Shi, L.; Wang, P., MXene Ti3C2: An Effective 2D Light-to-Heat Conversion Material. *ACS Nano* **2017,** *11* (4), 3752-3759.

144. Zhang, C. J.; Pinilla, S.; McEvoy, N.; Cullen, C. P.; Anasori, B.; Long, E.; Park, S.-H.; Seral-Ascaso, A.; Shmeliov, A.; Krishnan, D.; Morant, C.; Liu, X.; Duesberg, G. S.; Gogotsi, Y.; Nicolosi, V., Oxidation Stability of Colloidal Two-Dimensional Titanium Carbides (MXenes). *Chemistry of Materials* **2017,** *29* (11), 4848-4856.

145. Lin, Z.; Rozier, P.; Duployer, B.; Taberna, P.-L.; Anasori, B.; Gogotsi, Y.; Simon, P., Electrochemical and in-situ X-ray diffraction studies of Ti3C2Tx MXene in ionic liquid electrolyte. *Electrochemistry Communications* **2016,** *72*, 50-53.

146. Hu, M.; Li, Z.; Hu, T.; Zhu, S.; Zhang, C.; Wang, X., High-Capacitance Mechanism for Ti3C2 T x MXene by in Situ Electrochemical Raman Spectroscopy Investigation. *ACS nano* **2016,** *10* (12), 11344-11350.

147. Sun, D.; Hu, Q.; Chen, J.; Zhang, X.; Wang, L.; Wu, Q.; Zhou, A., Structural Transformation of MXene (V2C, Cr2C, and Ta2C) with O Groups during Lithiation: A First-Principles Investigation. *ACS applied materials & interfaces* **2015,** *8* (1), 74-81.

148. Liu, F.; Zhou, J.; Wang, S.; Wang, B.; Shen, C.; Wang, L.; Hu, Q.; Huang, Q.; Zhou, A., Preparation of High-Purity V2C MXene and Electrochemical Properties as Li-Ion Batteries. *Journal of The Electrochemical Society* **2017,** *164* (4), A709-A713.

149. Dall'Agnese, Y.; Taberna, P. L.; Gogotsi, Y.; Simon, P., Two-Dimensional Vanadium Carbide (MXene) as Positive Electrode for Sodium-Ion Capacitors. *J Phys Chem Lett* **2015,** *6* (12), 2305-9.

150. Bak, S.-M.; Qiao, R.; Yang, W.; Lee, S.; Yu, X.; Anasori, B.; Lee, H.; Gogotsi, Y.; Yang, X.-Q., Na-Ion Intercalation and Charge Storage Mechanism in 2D Vanadium Carbide. *Advanced Energy Materials* **2017,** *7* (20), 1700959.

151. Champagne, A.; Shi, L.; Ouisse, T.; Hackens, B.; Charlier, J.-C., Electronic and vibrational properties of V 2 C-based MXenes: From experiments to first-principles modeling. *Physical Review B* **2018,** *97* (11), 115439.

152. Zhang, C.; Beidaghi, M.; Naguib, M.; Lukatskaya, M. R.; Zhao, M.-Q.; Dyatkin, B.; Cook, K. M.; Kim, S. J.; Eng, B.; Xiao, X., Synthesis and charge storage properties of hierarchical niobium pentoxide/carbon/niobium carbide (MXene) hybrid materials. *Chemistry of Materials* **2016,** *28* (11), 3937-3943.

153. Ren, C. E.; Hatzell, K. B.; Alhabeb, M.; Ling, Z.; Mahmoud, K. A.; Gogotsi, Y., Charge- and size-selective ion sieving through Ti3C2T x MXene membranes. *The journal of physical chemistry letters* **2015,** *6* (20), 4026-4031.

154. Moncada, J.; Adams, W. R.; Thakur, R.; Julin, M.; Carrero, C. A., Developing a Raman-spectrokinetic approach to gain insights on the structure-reactivity relationship of supported metal oxide catalysts. *ACS Catalysis* **2018**.

155. Presser, V.; Naguib, M.; Chaput, L.; Togo, A.; Hug, G.; Barsoum, M. W., First-order Raman scattering of the MAX phases: Ti2AlN, Ti2AlC0. 5N0. 5, Ti2AlC,(Ti0. 5V0. 5) 2AlC, V2AlC, Ti3AlC2, and Ti3GeC2. *Journal of Raman Spectroscopy* **2012,** *43* (1), 168-172.

156. Spanier, J. E.; Gupta, S.; Amer, M.; Barsoum, M. W., Vibrational behavior of the M n+ 1 A X n phases from first-order Raman scattering (M= Ti, V, Cr, A= Si, X= C, N). *Physical Review B* **2005,** *71* (1), 012103.

157. Wu, M.; Wang, B.; Hu, Q.; Wang, L.; Zhou, A., The Synthesis Process and Thermal Stability of V2C MXene. *Materials* **2018,** *11* (11), 2112.

158. Yorulmaz, U.; Özden, A.; Perkgöz, N. K.; Ay, F.; Sevik, C., Vibrational and mechanical properties of single layer MXene structures: a first-principles investigation. *Nanotechnology* **2016,** *27* (33), 335702.

159. Went, G. T.; Oyama, S. T.; Bell, A. T., Laser Raman spectroscopy of supported vanadium oxide catalysts. *Journal of physical chemistry* **1990,** *94* (10), 4240-4246.

160. Olthof, B.; Khodakov, A.; Bell, A. T.; Iglesia, E., Effects of support composition and pretreatment conditions on the structure of vanadia dispersed on SiO2, Al2O3, TiO2, ZrO2, and HfO2. *The Journal of Physical Chemistry B* **2000,** *104* (7), 1516-1528.

161. Carrero, C.; Schlögl, R.; Wachs, I.; Schomaecker, R., Critical literature review of the kinetics for the oxidative dehydrogenation of propane over well-defined supported vanadium oxide catalysts. *Acs Catalysis* **2014,** *4* (10), 3357-3380.

162. Wachs, I. E.; Weckhuysen, B. M., Structure and reactivity of surface vanadium oxide species on oxide supports. *Applied Catalysis A: General* **1997,** *157* (1-2), 67-90.

163. Dresselhaus, M. S.; Jorio, A.; Hofmann, M.; Dresselhaus, G.; Saito, R., Perspectives on carbon nanotubes and graphene Raman spectroscopy. *Nano letters* **2010,** *10* (3), 751-758.

164. Dresselhaus, M. S.; Dresselhaus, G.; Saito, R.; Jorio, A., Raman spectroscopy of carbon nanotubes. *Physics reports* **2005,** *409* (2), 47-99.

165. Lukatskaya, M. R.; Halim, J.; Dyatkin, B.; Naguib, M.; Buranova, Y. S.; Barsoum, M. W.; Gogotsi, Y., Room-Temperature Carbide-Derived Carbon Synthesis by Electrochemical Etching of MAX Phases. *Angewandte Chemie International Edition* **2014,** *53* (19), 4877-4880.

166. Choi, J.-G., The surface properties of vanadium compounds by X-ray photoelectron spectroscopy. *Applied surface science* **1999,** *148* (1-2), 64-72.

167. Xie, Y.; Naguib, M.; Mochalin, V. N.; Barsoum, M. W.; Gogotsi, Y.; Yu, X.; Nam, K.-W.; Yang, X.-Q.; Kolesnikov, A. I.; Kent, P. R., Role of surface structure on Li-ion energy storage capacity of two-dimensional transition-metal carbides. *Journal of the American Chemical Society* **2014,** *136* (17), 6385-6394.

168. Chen, X. B.; Shin, J. H.; Kim, H. T.; Lim, Y. S., Raman analyses of co-phasing and hysteresis behaviors in V2O3 thin film. *Journal of Raman Spectroscopy* **2012,** *43* (12), 2025-2028.

169. Petrov, G.; Yakovlev, V.; Squier, J., Raman microscopy analysis of phase transformation mechanisms in vanadium dioxide. *Applied physics letters* **2002,** *81* (6), 1023-1025.

170. Hong-Tao, Y.; Ke-Cheng, F.; Xue-Jin, W.; Chao, L.; Chen-Juan, H.; Yu-Xin, N., Effect of nonstoichiometry on Raman scattering of VO2 films. *Chinese Physics* **2004,** *13* (1), 82.

171. Ureña-Begara, F.; Crunteanu, A.; Raskin, J.-P., Raman and XPS characterization of vanadium oxide thin films with temperature. *Applied Surface Science* **2017,** *403*, 717-727.

172. Phoempoon, P.; Sikong, L., Phase transformation of VO2 nanoparticles assisted by microwave heating. *The Scientific World Journal* **2014,** *2014*.

173. Wu, C.; Feng, F.; Xie, Y., Design of vanadium oxide structures with controllable electrical properties for energy applications. *Chemical Society Reviews* **2013,** *42* (12), 5157-5183.

174. Grant, J. T.; Carrero, C. A.; Love, A. M.; Verel, R.; Hermans, I., Enhanced two-dimensional dispersion of group V metal oxides on silica. *ACS Catalysis* **2015,** *5* (10), 5787-5793.

175. Carrero, C. A.; Keturakis, C. J.; Orrego, A.; Schomacker, R.; Wachs, I. E., Anomalous reactivity of supported V2O5 nanoparticles for propane oxidative dehydrogenation: influence of the vanadium oxide precursor. *Dalton Trans* **2013,** *42* (35), 12644-53.

176. Carrero, C. A.; Burt, S. P.; Huang, F.; Venegas, J. M.; Love, A. M.; Mueller, P.; Zhu, H.; Grant, J. T.; Mathison, R.; Hanraham, M. P., Supported two-and three-dimensional vanadium oxide species on the surface of β-SiC. *Catalysis Science & Technology* **2017,** *7* (17), 3707-3714.

177. Sakunthala, A.; Reddy, M.; Selvasekarapandian, S.; Chowdari, B.; Selvin, P. C., Energy storage studies of bare and doped vanadium pentoxide,(V 1.95 M 0.05) O 5, M= Nb, Ta, for lithium ion batteries. *Energy & Environmental Science* **2011,** *4* (5), 1712-1725.

178. Zhao, Z. J.; Wu, T.; Xiong, C.; Sun, G.; Mu, R.; Zeng, L.; Gong, J., Hydroxyl-Mediated Non-oxidative Propane Dehydrogenation over VOx/γ-Al2O3 Catalysts with Improved Stability. *Angewandte Chemie International Edition* **2018,** *57* (23), 6791-6795.

179. Liu, G.; Zhao, Z.-J.; Wu, T.; Zeng, L.; Gong, J., Nature of the Active Sites of VO x/Al2O3 Catalysts for Propane Dehydrogenation. *ACS Catalysis* **2016,** *6* (8), 5207-5214.

180. Osti, N. C.; Cote, A.; Mamontov, E.; Ramirez-Cuesta, A.; Wesolowski, D.; Diallo, S., Characteristic features of water dynamics in restricted geometries investigated with quasi-elastic neutron scattering. *Chemical Physics* **2016,** *465*, 1-8.

181. Osti, N. C.; Naguib, M.; Ostadhossein, A.; Xie, Y.; Kent, P. R.; Dyatkin, B.; Rother, G.; Heller, W. T.; Van Duin, A. C.; Gogotsi, Y., Effect of metal ion intercalation on the structure of MXene and water dynamics on its internal surfaces. *ACS applied materials & interfaces* **2016,** *8* (14), 8859-8863.

182. Shpigel, N.; Levi, M. D.; Sigalov, S.; Mathis, T. S.; Gogotsi, Y.; Aurbach, D., Direct assessment of nano-confined water in 2D Ti3C2 (MXene) electrode interspaces by a surface acoustic technique. *Journal of the American Chemical Society* **2018**.

183. Thakur, R.; VahidMohammadi, A.; Moncada, J.; Adams, W. R.; Chi, M.; Tatarchuk, B.; Beidaghi, M.; Carrero, C. A., Insights into the thermal and chemical stability of multilayered V 2 CT x MXene. *Nanoscale* **2019,** *11* (22), 10716-10726.

184. Jun, B.-M.; Kim, S.; Heo, J.; Park, C. M.; Her, N.; Jang, M.; Huang, Y.; Han, J.; Yoon, Y., Review of MXenes as new nanomaterials for energy storage/delivery and selected environmental applications. *Nano Research* **2019,** *12* (3), 471-487.

185. Verger, L.; Natu, V.; Carey, M.; Barsoum, M. W., MXenes: An Introduction of Their Synthesis, Select Properties, and Applications. *Trends in Chemistry* **2019,** *1* (7), 656-669.

186. Pang, J.; Mendes, R. G.; Bachmatiuk, A.; Zhao, L.; Ta, H. Q.; Gemming, T.; Liu, H.; Liu, Z.; Rummeli, M. H., Applications of 2D MXenes in energy conversion and storage systems. *Chemical Society reviews* **2019,** *48* (1), 72-133.

187. Siebert, J. P.; Bischoff, L.; Lepple, M.; Zintler, A.; Molina-Luna, L.; Wiedwald, U.; Birkel, C. S., Sol-gel based synthesis and enhanced processability of MAX phase Cr2GaC. *Journal of Materials Chemistry C* **2019,** *7* (20), 6034-6040.

188. Lukatskaya, M. R.; Mashtalir, O.; Ren, C. E.; Dall'Agnese, Y.; Rozier, P.; Taberna, P. L.; Naguib, M.; Simon, P.; Barsoum, M. W.; Gogotsi, Y., Cation intercalation and high volumetric capacitance of two-dimensional titanium carbide. *Science* **2013,** *341* (6153), 1502-1505.

189. Lukatskaya, M. R.; Kota, S.; Lin, Z.; Zhao, M.-Q.; Shpigel, N.; Levi, M. D.; Halim, J.; Taberna, P.-L.; Barsoum, M. W.; Simon, P., Ultra-high-rate pseudocapacitive energy storage in two-dimensional transition metal carbides. *Nature Energy* **2017,** *2* (8), 17105.

190. Bao, W.; Tang, X.; Guo, X.; Choi, S.; Wang, C.; Gogotsi, Y.; Wang, G., Porous cryo-dried MXene for efficient capacitive deionization. *Joule* **2018,** *2* (4), 778-787.

191. Shahzad, F.; Alhabeb, M.; Hatter, C. B.; Anasori, B.; Hong, S. M.; Koo, C. M.; Gogotsi, Y., Electromagnetic interference shielding with 2D transition metal carbides (MXenes). *Science* **2016,** *353* (6304), 1137-1140.

192. Mojtabavi, M.; VahidMohammadi, A.; Liang, W.; Beidaghi, M.; Wanunu, M., Single-Molecule Sensing Using Nanopores in Two-Dimensional Transition Metal Carbide (MXene) Membranes. *ACS nano* **2019,** *13* (3), 3042-3053.

193. Xie, Z.; Chen, S.; Duo, Y.; Zhu, Y.; Fan, T.; Zou, Q.; Qu, M.; Lin, Z.; Zhao, J.; Li, Y.; interfaces, Biocompatible Two-dimensional Titanium Nanosheets for Multimodal Imaging Guided Cancer Theranostics. *ACS applied materials* **2019,** *11* (25), 22129-22140.

194. Lin, H.; Chen, Y.; Shi, J., Insights into 2D MXenes for versatile biomedical applications: current advances and challenges ahead. *Advanced Science* **2018,** *5* (10), 1800518.

195. Ojima, I.; Tsai, C. Y.; Tzamarioudaki, M.; Bonafoux, D., The hydroformylation reaction. *Organic Reactions* **2000**.

196. Polo-Garzon, F.; Pakhare, D.; Spivey, J. J.; Bruce, D. A., Dry reforming of methane on Rh-doped pyrochlore catalysts: A steady-state isotopic transient kinetic study. *ACS Catalysis* **2016,** *6* (6), 3826-3833.

197. Buelens, L. C.; Galvita, V. V.; Poelman, H.; Detavernier, C.; Marin, G. B., Super-dry reforming of methane intensifies CO2 utilization via Le Chatelier's principle. *Science* **2016,** *354* (6311), 449-452.

198. Li, M.; van Veen, A. C., Tuning the catalytic performance of Ni-catalysed dry reforming of methane and carbon deposition via Ni-CeO 2-x interaction. *Applied Catalysis B: Environmental* **2018,** *237*, 641-648.

199. Yan, B.; Yang, X.; Yao, S.; Wan, J.; Myint, M.; Gomez, E.; Xie, Z.; Kattel, S.; Xu, W.; Chen, J. G., Dry reforming of ethane and butane with CO2 over PtNi/CeO2 bimetallic catalysts. *ACS Catalysis* **2016,** *6* (11), 7283-7292.

200. Köpfle, N.; Götsch, T.; Grünbacher, M.; Carbonio, E. A.; Hävecker, M.; Knop-Gericke, A.; Schlicker, L.; Doran, A.; Kober, D.; Gurlo, A., Zirconium-Assisted Activation of Palladium To Boost Syngas Production by Methane Dry Reforming. *Angewandte Chemie International Edition* **2018,** *57* (44), 14613-14618.

201. Liu, Z.; Grinter, D. C.; Lustemberg, P. G.; Nguyen-Phan, T. D.; Zhou, Y.; Luo, S.; Waluyo, I.; Crumlin, E. J.; Stacchiola, D. J.; Zhou, J., Dry Reforming of Methane on a Highly-Active Ni-CeO2 Catalyst: Effects of Metal-Support Interactions on C− H Bond Breaking. *Angewandte Chemie International Edition* **2016,** *55* (26), 7455-7459.

202. Le Saché, E.; Pastor-Pérez, L.; Watson, D.; Sepúlveda-Escribano, A.; Reina, T., Ni stabilised on inorganic complex structures: superior catalysts for chemical CO2 recycling via dry reforming of methane. *Applied Catalysis B: Environmental* **2018,** *236*, 458-465.

203. Theofanidis, S. A.; Galvita, V. V.; Poelman, H.; Dharanipragada, N. A.; Longo, A.; Meledina, M.; Van Tendeloo, G.; Detavernier, C.; Marin, G. B., Fe-containing magnesium aluminate support for stability and carbon control during methane reforming. *ACS catalysis* **2018,** *8* (7), 5983-5995.

204. Theofanidis, S. A.; Galvita, V. V.; Poelman, H.; Marin, G. B., Enhanced carbon-resistant dry reforming Fe-Ni catalyst: Role of Fe. *ACS Catalysis* **2015,** *5* (5), 3028-3039.

205. Aramouni, N. A. K.; Touma, J. G.; Tarboush, B. A.; Zeaiter, J.; Ahmad, M. N., Catalyst design for dry reforming of methane: analysis review. *Renewable Sustainable Energy Reviews* **2018,** *82*, 2570-2585.

206. Akri, M.; Zhao, S.; Li, X.; Zang, K.; Lee, A. F.; Isaacs, M. A.; Xi, W.; Gangarajula, Y.; Luo, J.; Ren, Y., Atomically dispersed nickel as coke-resistant active sites for methane dry reforming. *Nature Communications* **2019,** *10* (1), 1-10.

207. Arora, S.; Prasad, R., An overview on dry reforming of methane: strategies to reduce carbonaceous deactivation of catalysts. *RSC advances* **2016,** *6* (110), 108668-108688.

208. Chi, M.; Sun, X.; Sujan, A.; Davis, Z.; Tatarchuk, B. J., A quantitative XPS examination of UV induced surface modification of TiO2 sorbents for the increased saturation capacity of sulfur heterocycles. *Fuel* **2019,** *238*, 454-461.

209. Moncada, J.; Adams, W. R.; Thakur, R.; Julin, M.; Carrero, C. A., Developing a Raman Spectrokinetic Approach To Gain Insights into the Structure–Reactivity Relationship of Supported Metal Oxide Catalysts. *ACS Catalysis* **2018,** *8*, 8976-8986.

210. Mears, D. E., Diagnostic criteria for heat transport limitations in fixed bed reactors. *Journal of Catalysis* **1971,** *20* (2), 127-131.

211. Carberry, J., Physico-chemical aspects of mass and heat transfer in heterogeneous catalysis. In *Catalysis*, Springer: 1987; pp 131-171.

212. Ghidiu, M.; Lukatskaya, M. R.; Zhao, M.-Q.; Gogotsi, Y.; Barsoum, M. W., Conductive two-dimensional titanium carbide 'clay'with high volumetric capacitance. *Nature* **2014,** *516* (7529), 78.

213. Dall'Agnese, Y.; Taberna, P.-L.; Gogotsi, Y.; Simon, P., Two-dimensional vanadium carbide (MXene) as positive electrode for sodium-ion capacitors. *The journal of physical chemistry letters* **2015,** *6* (12), 2305-2309.

214. Naguib, M.; Unocic, R. R.; Armstrong, B. L.; Nanda, J., Large-scale delamination of multi-layers transition metal carbides and carbonitrides "MXenes". *Dalton transactions* **2015,** *44* (20), 9353-9358.

215. Hoffman, E. N.; Yushin, G.; Barsoum, M. W.; Gogotsi, Y., Synthesis of carbide-derived carbon by chlorination of Ti2AlC. *Chemistry of materials* **2005,** *17* (9), 2317-2322.

216. Hoffman, E. N.; Yushin, G.; El-Raghy, T.; Gogotsi, Y.; Barsoum, M. W., Micro and mesoporosity of carbon derived from ternary and binary metal carbides. *Microporous and Mesoporous Materials* **2008,** *112* (1-3), 526-532.

217. Abdelmalak, M. N., *MXenes: A New Family of Two-Dimensional Materials and its Application as Electrodes for Li-ion Batteries*. Drexel University Philadelphia, PA: 2014.

218. Li, Z.; Wang, L.; Sun, D.; Zhang, Y.; Liu, B.; Hu, Q.; Zhou, A., Synthesis and thermal stability of two-dimensional carbide MXene Ti3C2. *Materials Science and Engineering: B* **2015,** *191*, 33-40.

219. Lotfi, R.; Naguib, M.; Yilmaz, D. E.; Nanda, J.; Van Duin, A. C., A comparative study on the oxidation of two-dimensional Ti 3 C 2 MXene structures in different environments. *Journal of Materials Chemistry A* **2018,** *6* (26), 12733-12743.

220. Shen, W.-J.; Sun, K.; Lee, C., Electrical characterization and Raman spectroscopy of individual vanadium pentoxide nanowire. *Journal of Nanoparticle Research* **2011,** *13* (10), 4929.

221. Baktash, E.; Littlewood, P.; Pfrommer, J.; Schomäcker, R.; Driess, M.; Thomas, A., Controlled formation of nickel oxide nanoparticles on mesoporous silica using molecular Ni4O4 clusters as precursors: enhanced catalytic performance for dry reforming of methane. *ChemCatChem* **2015,** *7* (8), 1280-1284.

222. Li, Z.; Wu, Y., 2D Early Transition Metal Carbides (MXenes) for Catalysis. *Small* **2019**, 1804736.

223. Kosinov, N.; Coumans, F. J.; Li, G.; Uslamin, E.; Mezari, B.; Wijpkema, A. S.; Pidko, E. A.; Hensen, E. J., Stable Mo/HZSM-5 methane dehydroaromatization catalysts optimized for high-temperature calcination-regeneration. *Journal of Catalysis* **2017,** *346*, 125-133.

224. Gao, J.; Zheng, Y.; Jehng, J.-M.; Tang, Y.; Wachs, I. E.; Podkolzin, S. G., Identification of molybdenum oxide nanostructures on zeolites for natural gas conversion. *Science* **2015,** *348* (6235), 686-690.

225. Guo, X.; Fang, G.; Li, G.; Ma, H.; Fan, H.; Yu, L.; Ma, C.; Wu, X.; Deng, D.; Wei, M., Direct, nonoxidative conversion of methane to ethylene, aromatics, and hydrogen. *Science* **2014,** *344* (6184), 616-619.

226. Kosinov, N.; Uslamin, E. A.; Meng, L.; Parastaev, A.; Liu, Y.; Hensen, E. J., Reversible Nature of Coke Formation on Mo/ZSM-5 Methane Dehydroaromatization Catalysts. *Angewandte Chemie International Edition* **2019,** *58* (21), 7068-7072.

227. Lezcano-González, I.; Oord, R.; Rovezzi, M.; Glatzel, P.; Botchway, S. W.; Weckhuysen, B. M.; Beale, A. M., Molybdenum Speciation and its Impact on Catalytic Activity during

Methane Dehydroaromatization in Zeolite ZSM-5 as Revealed by Operando X-Ray Methods. *Angewandte Chemie International Edition* **2016,** *55* (17), 5215-5219.

228. Zhang, Y.; Jiang, H., A novel route to improve methane aromatization by using a simple composite catalyst. *Chemical communications* **2018,** *54* (73), 10343-10346.

229. Song, Y.; Zhang, Q.; Xu, Y.; Zhang, Y.; Matsuoka, K.; Zhang, Z.-G., Coke accumulation and deactivation behavior of microzeolite-based Mo/HZSM-5 in the non-oxidative methane aromatization under cyclic CH4-H2 feed switch mode. *Applied Catalysis A: General* **2017,** *530*, 12-20.

230. Anasori, B.; Gogotsi, Y., Introduction to 2D Transition Metal Carbides and Nitrides (MXenes). In *2D Metal Carbides and Nitrides (MXenes)*, Springer: 2019; pp 3-12.

231. Vollmer, I.; Yarulina, I.; Kapteijn, F.; Gascon, J., Progress in Developing a Structure-Activity Relationship for the Direct Aromatization of Methane. *ChemCatChem* **2019,** *11* (1), 39-52.

232. Razdan, N. K.; Kumar, A.; Bhan, A., Controlling kinetic and diffusive length-scales during absorptive hydrogen removal in methane dehydroaromatization on MoCx/H-ZSM-5 catalysts. *Journal of Catalysis* **2019,** *372*, 370-381.

233. Rahman, M.; Infantes-Molina, A.; Boubnov, A.; Bare, S. R.; Stavitski, E.; Sridhar, A.; Khatib, S. J., Increasing the catalytic stability by optimizing the formation of zeolite-supported Mo carbide species ex situ for methane dehydroaromatization. *Journal of Catalysis* **2019,** *375*, 314-328.

234. Sridhar, A.; Rahman, M.; Infantes-Molina, A.; Wylie, B. J.; Borcik, C. G.; Khatib, S. J., Bimetallic Mo-Co/ZSM-5 and Mo-Ni/ZSM-5 catalysts for methane dehydroaromatization: A study of the effect of pretreatment and metal loadings on the catalytic behavior. *Applied Catalysis A: General* **2020,** *589*, 117247.

235. Tessonnier, J.-P.; Louis, B.; Rigolet, S.; Ledoux, M. J.; Pham-Huu, C. J. A. C. A. G., Methane dehydro-aromatization on Mo/ZSM-5: About the hidden role of Brønsted acid sites. **2008,** *336* (1-2), 79-88.

236. Ruitenbeek, M.; Weckhuysen, B. M., A radical twist to the versatile behavior of iron in selective methane activation. *Angewandte Chemie International Edition* **2014,** *53* (42), 11137-11139.

237. Li, W.; Meitzner, G. D.; Borry III, R. W.; Iglesia, E., Raman and X-ray absorption studies of Mo species in Mo/H-ZSM5 catalysts for non-oxidative CH4 reactions. *Journal of Catalysis* **2000,** *191* (2), 373-383.

238. Zaikovskii, V.; Vosmerikov, A.; Anufrienko, V.; Korobitsyna, L.; Kodenev, E.; Echevskii, G.; Vasenin, N.; Zhuravkov, S. P.; Matus, E.; Ismagilov, Z., Properties and deactivation of the active sites of an MoZSM-5 catalyst for methane dehydroaromatization: Electron microscopic and EPR studies. *Kinetics and catalysis* **2006,** *47* (3), 389-394.

239. Martínez, A.; Peris, E., Non-oxidative methane dehydroaromatization on Mo/HZSM-5 catalysts: Tuning the acidic and catalytic properties through partial exchange of zeolite protons with alkali and alkaline-earth cations. *Applied Catalysis A: General* **2016,** *515*, 32-44.

240. Ma, D.; Shu, Y.; Cheng, M.; Xu, Y.; Bao, X., On the induction period of methane aromatization over Mo-based catalysts. *Journal of Catalysis* **2000,** *194* (1), 105-114.

241. Borry, R. W.; Kim, Y. H.; Huffsmith, A.; Reimer, J. A.; Iglesia, E., Structure and density of Mo and acid sites in Mo-exchanged H-ZSM5 catalysts for nonoxidative methane conversion. *The Journal of Physical Chemistry B* **1999,** *103* (28), 5787-5796.

242. Kumar, A.; Song, K.; Liu, L.; Han, Y.; Bhan, A., Absorptive Hydrogen Scavenging for Enhanced Aromatics Yield During Non-oxidative Methane Dehydroaromatization on Mo/H-ZSM-5 Catalysts. *Angewandte Chemie* **2018,** *130* (47), 15803-15808.

243. Tessonnier, J.-P.; Louis, B.; Walspurger, S.; Sommer, J.; Ledoux, M.-J.; Pham-Huu, C., Quantitative measurement of the Brönsted acid sites in solid acids: toward a single-site design of Mo-modified ZSM-5 zeolite. *The Journal of Physical Chemistry B* **2006,** *110* (21), 10390-10395.

244. Cook, B.; Mousko, D.; Hoelderich, W.; Zennaro, R., Conversion of methane to aromatics over Mo2C/ZSM-5 catalyst in different reactor types. *Applied Catalysis A: General* **2009,** *365* (1), 34-41.

245. Xiang, Y.; Wang, H.; Cheng, J.; Matsubu, J., Progress and prospects in catalytic ethane aromatization. *Catalysis Science & Technology* **2018,** *8* (6), 1500-1516.

246. Nahreen, S.; Praserthdam, S.; Perez Beltran, S.; Balbuena, P. B.; Adhikari, S.; Gupta, R. B., Catalytic upgrading of methane to higher hydrocarbon in a nonoxidative chemical conversion. *Energy & Fuels* **2016,** *30* (4), 2584-2593.

247. Rahman, M.; Sridhar, A.; Khatib, S. J., Impact of the presence of Mo carbide species prepared ex situ in Mo/HZSM-5 on the catalytic properties in methane aromatization. *Applied Catalysis A: General* **2018,** *558*, 67-80.

248. Majhi, S.; Mohanty, P.; Dalai, A. K.; Pant, K. K., Statistical Optimization of Process Variables for Methane Conversion over Zn-Mo/H-ZSM-5 Catalysts in the Presence of Methanol. *Energy Technology* **2013,** *1* (2-3), 157-165.

249. Vollmer, I.; Mondal, A.; Yarulina, I.; Abou-Hamad, E.; Kapteijn, F.; Gascon, J., Quantifying the impact of dispersion, acidity and porosity of Mo/HZSM-5 on the performance in methane dehydroaromatization. *Applied Catalysis A: General* **2019,** *574*, 144-150.

250. Ma, D.; Shu, Y.; Han, X.; Liu, X.; Xu, Y.; Bao, X., Mo/HMCM-22 catalysts for methane dehydroaromatization: a multinuclear MAS NMR study. *The Journal of Physical Chemistry B* **2001,** *105* (9), 1786-1793.

251. Shu, Y.; Ma, D.; Liu, X.; Han, X.; Xu, Y.; Bao, X., An MAS NMR study on the Mo-modified phosphoric rare earth (HZRP-1) penta-sil zeolite catalyst. *The Journal of Physical Chemistry B* **2000,** *104* (34), 8245-8249.

252. Li, S.; Zhang, C.; Kan, Q.; Wang, D.; Wu, T.; Lin, L., The function of Cu (II) ions in the Mo/CuH-ZSM-5 catalyst for methane conversion under non-oxidative condition. *Applied Catalysis A: General* **1999,** *187* (2), 199-206.

253. Wang, L.; Xu, Y.; Wong, S.-T.; Cui, W.; Guo, X., Activity and stability enhancement of MoHZSM-5-based catalysts for methane non-oxidative transformation to aromatics and C2 hydrocarbons: Effect of additives and pretreatment conditions. *Applied Catalysis A: General* **1997,** *152* (2), 173-182.

254. Aboul-Gheit, A. K.; El-Masry, M. S.; Awadallah, A. E., Oxygen free conversion of natural gas to useful hydrocarbons and hydrogen over monometallic Mo and bimetallic Mo–Fe, Mo–Co or Mo–Ni/HZSM-5 catalysts prepared by mechanical mixing. *Fuel processing technology* **2012,** *102*, 24-29.

255. Burns, S.; Hargreaves, J.; Pal, P.; Parida, K.; Parija, S., The effect of dopants on the activity of MoO3/ZSM-5 catalysts for the dehydroaromatisation of methane. *Catalysis Today* **2006,** *114* (4), 383-387.

256. Tempelman, C. H.; Hensen, E. J., On the deactivation of Mo/HZSM-5 in the methane dehydroaromatization reaction. *Applied Catalysis B: Environmental* **2015,** *176*, 731-739.

257. Liu, Z.; Li, L.; Iglesia, E., Catalytic pyrolysis of methane on Mo/H-ZSM5 with continuous hydrogen removal by permeation through dense oxide films. *Catalysis letters* **2002,** *82* (3-4), 175-180.

258. Li, L.; Borry, R. W.; Iglesia, E., Reaction-transport simulations of non-oxidative methane conversion with continuous hydrogen removal—homogeneous–heterogeneous reaction pathways. *Chemical engineering science* **2001,** *56* (5), 1869-1881.

259. Borry, R.; Lu, E. C.; Kim, Y.-H.; Iglesia, E., Non-oxidative catalytic conversion of methane with continuous hydrogen removal. *Stud. Surf. Sci. Catal* **1998,** *119*, 403-410.

260. Kumar, A.; Song, K.; Liu, L.; Han, Y.; Bhan, A., Absorptive Hydrogen Scavenging for Enhanced Aromatics Yield During Non-oxidative Methane Dehydroaromatization on Mo/H-ZSM-5 Catalysts. *Angewandte Chemie International Edition* **2018,** *57* (47), 15577-15582.

261. Rajagopal, S.; Marini, H.; Marzari, J.; Miranda, R., Silica-alumina-supported acidic molybdenum catalysts-TPR and XRD characterization. *Journal of Catalysis* **1994,** *147* (2), 417-428.

262. Arnoldy, P.; De Jonge, J.; Moulijn, J., Temperature-programed reduction of molybdenum (VI) oxide and molybdenum (IV) oxide. *The Journal of Physical Chemistry* **1985,** *89* (21), 4517-4526.

263. Liu, H.; Shen, W.; Bao, X.; Xu, Y., Identification of Mo active species for methane dehydro-aromatization over Mo/HZSM-5 catalysts in the absence of oxygen: 1H MAS NMR and EPR investigations. *Journal of Molecular Catalysis A: Chemical* **2006,** *244* (1-2), 229-236.

264. Liu, H.; Shen, W.; Bao, X.; Xu, Y., Methane dehydroaromatization over Mo/HZSM-5 catalysts: the reactivity of MoCx species formed from MoOx associated and non-associated with Brönsted acid sites. *Applied Catalysis A: General* **2005,** *295* (1), 79-88.

265. Liu, H.; Bao, X.; Xu, Y., Methane dehydroaromatization under nonoxidative conditions over Mo/HZSM-5 catalysts: Identification and preparation of the Mo active species. *Journal of Catalysis* **2006,** *239* (2), 441-450.

266. Hongmei, L.; Yide, X., H2-TPR study on Mo/HZSM-5 catalyst for CH4 dehydroaromatization. *Chinese Journal of Catalysis* **2006,** *27* (4), 319-323.

267. Bouchy, C.; Hamid, S. B. D.-A.; Derouane, E. G., A new route to the metastable FCC molybdenum carbide α-MoC1− x. *Chemical Communications* **2000,** (2), 125-126.

268. Bouchy, C.; Schmidt, I.; Anderson, J.; Jacobsen, C.; Derouane, E.; Hamid, S. D.-A., Metastable fcc α-MoC1− x supported on HZSM5: preparation and catalytic performance for the non-oxidative conversion of methane to aromatic compounds. *Journal of Molecular Catalysis A: Chemical* **2000,** *163* (1-2), 283-296.

269. Hamid, S. B. D.-A.; Anderson, J. R.; Schmidt, I.; Bouchy, C.; Jacobsen, C. J.; Derouane, E. G., Effect of the activation procedure on the performance of Mo/H-MFI catalysts for the non-oxidative conversion of methane to aromatics. *Catalysis today* **2000,** *63* (2-4), 461-469.

270. Liu, B.; Jiang, L.; Sun, H.; Au, C., XPS, XAES, and TG/DTA characterization of deposited carbon in methane dehydroaromatization over Ga–Mo/ZSM-5 catalyst. *Applied surface science* **2007,** *253* (11), 5092-5100.

271. Qi, S.; Yang, B., Methane aromatization using Mo-based catalysts prepared by microwave heating. *Catalysis today* **2004,** *98* (4), 639-645.

272. Jiang, S.; Zhang, H.; Yan, Y.; Zhang, X., Stability and deactivation of Fe-ZSM-5 zeolite catalyst for catalytic wet peroxide oxidation of phenol in a membrane reactor. *RSC Advances* **2015,** *5* (51), 41269-41277.

273. Liu, B.; France, L.; Wu, C.; Jiang, Z.; Kuznetsov, V. L.; Al-Megren, H. A.; Al-Kinany, M.; Aldrees, S. A.; Xiao, T.; Edwards, P. P., Methanol-to-hydrocarbons conversion over MoO 3/H-ZSM-5 catalysts prepared via lower temperature calcination: a route to tailor the distribution and evolution of promoter Mo species, and their corresponding catalytic properties. *Chemical science* **2015,** *6* (9), 5152-5163.

274. Liu, H.; Li, T.; Tian, B.; Xu, Y., Study of the carbonaceous deposits formed on a Mo/HZSM-5 catalyst in methane dehydro-aromatization by using TG and temperature-programmed techniques. *Applied Catalysis A: General* **2001,** *213* (1), 103-112.

275. Wang, L.; Tysoe, W., An investigation of ethylene hydrogenation catalyzed by metallic molybdenum using an isolatable high-pressure reactor: Identification of the reaction site and the role of carbonaceous deposits. *Journal of Catalysis* **1991,** *128* (2), 320-336.

276. Wang, D.; Lunsford, J. H.; Rosynek, M. P., Catalytic conversion of methane to benzene over Mo/ZSM-5. *Topics in Catalysis* **1996,** *3* (3-4), 289-297.

277. Moncada, J.; Adams, W. R.; Thakur, R.; Julin, M.; Carrero, C. A., Developing a Raman Spectrokinetic Approach To Gain Insights into the Structure–Reactivity Relationship of Supported Metal Oxide Catalysts. *ACS Catalysis* **2018,** *8* (10), 8976-8986.

278. Vakili, M.; Cagnetta, G.; Huang, J.; Yu, G.; Yuan, J., Synthesis and regeneration of a MXene-based pollutant adsorbent by mechanochemical methods. *Molecules* **2019,** *24* (13), 2478.

279. Zhang, J.; Li, S.; Hu, S.; Zhou, Y., Chemical Stability of Ti3C2 MXene with Al in the Temperature Range 500–700° C. *Materials* **2018,** *11* (10), 1979.